IN SITU CHARACTERIZATION OF DAMAGE KINETICS DURING FOREIGN OBJECT DEBRIS (FOD) IMPACT OF SILICON CARBIDE

by

Nesredin Kedir

A Dissertation

Submitted to the Faculty of Purdue University

In Partial Fulfillment of the Requirements for the degree of

Doctor of Philosophy

School of Materials Engineering

West Lafayette, Indiana

May 2021

THE PURDUE UNIVERSITY GRADUATE SCHOOL

STATEMENT OF COMMITTEE APPROVAL

Dr. Weinong W. Chen, Chair

School of Aeronautics and Astronautics

School of Materials Engineering

Dr. Rodney Trice

School of Materials Engineering

Dr. Elliott Slamovich

School of Materials Engineering

Dr. Sung R. Choi

Naval Air Warfare Center (NAVAIR)

Approved by:

Dr. David Bahr

In memory of, Prof. Laura LeMire. An amazing mentor, a devoted educator who strove to bring the best out of her students, and a tireless champion for the expansion of STEM education in underrepresented communities.

To my parents for instilling in me the values of hard work and uncompromising principles. As well as for their ever-present support of my personal endeavors.

ACKNOWLEDGMENTS

First and foremost, I want to express my sincere gratitude to Prof. Weinong Chen for accepting me as a student in his research group. In addition to lending valuable input to my research, Prof. Chen provided opportunities for me to hone my communication and leadership skills. Under his guidance, I have become more independent and capable as an engineer.

I want to thank my internal committee members Prof. Rodney Trice and Prof. Eliot Slamovich. They rendered honest feedback on my work and enabled me to improve on my research efforts.

I want to thank Dr. Sung Choi from the Naval Air Warfare Center (NAVAIR), for serving as an external member in my committee and for inspiring this work. His mentorship during my time at NAVAIR and his support during my graduate studies have been invaluable.

I want to thank Prof. Sanjay Sampath and Dr. Eugenio Garcia from the center for thermal spray research (CTSR) at Stoney Brook University for their generosity in processing the environmental barrier coatings (EBCs) for this research.

I want to thank Dr. Kamel Fezzaa, Dr. Tao Sun, Alex Deriy, and Pavel Shevchenko at the Advanced Photon Source in Argonne National Laboratory for their assistance in the experiments.

Finally, I want to thank all past and present members of my research group for providing a welcoming and collaborative atmosphere. I am grateful for all their help in my research efforts.

This research used resources of the Advanced Photon Source, a US Department of Energy (DOE) Office of Science User Facility operated for the DOE Office of Science by Argonne National Laboratory under Contract No. DE-AC02-06CH11357.

This research was financially supported in part by the Purdue Doctoral Fellowship and a grant (N00014-17 -1-2711) by the Office of Naval Research.

TABLE OF CONTENTS

LIST OF TABLES

LIST OF FIGURES

SYMBOLS

a	Hertzian radius of contact (μm)
α	Coefficient of thermal expansion ($°C^{-1}$)
β	Elastic contact time constant
C_L	Longitudinal wave velocity (m/s)
C_S	Shear wave velocity (m/s)
d_p	Coating penetration depth (μm)
d_p/V_{im}	Relative coating penetration depth (μm)
$\frac{d}{dt}\left(\frac{d_p}{V_{im}}\right)$	Rate of relative coating penetration depth (μm/m/s)
D_s	Spherical projectile diameter (mm)
E	Elastic modulus, Hertzian half space (GPa)
E'	Elastic modulus, spherical projectile (GPa)
E^*	Effective modulus (GPa)
E_{im}	Impact energy (J)
γ	Cone crack half-apex angle (°)
G	Shear modulus (GPa)
H_p	Projectile hardness (GPa)
H_t	Target hardness (GPa)
K_{IC}	Mode I fracture toughness ($MPa \cdot m^{1/2}$)
m	Mass of projectile (kg)
ν	Poisson's ratio, Hertzian half space
ν'	Poisson's ratio, spherical projectile
P	Impact load (kN)
p_m	Maximum contact pressure (GPa)
ρ	Density, Hertzian half space (kg/m^3)
ρ'	Density, spherical projectile (kg/m^3)
r	Radial distance from center of contact (μm)
R_s	Radius of spherical projectile (mm)
σ_m	Maximum Hertzian radial stress (GPa)
t_e	Predicted elastic contact time (μs)
t	Observed contact time (μs)
u_z	Normal displacement, Hertzian half space (μm)
u_z'	Normal displacement, spherical projectile (μm)
V_{im}	Impact velocity (m/s)
$V(t_i)$	Impact velocity at a given time t_i (m/s)
$\frac{\Delta V}{V_{im}}$	Relative change in projectile velocity during coating penetration
$\left(\frac{\Delta V}{V_{im}}\right)_{max}$	Maximum relative change in projectile velocity during coating penetration
w	Width of uncoated specimen (mm)
w'	Width of coated specimen (mm)

NOMENCLATURE

APS	Air (or atmospheric) plasma spray
Al_2O_3	Alumina
BSAS	Barium-strontium aluminosilicate
BSE	Backscattered electron (imaging)
CGT	Ceramic gas turbine
CMAS	Calcium magnesium aluminosilicate
CMCs	Ceramic matrix composites
CTE	Coefficient of thermal expansion
CSGT	Ceramic stationary gas turbine
CVD	Chemical vapor deposition
CVI	Chemical vapor infiltration
DG	Delay generator
EBCs	Environmental barrier coatings
EB-PVD	Electron beam physical vapor deposition
EDS	Energy dispersive X-ray spectroscopy
EOI	Edge on impact
FOD	Foreign object debris
FXR	Flash X-ray radiography
GPSSN	Gas pressure sintered silicon nitride
MMCs	Metal matrix composites
Na_2SO_4	Sodium sulfide (salt)
PCI	Phase contrast imaging
PDV	Pulsed doppler velocimetry
PIP	Polymer infiltration and pyrolysis
PSPVD	Plasma vapor physical vapor deposition
PSZ	partially stabilized zirconia
RF	Radio frequency
SE	Secondary electron imaging
SiC	Silicon carbide
SiC_f	Silicon carbide fiber
Si_3N_4	Silicon nitride
SiO_2	Silicon dioxide, silica
$Si(OH)_x$	Silicon hydroxide
SPS	Solution plasma spray
SPPS	Solution precursor plasma spray
TBCs	Thermal barrier coatings
TGO	Thermally grown oxide
TIT	Turbine inlet temperature
XRD	X-ray diffraction
$Yb_2Si_xO_y$	Ytterbium silicates
YSZ	Yttria stabilized zirconia

ABSTRACT

Silicon based ceramics and ceramic matrix composites (CMCs) are materials with a capacity to replace current metallic components in the hot-section of gas turbine engines. These materials enable higher gas turbine inlet temperatures, and this leads to decreases in both fuel consumption and greenhouse gas emissions. To date, only static CMC components have been implemented successfully. Attempts to transition rotating components have been unsuccessful primarily due to failures from impact damage by ingested or internally spawned foreign object debris (FOD).

This dissertation investigates the applicability of high intensity pulsed synchrotron X-ray radiography for *in situ* characterization/visualization of FOD impact at high temporal and spatial resolutions. Previous FOD impact studies relied on post-impact strength evaluations and/or postmortem fractography to establish damage mechanisms. These approaches fail to provide any information on the damage kinetics and in some cases lead to erroneous interpretations of damage.

In this effort, the facility for *in situ* experiments is initially established and three studies are conducted to evaluate the capability. The first study is a baseline in which silicon carbide (SiC) ceramic specimens are subject to FOD impact by spherical projectiles of partially stabilized zirconia (PSZ), silicon nitride (Si_3N_4), and steel. As an extension, the second study investigates the effect of an air plasma sprayed silicon/mullite environmental barrier coating (EBC) layer on the FOD impact response of SiC specimens by PSZ and Si_3N_4 projectiles. EBCs are prime reliant for thermochemical protection in gas turbine environments and very little is known about their damage tolerance under FOD impact. The third and final study, considers FOD impact in narrow SiC specimens with and without EBCs, by PSZ, Si_3N_4, and steel projectiles. Narrow specimen geometries mimic low curvature segments in ceramic gas turbine blades.

The results from all three studies indicated the exceptional capability of pulsed synchrotron X-ray radiography for characterizing damage kinetics during FOD impact. Damage histories showing multiple crack initiation and propagation in the ceramic, as well as penetration, ejecta formation, and delamination in the EBC, were retrieved. This transient data is extremely valuable for constructing reliable numerical FOD impact models and accurate life prediction of ceramic components. Additionally, the EBC layer and specimen geometry were found to control the level of damage in the SiC ceramic. For the EBC itself, the extent of damage was determined to depend mainly on projectile hardness and impact energy.

1. INTRODUCTION

Gas turbine engines are critical to the sustainment and growth of both aviation and energy industries across the globe. As the world population continues to grow, the demand for services from these sectors will also increase drastically. Over the next decade, global air travel by freight and passengers is expected to increase at an annual rate of 4 % and 5 % respectively [1]. Similarly, the world demand for electric power is expected to increase at a rate of 2.1 % per annum for the next three decades [2]. In the latter, gas fired power plants are growing rapidly at the expense of coal powerplants due to low prices in natural gas. Along with increase in demand for air transport and electricity, there is a major concern regarding increases in greenhouse gas emissions. One approach that addresses challenges in demand for energy and transport, as well as associated emissions is improvement in efficiency of gas turbine technologies.

Current gas turbines are relatively inefficient as compared to the ideal heat engine described by the Brayton cycle. For the case of power generators, the maximum thermal efficiency[1] attained from shaft output alone is ~ 45 % [3]. The shaft power is often combined with recoverable heat from exhaust gas (combined Brayton and Rankine cycles) to increase the efficiency to ~ 60 % [3,4]. In the case of aircraft engines, a slightly higher thermal efficiency of 55 % is noted to be possible with current technologies [5,6]. One of the key requirements for further increase in thermal efficiency is increase in the turbine inlet temperature (TIT). The latter is in turn dependent on the temperature capability of the turbine materials. Current engines use nickel base superalloys with ceramic thermal barrier coatings (TBCs) to attain a TIT at the component surface of ≤ 1200 °C, after cooling[2] the combustion gas from an initial temperature of ~ 1600 °C [7,8]. Increase in TIT would thus require a material which reduces or eliminates cooling and hence enables a greater portion of the compressed gas to be used during the combustion process. As will be discussed in the next section, a transition from metallic to ceramic materials is a promising approach for increasing the TIT.

[1] Thermal efficiency corresponds to the amount of heat energy (input) that is converted into useful work (output).
[2] Gas from the compressor section is diverted to the turbine for cooling the incoming combustion gas.

1.1 Application of Ceramics in Gas Turbine Engines

Ceramics are inorganic materials composed of ionically bonded compounds which often retain some level of covalent character. They can be as rudimentary as traditional silicates found in households (e.g. clays, brick, tiles, etc.) or as advanced as alumina and boron carbide ballistic armor plates. Among many of their characteristics, they are typically recognized for their insulative behavior, their optical transparency, and their brittle response under quasi-static or dynamic tensile stresses (i.e. exceptionally high hardness and low ductility). Since the mid 1940's, scientists have sought to harness their refractory nature to increase the inlet temperature in gas turbines [9]. These efforts considered a variety of approaches including ceramic coatings and ceramic inclusions in metals (cermet's), as well as standalone ceramic and ceramic matrix composites (CMCs) [10-14].

Initial attempts to study and implement ceramics were unsuccessful due to the inability of the materials to withstand the harsh engine environment. Oxide ceramics were found to lack the necessary thermal shock resistance, carbide ceramics were difficult to manufacture in pure form, and the endurance of cermet materials was found to degrade due to creep [12-14,]. However, silicon based ceramics (carbides and nitrides) did show potential for tolerating higher temperatures ($\geq$ 1400 °C) and thermal gradients [13-14]. These materials were also noted for their capacity to render higher strengths, lower densities, higher resistance to wear and creep, and enhanced stabilities under normal oxidizing environments. As a result, research efforts, starting in the 1960s, were geared towards development of processing methods and characterization of properties to build a materials database for silicon based ceramics [15]. The latter resulted in maturation of technologies for manufacturing relatively dense silicon carbide (SiC) and silicon nitride (Si_3N_4) via reaction bonding, reaction sintering, pressureless sintering, hot pressing, and hot isostatic pressing methods. Slight increase in toughness of the monolithic ceramics via crack deflection and bridging was also possible by either using additives to control the microstructure and form elongated grains (*in situ* toughening) or by incorporating whiskers as secondary phases (*ex situ* toughening) [16-18]. Still, these toughened monoliths were considered brittle relative to their metallic counterparts and in the late 1980s more attention was given to the development of continuous fiber reinforced CMCs. The most common CMCs retain fabrics of continuous fiber (with a weak interphase coating for SiC) and a ceramic matrix that can be formed by reactive melt infiltration (MI) [19], ceramic slurry infiltration [20], preceramic polymer infiltration and pyrolysis (PIP) [20], or chemical vapor infiltration (CVI) [21] processes. CMCs offer the same benefits as

advanced ceramics in addition to a nearly ten-fold increase in toughness/damage tolerance [21,22]. Over the past four decades, composites consisting of carbon, SiC, and alumina-mullite fabrics and various matrix materials (e.g. carbon, glass, SiC, Si_3N_4, alumina, etc.) have been investigated. From the multitude of options, SiC_f/SiC CMCs have shown the most promise for fielding in gas turbine engines.

The earliest program which applied ceramic components in gas turbines was the ceramic gas turbine (CGT) program in Japan [23-26]. The CGT program operated between1988 to 1998 and considered small single-shaft (CGT 301) and two-shaft (CGT 302 and 303) gas turbines for power generation (~ 300 kW). Nearly two dozen ceramic parts, manly Si_3N_4, were developed for these engines including combustors, turbine blades, and turbine nozzle assemblies. Over 2000 cumulative hours of rig testing at 1200 ℃ and 30 hours at 1350 ℃ have been achieved by these components. Shortly after the start of the CGT program, a similar effort denoted as the ceramic stationary gas turbine (CSGT) program was initiated in the United States [27-29]. Over a span of nine years (1992-2001), a larger single-shaft power generating gas turbine engine (> 4 MW) was used to evaluate ceramic nozzles (Si_3N_4 and SiC), blades (Si_3N_4), and combustor liners (SiC, SiC_f/SiC, and Al_2O_{3f}/Al_2O_3) for over 30,000 hours[3] at a temperature of 1010 ℃. Both the CGT and CSGT programs were continued after their conclusion albeit with more concentrated efforts. The CGT program led to work on an 8 MW hybrid (metallic and ceramic) gas turbine with Si_3N_4 combustor and nozzle [30]. Conversely, the successor to the CSGT program pursued CMCs (SiC_f/SiC and $oxide_f$/oxide) for the combustor liner [31]. These early efforts provided crucial information on the limitations of ceramics in real gas turbine environments, in addition to creating the necessary foundation for successful commercialization.

Currently, there is one CMC component that has been fielded successfully and many more are being considered. The fielded component is found in General Electric Co. (GE) Leap engine, commissioned in 2016, and it consists of a melt infiltrated SiC_f/SiC first stage turbine shroud with a proprietary environmental barrier coating layer [32,33]. The latter will also be followed in 2022 by the new GE9X engine which will include SiC_f/SiC combustor liners and nozzles in addition to turbine shrouds [33]. Further investment in the development and commercialization of CMCs is expected by multiple entities, including GE Co., in the near future. One avenue of work is in further

[3] This rig test time is for Si_3N_4 blades and nozzles as well as SiC_f/SiC liners. The SiC liners and nozzles were eliminated due to endurance issues during initial subscale rig tests.

increasing the temperature capability beyond ~ 1315 ℃ to near 1500 ℃ by eliminating residual silicon from the reactive melt infiltration process and using, instead, CVI to create a pure SiC matrix. Another undertaking may consider tackling the difficult task of replacing rotating parts (i.e. turbine blades) that experience significant centrifugal loads during operation.

1.2 Persisting Challenges for Broad Technology Transition

Materials used in the hot-section of gas turbines are subject to severe environmental conditions. The first set of challenges faced by emerging silicon based ceramics were related to poor mechanical performance at high temperatures and insufficient resistance to thermal shock [11,13,14]. Through microstructure development (i.e. purity, grain boundary tailoring by additives, and reduction in porosity) both the high temperature strength and creep behavior of SiC and Si_3N_4 monolithic ceramics have been greatly improved [15,17,34-36]. Their thermal shock resistance is also superior to oxide ceramics due to their low coefficient of thermal expansion [37]. One area of limitation has been their low toughness which led to the development of advanced CMCs. Similar to their monolithic counterparts [38], the specific strength and stress rupture of CMCs is more superior relative to current superalloys as shown respectively in Figures 1.1a and 1.1b [39,40].

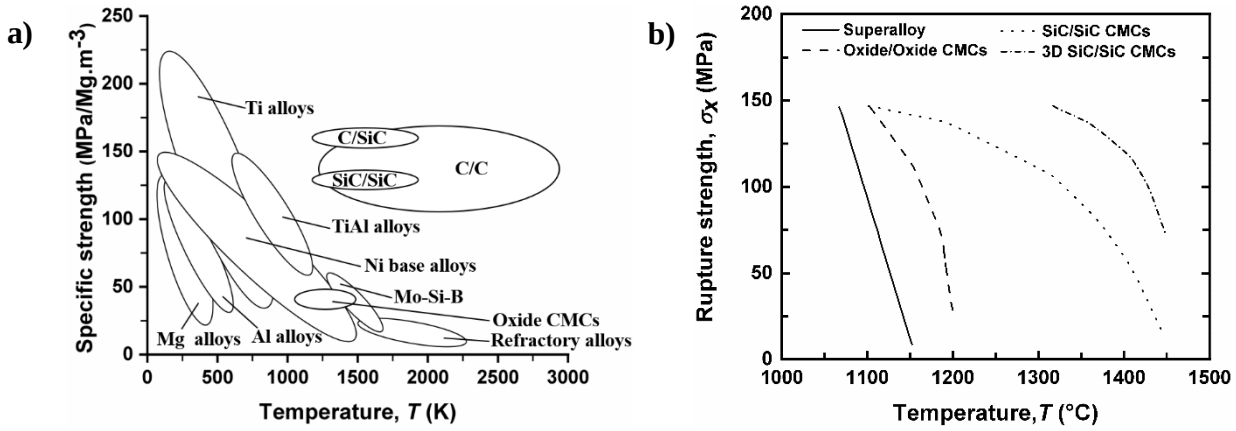

Figure 1.1. Comparison of specific strength (a) and 500 hour rupture strength (b) as a function of temperature for selected metals and ceramic matrix composites [39,40].

Still, additional challenges remain for the application of CMCs from a mechanical property's standpoint. The first issue concerns the susceptibility to creep by SiC fibers at relatively high temperatures ≥ 1400 ℃. This response is due to grain boundary sliding from viscoelastic

deformation of excess carbon (or silicon) [41]. As a result, an increase in purity and larger grain size is sought to improve the creep response. Another issue is low strength in out of plane direction. The interlaminar properties of most CMCs are governed by the weak matrix. This has led to initiatives which aim to incorporate flexible interlayer tows between individual laminas without hindering infiltration of the matrix phase [40]. Silicon based ceramics and CMCs are also susceptible to static fatigue (or slow crack growth) at high temperatures. This subcritical crack growth is postulated to results from a combination of stress and localized chemical attack of a critical defect [42]. Beyond issues in mechanical properties, reaction with the environment at high temperatures also leads to significant degradations.

As indicated in section 1.1, silicon based ceramics and CMCs are able to withstand oxidation in pure dry oxygen atmospheres and isothermal heating conditions. This behavior is attributed to their ability to readily form a dense protective silica (SiO_2) film which prevents diffusion of oxidizing agents to the substrate [43]. However, real gas turbine environments are more dynamic in temperature gradients and more severe in hot corrosion. In the case of monolithic SiC and Si_3N_4, severe damage occurs from interaction with molten salts formed from alkaline impurities (e.g. Na_2SO_4, NaCl, K_2SO_4, $CaSO_4$, $MgSO_4$) and water vapor, a major combustion byproduct. Based on studies by Tressler *et al.* [44] as well as Jacobson and coworkers [43,45-48], the molten alkaline corrodents form solids (e.g. $Na_2O_{(s)}$ and $K_2O_{(s)}$) and these products react with the protective silica scale to form permeable liquid sodium silicates, $Na_2O{\cdot}2(SiO_2)_{(l)}$. This induces pitting in the ceramic and diminishes the strength. In contrast, water vapor is identified to be more soluble in silica and in addition to further oxidation it creates bubbles within the silica scale due to evolution of hydrogen and carbon monoxide gas during reaction [49,50]. This porous silica layer is then more amenable to transport of additional oxidizing agents to the underlying substrate. Opila and coworkers [51,52] have also identified material recession (i.e. weight loss) due to gasification of silica into $SiO_{(g)}$, $Si(OH)_{4(g)}$, and $Si(OH)_{x(g)}$. Most of the current knowledge base has been derived from bench level examinations of materials in simulated environments. However, engine rig evaluations in the CSGT program [31] and the 8 MW hybrid gas turbine program [30] have also shown that the Si_3N_4 turbine components form deposits indicative of appreciable oxidation in real engine environment.

As would be anticipated, non-oxide CMCs also face similar environmental degradation challenges as their monolithic counterparts. However, due to their multi component architecture,

the issues are slightly more complex where both surface and interior oxidation and corrosion scenarios are possible [53]. The surface degradation is similar to that of the monolithic ceramics described above. The internal oxidation is facilitated by channeling porosities and surface cracks. In this event, exposed SiC fibers show a similar response as the monolithic counterpart. However, the carbon and boron nitride (BN) interphase coatings on the fiber induce a change in damage. For carbon coatings, significant recession from interaction with water vapor and oxygen is critical [41,53]. By contrast, BN coatings are susceptible to both hot corrosion and oxidation. Herweyer and Opila [54] report that exposure to Na_2SO_4 leads to an appreciable reduction in the corrosion temperature of BN coated SiC and subsequent formation of a porous silica layer. Furthermore, when BN is oxidized it forms liquid boria ($B_2O_{3(l)}$) and reacts with the silica layer to form a more adherent and brittle borosilicate phase [41]. This prevents fiber pullout and ultimately results in fiber breakage. In engine rig tests for the CSGT program [29], both carbon and BN coated SiC_f/SiC combustor liners were examined, and both showed significant oxidation and recession damage.

The challenges associated with chemical interactions of engine grade ceramics and CMCs with the combustion environment are expected to be addressed by application of environmental barrier coatings (EBCs). These coatings still face significant challenges in their ability to remain stable during operation and prevent degradation of the underlying substrate. Instead of briefly addressing the different EBCs and their performance here, a more comprehensive discussion will be provided in follow on section.

Another critical environmental challenge, which is also the primary subject of this dissertation, is damage induced by foreign object debris (FOD) impact. FOD can originate external to the engine (e.g. ingested sand, runway concrete, maintenance tools, etc.) or within the engine (e.g. compressor blade chips, loose pins, spalled ceramic coating, etc.). These debris are carried in the gas stream and impact rotating turbine components which retain tangential speeds exceeding Mach velocities (> 340 m/s) [55]. Impact damage results from larger particles (≥ 1 mm) while smaller particles can induce erosion damage [56]. Ceramics and CMCs are inherently brittle and suffer significant damage during impact to the point of catastrophic failure. This will likely induce a cascading failure event as pieces of the fractured rotating component turn into FOD sources and impact the remaining parts. In practice, engine rig tests in the CGT program have reported FOD impact induced chipping of the leading and trailing edges of Si_3N_4 turbine blades [57]. An increase in curvature of the leading edge as well as a reduction in number of blades and rotation speed was

needed to reduce susceptibility to FOD impact. However, there was an attendant reduction in performance/efficiency. Similar failure was also reported for the engine rig tests in the CSGT program and FOD impact was deemed to be a critical limiting factor for developing ceramic rotating parts [58]. There are no public reports of rotating CMC turbine components examined in an engine rig. However, several bench-top studies of simulated FOD impact on both CMCs and monolithic ceramics indicate a susceptibility to damage for both materials. These studies will be discussed in detail in section 1.4.

1.3 Environmental Barrier Coatings (EBCs)

Environmental barrier coatings (EBCs) correspond to refractory ceramic layers that are typically applied to the surface of silicon based ceramics and CMCs to protect against oxidation and hot corrosion damage within the harsh gas turbine environment. These coatings are typically manufactured using air or atmospheric plasma spray (APS) units. In this process, powders with the desired EBC composition are injected into a high velocity plasma jet where they are partially molten and propelled towards a substrate. The high kinetic energy causes these droplets to deform into disc like splats upon impingement. Solidification of these splats occurs rapidly, due to a high temperature gradient, and the coating layer is built over time. Durable EBCs require the following characteristics: matching coefficient of thermal expansion (CTE), chemical stability and compatibility, and phase stability. EBCs which meet some of these characteristics have been developed and examined over the past three decades, and the findings, as well as limitations, are discussed below.

The first generation of EBCs sought to apply oxides which are more resistant to oxidation than silicon based ceramics. Mullite which is a mixture of silica and alumina ($2Al_2O_3 \cdot SiO_2$) was identified to be the most promising candidate owed to its close match in CTE with SiC ($5\text{-}6\times10^{-6}$ °C^{-1} vs $4.5\text{-}5.5\times10^{-6}$ °C^{-1}; mullite vs SiC)[4] and exceptional high temperature properties (resistance thermal shock and high thermal stress) [59-61]. However, initial high temperature exposure of dense APS mullite resulted in significant cracking due to volumetric contraction from crystallization of the amorphous as-processed coating above 1000 °C. Lee *et al.* [62] circumvented this issue and successfully created crystalline APS mullite coatings by heating the substrate during

[4] Values of thermal expansion were retrieved from Ref. 61.

the deposition process. The crystalline coatings were more resistant to cracking and chemically stable at high temperatures (< 1300 ℃) [62,63]. However, due to high silica activity (0.3-0.4) significant recession of SiO_2 from the coating was observed in a water vapor environment [64]. Lee and coworkers [64-67] applied yttria stabilized zirconia (YSZ; 8 wt% Y_2O_3-ZrO_2)[3] overlay coating to protect the mullite undercoat from volatilization. This duplex coating was able to withstand high temperature exposure in air without cracking and ≤ 100 hrs at 1300 ℃ in a water vapor environment. For extended exposures (> 100 hr) at 1300 ℃ and short-term exposures above 1400 ℃, cracking and spallation of the EBC occurred. This was attributed to the high CTE mismatch between YSZ and mullite ($10\text{-}11\times10^{-6}$ $℃^{-1}$ vs $5\text{-}6\times10^{-6}$ $℃^{-1}$; YSZ vs mullite)[3], as well as reversible tetragonal to monoclinic transformation of YSZ (volumetric expansion) [67]. The crack network then enables oxidation of the SiC–mullite interface.

Relative to first generation EBCs, second generation variants considered application of alkaline-earth aluminosilicates. The material which garnered the most attention was barium-strontium-aluminosilicate (BSAS; $(Ba_{1-x}\,Sr_x)O$-Al_xO_3-SiO_2). BSAS is more resistant to cracking at high temperatures due to its low CTE ($4\text{-}5\times10^{-6}$ $℃^{-1}$)[3] and modulus. It also retains a low silica activity (< 0.1) and hence a slightly improved chemical stability [67,68]. Initial assessment of a BSAS EBC layer in a water vapor atmosphere at 1300 ℃ was found to result in oxidation of the SiC substrate, as well as formation of porosities (due to escape of gas species during oxidation) and low viscosity silica–BSAS reaction layers [68]. Subsequent efforts aimed to alleviate this chemical incompatibility with SiC by incorporating a mullite layer as a bond coat. This duplex coating was shown to have extended durability in water vapor at 1300 ℃, with only a benign diffusion layer being established at the mullite/BSAS interface [69]. Still, the mullite layer was found to be amenable to cracking from thermal cycling and result in the degradation of the EBC. A proposed solution to the latter involved substitution of the mullite bond coat with a crack resistant composite coating consisting of mullite and ~ 20 wt % BSAS [67,69]. The mullite+BSAS/BSAS EBC was assessed under similar environmental conditions to the mullite/BSAS EBC and it showed excellent durability with limited oxidation of the substrate and limited reaction of silica with the BSAS modifier in the composite bond coat. For temperatures ≥ 1400 ℃, enhanced formation of low melting eutectic glassy phase between silica and BSAS was observed followed by spallation [69]. In addition to directly modifying the mullite bond coat, an

additional layer of silicon was also added at the substrate interface (Si/mullite or mullite+BSAS/BSAS) in order to improve the adherence and reduce oxidization.

BSAS EBCs still face additional challenges in combustion environments. The first challenge relates to an increase in recession at higher pressures and gas velocities. As noted above, BSAS shows low volatility to water vapor atmosphere under standard pressure and near stagnant gas velocities. In specialized high flow and high pressure burner rig testing, the same coating showed increased level of recession [31,61,69]. This behavior was subsequently attributed to silica loss in both BSAS and mullite layers. Further increase in temperature (> 1300 °C) was also observed to result in accelerated recession of the EBC [69]. Another challenge for BSAS EBCs, besides recession, is phase stability. Conventional application of BSAS results in an amorphous phase that is readily converted in a short heat cycle (10 min at 1200 °C) to a hexagonal celsian (hexacelsian) phase [69]. This hexacelsian BSAS is detrimental to the overlay coating since it retains a higher CTE than the more desirable monoclinic celsian (monoceslsian) phase (7-8×10^{-6} $°C^{-1}$ vs 4-5×10^{-6} $°C^{-1}$; hexa- vs mono-celsian BSAS)[3]. The transformation from hexagonal to monoclinic is also slower relative to the fast amorphous to hexagonal transformation [69,70]. Structurally, there is a potential for damage due to thermal stress and a primarily monoclinic BSAS phase must be insured for high temperature durability.

The limitation in service temperature of BSAS and its susceptibility to recession in real gas turbine environments have led to development of third generation EBCs with rare-earth silicate compositions. Among the many compositions, ytterbium mono silicate (Yb_2SiO_5) and disilicate ($Yb_2Si_2O_7$) are deemed promising for durability [61]. They are however chemically incompatible with the silicon based substrate and require a bond coat similar to BSAS. Subsequently, Si/mullite/Yb_2SiO_5 EBCs were found to retain a low silica activity (~ 0.01) and hence low volatility in water vapor [61]. However, the high CTE of Yb_2SiO_5 (7-8×10^{-6} $°C^{-1}$) results in cracking and subsequent oxidation of the silicon bond coat layer [61,71,72]. By contrast, Si/$Yb_2Si_2O_7$ EBCs were found to show improved resistance to cracking due to lower CTE of $Yb_2Si_2O_7$ (4-5×10^{-6} $°C^{-1}$) [73]. The most critical drawbacks of the latter EBC system are volatilization due to higher silica activity (0.3) and reduced resistance to creep [61,74]. Further work is thus being performed to improve the durability of the topcoat and to reevaluate the low melting silicon bond coat (~ 1400 °C) in order to raise the temperature capability of the EBC [75]. Additionally, there are efforts to address an emerging chemical degradation associated with

interaction of EBCs (irrespective of composition) with molten sand and volcanic or fly ash deposits (calcium magnesium aluminosilicate; CMAS) [76].

Clearly, EBCs are prime reliant for the application of silicon based ceramics and CMCs in gas turbine engines. These coatings face significant challenges associated with hot corrosion, oxidation, volatilization, and cracking. As shown above, these issues are being studied and progress is being made towards the design of more durable EBCs. Still, the FOD impact resistance of these coatings has yet to be studied in detail despite being one of the limiting factors for application in rotating components. This is a critical knowledge gap which must be addressed in order to accurately establish/predict the service life of components and to potentially design new EBCs that are also tolerant to FOD impact damage.

1.4 Review of Studies on Foreign Object Debris (FOD) Impact

In the past four decades, several controlled studies of FOD impact have been performed on ceramics, CMCs, and protective coatings (TBCs and EBCs). These studies have examined several FOD impact conditions including temperature, target and projectile size, target microstructure, and type of backing (support). The follow-on paragraphs discuss the findings from these studies, starting with monolithic ceramics and concluding with protective coatings.

Silicon nitride, reinforced silicon nitride, and silicon carbide are the three types of monolithic ceramics which have been examined under FOD impact. For Si_3N_4, the damage morphology was shown to depend on several factors. For projectiles with hardness less than that for Si_3N_4, ring, radial, and cone cracks are commonly formed with slight cratering below the impact site [77-80]. Projectiles with higher hardness are observed to also induce median and lateral cracks, as well as slightly deeper craters. In addition, Harra *et al.* [81] and Choi *et al.* [82] have independently identified the formation of flexural back-surface radial cracks in disc shaped specimens relative to cone cracks that are typically found in prismatic specimens. Akimune *et al.* [83] has also identified that radial cracks in prismatic Si_3N_4 specimens only form for thicker specimens (>1 mm), with cone cracks dominating for thin specimens. FOD impact at oblique angles (< 60°) has been shown to modify the damage morphology to predominantly ring cracking [84]. High temperature experiments (~ 1400 °C) by Shockey *et al.* [85] also showed increased cratering and radial cracking for Si_3N_4 specimens.

Akimune and coworkers [86-88] have performed the bulk of studies on the effect of microstructure and properties on the response to FOD impact in Si_3N_4. In the case of *in situ* modification [86], gas pressure sintered silicon nitride (GPSSN), which retains a dense microstructure and a glassy phase in between grain boundaries, was shown to result in typical FOD impact damage (ring, radial, and cone crack with shallow crater). By contrast, a slightly porous bulk with a long intergranular glassy phase was formed by pressureless sintering and this microstructure showed an elastic/plastic response to FOD impact (i.e. increased cratering and predominant radial/median crack). As determined by post-impact residual strength measurement, the GPSSN microstructure was found to be more resistant to FOD impact damage due to its higher density (i.e. low defect as well as high modulus, hardness, strength, and toughness). Silicon carbide particles, whiskers, and plates have also been used for *ex situ* modification of Si_3N_4 microstructure [87,88]. In almost all cases, the damage morphology remained the same as non-reinforced Si_3N_4. However, the reinforcement which produced a dense and tough microstructure was found to resist post-impact crack growth. Choi *et al.* [89] has also identified target toughness and projectile hardness as the two critical parameters which influence FOD impact damage for Si_3N_4.

It is important to note that complete fracture upon impact has been shown to occur above a specific (critical) impact velocity [80,89]. However, this velocity depends on the target geometry (width and thickness) and projectile hardness. As target volume increases and projectile hardness decreases, the critical velocity increases, and cracks are arrested within the boundaries of the target.

Similar to Si_3N_4 targets, the FOD impact behavior of monolithic SiC also depends on projectile properties and impact conditions. Impact by hard SiC and Si_3N_4 projectiles was found to produce ring, radial, cone, and in some cases lateral/median cracks [79,90,91]. By contrast, only ring and cone cracks are found to form for impact by less hard partially stabilized zirconia (PSZ) and steel projectiles [90,92]. This is similar to the behavior noted above for Si_3N_4 targets and it is directly associated with the relative ratio between target and projectile hardness (H_t/H_p). For $H_t/H_p > 1$, the contact is more elastic (leads to Hertzian damage) while elastic–plastic contact damage persists for $H_t/H_p < 1$. Akimune *et al.* [92] also determined that the semi-apex cone crack angle increases with decreasing impact velocity and that impact by steel projectiles induced greater cone crack angles across the velocity spectrum than impact by PSZ projectiles. The velocity dependence was attributed to an increase in impact load (i.e. critical radial stress for cone crack) with increase in impact velocity, and the higher cone angle for steel projectiles was noted to result from greater

level of deformation (i.e. larger contact area before crack formation). Maekawa *et al.* [93] also investigated the effect of incidence angle and temperature variation on impact. Similar to Si_3N_4 targets, radial cracks were enhanced for high temperature (1200 °C) impact and the overall impact damage was reduced for oblique (< 60°) impacts. Unlike Si_3N_4, high temperature impact on SiC also resulted in higher frequency of lateral cracks. The effects of target geometry on FOD impact have yet to be investigated for SiC (i.e. disc vs bar as well as thin vs thick specimens) and these will need to be considered in future studies. On the other hand, the effects of target toughness have been investigated previously using CMCs and the findings will be discussed next.

Despite the increase in toughness/damage tolerance, CMCs are still susceptible to damage from FOD impact. Choi and coworkers [94-96] have performed studies on the effect of support type on FOD impact response of SiC_f/SiC and $oxide_f$/oxide ($N720_f$/A or AS) CMCs. In terms of damage morphology, SiC_f/SiC CMCs showed cratering (fiber and matrix fracture with material loss) that is independent of support type and increases with impact velocity. Below the impact site, fully backed targets formed a cone like crack (ply shear) and some delamination. By contrast, partially backed samples also retained back-surface flexure damage (cracking and spallation) in addition to significant internal delamination. $Oxide_f$/oxide targets showed enhanced cratering and lower threshold (impact velocity) for surface damage due to their low stiffness. Their subsurface damage morphology is similar to SiC_f/SiC for both partial and full support configuration with the addition of a compaction region below the impact zone. All of these studies used steel spheres as projectiles and two-dimensional (0°/90°) woven laminates. However, a study by Akimune *et al.* [97] did implement PSZ projectiles on fully supported SiC_f/SiC targets and the results showed similar damage morphology and threshold as those noted earlier for steel projectiles. In a study of FOD impact on SiC_f/SiC CMCs, Faucett *et al.* [98] used unidirectional SiC laminates, as well as assessed the behavior for cantilever support in addition to full and partial support conditions. The unidirectional composite showed back-surface scabbing damage in full support and more excessive back-surface damage for targets impacted in cantilever support (as compared to partial support). Furthermore, Ogi *et al.* [99] and Presby *et al.* [100] have independently explored three-dimensional SiC_f/SiC laminates with orthogonal yarns between plies. These three-dimensional CMCs were found to restrict damage to the impact surface and suppress extensive subsurface fracture. Beyond laminate architecture, analysis of curvature was also performed by Presby *et al.* [101]. The latter study found that low curvature targets result in a damage zone (cratering and

material removal) that is localized to the impact surface. This differs from the damage that is found in flat (infinite curvature) targets where the smaller crater expands into a larger damage volume along the cone crack, down to the back-surface. Similar to the critical velocity for immediate fracture upon impact in monolithic ceramics, CMCs retain a critical velocity for perforation in partial and cantilever support configurations. However, perforated CMC targets still retain some level of load bearing capacity, unlike fractured monoliths.

Combined influences of FOD impact with temperature, corrosive melt deposits, or stress have also been assessed for CMCs. In the case of FOD impact at high temperature for SiC_f/SiC, no significant change in damage morphology is observed. However, the post-impact strength was lower relative to low temperature impact due to thermal degradation of the composite as a whole [55,94,99,100,102]. For melt deposit, Choi *et al.* [103] used post-exposure and post-impact strengths to conclude that FOD impact significantly degrades SiC_f/SiC relative to the corrosive CMAS plus salt deposit. In the same study, it was determined that the CMAS plus salt combination was found to be more detrimental to $oxide_f$/oxide CMCs than FOD impact. A combination of applied uniaxial stress and impact load has also been shown to debilitate the performance of $oxide_f$/oxide CMCs above the extent observed for impact damage alone [104]. Further work on this topic is needed for SiC_f/SiC CMCs as they are being considered for rotating components which require high strength due to the high centripetal loads. The studies covered here give a well-rounded account of current understanding on damage induced in CMCs by FOD impact. Next, FOD impact studies on protective ceramic coatings are considered.

Relative to monolithic ceramics and CMCs, there are very few studies which address the FOD impact behavior of protective ceramic coatings. Much of the available work also focuses on TBCs instead of EBCs. Nichols *et al.* [105] performed one of the earliest studies of FOD impact on YSZ TBCs made by electron beam physical vapor deposition (EB-PVD) process. This study was later expanded by Chen *et al.* [106]. In both instances, the examination was extremely stochastic where particles with sizes ranging between 50-1000 μm were projected onto samples at high temperatures (900-1200 °C). The damage which showed large deformation of TBC columns was attributed to FOD impact. This damage region also included densification below the impact surface, column shearing/cone like crack (kink band), and delamination at the ceramic topcoat–metallic bond coat interface. In a more controlled study using single 1.59 mm steel projectiles, Choi *et al.* [107] confirmed these damage morphologies for impact at room temperature. However,

the latter study also found that for a large impactor at high velocities (~ 300 m/s) the metallic bond coat and substrate deform significantly, and spallation of the delaminated topcoat occurs. A similar study by Faucett *et al.* [108] on APS YSZ coating showed significant material loss and delamination within the ceramic topcoat. The difference in response between the two types of coatings (EB-PVD vs APS) is attributed to their fundamentally unique microstructure. The column like EB-PVD coating absorbs impact loads by buckling, compaction (densification), shearing/kinking, and then delamination. By contrast, the APS coating is made of weak lamellar deposit (or splat) boundaries and porosities which facilitate lateral cracks during the impactor penetration process.

Only two empirical studies of FOD impact have been performed on EBCs. The first of these studies was conducted by Akimune *et al.* [109]. In the latter, either silicon nitride or silicon carbide was initially deposited onto silicon nitride substrates via chemical vapor deposition (CVD) process. Post impact damage analysis showed that the CVD Si_3N_4 coating prevented the extension of cone cracks from the coating into the substrate relative to the CVD SiC coating. Both coatings showed material removal and radial cracks, yet only the CVD Si_3N_4 coating was found to completely delaminate from the substrate. The delamination was deemed to absorb energy required to drive the Hertzian cone cracks deep into the substrate. More traditional EBCs consisting of trilayer APS Si/mullite+BSAS/BSAS on SiC_f/SiC CMCs were later studied by Bhatt *et al.* [110]. This study identified spallation at the intermediate coat–bond coat interface as the key damage mode for the EBC. Furthermore, thicker (525 μm vs 225 μm) coatings were found to prevent significant back-surface damage in the SiC_f/SiC CMC substrate. The effect of combined temperature and FOD impact was also explored and the findings suggest a reduced damage level at high temperature due to softening (i.e. increased plasticity) of the coating and substrate.

The above review clearly shows that current knowledge of FOD impact in protective coatings is severely limited relative to that of monolithic ceramics and CMCs. Given that these coatings are prime reliant for survival of the underlying substrate in the harsh engine environment, insight into this unique mode of failure must be gained to properly determine the life of parts in-service and to potentially design methods for damage mitigation.

1.4.1 Consideration of FOD (particle) geometry

Nearly all FOD impact studies noted above used spherical projectiles. The spherical geometry makes these experiments easier to conduct by enabling higher velocities and repeatable results. By contrast, projectiles with complex geometries are difficult to control due to their stochastic aerodynamic behavior. Still, it is important to consider the difference in damage induced by the two projectile geometries. The most notable example, from a controlled study standpoint, is sharp tipped vs round tipped cylindrical projectile impacts on ceramic armor plates. The study by Woodward and Baxter [111] has examined this geometry effect and the results suggest a lower efficiency of penetration by sharp projectiles than round projectiles. This was attributed to energy loss as the tip of the sharp projectile breaks off immediately after contact. Unlike the sharp projectile, the round projectile maintains a point load contact (higher stress) for an extended period and can impart more damage prior to erosive wear.

Following the ballistic impact example, the case of a non-spherical particle impact would correspond to impact with only the tip portion of the sharp projectile. This impact configuration was attempted by Chaudhri and Brophy [112] using 1 mm long conical tungsten carbide (WC) projectiles with a tip radius of ~ 5 μm. As expected, it was difficult to control the spin of the cone before it contacted the fused silica targets. In one slightly angled impact, the projectile was found to induce radial, median, and lateral cracks. A similar experiment using 1.0 mm diameter WC spheres resulted in the same crack patterns in addition to the characteristic Hertzian cone crack. Using an erosion like multiparticle impact approach, Choi *et al.* [89] also observed the damage induced on Si_3N_4 targets by irregular shaped SiC particles ranging in size between 0.55 and 1.65 mm. Similar to the findings on fused silica, a predominantly elastic–plastic damage consisting of median and radial cracks was observed for Si_3N_4. The targets impacted by these irregular particles also resulted in more significant strength degradation relative to targets impacted by spherical particles of similar size.

Clearly, particle geometry affects the response of targets subject to FOD impact. Yet, current capabilities are insufficient to perform controlled single particle impact experiments using irregular shaped particles. From the limited studies that are available, including multi particle impact, the damage for these particles is likely more severe relative to spherical particle impacts. Thus, it is important to acknowledge that the spherical particle impact studies considered thus far and those performed in this dissertation are in the lower end of severity.

1.5 Approaches for *In Situ* Visualization of FOD Impact

The data that can be captured during FOD impact experiments is severely limited. In most instances, only the impact and rebound velocities of the projectile are recorded. Post-impact analysis such as strength testing and fractography of the target surface and cross-section have been key drivers for current understanding of damage. However, for the case of transparent targets (e.g. float glass), Chaudhri and coworkers [112-114] have pioneered high speed imaging for *in situ* determination of damage histories during FOD impact. This type of characterization has enabled a greater understanding of the cracks and stress states which evolve in the target at very short time scales (~ 0.5 μs). There have been attempts to apply similar capabilities to characterize opaque targets in real-time. The follow-on sections render brief overviews of three distinct capabilities with a focus on method of operation, as well as advantages and disadvantages for application. One of these capabilities (pulsed synchrotron X-ray radiography) is a critical component of the work presented in this dissertation.

1.5.1 Edge on impact (EOI) imaging

The opacity makes it impossible to visualize the internal damage initiation for a large ceramic tile subject to ballistic impact. This limitation has been overcome to an extent by the edge on impact (EOI) experimental configuration. As shown in Figure 1.2, EOI only uses a thin segment of the ceramic tile. Before impact, one side of the target is polished to a mirror finish and in most cases, a thin (~ 1 μm) layer of silver or aluminum coating is applied to the polished surface [115,116]. During impact, a light source (typically a high intensity flash lamp) illuminates the polished surface and the reflected light is imaged using a high speed camera. Areas where the intensity of the reflected light diminish (dark in color) correspond to damage regions (i.e. fragmentation, cracking, etc.). A transparent confinement plate may also be added to the sides to preserve the fragments in place for postmortem analysis.

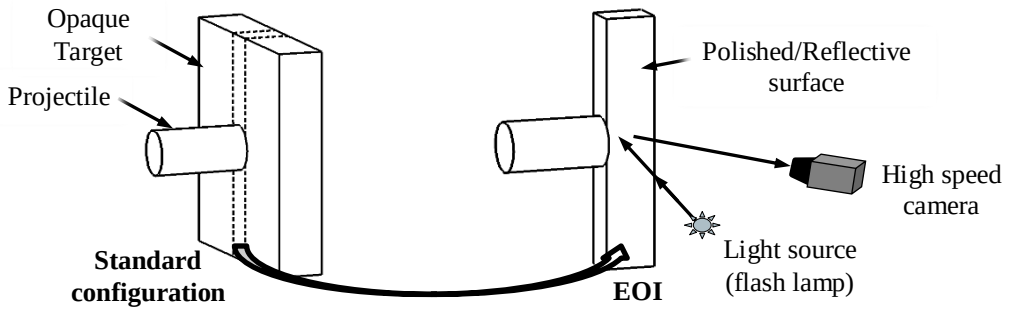

Figure 1.2. Basic configuration of edge on impact (EOI) experiments for opaque targets.

The major advantage of the EOI method is that it is able to capture the damage for a large field of view (e.g. 100 mm x 100 mm). Observable damages include outline of the compression induced comminution zone and tensile cracking. The method can also accommodate any desired target material. The main drawbacks are low resolution, limit in projectile geometry, and loss of self-confinement. In the case of image resolution, it is difficult to capture hairline microcracks. Additionally, the comminution zone is significantly low in intensity making it impossible to capture the microfractures within. From a projectile geometry standpoint, EOI requires that the contact area (between target and projectile) prior to damage initiation be larger than the target width. As shown in Figure 1.2, cylindrical projectiles with a diameter that exceeds the target width are typically used for these experiments. Finally, it is important to note that the reduction in size reduces the confinement around the impact site and this can lead to different results than those obtained under standard impact configurations. The latter can also be considered as a change from plain strain (thick section) to plain stress (thin section) for EOI targets.

EOI has not been applied to FOD impact to date. The main issue for application would be the projectile geometry. As noted above (see section 1.4), spheres and to some extent irregular shaped particles are commonly used for FOD impact studies. If applied, EOI would only show the intersection of internal cracks with the sidewalls of the target. Despite being effective for *in situ* visualizations in large targets, EOI is deemed not well suited for FOD impact studies and a more sophisticated method must be explored.

1.5.2 Flash X-ray radiography

Penetration dynamics of projectile into an opaque target is more difficult to characterize using the EOI method describe above. One approach that can be used for this purpose is flash X-ray radiography (FXR). The most basic FXR setup is depicted in Figure 1.3. It consists of an X-ray tube and a detector. During operation, the typical FXR system uses a Marx generator to store and supply a high voltage (hundreds of kilovolts to tens of megavolts) pulse to a vacuum sealed X-ray tube [117]. The X-ray tube retains a diode which consists of a pin type anode typically made of a high-Z material (e.g. tungsten, talinum, etc.) and a flat (or disc) type cathode (e.g. stainless steel) [117,118]. A strong electric field is established in this diode arrangement when the high voltage pulse is supplied. Electrons are subsequently released from the cathode via field emission mechanism. The latter enables the flow of high current (~ 10^3-10^6 A) electron beam which interacts with the anode. Intense flashes of bremsstrahlung X-rays with durations of 10 ns to 1μs are generated as the electron beam is decelerated by the nuclei of the anode material [117]. The X-ray flash energy is not equivalent to the input voltage, rather it is composed of a broad energy band (i.e. continuous spectrum). During an impact experiment, the X-ray flash is triggered and any X-rays that are transmitted through the target are projected onto an X-ray film that is chemically developed or a digital phosphor plate that is scanned into a computer. Transmission of X-rays depends on the absorption which is directly related to the atomic mass of the elements which make up the target and projectile.

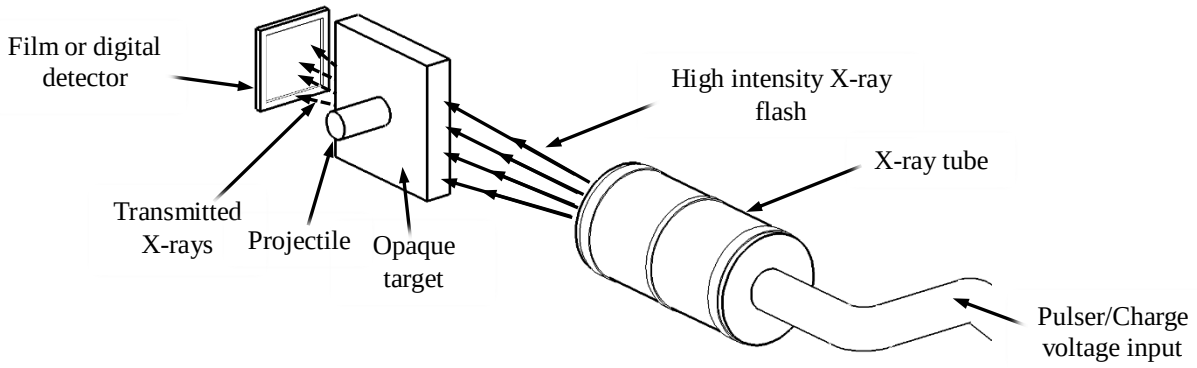

Figure 1.3. Basic flash X-ray experiment setup used in a high velocity impact event for an opaque target.

The advantages of FXR are large field of view and the ability to image internal penetration damage. Furthermore, FXR is flexible in configuration. A linear or a helical array of X-ray tubes can be used to continuously image a fast-moving object, or a stationary circular array of X-ray tubes can be used to image a projectile as it goes through interface defeat on a target surface. Another unique advantage of the circular FXR array is the possibility for transformation/reconstruction of two-dimensional radiographic projections of damage, obtained from different angles, into three-dimensional volumes [119]. Key disadvantages of FXR are its limited frame rate, low resolution (or definition), and reliance on absorption contrast. A single X-ray tube cannot continuously flash and requires over a millisecond to reenergize [117]. Hence, the number of X-ray tubes available and their efficient organization around the target will determine the number of frames captured during the impact experiment. Even when the number of frames is maximized, the quality of the images is often grainy/noisy (likely due to scattering). The finite size of the X-ray source and its poor collimation also introduces some level of blurring (i.e. geometric unsharpness or penumbra). Finally, low resolution coupled with absorption contrast imaging in FXR makes detection of cracking during impact difficult.

FXR, similar to EOI, has yet to be applied for FOD impact studies or other studies with similar scales in sample size. The resolution limit of the method (submillimeter scale) will make it difficult to assess the crack morphologies. It may however be useful for understanding the penetration into quasi-ductile ceramic coatings when more advanced methods of characterization are not available. The follow-on section discusses an advanced version of FXR (pulsed synchrotron X-ray radiography) which is more viable for characterizing FOD impact.

1.5.3 Pulsed synchrotron X-ray radiography

Synchrotron radiation is another X-ray source that enables imaging of dynamic events. Unlike the single pulse generated in the FXR system, the synchrotron can emit pulses ($\sim 10^{-12}$ s in duration and $\sim 10^{-9}$ s in frequency) in a semi continuous manner [120,121]. The process of generating X-rays in a synchrotron is best described by the diagram in Figure 1.4a. Initially, electrons are generated by an electron gun using a process similar to thermionic emission under vacuum. These electrons travel in a linear accelerator where a strong electric field accelerates them to high velocities. They are then injected into a booster ring which consists of linear radiofrequency (RF) cavities connected by dipole magnets. Injected electrons circulate the booster ring with the

aid of the dipole magnets while their energy and velocity are further enhanced to the maximum attainable values (e.g. ~ 7 GeV energy and > 99.999 % the speed of light) by an electric field emitted from the RF cavities [121]. After attaining near relativistic velocities, the electrons are bunched (~ 10^9 electrons/bunch) and injected into the main storage ring [122]. The number of electron bunches and their spacing (in time) will respectively determine the beam current (i.e. intensity) and the pulse frequency. The main storage ring contains linear electromagnets and RF cavities which maintain the energy and velocity of the electron bunches at a constant. A wiggler or an undulator (series of strong alternating dipole magnets) may also be added at the end of the linear section [121]. These magnets are called insertion devices and the magnetic field generated by them causes the electron bunches to oscillate. The associated deceleration leads to energy loss via emission of high energy polarized bremsstrahlung radiation. Dipole magnets similar to those in the booster ring are also present at the corner of each linear section in the storage ring. These 'bending magnets' guide the electrons around the ring and in the process produce useful bremsstrahlung radiation. The bend magnets result in radiation with a wide energy band (whitebeam) and the undulators produce a much more confined beam with a well-defined harmonic (pink beam) [121]. In both cases, the pulsed beam (mainly composed of X-rays) gets refined (i.e. focused, steered, filtered, etc.) in an optics hutch. It is then gated into the experimental hutch and penetrates through the target (see Figure 1.4b). In the case of impact studies, a scintillating crystal converts the X-rays transmitted through the target into visible light and a high speed camera captures the resulting radiographs.

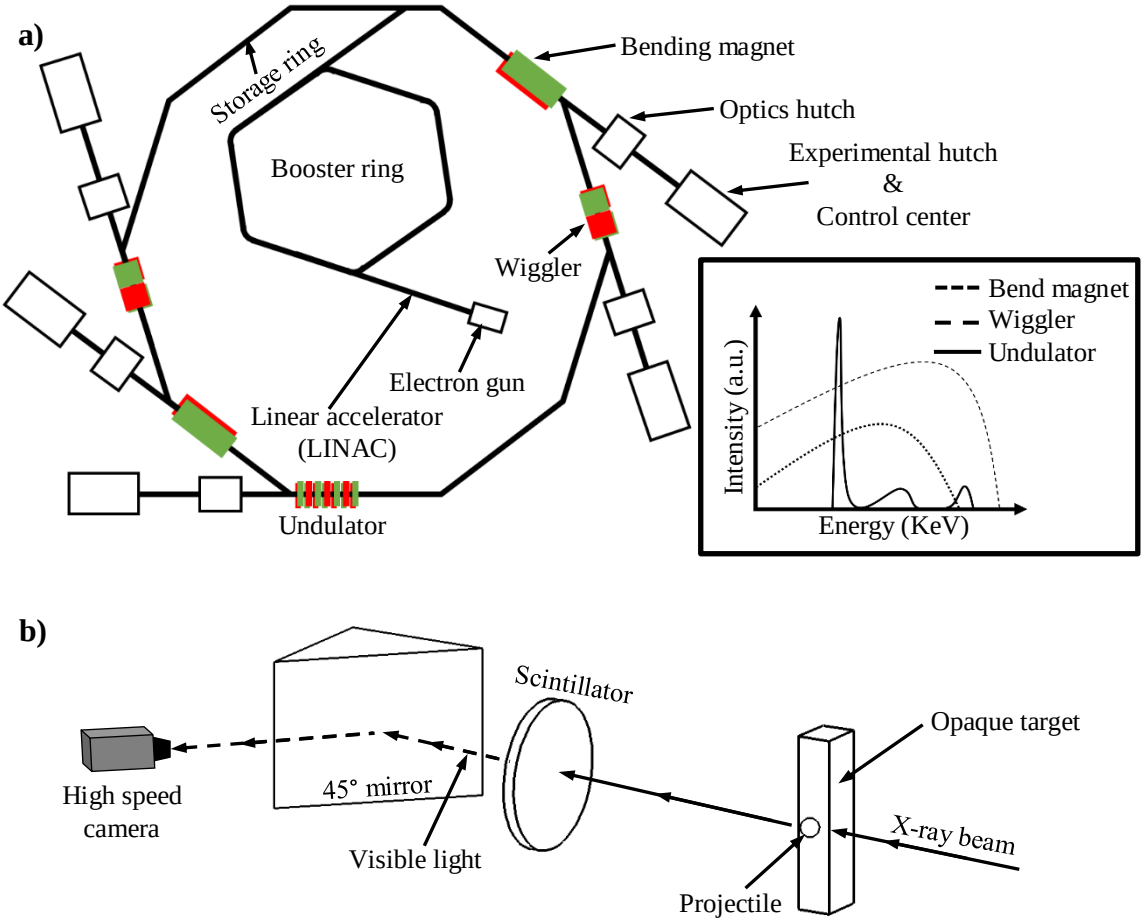

Figure 1.4. Segments of a synchrotron X-ray source facility (a) and basic arrangement of setup for impact experiments (b).

The main advantages of pulsed synchrotron X-ray radiography are ability to continuously image, ability to visualize internal damage in real-time, high spatial and temporal resolution, and dual phase and absorption contrast imaging. Unlike FXR, continuous pulses can be generated at high frequency with a synchrotron source. For instance, the source used in this work (Advanced Photon Source at Argonne National Laboratory, Lemont, IL, USA) emits a ~ 24 keV pink beam at a frequency of ~ 6.5 MHz (153 ns/pulse) under standard operation mode with 24 equidistant 4.25 mA electron bunches [120,121]. The ability to observe internal damage is a shared commonality between FXR and pulsed synchrotron X-ray radiography. However, the latter is a beam instead of a flash, therefore, it retains a higher coherence and low emittance (beam size x divergence). This means it can image finer features that are difficult in FXR. The coherent synchrotron source also enables assessment of change in phase of the transmitted X-rays [123]. This form of radiography

is known as propagation-based phase contrast imaging (PCI) and it uses change in refractive index along edges in low density materials to identify features such as cracks and pores. In terms of limitation, pulsed synchrotron radiography, unlike FXR, can only produce two-dimensional projections (flattening) of three-dimensional features. This results in loss of information when three-dimensional damage features (such as cone cracks during impact) are present. Additionally, the beam size and beam energy are both lower as compared to FXR. This reduces the area that can be observed and the X-ray penetration length. Finally, the synchrotron X-ray source is not easily accessible (cost) and portable (stationary setup) as compared to either EOI or FXR approaches.

Pulsed synchrotron X-ray radiography, similar to EOI and FXR, has not been used thus far for FOD impact studies. However, it has been used to study the dynamic behavior of materials having the same scale as those used in FOD impact studies. Jensen *et al*. [124] has used this capability to visualize fracture in 0.5 mm diameter borosilicate glass spheres during impulse loading at 275 m/s. Parab *et al*. [125] has performed similar experiments at lower loading rates (~ 6 m/s) and using slightly larger (~ 1 mm) soda lime glass spheres. In both studies, synchrotron X-rays were applied in PCI configuration and it was possible to identify the complete damage history including initiation, propagation, and bifurcation of microcracks prior to complete fracture. Based on these observations, pulsed X-ray radiography clearly retains the spatial and temporal resolution to evaluate the damage history during FOD impact of ceramic targets with ceramic coating layers.

1.6 Dissertation Objectives and Outline

A clear understanding of the damage history for an FOD impact event is critical to capturing the true interaction between the particle and target. As noted in section 1.5, most of the current knowledge of damage originates from postmortem analysis. This approach has significant drawbacks. First, the most basic techniques (optical and scanning electron microscopy) can only render accurate information for features on the impact surface. Second, subsurface damage may be determined by a sectioning and polishing procedure. However, it is often the case that the sectioning and polishing process induces additional damage. X-ray computed tomography may be used instead, to preserve the original subsurface damage. However, this method is time consuming and costly in both monetary and computational resources. More importantly, regardless of the method used, postmortem analysis only provides information on the damage features present within the impacted specimen. Most damage prediction models to date rely on their ability to

reproduce virtual results that match these damage features, despite the knowledge that impact damage occurs within microseconds of contact. An accurate prediction model (analytical or numerical) needs empirical data on the kinetics of damage propagation. This in turn requires development of a characterization method that enables visualization of damage in opaque specimens with a high spatial and temporal resolution.

The overarching objective of this dissertation was to determine the viability of pulsed X-ray radiography for imaging FOD impact damage in ceramic targets with and without protective coatings (i.e. EBCs). The first goal for this effort was development of experimental facilities/capabilities for *in situ* FOD impact testing. This required design of new components and integration with a preexisting setup. The second goal was to assess the ability of this newly developed facility to effectively visualize damage in uncoated ceramic targets. The third goal was to deposit an EBC on the bare ceramic and evaluate the response to FOD impact damage under similar conditions. The fourth and final goal was to assess the effect of specimen geometry on the response to FOD impact for both coated and uncoated ceramics. For all these goals, detailing the damage evolution was of primary concern. Furthermore, the viability of pulsed X-ray radiography for evaluating FOD impact performance (or resistance) between coated and uncoated ceramics was examined. As noted in section 1.4, studies on FOD impact of current EBC material system are severely lacking and this dissertation contributes towards closing this critical knowledge gap.

This dissertation is composed of six chapters. Chapter 1 has outlined the need to address the issue of FOD impact in ceramic materials aimed for transition into gas turbine engines. An empirical determination of the damage evolution during impact was also identified as a requirement for addressing this issue. In Chapter 2, the idea of pulsed X-ray radiography is evaluated as a method for visualizing FOD impact damage *in situ*. In this effort, a preexisting ballistic impact facility is redesigned to enable particle impact and it is integrated with the X-ray beamline at the Advanced Photon Source. A preliminary study is then performed using SiC ceramic as target and different types of spheres (Si_3N_4, PSZ, and steel) as projectiles. There have been several studies that describe the final (i.e. post-impact) damage features (see section 1.4) for SiC targets and this preliminary study is a good way to check the fidelity of the *in situ* observations. Chapter 3 examines the applicability of the *in situ* radiography method for evaluation of a SiC ceramic with an APS EBC layer consisting of a silicon bond coat and a mullite topcoat. The EBC materials are chosen for their low absorbance under the X-ray energies available at the synchrotron

facility (see section 1.5.3). Similar to the bare SiC studies in Chapter 2, Si_3N_4 and PSZ spheres are used to evaluate the change in the observed damage with change in projectile properties. A comparison of damage evolution between the uncoated and coated SiC samples is offered. Chapter 4 extends the studies in the two preceding chapters by considering the effect of specimen geometry on the FOD impact response of both coated and uncoated specimens. This study is motivated by turbine blade structures that retain low curvature segments. Thin specimens with and without EBC are examined under similar FOD impact conditions as before (including different spherical impactors). The *in situ* radiographic observations are compared with those for wide specimens (i.e. Chapters 2 and 3). In all preceding chapters, postmortem analysis is carried out when specimens are recoverable, and a qualitative understanding of the damage features, with emphasis on stress states, is also offered. Finally, Chapter 5 presents a global summary of the findings, and Chapter 6 proposes topics for future studies. Overall, the dissertation will provide a clear understanding of how *in situ* characterization via pulsed X-ray radiography uncovers the true nature of FOD impact damage in gas turbine grade ceramics and EBCs. It will also render insights on the FOD impact resistance of a brittle ceramic with a standard EBC layer and the dependency of the ensuing damage on projectile properties and target geometry.

2. REAL-TIME VISUALIZATION OF IMPACT DAMAGE IN MONOLITHIC SILICON CARBIDE (SIC)

The following chapter contains content reproduced with permission from Kedir N, Kirk CD, Guo Z, Kreschen NE, Tao S, Fezzaa K, et al. Real-time visualization of impact damage in monolithic silicon carbide and fibrous silicon carbide ceramic composite. Int J Impact Eng. 2019;129:168-179. DOI: 10.1016/j.ijimpeng.2019.01.012

2.1 Introduction

As discussed in Chapter 1 above, advanced ceramic and ceramic matrix composites (CMCs) are enabling materials for the development of efficient gas turbine engines. The touted efficiency stems from higher turbine inlet temperatures that are achieved by replacing traditional metallic superalloy structures, in the hot section of the engine, with uncooled high-temperature ceramics. Further gains, in engine performance and component life, are also achieved, due respectively to reduction in weight and improvement in creep resistance [28,126-128]. Over the past four decades, several technology transition efforts have been spurred to realize these benefits in-service. These efforts have yielded both dynamic and stationary prototypes ranging from silicon nitride (Si_3N_4) turbine nozzle guide vanes and blades [28,126,127,129] to silicon carbide CMC (SiC_f/SiC) turbine shrouds [128]. Still, these materials have demonstrated poor reliability under harsh engine operating environments, as they are prone to damage via oxidation [128,129] and impact by debris [107,126]. The former is currently being addressed through material processing efforts [126,128,129]. The issue of impact remains a challenge, as the fundamental attributes of the damage process have yet to be entirely elucidated.

The response of brittle targets to impact by small particles has been considerably investigated. Initial studies were focused on glass, which examined the post-impact strength of targets [130,131]. The resulting damage features included ring, cone, radial, and median cracks, in addition to localized inelastic fracture. A threshold velocity for rapid decay of strength was established and attributed to unstable propagation of the cone or median crack vents [131]. Similar observations have also been made for impact in monolithic ceramics [80,86,132]. Unlike glass, however, frontal and back-surface radial cracks were also shown to activate and drive failure in microstructurally toughened ceramics. Despite their improved toughness, CMCs have also demonstrated a susceptibility to impact in the form of (front and backside) spallation and cone

cracking [94,95]. However, their capacity to resist penetration is considerably higher for equivalent ranges of velocities. Across different target materials, target hardness, fracture toughness, and microstructure have all been identified as critical material properties that control the ensuing fracture behavior. These investigations clearly showed that several fracture mechanisms operate during impact; hence, current understanding of damage is determined by the capability to accurately characterize each mechanism as it develops with time.

Postmortem analysis is the most common method used for investigating impact damage in advanced ceramics and composites. The two predominant approaches in use are specimen cross-sectioning [94,95,133] and interface-bonded specimens [134]. In both cases, damage mechanisms are inferred by microscopic examinations. However, these methods are incapable of fully capturing the transient impact process. For instance, crushing of the surface due to continued impact loading erodes crack initiation markers. Secondary strikes by rebounding projectiles or projectile debris also alter the original damage features. Specific to cross-sectioning, loss of vital information occurs during the cutting and surface preparation stages. Similarly, interfacial bonds can absorb energy through sliding or break down during dynamic loading. Hence, a more appropriate method considers real-time observation. Chaudhri *et al.* [135] has successfully applied this approach in the form of high speed photography for glass targets. The opacity of ceramics and CMCs renders traditional optical methods of observation unfeasible.

The objective of the present study is to introduce a novel method that enables *in situ* characterization of impact on low density ceramics and CMCs. This method uses a pulsed polychromatic X-ray beam, from a high-energy synchrotron source, to probe the interior of the target material during the impact process and produce radiographic records of the transient event. A limited set of monolithic SiC targets are used to perform a proof of concept study on the characterization method. Partially stabilized zirconia (PSZ), Si_3N_4, and steel projectiles are used to assess the effects of projectile density and hardness. A detailed analysis of the observed impact damage evolution is provided with accompanying radiographic evidence. A geometric analysis of elastic contact depth is performed and analytical Hertzian contact solutions are applied for comparison. The limited quantitative efforts aim to merely demonstrate the range of capabilities offered by the proposed real-time observation method.

2.2 Materials and Experimental Methods

2.2.1 Target and projectile materials

Experiments were conducted on a Hexoloy SA SiC ceramic (Saint-Gobain Advanced Ceramics, Niagara Falls, NY, USA). Targets for impact testing were obtained by sectioning large plates using a low speed diamond saw. The target dimensions were 10.56±0.17 mm × 4.01±0.14 mm × 2.98±0.23 mm. Silicon nitride (CoorsTek, Golden, CO, USA), partially stabilized zirconia (MSE Supplies, Tucson, AZ, USA), and chrome steel (52100, Fastenal, Winona, MN, USA) spheres with a diameter of 1.5 mm were used as projectile materials. The general microstructure of the target and projectiles and their corresponding material properties are respectively provided in Figure 2.1 and Table 2.1.

The SiC ceramic used in this work is produced in plate form via pressureless sintering of submicron α-SiC powder. As shown in the micrograph of Figure 2.1a, the sintered ceramic has a dense (≥ 98 %) microstructure with retained porosity highlighted in dark. It is also noted to have fine grains (< 10 μm) [136]. The unique physical and thermomechanical properties of the ceramic include low density, high hardness, high thermal conductivity, low thermal expansion, and enhanced creep resistance. These properties make it an excellent candidate for wear, ballistic protection, and resistive heating applications. It is also often employed in studies as a model substrate material for gas turbine grade environmental barrier coatings (EBCs) [71].

Microstructures for the three spherical impactors used in this study are shown in Figures 2.1b-d. The PSZ sphere (Figure 2.1b) retains a homogeneous microstructure with some internal porosities. These porosities also contain uninterred particles. This suggests that the sphere was produced by molding a starting powder mixture into a green body and subsequently sintering at a high temperature. Additionally, the 5.2 wt % (~ 3 mol %) Yttria (Y_2O_3) dopant yields a mixture of metastable cubic and tetragonal zirconia phases. By contrast, the Si_3N_4 sphere is found to retain a highly dense and heterogeneous microstructure, as shown in Figure 2.1c. The primary phase appears to consist of long acicular beta (β) Si_3N_4 grains. Moreover, rare-earth oxide sintering additives are represented by high intensity (bright) features located at grain boundaries. These microstructural features have been shown in past studies to result in increased toughness of Si_3N_4 [80,127,129]. The third and final projectile is high carbon chromium bearing steel sphere. Per the micrograph in Figure 2.1d, the steel retains a heterogeneous microstructure with submicron

porosities. Based on the steel grade (i.e. SAE 52100) composition and heat treatment [137], the sphere also retains a martensite matrix with carbide particles around grain boundaries.

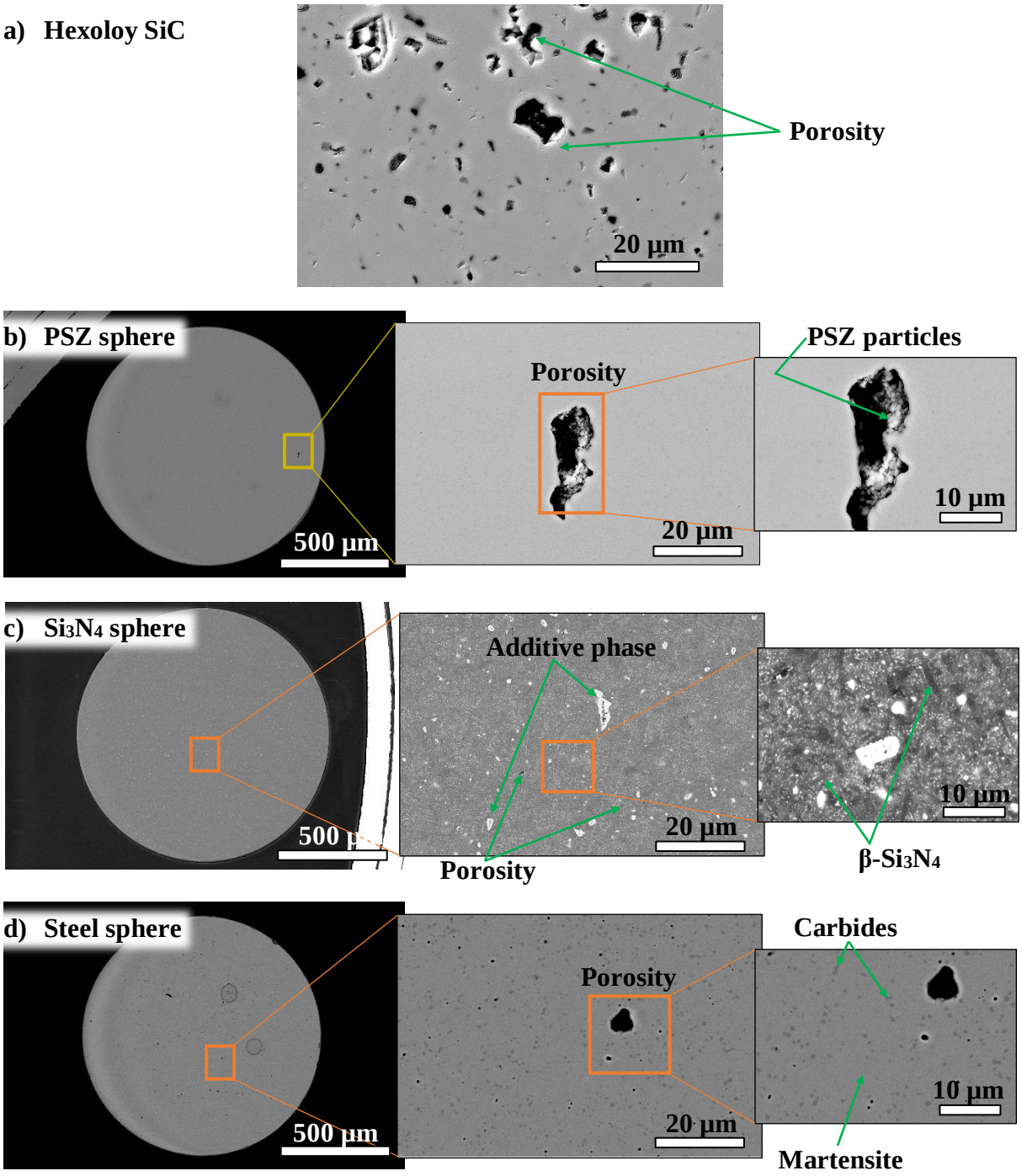

Figure 2.1. Back-scatter electron (BSE) micrographs showing microstructures of the SiC target (a) as well as PSZ (b), Si_3N_4 (c), and steel (d) spheres/projectiles.

Values for selected set of physical and mechanical properties for the target and projectile materials are given in Table 2.1. As noted above, the target is a hard ceramic with low density. By comparison, the quasi-ductile PSZ and ductile steel projectiles retain a high density and toughness. Similar to the target, the Si_3N_4 projectile is lightweight and comparatively hard. Unlike the target, the Si_3N_4 projectile is nearly three times as tough. These differences in properties are imperative to note since they lead to variation in the type of contact that is observed between the projectile and target during impact (i.e. rigid, elastic–quasi-plastic, or elastic–plastic).

Table 2.1. Properties of the target and projectiles materials at standard temperature and pressure.

	Target	Projectiles		
Properties	Hexoloy SA SiC[1,2]	PSZ (5.2 wt % Y_2O_3)[3]	Si_3N_4[4]	Steel (AISI 52100)[5,6]
Density, ρ (g/cm^3)	3.10	6.10	3.20	7.78
Poisson's ratio, ν	0.14	0.30	0.26	0.30
Elastic Modulus, E (GPa)	410	200	320	200
Hardness, H (GPa)	25.20	12	15.50	8.20
Fracture toughness, K_{IC} ($MPa\sqrt{m}$)	2.50	9	6	18.90
Longitudinal wave speed, C_L (km/s)[7]	11.50	5.70	10	5.10

1. Modulus, Density, and Poisons Ratio – from supplier data sheet (Saint-Gobain Ceramics, Inc).
2. Vickers Hardness and Fracture Toughness – from reference [136].
3. All properties, except C_L, obtained from supplier data sheet (MSE Supplies LLC).
4. All properties, except C_L, obtained from supplier data sheet (Coors Tek, Inc).
5. Density, Modulus, Poisson's ratio, and Vickers Hardness (HV0.5) of 52100 Steel referenced from Choi [80].
6. Fracture toughness of 52100 steel referenced from Nakazawa and Krauss [137].
7. Calculated directly assuming a 1-D wave and no lateral deformation, $C_L = \sqrt{E/\rho}$.

2.2.2 Impact experiments

Impact experiments were conducted using a single stage light-gas gun system integrated with a pulsed synchrotron X-ray source for real-time imaging. The *in situ* X-ray visualization capability has previously been applied with a single-loading Kolsky bar device to study the dynamic mechanical behavior of several material systems [138,139]. Alternatively, a gas gun enables much higher strain rates ($> 10^5\ s^{-1}$) [140] in comparison to the bar setup (10^2-$10^5\ s^{-1}$) [141]. The current effort utilizes a configuration that is subdivided into three components: gas gun, X-

ray source, and triggering/synchronization system. A detailed schematic of the overall impact experimental facility is provided in Figure 2.2.

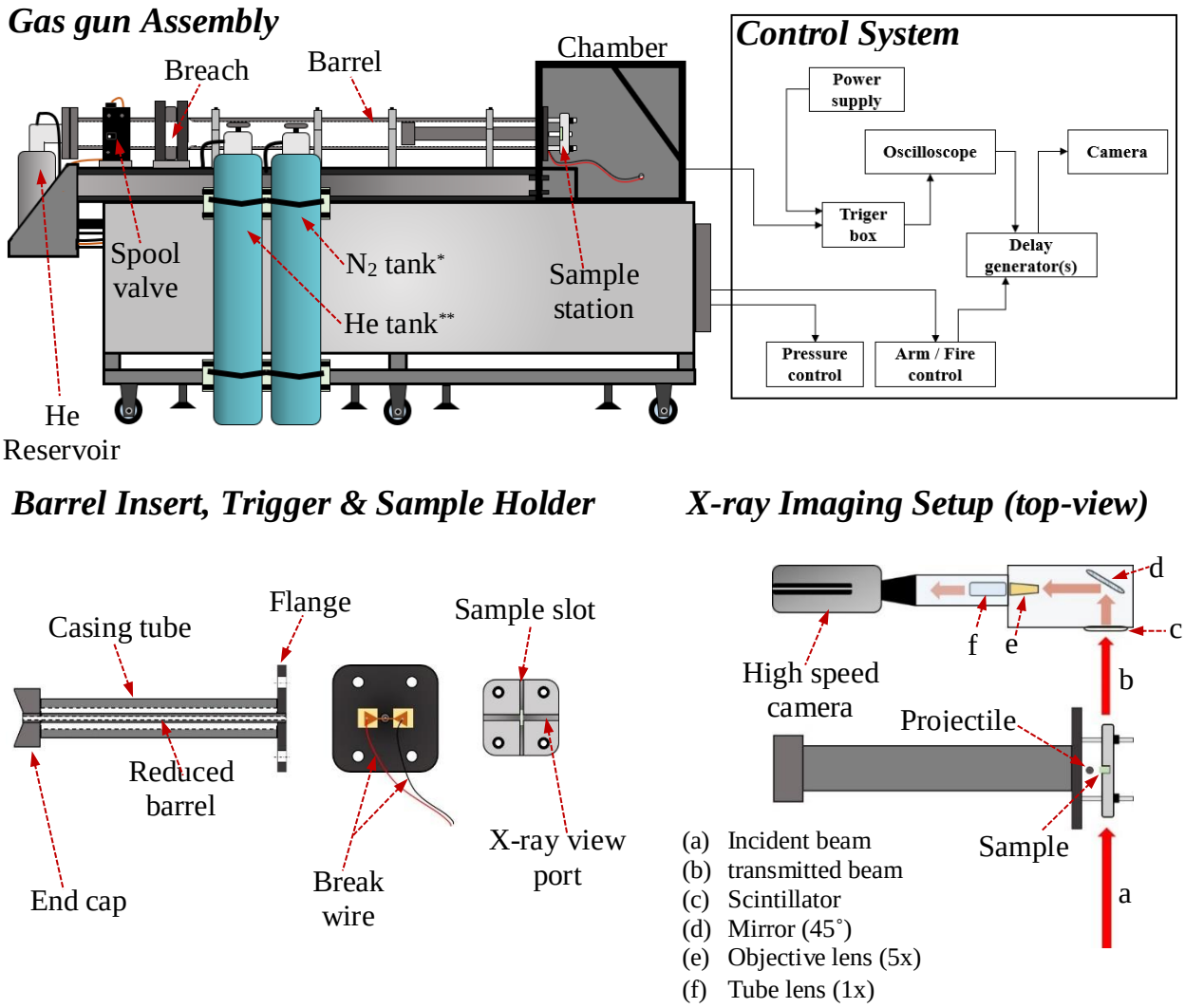

Figure 2.2. Schematics of the light gas gun facility with high-energy synchrotron X-rays for in situ studies. A side-view of the gas gun and an outline of the control systems (Top). A side view of the barrel insert cross-section and front views of the sample holder, and the chamber flange containing the break wire (Bottom Left). A top view of the barrel insert and X-ray visualization step (Bottom Right).

A single-stage, smoothbore, light-gas gun equipped with a custom barrel insert was used to perform the impact experiments. The gun barrel retains an internal diameter (I.D.) of 38.1 mm and a length of 1.83 m. High pressure helium gas is used to propel the projectile and nitrogen gas is used to actuate the fast switching spool valve. The fast actuation ensures reliability in timing the

event between the fire and trigger signals. An insert containing a secondary barrel with an I.D. of approximately 1.5 mm and a length of 0.381 m is used to guide the small projectiles. As shown in the bottom left of Figure 2.2, the insert consists of a high-pressure tube (small barrel), a support tube, an end-cap (with an internal taper), and a flange. The taper on the end-cap directs the gas flow through the orifice of the small barrel, while the flange bolted to the inside of the chamber prevents displacement of the insert. In this arrangement, the spherical projectile is loaded into the small barrel from the chamber-side using a wire ramrod. As shown in the bottom right of Figure 2.2, four linear motion shafts, 12.7 mm in diameter, are threaded to the flange and used to support the stainless steel sample holder. Before installing the sample, four spacers with an I.D. of 12.83 mm and length of 25.4 mm are inserted to provide a reasonable standoff dance between the barrel-end and the sample holder. This separation distance aligns the impact surface of the specimen to the window of the chamber. The 25.4 mm thick stainless steel sample holder retains a 3 mm wide by 1.5 mm deep vertical slot for positioning the sample and a 6.0 mm wide by 6.0 mm deep horizontal slot for passage of the incident X-ray beam. The latter yields a partially supported configuration (6.0 mm deep slot vs a 1.5 mm deep channel for the specimen). Hence, a 6.0 mm by 4.5 mm aluminum insert added to this horizontal slot served as a full support backing for the specimens. The specimen is positioned into the slot and has a snug fit with sufficient wall friction to prevent it from sliding. It is not fixed in place by a brace of screw down ties. Once the specimen is in place, the assembly (holder and specimen) are installed onto the flange and secured using plastic spacers and wing nuts. In the current work, experiments were performed under standard conditions with projectile velocities in the range of 200-340 m/s and a projectile vector normal to the target surface. For the PSZ and Si_3N_4 projectiles impacts were made at low-end (200-260 m/s) and high-end (> 300 m/s) velocities. Only high-end velocity impacts were performed for the steel projectile. The impact velocity in each experiment was measured directly using two consecutive frames from high speed X-ray radiographs (described below).

Fast synchrotron X-ray radiography capability was developed by the Advanced Photon Source, beamline 32-ID-B, at US Argonne National Laboratory (Lemont, IL, USA). This type of radiography is performed using polychromatic (i.e. multi harmonic) X-rays in phase contrast imaging (PCI) configuration. As noted in Chapter 1.4.3, relative to attenuation based X-ray imaging, PCI utilizes the phase shift of transmitted X-rays. This shift results from the difference

in thickness and refractive index between specimen features. Interference fringes from the phase shift enable enhanced visualization of edges/boundaries such as cracks in brittle materials.

A detailed description of the operating methodology for radiographic PCI has previously been presented [139] and will be reiterated here briefly. In standard operating mode, 24 electron bunches with a temporal spacing of 153 ns and a duration of 100 ps orbit the circular synchrotron storage ring near relativistic speeds. The electron bunches are allowed to exit the ring along tangential corridors (beamlines) and enter experimental stations (or X-ray hutches). An insertion device (undulator or wiggler) imposes a periodic magnetic field of opposite polarity on the electrons causing them to oscillate with a narrow frequency band along its path. The accompanying deceleration results in energy losses which facilitate emissions of coherent X-rays of high-brilliance. In the current study, a U18 undulator with a period of 18 mm, length of 2.4 m, and period of 133 ns was used at a gap of 11 mm. The resulting X-ray emission retained a pulse width of 33 ps and harmonic energy of ~ 24 keV. Before interacting with the sample, the beam was shaped by an adjustable slit into a rectangular spot with dimensions of ~ 2500 x 1600 μm^2. X-rays transmitted through the sample were projected onto a 100 μm thick single crystal $Lu_3Al_5O_{12}$: Ce scintillator (decay time: 70 ns, Crytur Ltd, Turnov, CZ). The scintillator was used to convert the X-rays into visible light. The visible light was reflected off a 45˚ mirror where it was magnified by a 5x objective lens and tube lens before being captured by a high speed camera (Shimadzu Hyper Vision HPV-X2, Kyoto, JP). The approximate spatial resolution of the imaging setup was 6.4 μm/pixel. For all experiments except one, a total of 256 frames (400 x 250 px^2) were captured with a frame rate and exposure time of 2MHz and 200 ns respectively. The outlier experiment (using steel projectile) was performed at a frame rate of 5MHz and with a corresponding exposure time of 110 ns.

A multifaceted triggering system was used to capture the impact event. The experiment was initiated by a ‘fire’ signal from a control box to a delay generator (DG 535, Stanford Research Systems, Sunnyvale, CA, USA). The delayed signal was subsequently relayed to a water cooled copper block “slow” X-ray shutter system, causing it to open starting from a fully closed state. The slow shutter fully opened within ~ 53 ms and remained open for ~ 33 ms before closing. The opening of the slow shutter also generated a secondary trigger signal which was sent to a separate DG. Again, a delayed trigger was sent out by the second DG, but this time to the “fast” X-ray shutter. Actuation of the fast shutter required 3 ms, with 1 ms in a fully opened state. Hence, a total

of 1 ms capture window was made accessible by the latter triggering approach. A copper break-wire system functioning via a 5V power supply was also used to independently trigger the recording process and to time the closing of the fast shutter. In the present study, the wire was adhered to the barrel insert flange (see Figure 2.2 bottom left). An oscilloscope (Tektronix MDO3014, Tektronix Inc, Beaverton, OR, USA) was used to record the trigger signal generated by an open circuit in the break wire as it is ruptured by the projectile. This event also prompted an output signal from the oscilloscope to trigger the high speed camera. The time between 'fire' and wire break (or function time) was also recorded by the oscilloscope. For the current study, it was determined to be 72 ± 2 ms. This timing was critical in selecting appropriate DG settings for successful synchronization of the gas gun and imaging systems.

2.2.3 Post-impact analysis

After impact loading, recovered debris of the failed samples were used to perform postmortem analysis. This was accomplished with the aid of a SEM (FEI Nova Nano 200, FEI Technologies Inc., Hillsboro, OR, USA). Further, the open-source image analysis software, Fiji (ImageJ), was used to enhance the details of the captured high speed X-ray radiographs, as well as to extract qualitative and quantitative data on the impact response. The qualitative information was used to highlight the observed damage mechanisms during impact. Further, the retrieved quantitative data on impact damage depth was compared against estimations from elastic Hertzian contact formulations.

2.3 Results

In this study, a total of seven experiments were performed due to limitations in beam time and materials. The *in situ* observations revealed the propagation of failure modes for the ceramic under impact by Si_3N_4, PSZ, and steel projectiles. Details of these observations are provided in the proceeding sections.

2.3.1 Impact by PSZ projectile

Three successful experiments were performed for this case and all showed similar failure modes. Figure 2.3 depicts the sequence of dynamic X-ray radiographs for one of the samples

impacted at ~ 211 m/s. The radiographs for the two other experiments are provided in Figures A.1 and A.2 (Appendix A). In the first frame of Figure 2.3, the outline of the two bodies before contact is depicted. The sphere contacts the target surface before the next frame and the elapsed time is estimated to be 0.25 µs. Initial damage is observed after 0.5 µs, in the form of a faint partially developed cone crack. A more distinct outline of the cone crack is shown in the third frame (t = 1.25 µs). Concurrent radial deformation of the projectile also results in the ejection of debris. A half-apex angle of 47.6˚ is measured directly from the frame at t = 1.75 µs. In comparison, the experiments performed at an impact velocity of ~ 216 and ~ 320 m/s resulted in cone crack half-apex angles of 46.2˚ and 33.8˚ respectively. As time progresses (t = 2.25 µs), a median crack vent initiates and propagates towards the back-surface of the target. A secondary cone crack (or outer cone crack) also develops during this loading period. The measured values for the half-apex cone crack angle are 56.5˚, 55.9˚, and 52.5˚ for corresponding impact velocities of ~ 211, ~ 216, and ~ 320 m/s. The PSZ projectile experiences extensive deformation during the latter events, prior to complete pulverization at t = 6.75 µs. As the projectile breaks apart at the contact interface, the cone and median crack vents open-up rapidly resulting in complete fracture of the target. It's important to note that the cone crack initiation points were difficult to locate. This was overcome by the crack mouth openings in later stages which were used to trace back to the crack origins. The only outlier event in the damage propagation occurred for the specimen impacted at ~ 216 m/s (Appendix A, Figure A.1)where back-surface cracks initiated after cone cracking and preceding median cracking.

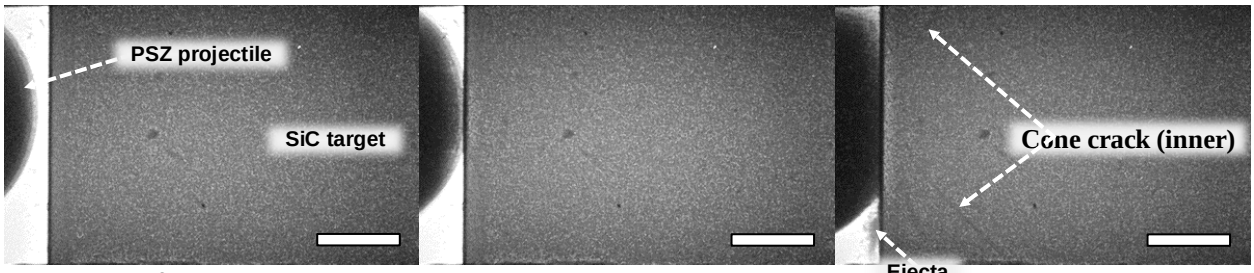

Figure 2.3. X-ray radiographs depicting impact of 1.5 mm PSZ sphere on a Hexoloy SiC ceramic. Impact velocity of 211 m/s and high speed imagining at 2MHz. Scale bars in each frame – 500 µm.

Figure 2.3. Continued.

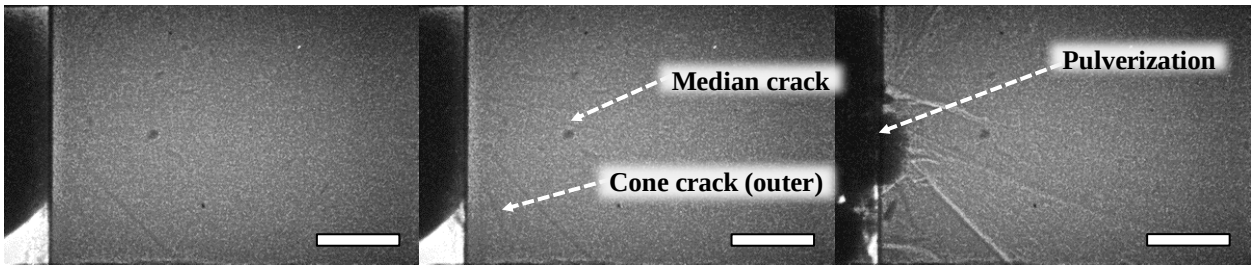

2.3.2 Impact by Si_3N_3 Projectile

Only two out of three ceramic samples were successfully examined by the X-ray imaging setup, for impact by Si_3N_4 projectile. The third experiment was not captured due to early trigger of the system by a sudden spike in noise signal. Assessments of the retrieved X-ray radiographs show the evolution of identical failure modes for both experiments. Figure 2.4 provides radiographs for one of the experiments which was performed at a velocity of ~ 256 m/s. The radiographs for the other experiment are provided in Figure A.3 (Appendix A). An outline of the two bodies (ceramic and projectile) prior to contact is depicted in the first frame. The next frame captures the projectile which is already in contact with the target surface. The elapsed time after contact is estimated to be 0.34 μs. At this time, a segment of the fully formed cone crack is observed in the target, in addition to several diametral cracks in the projectile. The half-apex angle of the cone crack is determined to be 42.5˚. Similarly, a half-apex angle of 43.2˚ is determined for the second sample which was impacted at ~ 339 m/s (t = 0.64 μs, Appendix A, Figure A.3). Continued loading primarily results in damage to the projectile in the form of diametral crack bifurcations (t = 0.84μs). As the projectile fragments into debris (t = 2.34 μs), a 'vertical' crack (i.e. crack perpendicular to the impact direction) approximately 1.8 mm from the surface and a median crack vent near the impact site are developed in the target. Separation of the projectile debris from the target surface causes the cone crack, median crack, and vertical crack to open-up at their respective nucleation points (t = 6.84-2.34 μs). In the final stages, the three crack vents intersect leading to complete fracture of the target.

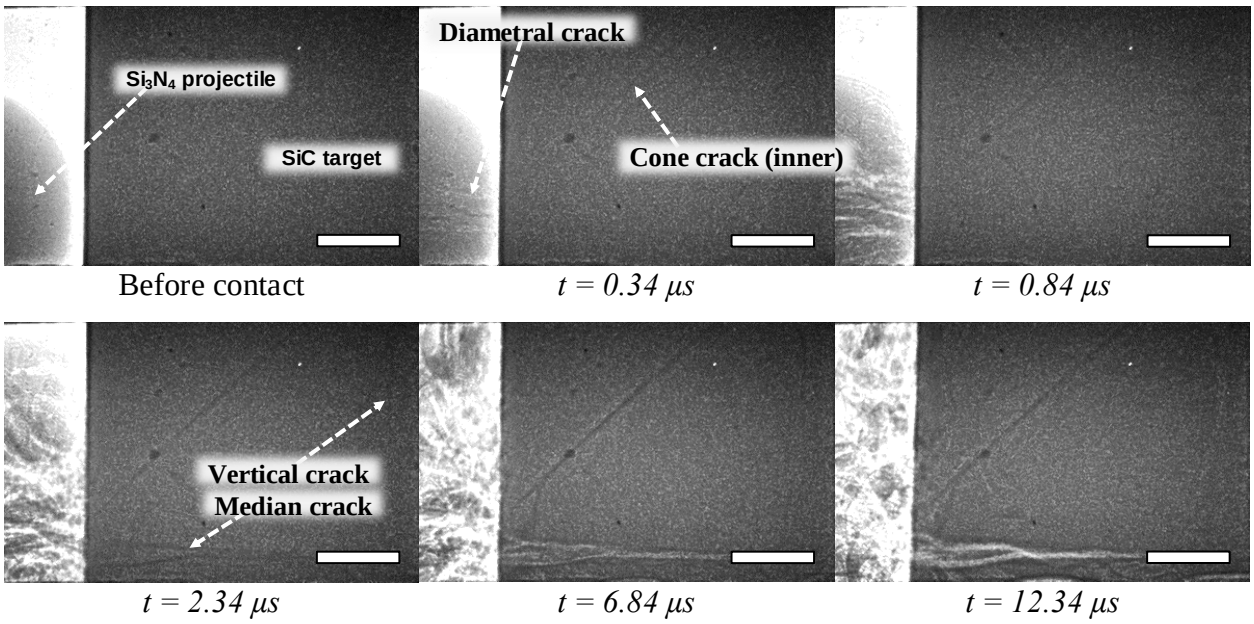

Figure 2.4. X-ray radiographs depicting impact of 1.5 mm Si_3N_4 sphere on a Hexoloy SiC ceramic. Impact velocity of 256 m/s and high speed imagining at 2MHz. Scale bars in each frame – 500 μm.

Comparison of the failure modes developed during impact of the ceramic by PSZ and Si_3N_4 spheres yields both similarities and differences. In both cases, a cone crack is observed to develop followed by a median crack. However, a secondary cone crack also emerges for impact by PSZ while a vertical crack emerges for impact by Si_3N_4. Additionally, the cone crack half-apex angle for impact by PSZ sphere is found to decrease with an increase in impact velocity. Under similar impact velocity ranges, the half-apex angle for impact by Si_3N_4 does not show any significant difference. In terms of the projectile material, the PSZ spheres quasi-plastically deform in the radial direction before pulverization while the Si_3N_4 spheres crack and then fragment into pieces.

2.3.3 Impact by steel projectile

Due to limitation in material, only one ceramic sample was examined for impact by a steel sphere at a velocity of ~ 316 m/s. The resulting X-ray radiographs are depicted in Figure 2.5. In the first frame, the projectile and ceramic are observed prior to contact. The following frame (t = 0.46 μs) shows contact between the two bodies in which the steel projectile is deformed slightly, and the ceramic contains a segment of a cone crack. Measurement of the cone crack half-apex angle yields a value of 51.2˚. Given this observation for impact by PSZ sphere (Figure 2.3), this is

designated as the outer cone crack. A median crack is observed next (t = 0.86 µs), with increase in radial deformation of the projectile. At t = 1.46 µs, the inner cone crack with a measured half-apex angle of 31.8˚ is observed. Subsequent deformation of the sphere causes extension and some bifurcation of the existing cracks. The latter is then followed by rebound of the deformed sphere at a velocity of ~ 48 m/s and initiation/extension of back-surface cracks (t = 2.06 µs). Using the density of the steel (Table 2.1), ~ 98 % of the initial impact energy is determined to be consumed by deformation of the projectile and fracture of the ceramic. Finally, complete fracture of the ceramic occurs by opening of the crack networks.

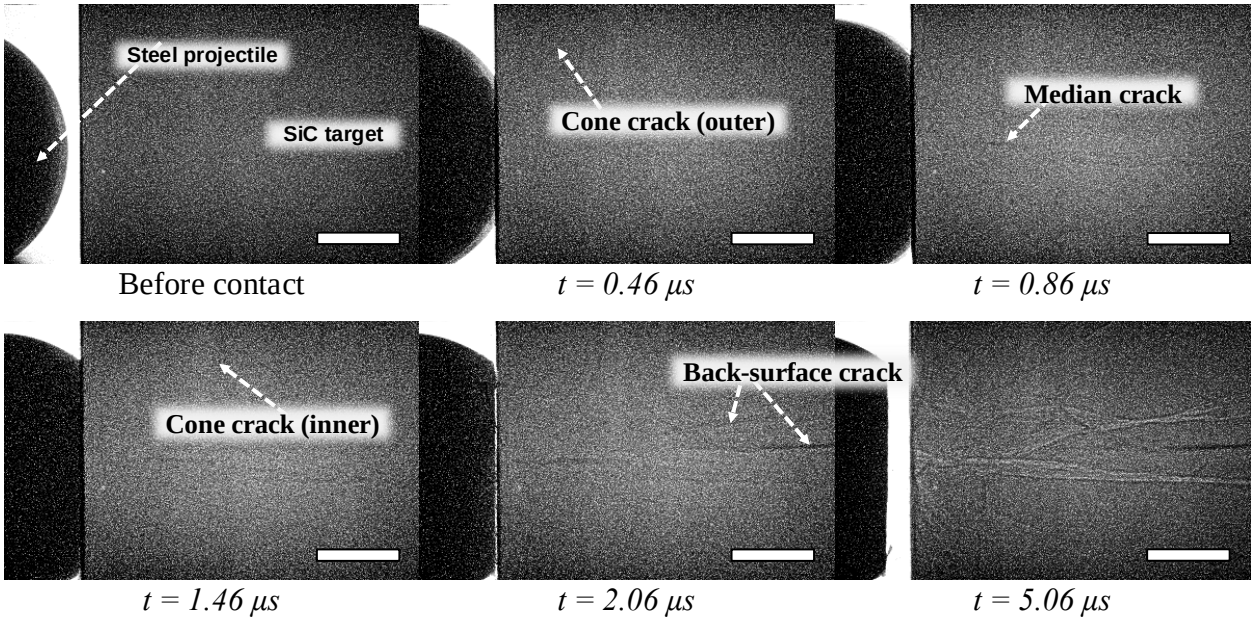

Figure 2.5. X-ray radiographs depicting impact of 1.5 mm steel sphere on a Hexoloy SiC ceramic. Impact velocity of 316 m/s and high speed imagining at 2MHz. Scale bars in each frame – 500 µm.

Based on the observation above, impact by a steel sphere results in the propagation of similar damage modes within the ceramic as those induced by the PSZ sphere. Specifically, both inner and outer cone cracks and median cracks are observed for both cases. The back-surface cracks on the other hand are not consistently observed for impact by PSZ spheres. Moreover, the impact response of the two spherical projectiles differs significantly. Although both spheres undergo deformation (elastic–plastic for steel and elastic–quasi-plastic for PSZ), the steel sphere remains intact and rebounds while the PSZ sphere gets pulverized.

2.3.4 Impact damage morphology

As was shown in the X-ray PCI radiographs, nearly all of the projectiles and targets were fragmented into several pieces during the impact experiments. The fragmented pieces of the projectile were too small to be captured for post-mortem analysis. However, at least one remnant of the target impacted by Si_3N_4 and PSZ projectiles was retrieved and analyzed using a SEM in secondary electron mode. Unfortunately, it was not possible to recover any remnants for the single sample subject to impact by a steel projectile. A discussion of the observed damage features is offered next.

In the two-dimensional dynamic X-ray visualizations, the Hertzian cracks were identified by the propagation of two angled cracks. In reality, the cracks are three-dimensional and encompass a conical volume, however, the path of the X-rays results in a two-dimensional projection of the fracture volume. Figures 2.6a-c show the conical domes formed in the SiC targets by both PSZ and Si_3N_4 projectile impacts. Similar cone plugs have been observed for thinner Si_3N_4 disks impacted by Steel projectiles [82]. The median and/or vertical cracks are contained within the cone plug (Figure 2.6c) or induce the portion of the cone to be fragmented (Figures 2.6a-b). Impact energy appears to play a role in the latter, where higher impact energy by PSZ projectile (Figures 2.6a-b) drives the median crack deeper towards the back-surface and causes fragmentation. Further analysis of the cone plugs was performed by studying the fracture morphology at the impact site (i.e. top of cone), cone surface, cone base, and vertical segments. Irrespective of impact by PSZ or Si_3N_4 sphere, a predominantly intragranular fracture is observed in all four locations. This type of fracture cuts through the grains and is highlighted by flat surfaces and signs of cleavage/striation markers. Intergranular modes of fracture do occur as shown in Figure 2.6a (bottom right image) further away from the impact location (i.e. base of cone and vertical segment). Previous studies of low rate (10^{-5}-10^{-2} s^{-1}) and high rate (10^{2}-10^{3} s^{-1}) compression studies of sintered SiC show that the compressive strength increases with rate, while the fracture mode remains predominantly intragranular [142-144]. This rate sensitivity is likely associated with increase in microfracture with increase in loading rate due to reduced response time for growth of large segment/splitting cracks found under quasi-static conditions. Higher rate experiments (ballistic and explosive blast) have also indicated that the fracture mode for SiC remains intragranular [145,146]. Finally, it is noted that the top of the recovered cone plug does

not correspond to the actual impact surface. As shown in Figure 2.6c, this is a recessed region and the actual impact surface gets detached when the material surrounding the cone plug falls apart.

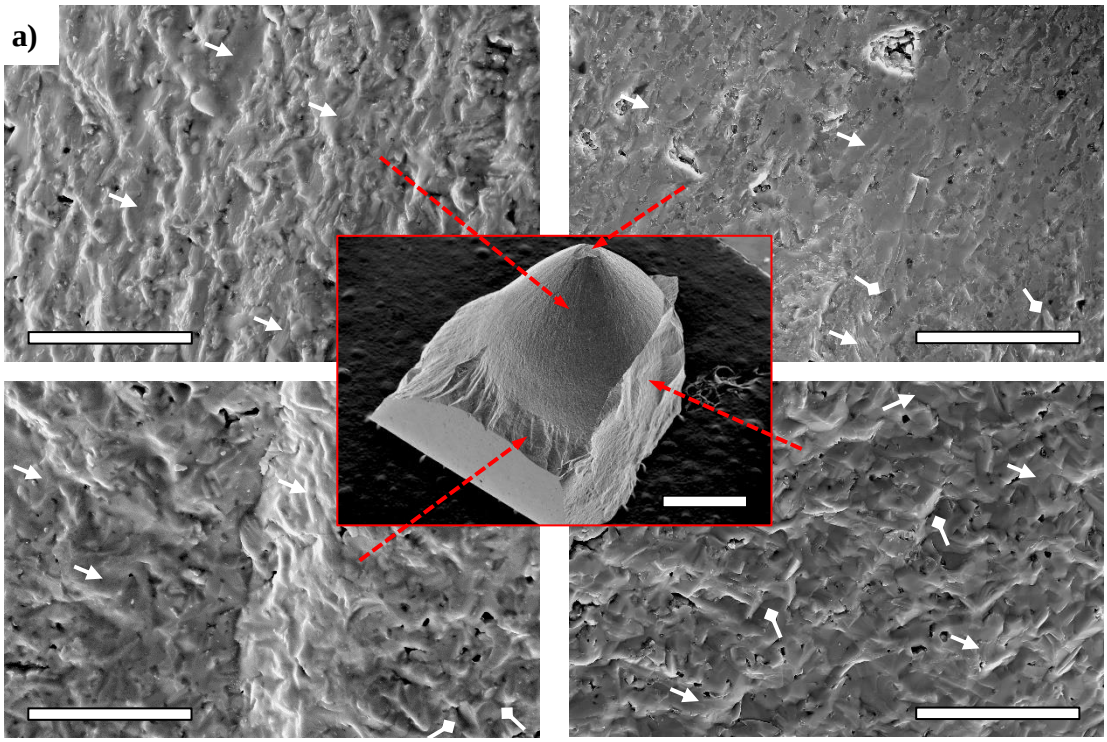

Figure 2.6. Fracture surfaces of the SiC targets impacted with a 1.5 mm diameter PSZ projectile at 211 m/s (a) and at 320 m/s (b), as well as Si_3N_4 projectile at 339 m/s (c). In all micrographs, locations of intragranular and intergranular fracture are identified by arrows with triangular and diamond tips respectively. Scale bar for center images – 1 mm, scale bar for magnified images – 50 μm.

Figure 2.6. Continued.

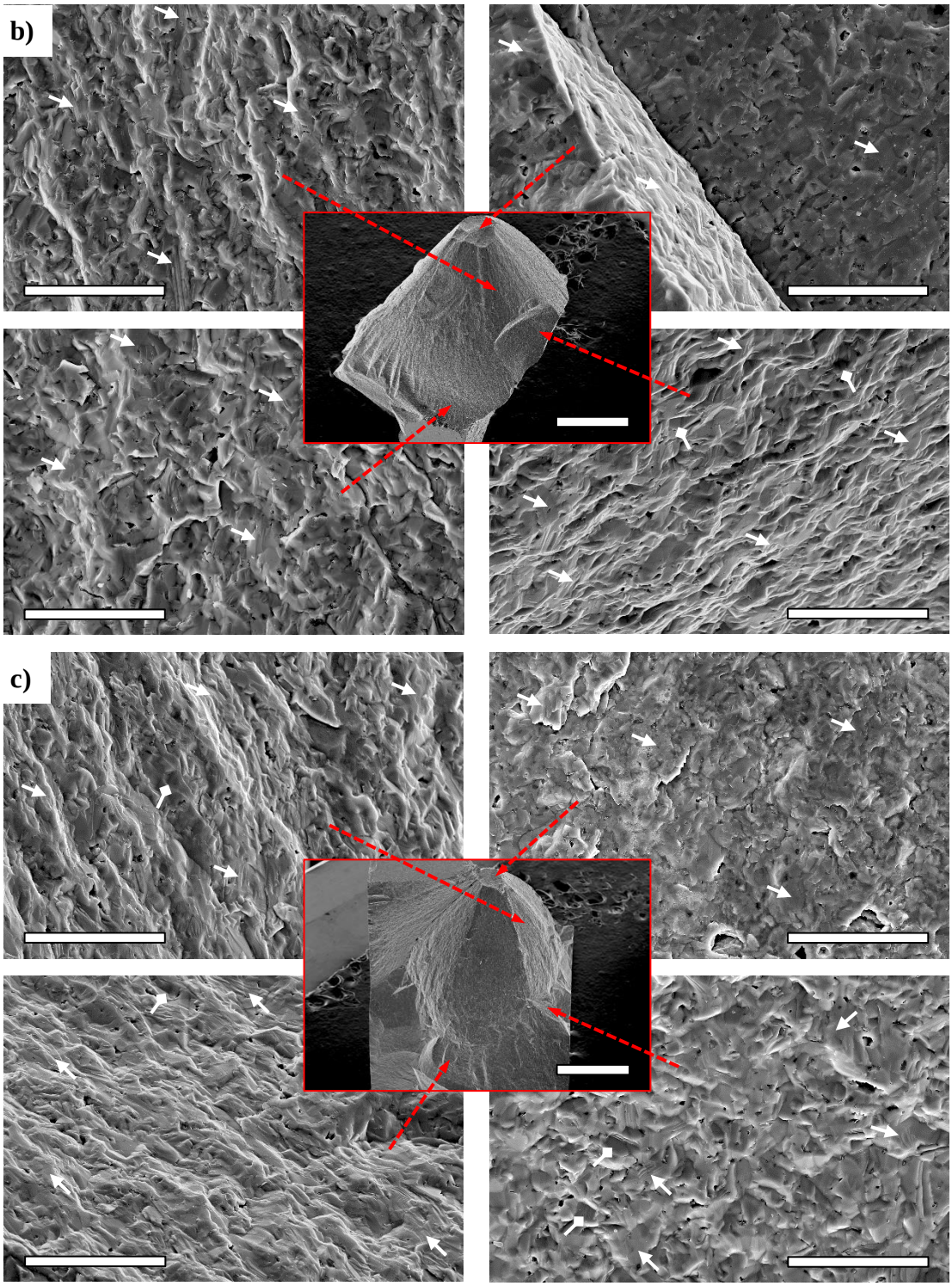

2.4 Discussion

2.4.1 Assessment of damage

Irrespective of the projectile material, a brittle elastic impact response was observed for the monolithic SiC target. In all cases, the projectile initially deformed elastically until a critical contact area was attained for the initiation of a Hertzian cone crack. Similar observations have been reported during spherical indentation and impact of brittle monolithic ceramics and glass [80,86,94,95,132,135,147]. Typically, cone cracks are formed by a decaying radial tensile stress which develops a maximum in magnitude near the edge of contact [147]. Continued loading then induces a median crack and additional crack systems appear upon unloading. Similar impact behaviors have been reported for SiC by Akimune *et al.* [92], Shin *et al.* [79], and Takahashi *et al.* [91]. These studies also used steel, PSZ, SiC, and Si_3N_4 projectiles with slightly different diameters (0.8-1.6 mm) and velocities ranging between 10 to 500 m/s. The findings suggest that impact crater size increases with projectile hardness and median crack formation occur at higher impact velocities (> 155 m/s). This complements the current findings where a visible crater is not observed in all cases and a median crack is observed due to the higher impact velocities.

In addition to the inner cone crack, secondary cone cracks are also observed for impact by PSZ and steel spheres. This response is directly related to the deformation behavior (or toughness) of the projectile material. Specifically, both projectiles retain higher toughness and were observed to deform on the target surface and continue to load the specimen for a longer period than the Si_3N_4 projectile. With increase in the contact area, new regions of maximum radial tensile stress are established and serve as the initiators for surface ring cracks which are initiation points for additional subsurface cone cracks. Previous empirical studies [79,80,86,91,92,132] and numerical studies [148] have also shown the possibility of secondary ring and cone cracking due to continued projectile deformation.

Projectile properties, as highlighted, can have significant effects on the impact response. Effects of projectile hardness on impact response have been highlighted previously in the form of an elastic–plastic (E-P) parameter[1] [149]. In this approach, a purely elastic response is generalized as having an E-P parameter of << 1, and a combined elastic–inelastic response is characterized by an E-P parameter of >1. Per the properties listed in Table 2.1, E-P values ranging between 0.3 to

[1] Elastic-plastic parameter is defined as the ratio of projectile hardness to target hardness (i.e. H_p/H_t) [149].

0.6 are obtained. The latter values provide a more quantitative justification of this initial conclusion above that the SiC target responds elastically under impact for the three impactor material types. Furthermore, a slight delay in cone crack formation is observed for impact by PSZ and steel projectiles. This delay is also postulated to arise from differences in hardness, with increasing projectile hardness leading to more immediate cone crack (i.e. pure rigid contact). Finally, a decrease in the half-apex angle of cone cracks is observed for impact by PSZ and steel projectiles while it remains consistent for Si_3N_4. This behavior has been reported before [92,150] and a compilation of the half-apex angles is presented in Figure 2.7 for reference. The trend is attributed to reduced deformation and hence smaller contact area of the projectile at higher impact velocities. The resulting cone crack would then be steeper and yield a more acute half-apex angle. By contrast, the Si_3N_4 projectile undergoes only elastic deformation and would have a lower sensitivity to variation in strain rate (i.e. impact velocity).

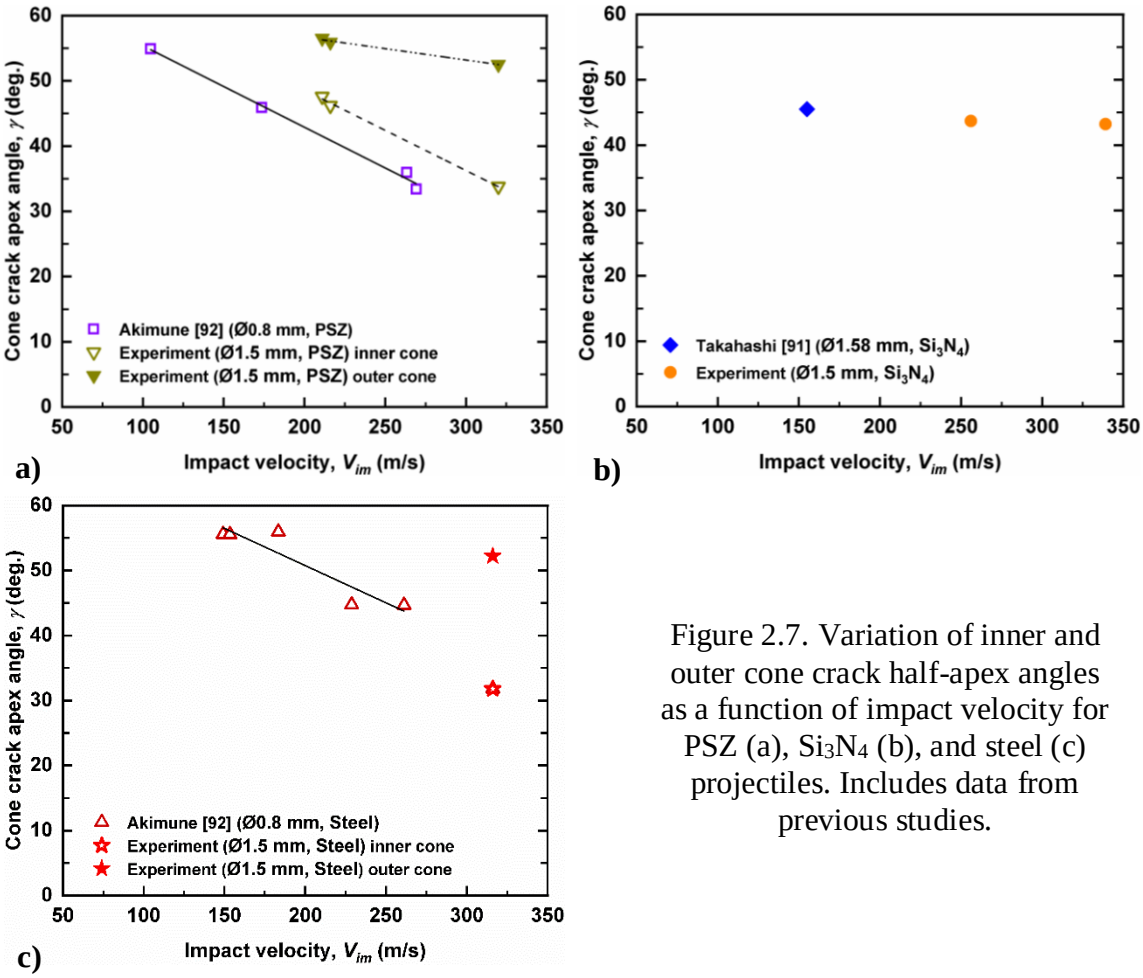

Figure 2.7. Variation of inner and outer cone crack half-apex angles as a function of impact velocity for PSZ (a), Si_3N_4 (b), and steel (c) projectiles. Includes data from previous studies.

Vertical cracking and back-surface cracking are also observed for impact by Si_3N_4 and steel projectiles respectively. Both cracks are formed during the unloading stage of impact. However, the underlying driving force for each differs. The vertical crack is likely a tensile crack that results from interaction of the release pressure wave, generated by the fracture of the projectile, and the initial pressure wave of impact reflected off from the back-surface of the target. The latter is confirmed by considering the impedance mismatch at the specimen/aluminum backing interface. For aluminum, $C_L \approx 5050$ m/s (with $E = 68.9$ GPa and $\rho = 2.7$ g/cm^3) and the resulting impedance ($Z = \rho C_L$) is ~ 2.5 times lower than that for monolithic SiC (see Table 2.1). This mismatch yields an inversion of the incident compressive stress wave (from compressive) to a tensile reflected wave at the interface. A tensile (i.e. vertical) crack is then expected to result within the ceramic. By contrast, back-surface cracking occurs due to flexural tensile stress (or bending stress). This response is very similar to three-point bend loading. Based on this observation, back-surface cracks primarily occur for impact by steel projectiles. This projectile has both an extended contact duration and a clear unloading stage. It thus predicted that the projectile deformation behavior or toughness determines the formation of back-surface crack for the target geometries considered in this study. The only other occurrence of back-surface crack was for one of the targets impacted by PSZ projectile (see Appendix A, Figure A.1). However, this crack initiated away from the central axis of impact and it likely arose from a significant defect such as machining damage on the back-surface of the target. Although these limited studies provide some consistent observations, the latter shows that ceramics are inherently flaw sensitive and more experiments are needed to further refine the current findings.

2.4.2 Application of Hertzian contact

An all-encompassing quantitative analysis of the impact damage observed in the SiC targets is complex and beyond the scope of this study. Instead, a narrow application is offered here where only the elastic damage regime is considered. This is performed using simple Hertzian contact formulations. Hertzian contact is quasi-static and in order to be applicable for dynamic loading conditions the duration of contact must be assumed to be sufficient for the passage of several elastic pressure waves within the target and projectile [130,131,135,150]. The latter holds in the current study due to an order of magnitude difference between the longitudinal wave velocities (see Table 2.1) and the impact velocities.

This analysis applies the Hertzian contact solution for displacement of the contact boundary to estimate the damage profile for a given impact condition. The resulting deformation contours are compared with direct measurements from the *in situ* impact experiments. The latter is performed using a single camera frame near the transition point from elastic damage. This is typically identified by the frame which only contains the inner cone crack since it is a characteristic feature of elastic–elastic (or rigid) contact. Following the comparison, additional calculations are performed to estimate the impact (i.e. contact) force, maximum radial stress, and loading duration.

In Hertzian contact [151], the radius of the circular impression area resulting from the application of a normal load P on a rigid sphere in contact with an elastic half space is given by:

$$a = \left(\frac{3}{4}\frac{PR_s}{E^*}\right)^{1/3} \tag{2.1}$$

where R_s is the radius of the sphere and E^* is the combined effective modulus. The latter material dependent parameter is explicitly expressed as:

$$E^* = \left[\frac{(1-\nu^2)}{E} + \frac{(1-\nu'^2)}{E'}\right]^{-1}. \tag{2.2}$$

In Equation 2.2, the variables E' and E are the elastic modulus of the sphere and half-space (i.e. target), and the variables ν' and ν are the corresponding Poisson's ratio. The applied normal load from Equation 2.1 is distributed across the contact region and yields a maximum value of contact pressure at the center which is given by:

$$p_M = \frac{3}{2}\frac{P}{\pi a^2} \tag{2.3}$$

This pressure distribution[2] was shown by Hertz to induce surface displacement of the half-space (or sphere) [152] and the resulting axisymmetric displacement profile has the form,

$$u_z = \frac{(1-\nu^2)}{E} p_M \frac{\pi a}{4}\left[2 - \frac{r^2}{a^2}\right] \qquad r/a \leq 1 \tag{2.4}$$

[2] The resulting pressure distribution was proposed by Hertz [153] and has the form, $p(r) = p_m\sqrt{1-(r/a)^2}$.

where r is the location of a point in the contact region measured relative to the central axis of contact. A corresponding equation for the sphere, u_z', is formulated by replacing E and ν in Equation 2.4 with their respective counterparts for the sphere. With these equations, a purely geometric relation between u'_z and a can be constructed. This is accomplished by first solving for P in Equation 2.1, then substituting into Equation 2.3, and finally plugging the result into Equation 2.4 to eliminate p_M.

$$u'_z = \frac{(1-\nu^2)E^*}{2E'}\frac{a^2}{R_s}\left[2-\frac{r^2}{a^2}\right] \qquad r/a \leq 1 \tag{2.5}$$

The Hertzian approach was applied to all three impact conditions since each retained an elastic contact regime. Moreover, only the spherical impactors were observed to deform with no discernable deformation by the ceramic target. The expected displacement by the flattened spheres was thus determined from the *in situ* radiographs per the schematic in Figure 2.8.

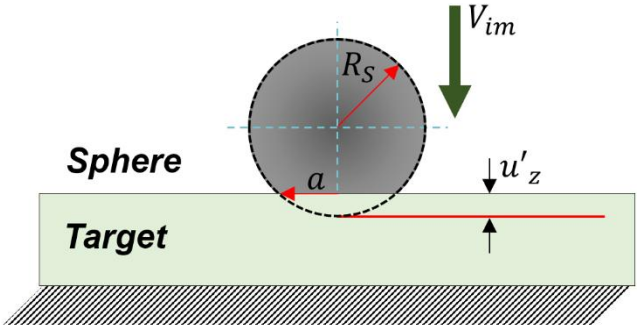

Figure 2.8. Schematic view of the contact geometry showing the elastic deformation of the PSZ, Si3N4, or steel sphere of radius R during impact. The doted circular boundary represents the expected range of projectile displacement u'_z for a given contact radius a.

The resulting depth profiles and their respective theoretical estimations (Equation 2.5) are shown in Figures 2.9a-f. It is noted that each X-ray radiograph retains a random timing for initial contact between projectile and target, with some occurring in between radiographs and others captured within the radiographs. Subsequently, the level of elastic deformation interpreted for each experiment varies greatly. The first three conditions consider the PSZ projectile in contact with a monolithic SiC substrate. As shown in Figures 2.9a-c, a reasonable fit is obtained for u'_z in all cases. The estimated Hertzian profiles are slightly larger across the region of contact, with the first (Figure 2.3), second (Appendix A, Figure A.1), and third (Appendix A, Figure A.2) experiments

yielding approximate errors of ~ 14 %, ~ 12 %, and ~ 10 % respectively for $r = 0$ (i.e. the point of maximum displacement). It is also evident that the lowest error is associated with the experiment (Appendix A, Figure A.2) which rendered radiographs of the projectile ≤ 0.1 μs after contact (i.e. frame with the least u'_z displacement). This finding suggests that the overall error between experiment and theory arises from the quasi-static nature of Hertzian contact analysis which requires very limited energy loss beyond rigid contact. Further examination of energy loss concerns the granular microstructure of the PSZ sphere which has the potential to restrict the level of deformation during impact via interparticle friction between grains [154]. By contrast, a good fit ($\leq$ 3 % error in u'_z, $r = 0$) is obtained between theoretical estimations and measured experimental displacement contours for impact by Si_3N_4 projectile (Figures 2.9d-e). The favorable results stem from reduced compliance of Si_3N_4 which influenced a predominantly elastic–elastic contact condition with negligible compaction. A displacement profile comparison for steel projectile impact is also provided in Figure 2.9f. The response is very similar to that observed for PSZ projectile where slight deviation from theoretical estimation (~ 10 %) results. This deviation is likely associated with energy dissipation at the contact interface via friction during radial expansion of the projectile. For all cases, a spherical contact was assumed in the measurement of the relative displacement by the flattened or deformed sphere. This results in the hemispherical contact profiles and leads to a large increase in error from the theoretical estimation curve when traversing away from the center of contact.

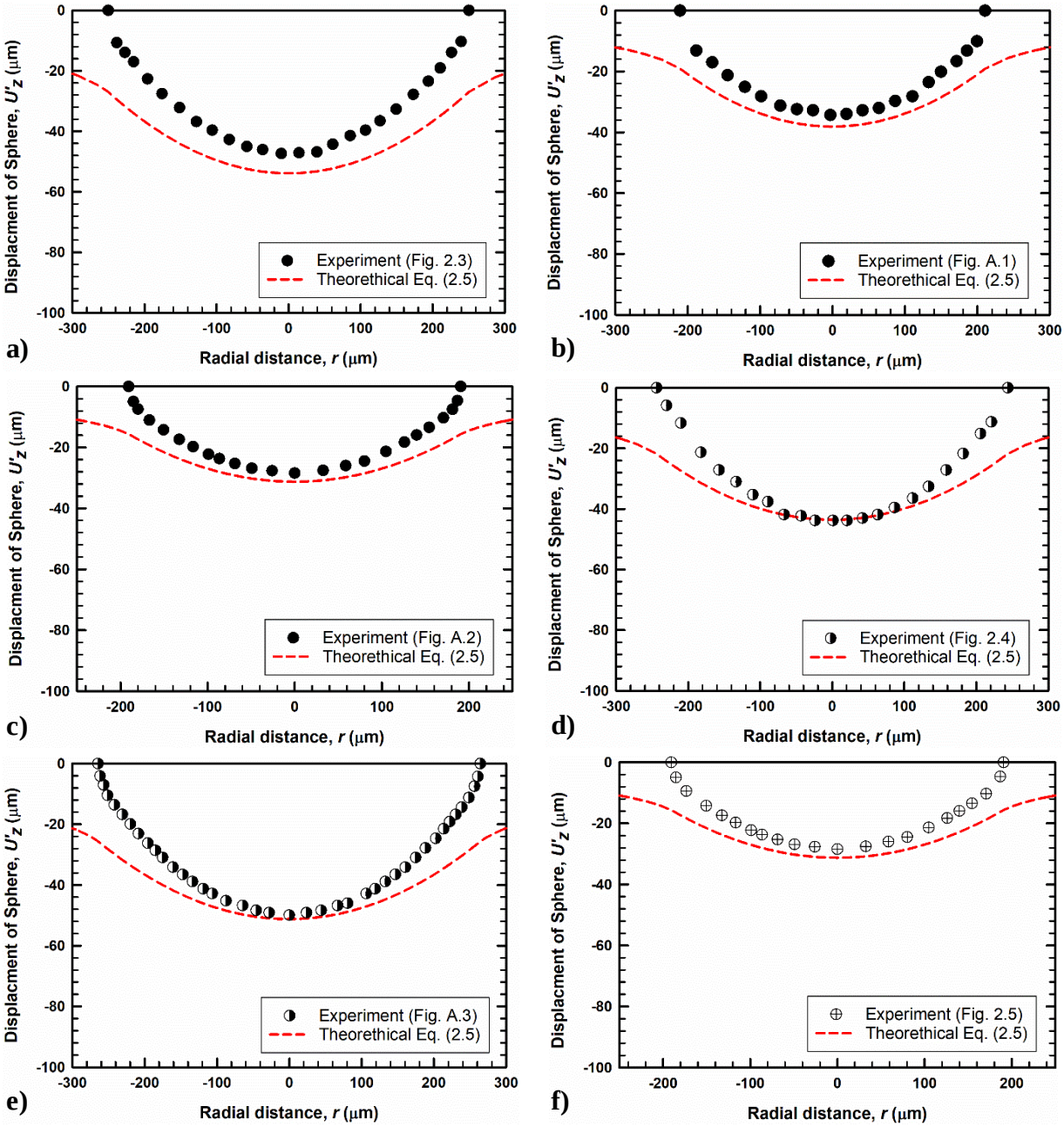

Figure 2.9. Measured elastic displacement profiles and their respective Hertzian estimations for impact of monolithic SiC target by a PSZ (a, b, and c), Si_3N_4 (d and e), and steel (f) projectiles.

The latter analysis on impact induced elastic displacement showed the relative soundness of the quasi-static Hertzian formulations in early stages of contact. This realization enables us to determine other quantities of interest such as the contact load, which in the current case is considered as an impact force. A straightforward approach to accomplish this entails solving Equation 2.1 for P. Additionally, the maximum radial tensile stress acting at the edge of contact can be estimated [151]. Analytically, this stress is related directly to the impact force by the following expression:

$$\sigma_m = \frac{1-2\nu'}{2\pi a^2} P \quad r/a = 1 \tag{2.6}$$

It was noted in a previous section that σ_m promotes the initiation of critical Hertzian cone cracks, which is indeed observed throughout the *in situ* impact experiments. Lastly, the elastic loading duration can be approximated using the momentum based formulation of Timoshenko and Goodier [151]

$$t_e = \beta \left(\frac{5\rho'\pi}{4E^*} \right)^{2/5} \frac{R_s}{{V_{im}}^{1/5}} \tag{2.7}$$

where β is a constant, ρ' is the projectile density, and V_{im} is the impact velocity.

Table 2.2 provides a summary of the impact force, radial stress, and elastic loading duration determined for the three impact conditions. Given the limited number of experiments, a detailed comparison between the results is inconsequential. Instead, an individualized assessment is advanced. For impact force, the contact diameter is considered as the governing parameter and compared with available databases.

In the case of impact by a PSZ projectile on a monolithic SiC substrate, a similar contact diameter has been reported previously by Akimune *et al.* under analogous impact conditions [149]. Hence, the determined impact force is deemed reasonable. Previous assessments of impact on monolithic SiC by Si_3N_4 and steel projectiles have also reported contact diameters which encompass the values obtained in the current work [79,90].

In terms of radial stress, it is compared with numerical simulations. One of the applicable works is by Takahashi *et al.* [91], where an explicit finite element model was used to predict a maximum stress of ~ 4 GPa for impact of a SiC monolith by a Si_3N_4 projectile at 100 m/s. Given that the radial stress increases with impact velocity, a revision of the FEM is expected to render a

stress near the values determined in the current work. A similar analysis for the PSZ and steel projectiles is not available; however, the lower impact force suggests a lower resultant radial stress.

Finally, the loading duration is compared in Table 2.2 against values extracted from the *in situ* experiments. Clearly, the prediction (t_e) overestimates the observed loading duration (t). Chaudhri *et al*. has shown similar overestimations by Equation 2.7, for impact velocities > 120 m/s [135]. The momentum based estimations then provide an upper bound for the elastic loading duration and by adjusting the constant β the error can be reduced. In the current work, $\beta = 2$ yields correlating values for t_e as compared with the typical value of 2.94 used to determine the values in Table 2.2.

Table 2.2. Summary of values for impact force, radial stress, and loading duration under the three impact conditions.

Impact condition[#]	Impact force, P (kN)	Max. radial stress, σ_m (GPa)	Predicted loading duration, t_e (μs)	Observed loading duration, t (μs)[*]
PSZ - SiC	2.71	3.59	1.41	1.08
Si_3N_4 - SiC	5.53	6.51	0.96	0.63
Steel - SiC	1.83	3.20	1.48	1.06

* Loading duration, t, is an estimated elastic contact duration based on three frames after contact.

Despite the reasonable approximations, it is important to emphasize that the Hertzian formulations are limited in applicability for impact induced damage. More comprehensive estimations must include dynamic and frictional effects as well as inelastic deformations. The empirical side can also be bolstered by use of particle velocity tracking methods such as photon doper velocimetry (PDV) or high pressure stress/strain gauges. Coupled with the dynamic X-ray *in situ* visualization method, a robust model can be developed to enable prediction of damage evolution during impact. This has practical consequences for the gas turbine materials community where impact damage of ceramic hot-section components is a key obstacle for technology transition into service.

2.5 Summary and Implications

The capability of a pulsed synchrotron X-ray radiography for visualizing damage in ceramic materials during impact was investigated. An emphasis was placed on the ability to obtain time-resolved information of the individual damage mechanisms. The resulting observations and analysis have led to the following findings:

1. Impact of monolithic SiC ceramic by a PSZ sphere initially results in a primary cone crack. This is then followed by an outer (or secondary) cone crack and a median crack. Subsequent loading results in crack extension and complete fracture of the target. The PSZ projectile was observed to undergo elastic and quasi-plastic deformation with some material loss (ejecta formation). The latter was followed by pulverization/crushing and hence unloading of the target.
2. Impact by a Si_3N_4 projectile also results in an initial cone crack in the target. The latter is followed by median and vertical cracks. The activation of a vertical tensile crack is due to interaction of the release (unloading) stress wave from projectile fracture and reflected stress waves from impedance mismatch between the target and aluminum backing. Lack of a second cone crack is attributed to very limited loading duration relative to PSZ and steel projectiles. Subsequent unloading of the target due to projectile fracture results in extension and opening of the formed cracks before complete fracture. For the Si_3N_4 projectile, diametral cracking occurred right after contact. Continued loading results in additional cracks until complete fragmentation.
3. Impact by steel projectile results in a primary cone crack much like Si_3N_4 and PSZ projectiles. This is followed by secondary cone, median, and back-surface cracks. The back-surface cracks are tensile cracks that result from flexural bending of the target. Rebound of the projectile from the target surface leads to unloading crack growth and opening before complete target fracture. The steel projectile sustains elastic and plastic deformation during loading followed by rebound from the target surface. The rebound kinetic energy is negligible (< 5%) relative to the initial impact energy.
4. Postmortem analysis of the fracture surfaces shows a predominantly intragranular fracture, similar to the fracture behavior of SiC at quasi-static loading rates.
5. A reasonable match is determined between the Hertzian contact estimations and direct measurements of projectile deformations from the *in situ* X-ray images. The method of

estimation is still deemed ideal and very limited in scope. More complex modeling approaches are needed for reliable prediction of impact damage.

This study successfully confirmed the viability of pulsed synchrotron X-ray radiography approach for studying FOD impact damage in low density ceramics. As demonstrated in silicon carbide targets, the method can identify (i.e. visualize) transient (≤ 0.5 μs) microscale (≥ 6.4 μm) damage features such as deformation and cracking accurately. This capability unburdens us from relying on postmortem analysis to reconstruct the damage progression/history (often with erroneous assumptions). The simulation/modeling community also needs this raw (or unfiltered) data from the X-ray radiographs to create damage models that can better predict FOD impact failures. With the positive outcome in this initial/calibration study, follow on studies consider the viability of the dynamic X-ray method to visualize FOD impact damage in a silicon carbide ceramic with an environmental barrier coating (EBC) layer. Although the EBC is designed for protection against thermochemical degradation of the ceramic, its resistance to FOD impact must also be considered for the ascertainment of reliability/survivability of related components under engine operating conditions.

3. *IN SITU* CHARACTERIZATION OF FOREIGN OBJECT DEBRIS (FOD) IMPACT IN ENVIRONMENTAL-BARRIER-COATED SILICON CARBIDE (SIC) CERAMIC

The following chapter contains content reproduced with permission from Kedir N, Garcia E, Kirk CD, Guo Z, Gao J, Zhai X, et al. In situ characterization of foreign object damage (FOD) in environmental-barrier-coated silicon carbide (SiC) ceramic. J Am Ceram Soc. 2020;103(8):4586-4601. DOI: 10.1111/jace.17165

3.1 Introduction

Silicon based advanced ceramics and CMCs have garnered wide attention as leading candidates for application in the hot-section of advanced gas turbine engines. However, these materials are limited by their susceptibility to hot corrosion, oxidation, and impact fracture under engine operating environments.

In dry conditions, silicon carbide (SiC) ceramics and CMCs form a thin protective scale of silica (SiO_2) which serves as a barrier for diffusion of oxygen to the substrate [43]. However, molten alkali deposits such as Na_2SO_4 (sodium sulfate), derived from fuel impurities, degrade the SiO_2 scale [59,155]. Additionally, the oxide scale is amenable to volatilization under prolonged high-temperature exposure in reducing atmospheres of water vapor [51]. These issues are being addressed through implementation of environmental barrier coatings (EBCs) [51,59,62,156-158]. Despite this progress on protection against thermochemical degradation, a critical limitation remains in terms of resistance of the EBC (and substrate) to impact damage by ingested and/or internally spawned foreign object debris (FOD) [26,29].

Current knowledgebase on mechanisms of FOD impact failures in engine grade coatings is limited. FOD impact of thermal barrier coatings (TBCs), deposited by electron beam physical vapor deposition (EB-PVD), have been shown to result in crushing and buckling of the TBC columns (kink banding) and delamination along the thermally grown oxide (TGO) interface. By comparison, coatings made by atmospheric plasma spraying (APS) process tend to form craters and delamination cracks either within the coating inter-splat layers or at the TGO interface [108,159]. The only relevant work available in the open literature regarding FOD impact of EBCs is done by Bhatt *et al.* [110] on SiC_f/SiC CMC with an APS EBC layer. In this work, coating compaction and spallation are identified as primary failure mechanisms at low and high velocities

(> 300 m/s) respectively. These observations are based on postmortem analysis and do not provide fundamental understanding of the progressive damage mechanisms that are essential for constructing reliable models.

The current effort investigates the applicability of pulsed synchrotron X-ray radiography in determining the progressive damage within an EBC layer and underlying substrate during a simulated FOD impact event. In a preliminary study, damage induced during FOD impact in the SiC substrate was successfully visualized at temporal and spatial resolutions of 0.5 μs and 6.4 μm/pixel respectively (see Chapter 2). In the current work, an APS bilayer coating consisting of a mullite topcoat and a silicon bond coat is applied to the SiC substrate. Mullite is a rudimentary EBC material which does not provide comparable protection relative to advanced rare-earth based coatings such as ytterbium silicates ($Yb_2Si_2O_7$ and Yb_2SiO_5) [68]. This topcoat material is used here due to its reasonable attenuation (i.e. low absorption) of the polychromatic synchrotron X-ray beam. Samples extracted from the coated substrate are subject to impact in a supported configuration under a narrow velocity profile. Partially stabilized zirconia (PSZ) and Si_3N_4 spheres are used to study the effects of projectile properties. A detailed account of the damage history is provided for the two experimental conditions along with accompanying radiographs. Qualitative interpretations of the underlying mechanisms of failure are presented using experimental evidence and literature with similar loading configurations.

3.2 Experimental

3.2.1 Materials

The EBC consisting of a mullite ($2Al_2O_3$-SiO_2) topcoat and a silicon (Si) bond coat was deposited via APS process at the Center for Thermal Spray Research (CTRS, Stony Brook University, Stony Brook, NY, USA). Fused and crushed powders of mullite (#1020, Saint-Gobain Ceramic Materials, Latrobe, PA, USA) and silicon (Metco 4810, Oerlikon Metco, Westbury, NY, USA) were used as feedstock materials. The silicon powder was provided by CTRS and retains an irregular morphology with a nominal particle size of 75±15 μm. For the mullite powder, the size distribution and morphology were studied using a laser diffraction technique (Mastersizer 3000, Malvern Instruments Ltd., Worcestershire, UK) and a scanning electron microscope (SEM) (Quanta 650, FEI Technologies Inc., Hillsboro, OR, USA) respectively. Figure 3.1a depicts the

distribution of particle size from the laser diffraction measurements. The distribution suggests that the mullite powder retains particles with sizes ranging between 8 to 100 µm and a mean size of 34.32±0.09 µm (34.52±0.05 µm from supplier). An electron micrograph of the powder is shown in Figure 3.1b, where the highly irregular shape and widespread in sizing of the particles is clearly highlighted.

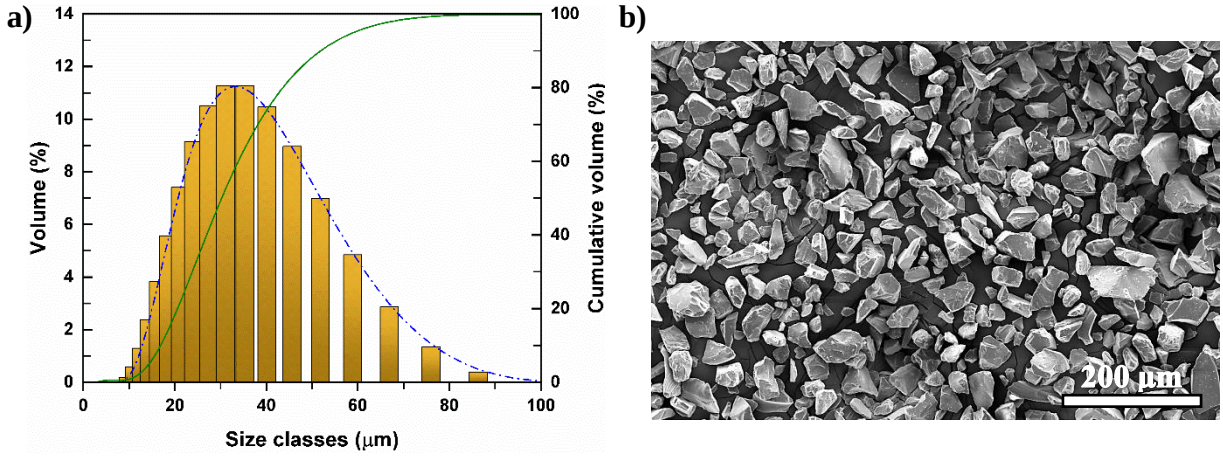

Figure 3.1. Particle distribution (a) and secondary electron micrograph (b) of the mullite feedstock.

Sintered α-SiC (Hexoloy SA, Saint-Gobain Advanced Ceramics, Niagara, NY, USA) ceramic was used as the substrate for the coating. Prior to deposition of the bond coat, the ceramic substrate was roughened by grit blasting using a #24 mesh SiC media at a pressure of ~ 0.4 MPa. Subsequently, a plasma torch with a 9 mm internal diameter nozzle (SinplexPro^{TM}/9MC console, Orlikon Metco, Westbury, NY, USA) was used to deposit the silicon and then the mullite powder to form the EBC layer. The specific processing parameters for the deposition, as well as the resulting coating thickness, are provided in Table 3.1. A water cooled slow speed diamond saw was used to section the coated substrate into FOD impact specimens with dimensions of 2.97±0.21 mm x 4.03±0.11 mm x 14.98±0.09 mm. During the sectioning process, the coating side was faced to the blade to prevent damage (i.e. coating delamination and substrate chipping). A selected set of mechanical and physical properties for the individual layers of the EBC and the substrate are provided in Table 3.2 for reference.

Table 3.1. Summary of the atmospheric plasmas spray (APS) processing parameters.

	Silicon (Si) bond coat	Mullite ($2Al_2O_3$-SiO_2) topcoat
Ar Flow (slpm)[a]	50	50
H_2 Flow (slpm)[a]	3	6
Arc Current, I (A)	230	380
Deposition Power, P (kW)	16.8	34.2
Stand-off distance, d (cm)	10	10
Layer thickness, t (μm)[b]	58.2±2.3	165.8±2.2

[a] Corresponds to primary argon gas and secondary hydrogen gas flow rates in standard liters per minute (slpm).
[b] Coating layer thickness was measured using pre-impact radiographs from *in situ* X-ray visualization.

Table 3.2. Selected properties of the target and projectile materials.

Properties[1]	Target			Projectiles	
	Mullite topcoat[2,3]	Silicon bond coat[2,3]	SiC substrate[2,4,5]	PSZ (5.2 wt % Y_2O_3)[6]	Si_3N_4[7]
Density, ρ (g/cm^3)	3.0	2.2	3.10	6.10	3.20
Poisson's Ratio, v	0.28	0.22	0.14	0.3	0.26
Elastic Modulus, E (GPa)	112.2±8.4	142.8±7.6	407.6±26.3	200	320
Hardness, H (GPa)	8.8±1.0	10.8±1.4	34.4±3.7	12.0	15.5
Fracture toughness, K_{IC} (MPa$\sqrt{m}$)	-	-	2.5±0.1	9.0	6.0
P-Wave velocity, C_L (km/s)[8]	6.1	8.1	11.5	5.7	10.0
S-Wave velocity, C_S (km/s)[9]	3.8	5.2	7.6	3.6	6.3

1. Properties are for standard temperature (~ 25 ˚C) and pressure (1 atm) conditions.
2. Hardness and modulus were obtained from nanoindentation experiments using a Berkovich diamond tip indenter (250 mN maximum load). Details of the experiment and data are provided in Appendix B.
3. Density and Poisson's ratio based on reports by Richards *et al.* [71].
4. Density and Poisson's ratio– from supplier data sheet (Saint-Gobain Ceramics, Inc).
5. Fracture Toughness – from reference [136].
6. All properties, except C_L, obtained from supplier data sheet (MSE Supplies LLC).
7. All properties, except C_L, obtained from supplier data sheet (Coors Tek, Inc).
8. The primary (or longitudinal) wave velocity determined by the equation: $C_L = \sqrt{E/\rho}$.
9. The secondary (or shear) wave velocity determined by the equation: $C_S = \sqrt{G/\rho}$. Assuming linear elastic solid, the shear modulus, G, is given by the relation: $G = E/2(1+\nu)$.

Spheres of partially stabilized zirconia (MSE Supplies, Tucson, AZ, USA) and silicon nitride (Coors Tek, Golden, CO, USA), with nominal diameters of 1.5 mm, were used as projectiles for the impact experiments. Details of the microstructures for these projectile materials are documented in Chapter 2, Figure 2.1. In short, the PSZ spheres were shown to retain patches of large internal porosities which expose unsintered particles that compose the overall structure. By comparison, a denser heterogeneous microstructure was observed for the Si_3N_4 spheres which contain a toughening β phase formed by the inclusion of sintering additives. The PSZ spheres retain a higher mass per unit volume in comparison to Si_3N_4, based on their respective theoretical densities (see Table 3.2). Subsequently, the PSZ spheres retain higher impact energies for an equivalent velocity of impact. Further, the hardness and modulus of Si_3N_4 spheres are much higher in comparison to those for PSZ spheres.

3.2.2 Coating characterization

Microstructural evaluation was performed using a SEM for both the surface and cross-section of the as-processed coating. For the cross-sectional analysis, one of sectioned pieces of the coated substrate was initially mounted in epoxy and then polished to a 0.25 μm finish using a combination of diamond embedded abrasive pads, diamond paste, and colloidal silica solution. The surface imaging was performed in secondary electron (SE) mode to highlight the morphology and backscattered electron (BSE) mode was used for the cross-section to highlight the variation in composition. An energy dispersive X-ray spectroscopy (EDS) detector (Octane Elect, EDAX, Mahwah, NJ, USA) was also used to qualitatively characterize the coating chemistry.

X-ray diffraction (Bruker D8, Bruker, Billerica, MA, USA) was performed for the mullite feedstock and the as-processed topcoat surface. An additional scan was performed on an annealed sample, to assess the effect of a steep thermal gradient during the APS deposition process. The latter heat treatment of the topcoat was carried out at 1300 ˚C for 12h. All measurements were performed using Cu Kα radiation (λ = 1.5406 Å) with a 2θ range of 20-80˚, an increment of 0.02˚, and a scan rate of 2˚/min.

Micro-Raman spectroscopy (Renshaw inVia, Renishaw, Gloucestershire, UK) was explored as a source for qualitatively determining the presence of any thermally induced residual stress in the mullite and silicon coating layers. A diode pumped laser with a wavelength of 532 nm and a maximum power of 500 mW was used to excite vibrational modes. In all experiments, a

100x objective lens (N.A. = 0.85, ~ 0.8 μm spots size) was used with a holographic grating of 2400 groves/mm. The spectra acquisition parameters were varied by material type. All measurements were performed on the polished cross-section. For mullite, an excitation power of 100 % was used with an exposure time of 10 s and five accumulations. A reduced power level of 10 % (50 mW) was used for the silicon, with the excitation adjusted to a single acquisition of one second exposure. Measurement was performed for mullite near the silicon interface. Conversely, three distinct locations were probed for the silicon layer: near the mullite interface, at the center, and near the SiC interface. Mullite coating spectra were compared to spectra from the feedstock and an internal silicon calibration was used for comparison against spectra for the silicon coating.

3.2.3 *In situ* FOD impact

A description of the combined light-gas gun and *in situ* dynamic X-ray radiography facility can be found in [160,161] and in Chapter 2.2.2. Only a brief overview is offered here. The gas gun retains a barrel with a bore size of 38.1 mm and a length of 1.83 m. The barrel was modified to propel small projectiles using a custom insert with a reduced length and bore size of ~ 1.5 mm and 381 mm respectively. As shown in Figure 3.2a, a coated sample is positioned and centered on a slot machined onto a stainless steel support fixture with a full support backing configuration before experiments. The sample is snug fit into the slot. The friction from the walls of the slot is sufficient to hold the sample in place and a tiedown (plate or screw) was not needed. A projectile is then loaded from the front end of the miniature barrel (see Figure 3.2b). After securing the experimental station and positioning the X-ray on the sample, Nitrogen (N_2) gas is used to open the fast acting spool valve and release the compressed helium (He) gas reservoir which accelerates the projectile towards the sample. As the projectile exits the barrel cavity, it breaks the signal between two sets of laser diode/detector assemblies that are separated by a distance of 10 mm. The laser system was implemented here instead of the previous wire break approach (Chapter 2.2.2) for increased reliability in triggering. In addition to providing the trigger signals for the X-ray fast shutter and high speed camera, the timing in the break between the two laser beams enables calculation of the projectile velocity prior to impact. The He gas pressures utilized for the current work (3.0-3.7 MPa) yielded impact velocities ranging between 300-355 m/s, with the lower end velocities attributed to the heavier PSZ spheres.

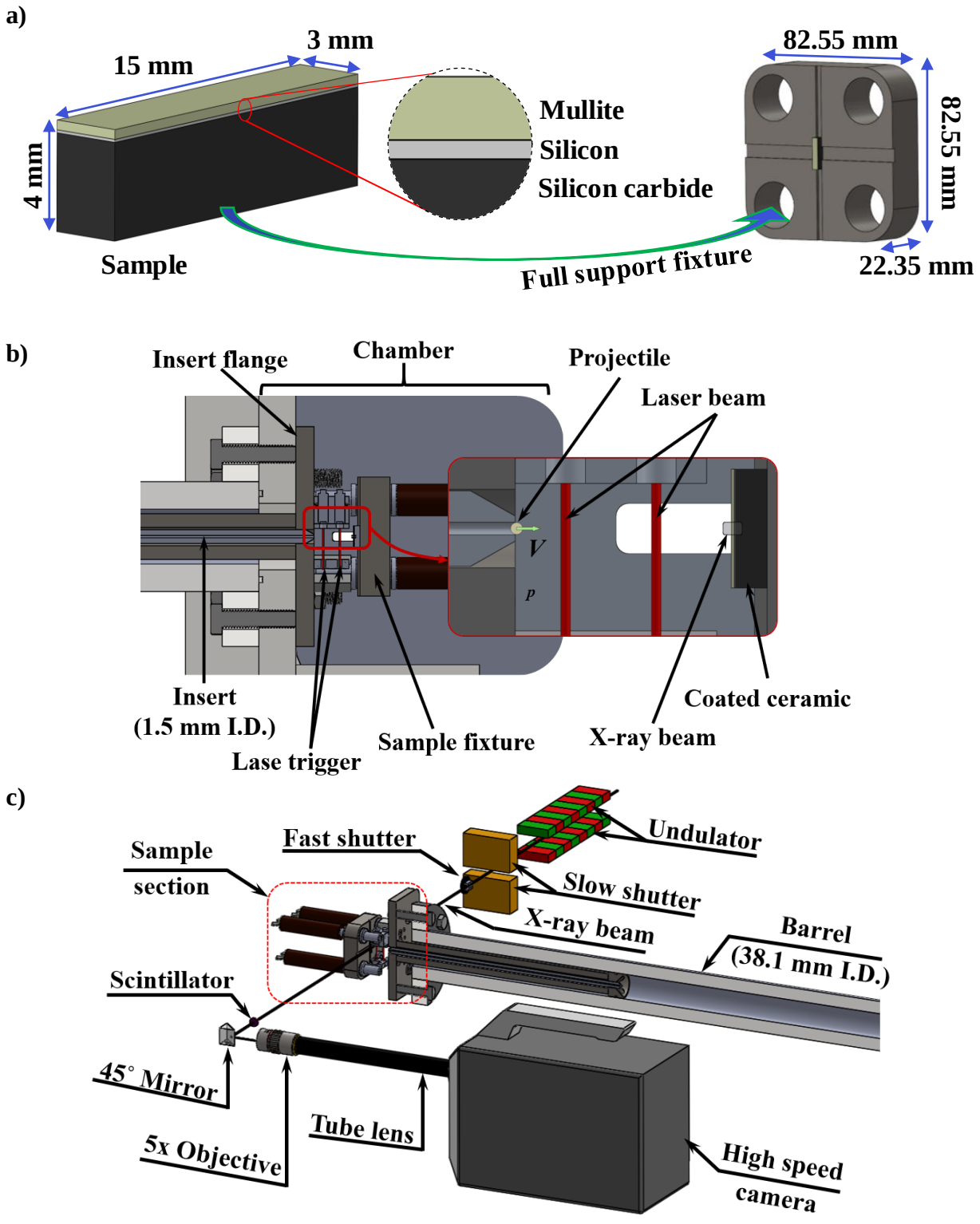

Figure 3.2. Schematics of the sample and support fixture (a). Schematics of the custom barrel insert assembly (b) and combined gas gun/*in situ* X-ray phase contrast imaging (PCI) setup (c) used for the FOD impact studies.

A synchrotron X-ray source at the Advanced Photon Source in Argonne National Laboratory (Beamline 32-ID, Lamont, IL, USA) was integrated with the gas gun apparatus for *in situ* observation. A schematic of the experimental setup is provided above in Figure 3.2c. During impact, high-intensity X-rays pass through the target at a frequency of ~ 6.5 MHz and impinge a single crystal $Lu_3Al_5O_{12}$:Ce scintillator (decay time: 70 ns, Crytur Ltd, Turnov, CZ). The scintillator luminesces in the visible spectrum. The visible emission from the scintillator is redirected by a 45˚ mirror and focused by a tube lens and 5x objective onto a high speed camera (Hyper Vision HPV-X2, Shimadzu Co., Kyoto, JP). Image sequences consisting of 256 frames (400×250 px^2), with a spatial resolution of ~ 6.4 µm/pixel are captured at 2 MHz and 200 ns exposure. For the current study, the X-ray beam was focused using a U18 undulator (18 mm/period, 2.4 m long) operated at a gap of 12 mm. This configuration produces a beam with a first harmonic energy of ~ 24 keV. Phase contrast imaging (PCI) configuration rendered by a long sample to detector distance was used to image the dynamic response in the coating and substrate.

The diagram in Figure 3.3 shows a simplified synchronization map of the three major components comprising the experimental apparatus: gas gun, X-ray shutters, and high speed camera. For a typical experiment, the function time (or the time between the fire signal to open the gas gun spool valve (t_{-3}) and the laser break (or trigger) signal (t_0)) is initially measured by performing a trial shot for a given spherical projectile material and firing pressure. The function time is monitored using one of two oscilloscopes (Tektronix MDO3014, Tektronix Inc, Beaverton, OR, USA). The difference between the function time and the predetermined time required to open the X-ray slow shutter, ~ 53±5 ms, renders the delay time required to synchronize the fire signal to a time when the slow shutter is fully opened. This delay time is stored in a delay generator (DG 535, Stanford Research Systems, Sunnyvale, CA, USA), which sends the signal to the slow shutter at time t_{-3}, such that the slow shutter is fully open at time t_{-1}. When the projectile breaks the laser beam closest to the sample at time t_0, an output (trigger) signal is sent from the second oscilloscope to the fast shutter DG. Finally, the fast shutter DG sends an immediate signal to the high speed camera and a delayed signal (typically 1 ms) at t_1 to initiate the closure of the fast shutter. An additional delay time for capturing the dynamic X-ray radiographs is set through the high speed camera software or a DG. The latter accounts for the gap between the laser trigger position and sample surface (see Figure 3.2b).

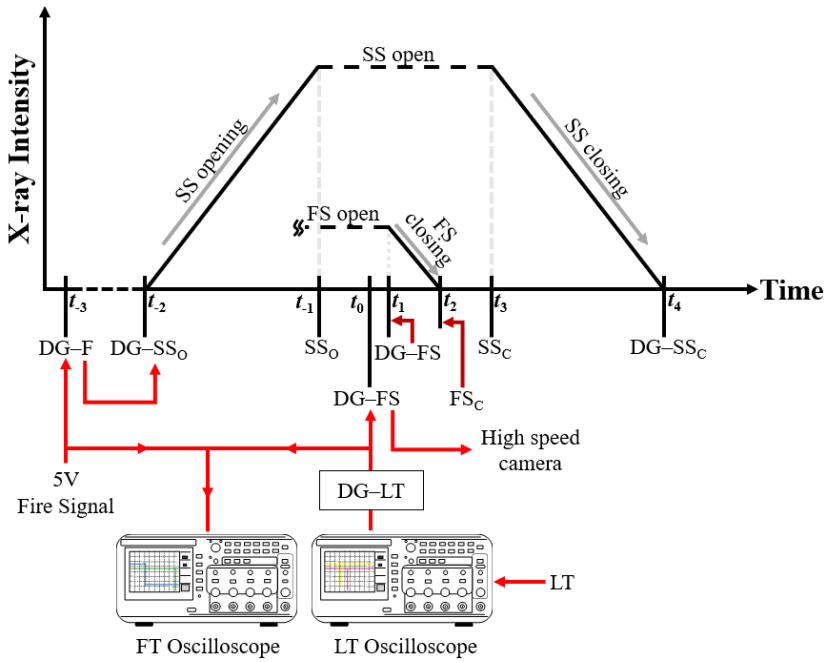

Figure 3.3. Synchronization chart between the X-ray beam, gas gun system, and high speed camera. DG: delay generator, F: fire, SS: slow shutter, SSo: slow shutter open, SSc: slow shutter close, FS: fast shutter, FSc: fast shutter close, FT: function time, LT: laser trigger, $t_{\_i}$: characteristic times before LT, t_i: characteristic times after LT. A total of four DGs and two oscilloscopes were required to achieve synchronization of the various signals.

3.2.4 Postmortem analysis

The coating layer was not recoverable after exposure to FOD impact due to complete pulverization. However, fractured segments of the underlying SiC substrate were recoverable, and they were used here to perform postmortem analysis. Specifically, visual inspection of the fracture surface morphology was carried out using a SEM. The latter investigation was critical in the effort to establish the damage features in the substrate which were initially identified from the *in situ* observations.

3.3 Results

3.3.1 Coating microstructure and composition

Electron micrographs which depict microstructures of the air plasma sprayed mullite and silicon coating layers as well as SiC substrate are provided in Figure 3.4. Figure 3.4a shows a scan of the mullite topcoat surface in SE mode. The resulting radiographs reveal a rough morphology

with stacked globular and pancake like structures. There are also crevices, microcracks, and well as dispersed micro porosities. These morphological findings are expected for APS coatings which form by successive impingement of molten particles at high velocities (≤ 450 m/s) [162]. Following the surface scan, cross-sectional scans of the polished coated sample was performed in (BSE) mode to reveal both the morphology and chemistry of the individual layers. The resulting images are shown in Figure 3.4b. In the mullite topcoat, subsurface porosities, microcracks, splat boundaries, and partially molten particles are observed. These same features are also observed in the silicon bond coat. The boundary between the topcoat and bond coat appears well bonded with no discernable cracking. In contrast, cracks and voids are found uniformly distributed along the silicon bond coat–SiC substrate interface. This weak boundary likely resulted from an insufficiently rough surface which limits the adhesion of the molten silicon particles during deposition. The difference in chemistry of the layers is highlighted by the changes in intensity of the BSE images. Pure silicon bond coat appears brighter than the multi element (i.e. aluminum, silicon, and oxygen) mullite topcoat. A more definitive chemical analysis was done using an EDS detector and the results are presented next.

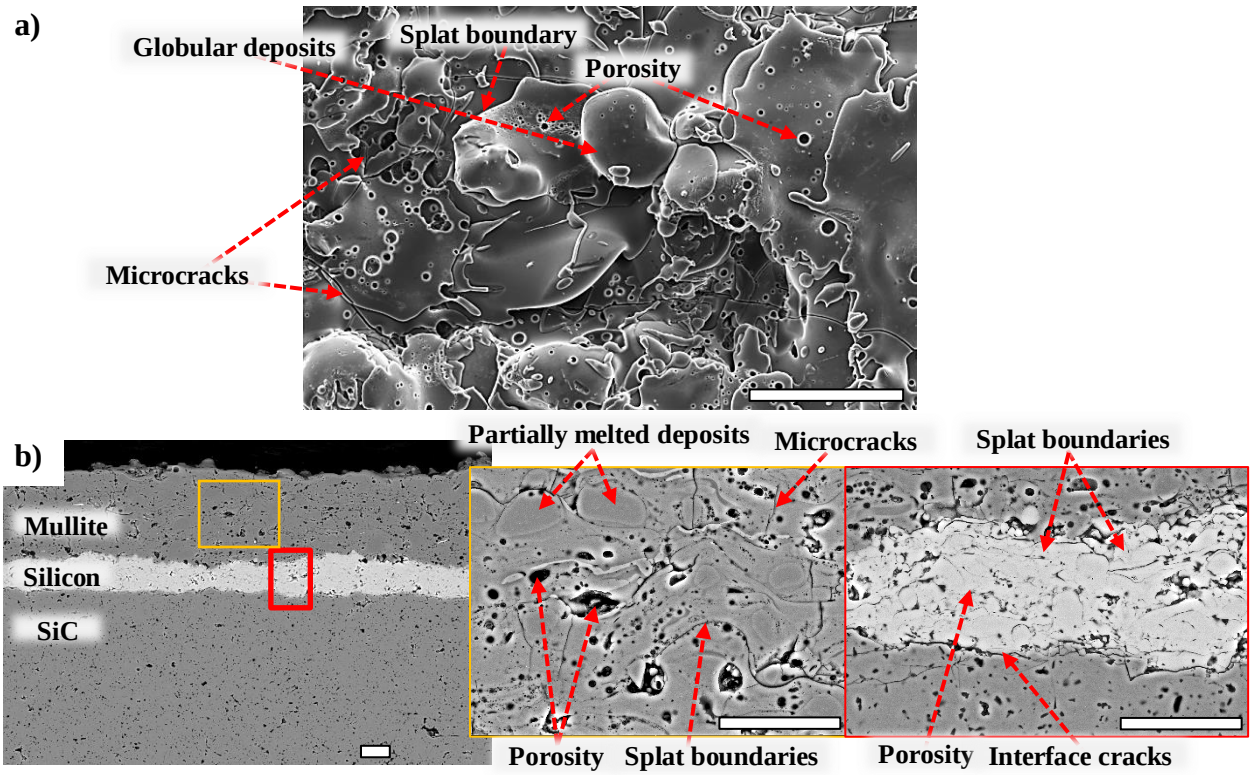

Figure 3.4. Scanning electron micrographs of the APS mullite topcoat surface in secondary electron (SE) mode (a), and full EBC cross-section in backscatter electron (BSE) mode (b). Scale bars in each image – 50 µm.

A comprehensive elemental map of the coating cross-section, as well as individual element maps, is provided in Figure 3.5a. As expected, aluminum and oxygen are found exclusively in the mullite topcoat owed to the ~ 77 wt % alumina (Al_2O_3) content in the feedstock. A predominant concentration of silicon is found at the silicon bond coat and SiC substrate, while the small content of silicon within SiO_2 (~ 22.5 wt %) of the mullite feedstock is barely detected. There are also two interesting features in the comprehensive elemental map that stand out: overwhelmingly red (aluminum rich) and overwhelmingly yellow (aluminum poor) regions in the mullite topcoat. The red regions represent a potential secondary phase. Subsequently, a more localized analysis was performed by taking a line scan. The results, as shown in Figure 3.5b, suggest that silicon is depleted in this region while a slight increase occurs for aluminum. In contrast, the yellow regions are those where aluminum counts decrease. Corresponding line scans were not possible due to edge effects and charging at these points. More concrete confirmation of the phases was performed via X-ray diffraction analyses and the results are presented next.

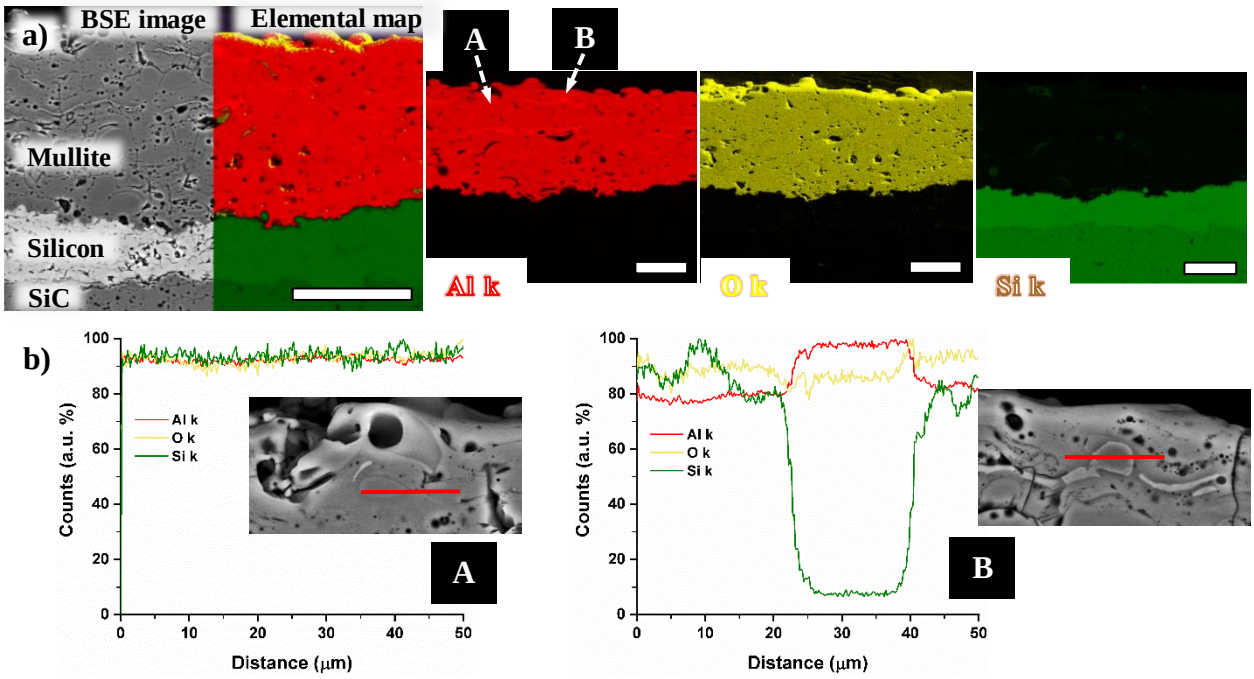

Figure 3.5. Elemental map of the coated ceramic cross-section (a) as well as line scans of typical and aluminum rich regions of the mullite coating (b). The chemical analysis was performed using the energy dispersive X-ray spectroscopy (EDS) unit in the SEM. Scale bars in (a) – 100 μm.

X-ray diffraction (XRD) patterns for the mullite feedstock, as well as the coating in both as-processed and thermally treated states, are provided in Figure 3.6. Each pattern was indexed independently, and a major phase of mullite and a minor phase of stable alumina (α-Al2O3) were identified as the predominant constituents. The latter secondary phase is noted to correspond to the aluminum rich regions in the elemental maps (and line scans) of the coating cross-section (see Figure 3.5b). However, an independent silica phase is not observed. The latter suggests that the aluminum poor regions detected in the elemental maps near the topcoat surface (Figure 3.5a) are due to oversaturation of the detector vis electron accumulation (charging). Compared to the pattern for the standard mullite powder, the XRD pattern for the as-processed coating retains a slight hump for peaks below $2\theta \approx 30^{\circ}$ and reduced peak intensities at higher 2θ values. The difference in the as-processed coating is associated with rapid cooling during APS deposition. The fast cooling rate has been shown to result in incomplete crystallization of the mullite phase and produce broadening for XRD peaks between 20°- 40˚ in 2θ [62,163,164]. For the current work, the higher primary Ar gas flow rate and lower torch power yields lower deposition temperatures and hence a reduced extent of amorphization. Still, the as-processed coating was thermally annealed at 1300 ˚C for 12h

to induce crystallization of any retained amorphous mullite phase. The resulting XRD pattern for the thermally treated coating confirms the complete crystallization of the as-processed coating. Specifically, the peak broadening at lower 2θ values is extensively reduced and the peak intensities at higher 2θ values are more pronounced. Crystallinity of the coating was also quantitively assessed by determining the integrated area for crystalline peaks and dividing by the area for the overall XRD pattern (i.e. combination of amorphous and crystalline signals). The results suggest a crystallinity of ~ 68.3 % and ~ 98.8 % for the as-processed and thermally treated coatings. The latter result is in line with the qualitative determinations.

A slight shift in the peak position along the two-theta axis is also observed for both the as-processed and thermally treated samples as compared to the reference for mullite (PDF# 73-1389). The average shift of peaks is found to be nearly consistent for all peaks in the two sample types with averages of 0.158±0.033˚ and 0.322±0.061˚, for the as-processed and thermally treated sample respectively. Theoretically, a positive shift is associated with a reduction in the lattice spacing (i.e. compressive lattice strain). However, the dominant residual stress which results during post-deposition cooling would induce a tensile strain on the mullite surface based on the slightly lower coefficient of thermal expansion (CTE) for the silicon bond coat[1]. This is the inverse of what is obtained from the diffraction measurements and the interpretation of a residual stress is not merited. Given that the shifts are considerably small (< 0.5˚), they are then postulated to potentially result from scattering by imperfections (roughness) on the coating surface and/or the elimination of the α-Al2O3 peaks (2θ ~ 43.2˚, 66.4˚, 68.1˚). Despite the presence of an amorphous phase, the FOD impact behavior of the as-processed coating without heat treatment was examined to reduce adverse effects including sintering, oxidation, and thermomechanical damage.

[1] The CTE for SiC, silicon and mullite are reported in [71] as 5, 4, and 5.4 ($\times 10^{-6}$) $^{\circ}C^{-1}$ respectively. The thermal residual stress from cooling, σ_i, in each layer is the product of the difference in thermal expansion with the designated substrate, α_s, and the change in temperature, $\sigma_i \propto (\alpha_s - \alpha_i)\Delta T$.

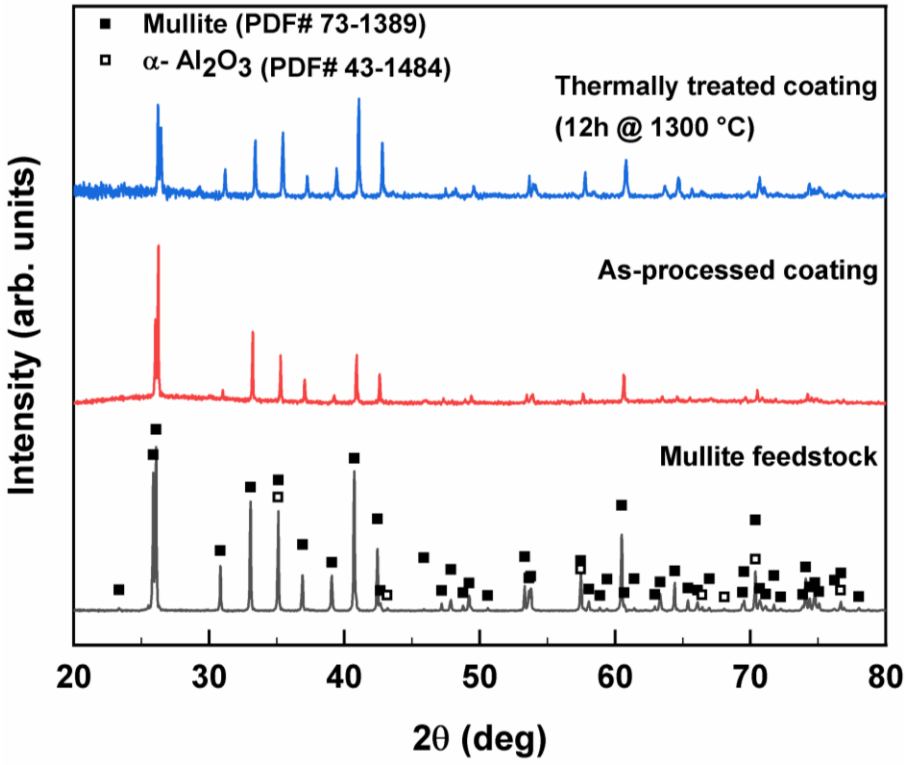

Figure 3.6. XRD spectra of mullite feedstock, as-processed coating, and thermally treated coating (12 h @ 1300 ˚C). Indexed peaks using PDF cards from the Joint Committee on Powder Diffraction Standard (JCPDS) for the major constituent of mullite and minor constituent of mullite and minor constituent of α-Al_2O_3.

3.3.2 Analysis of Raman spectra

As noted above, the difference in CTE between the EBC layers and SiC substrate may lead to stress during post-deposition cooling period. Empirical assessment of this localized residual thermal stress in thin coatings is possible through Micro-Raman spectroscopy. The Raman spectra reveals the rovibronic states of the atoms (or molecules) composing the lattice structure of a material. Silicon, for instance, has a characteristic Raman band at ~ 520 cm^{-1} corresponding to a longitudinal transverse optical (LTO) phonon vibration of the lattice. When stress is applied or a residual stress is present, there is a shift in the frequency of the characteristic band(s) owed to the alteration in the lattice spacing. Several studies on the effects of stress on Raman spectra have shown that a shift of peak(s) to higher spatial frequencies results from a compressive stress and the inverse (shift to lower frequencies) occurs for a tensile stress [165]. As shown in Figure 3.7, the LTO peak for the silicon bond coat does not shift appreciably from the standard peak position irrespective of the region (i.e. near the topcoat, at the center, and near the substrate). For each

region, over 20 measurements were made at different locations along the coating length and the results are displayed as cumulative averages with standard error bands. In order to establish statistical variability, a two-sample t-test with a P-value condition of > 0.05 was performed between the three curves and the standard curve. The results yielded P-values that ranged between 0.25 and 0.4 indicating no significant difference (i.e. no band shift) between the standard and the measurements.

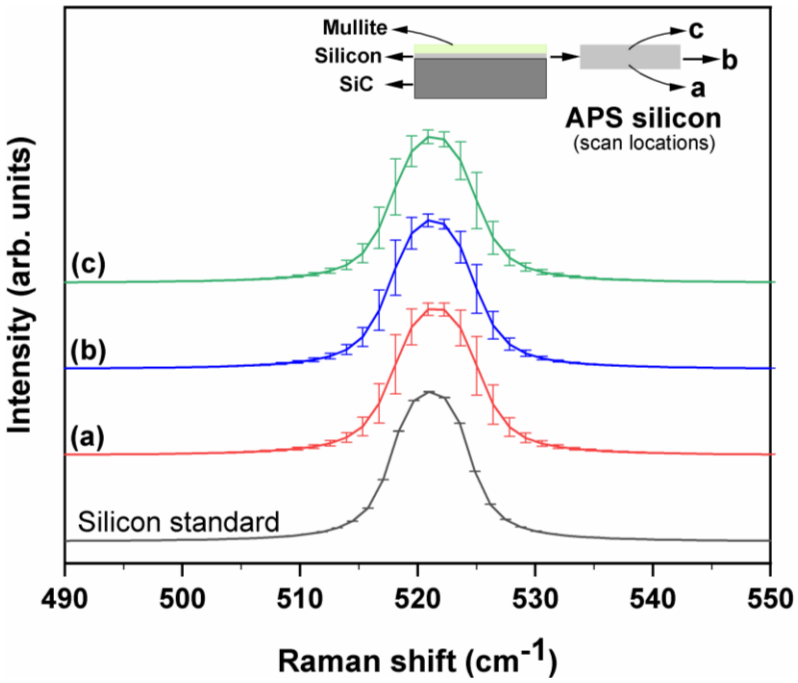

Figure 3.7. Characteristic Raman shift of the silicon bond coat near the SiC substrate interface (a), at the center (b), and near the mullite topcoat (c). These spectra are compared with that obtained from an internal silicon.

In addition to the silicon bond coat, the Raman spectra collected for the mullite topcoat near the bond coat interface is also examined. As shown in Figure 3.8, six bands which match between the mullite coating and powder/feedstock reference are clearly identified. The silicon LTO peak is also observed due to measurements being taken at close proximities to the bond coat. A two-sample t-test, between mullite powder and coating was conducted for each value of the three A_g peaks (303, 957, and 1129 cm^{-1}) and one B_{1g} peak (409 cm^{-1}). The analysis yielded P-values which ranged between 0.06 to 0.85 indicating no significant shift between the Raman

spectra for the mullite powder and coating. The B_{2g} (606 cm^{-1}) and B_{1g} (1028 cm^{-1}) peaks were not included in the t-test due to lack of clear maxima in the coating spectra.

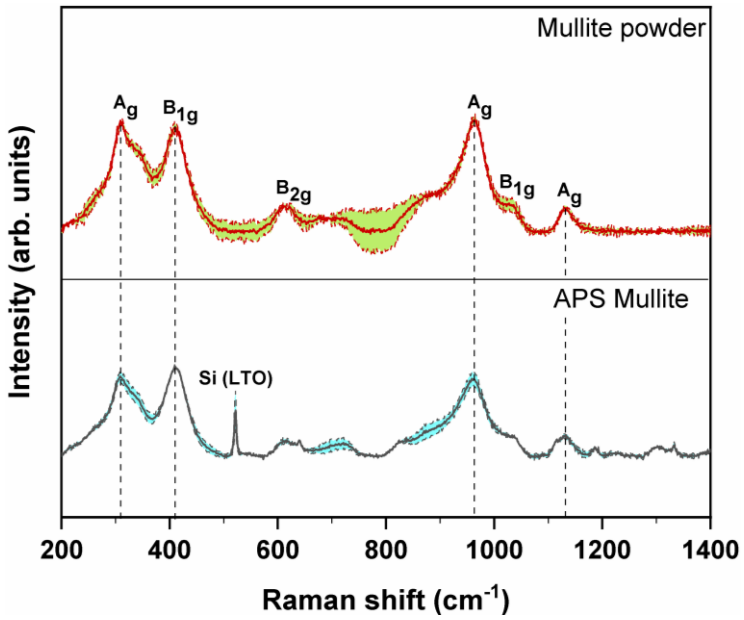

Peak list (cm^{-1})	Assignments [166]
A_g (303)	B: Al(o)-O-Si B: O-Al(o)-O
B_{1g} (409)	B: O-Al(t)-O
B_{2g} (606)	S: O-Al(t) S: Al(o)-O-Al(t) B: Si-O-Al(t) B: O-Si-O
A_g (957)	S: O-Si
B_{1g} (1028)	S: O-Si
A_g (1129)	S: O-Si

B (bond bending), S (bond stretching), O (oxygen), Si (silicon), Al (aluminum), o,t (octahedra, tetrahedra)

Figure 3.8. Raman spectra of mullite feedstock and APS mullite coating.

These observations affirm the X-ray diffraction results by qualitatively indicating that the EBC layer forms with little to no residual thermal stress from deposition. A residual stress has the potential to weaken the EBC layer and reduced in-service life (i.e. early fatigue fracture and delamination) [167,168]. In the case of FOD impact, a residual stress will affect the failure mode of the coating. Especially under residual tension, the localized (compressive) impact load would catalyze the release of stored strain energy and induce delamination/spallation of the coating.

3.3.3 Dynamic X-ray observations

A total of eight *in situ* impact experiments were performed with the coated SiC samples. These experiments were segmented by projectile material, with four observations utilizing PSZ spheres and the remaining four Si_3N_4 spheres. The retrieved high speed X-ray radiographs were post processed using an open-source image analysis software, Fiji (ImageJ). It is important to note that these radiographs are two-dimensional projections of the three-dimensional failure in the bulk and that the features being observed will lie in different planes. The follow-on sections provide an

in-depth evaluation of the results, starting with observations of FOD impact by PSZ and Si_3N_4 projectiles respectively.

3.3.3.1 Impact by PSZ projectile

The response of the coated SiC ceramic to FOD impact, by PSZ projectiles, was found to be consistent across all four experiments. Representative dynamic X-ray radiographs for the first experiment performed at a velocity of ~ 316 m/s are shown in Figure 3.9. The first frame depicts the sphere, EBC layer, and substrate before impact. After the sphere contacts the surface, both deformation and localized protrusion of the mullite topcoat (t = 0.5 µs) are observed. The sphere then penetrates the coating as it continues to displace towards the substrate. A delamination crack emerges when the sphere penetration reaches the topcoat–bond coat interface. As evidenced in Figure 3.9 (t = 1.5 µs), continued loading compresses the thin bond coat layer and induces radial deformation in the sphere. Several damage features are also observed to occur simultaneously including the ejection of a plume of coating material, the complete delamination of the topcoat at the bond coat interface, and the initiation of Hertzian cone cracks in the substrate (see magnified image within in Figure 3.9, t = 1.5 µs). A general half apex angle of 48.6±2.3˚ was determined for the cone cracks, from the dynamic X-ray radiographs. The delaminated topcoat then starts to liftoff gradually in response to the deforming sphere, while back-surface cracks develop and bifurcate in the SiC substrate before propagating towards the bond coat interface (t = 2.5 and 3.5 µs). The sphere continues to deform until it reaches a critical strain, after which it begins to separate into small debris (t = 17.0 µs). As the projectile debris fly apart, they also excavate both the topcoat and bond coat. The latter unloading at the bond coat–substrate interface promotes complete failure of the SiC substrate through opening of the back-surface crack vents. The development of damage modes was identical for the other three experiments, with only slight variations in the extent of substrate cracking prior to failure. Radiographs for these experiments are provided in Appendix C, Figures C.1 to C.3.

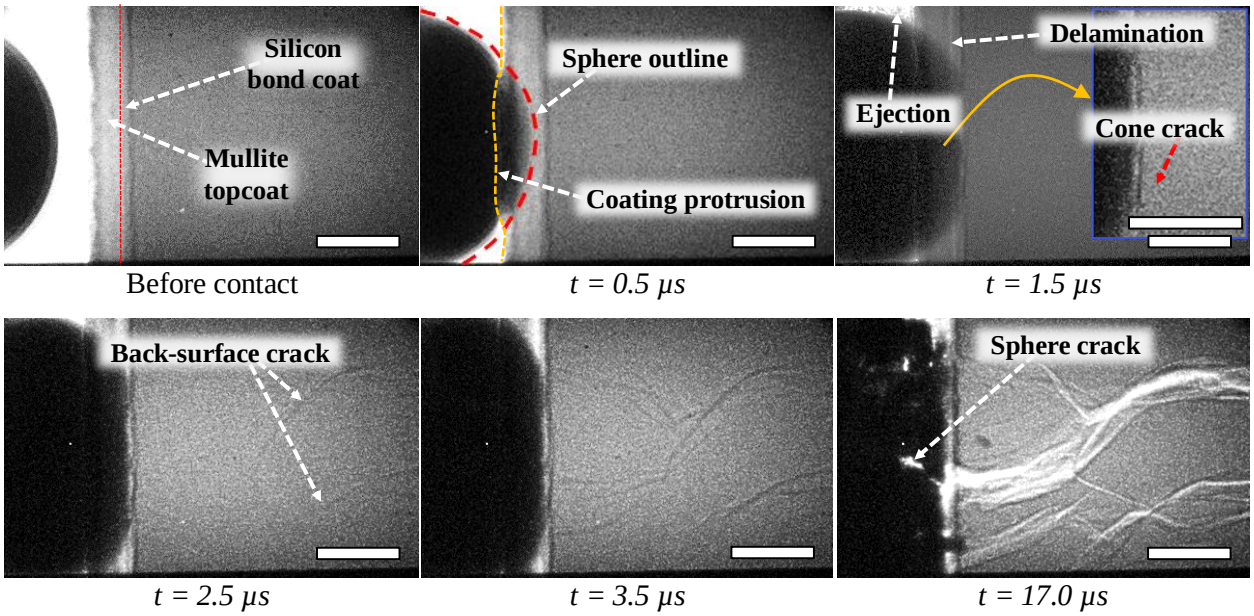

Figure 3.9. X-ray radiographs depicting impact of a coated SiC substrate by a spherical (1.5 mm diameter) PSZ projectile at a velocity of 316 m/s. Images were recorded at 2M frames per second with an exposure time of 200 ns. Scale bars in each frame – 500 μm.

3.3.3.2 Impact by Si_3N_4 projectile

As an approach to examine the effect of projectile material properties on the FOD impact behavior of the coated SiC ceramic, an additional four experiments were performed using spheres of Si_3N_4. Only three of the four *in situ* observations were found to meet the required full support boundary condition due to misalignment in one of the samples. Still, assessment of the dynamic X-ray radiographs revealed a consistency across all three valid experiments in the evolution of damage mechanisms. The approach of using a single radiograph for reference is thus adopted here once more to assist in detailing the generally observed behavior. Figure 3.10 depicts the response for the first coated sample impacted at a velocity of ~ 323 m/s. The first frame highlights the boundaries of the sphere, topcoat, bond coat, and substrate before impact. Initial contact between the sphere and topcoat results in slight deformation of the asperities on the rough surface (not shown). After the asperities are completely deformed, the sphere continues to displace rapidly towards the bond coat interface (t = 0.56 μs) and then to the substrate interface. Penetration of the coating by the projectile produces a plume of the topcoat material as shown in Figure 3.10, t = 1.56 μs. In addition to the ejection of coating material, signs of delamination at the bond coat–substrate

interface and diametral cracking in the Si_3N_4 sphere are observed. Once coating delamination occurs, the sphere begins to bounce back from the substrate (t = 2.06 µs). Direct measurements from the X-ray radiographs render an average fragment-front rebound velocity of 22.7±1.8 m/s for the sphere and a corresponding coefficient of restitution of 0.068±0.005. During this event, where the sphere fragments and coating conjointly separate from the substrate, the sphere fragments are observed to fracture significantly while some cracks initiate in the coating. The latter unloading step is also associated with the emergence of back-surface cracks in the substrate (t = 2.56 µs). As shown in Figure 3.10, t = 7.06, the final stages of impact damage consist of pulverization of the sphere which causes the delaminated coating to fracture apart, and fracture of the substrate from opening of the fully formed back-surface cracks. The other two experiments were also observed to retain similar evolution of damage modes during impact, albeit having minor differences in the extent of cracking within the sphere (prior to pulverization) and substrate (before complete failure). Visual depictions of these experiments are provided in Appendix C, Figures C.4 to C.5.

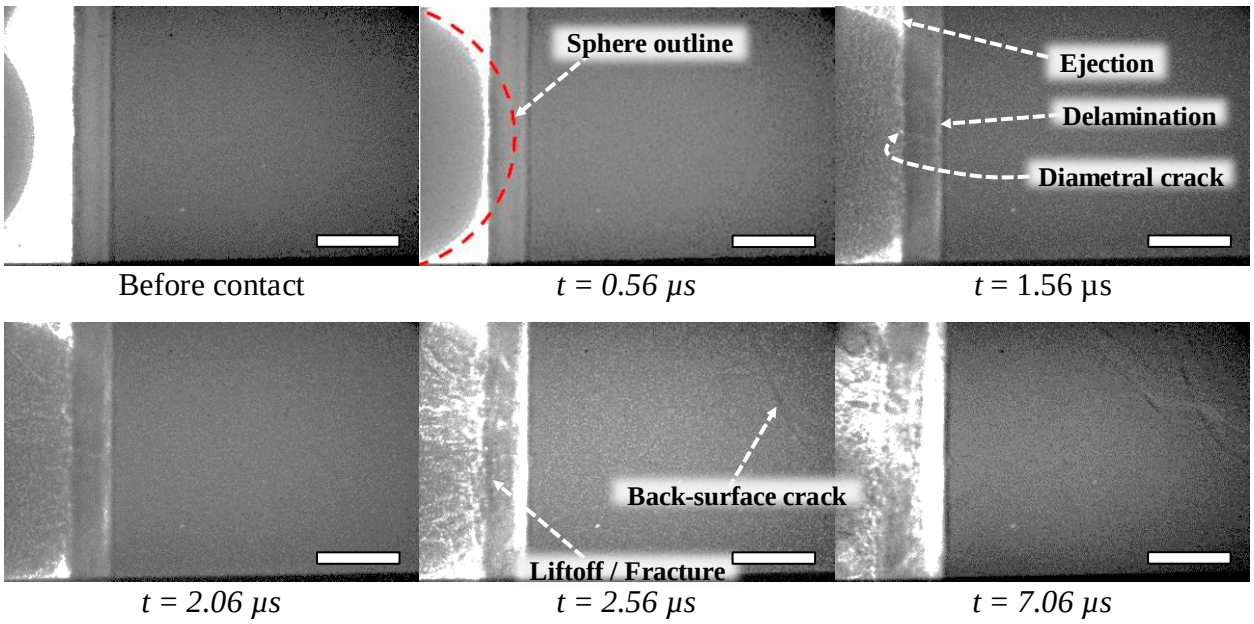

Figure 3.10. X-ray radiographs depicting impact of a coated SiC substrate by a spherical (1.5 mm diameter) Si_3N_4 projectile at a velocity of 323 m/s. Images were recorded at 2M frames per second with an exposure time of 200 ns. Scale bars in each frame – 500 µm.

3.4 Discussions

Fundamentally, the observed impact damage in the coating by the PSZ sphere may be understood through microstructure and material properties considerations. The plasma sprayed EBC is highly porous as observed in Figure 3.4b. This porous microstructure has been shown in previous studies to promote deformation during spherical (or Hertzian) contact via localized micro-fractures and pore collapse (i.e. compaction) [169,170]. Hence, the mullite topcoat is deformed upon contact, and the radially displaced material piles up around the perimeter of the PSZ projectile. The latter produces the observed subsurface protrusion in Figure 3.9, t = 0.5 μs. It is also important to note that the PSZ projectile retains a higher hardness (see Table 3.2) relative to the mullite coating and this enables it to indent (or inelastically deform) the coating during impact. The projectile does eventually become amenable to deformation, as it experiences resistance to additional displacement by the hard SiC substrate. Deformation of the projectile is facilitated by localized fracture of porosities in the microstructure which are formed during sintering of the precursor PSZ particles. In addition to producing a plume of topcoat, the radial deformation in the sphere also induces a shear stress at the topcoat–bond coat interface. Since the sphere does not penetrate through the bond coat, continued loading (i.e. buildup of interfacial shear stress) produces the observed delamination of the topcoat from the bond coat. Finally, removal of the silicon bond coat occurs through erosion by the fractured pieces (debris) of the hard PSZ sphere.

Similar to the observation for the PSZ projectile, deformation of the coating results when the Si_3N_4 projectile makes contact with the surface. This is again attributed to the porous EBC microstructure and the higher hardness for Si_3N_4. Unlike the tough PSZ projectile, the highly brittle Si_3N_4 sphere does not flow radially as it displaces further into the coating. As a result, significant ejection of the topcoat material and no evident accumulation of displaced material about the sphere perimeter is observed. Once the sphere penetrates the topcoat and bond coat, a brittle elastic contact is established between the two bodies where further increase in strain energy is partially dissipated through fracture. A diametral crack is thus initiated first in the sphere as it experiences a compressive stress from both the contact side (interaction force) and the free surface side (inertial force). Concurrently, a delamination crack forms at the interface between the bond coat and substrate. Akin to impact by the PSZ projectile, a global displacement of material by the penetrating Si_3N_4 projectile likely produces sufficient shear stress at the contact interface between the bond coat and substrate to yield the observed delamination behavior.

Overall, the FOD impact of the coating by the Si_3N_4 projectile is observed to be more catastrophic relative to the PSZ projectile. Specifically, complete and immediate EBC delamination is observed for impact by Si_3N_4. As noted, the harder Si_3N_4 projectile is more brittle relative to the PSZ projectile. As such, it retains its spherical shape during the deformation of the coating, and this allows for a concentrated application of the impact load and thus results in penetration of both the topcoat and bond coat. The inverse is true for the tough PSZ projectile which flows radially and hence blunts at the topcoat–bond coat interface, where delamination is observed to occur. In addition, the Si_3N_4 projectile appears to become partially embedded, and as it rebounds from the substrate surface it induces an accelerated liftoff of the already delaminated coating from the substrate. Again, the inverse is evidenced for the PSZ projectile due to the extended loading of the bond coat surface with no observable rebound event. Further, the Si_3N_4 projectile induces significant fracture in the delaminated coating as it separates into smaller debris. The radial fragmentation of the Si_3N_4 projectile induces a tensile stress on existing defects (i.e. porosities and inter-splat boundaries) of the topcoat and these defects facilitate the observed fracture process. In contrast, the PSZ projectile appears to pulverize the topcoat due to its high impact energy[2] and erode the bond coat as it simultaneously deforms and fragments on top of it. A similar response has been observed previously in fibrous SiC ceramic composites where a higher degree of fracture is observed for FOD impact by the Si_3N_4 sphere and more pulverization for the PSZ sphere [160].

The current study helps to both reinforce and advance previous understandings of the damage mechanisms associated with FOD impact of plasma sprayed coatings (both EBCs and TBCs). Past efforts provide information on impact experiments at standard ambient conditions by steel spheres with diameters ranging between 1.5 to 5 mm and velocities ranging between 65 to 400 m/s [106-108,159,171]. Irrespective of the impact velocity, projectile size, or coating thickness, almost all of these studies show two critical damage mechanisms that are also observed in the current work: deformation and ejection (or removal) of topcoat material. The deformation aspect is agreeably attributed to the porous nature of the coating and the relative hardness of the projectiles, while the material removal has been thought to result from spallation within the topcoat or at the

[2] Here, the impact energy is considered as the kinetic energy, $E_{im} = 1/2(mV^2)$. The mass, m, of the spherical projectile is calculated using the volume for a 1.5 mm radius sphere and the density reported in Table 3.2. Impact velocities are those reported here for PSZ and Si_3N_4 (i.e. 316 and 323 m/s). Respective values of 0.54 J and 0.29 J are determined for impact by PSZ and Si_3N_4 spheres.

bond coat interface for thick and thin coatings respectively. However, the *in situ* observations clearly show that coating material removal occurs via erosion mechanisms during penetration by the sphere. A potential path for the erosion process would be concentration of the impact stress at defect sites (i.e. splat boundaries and porosities) and subsequent growth of microcrack networks that facilitate excavation of the coating as a plume of debris. In order to empirically validate the latter hypothesis, a localized ($\geq$ 20x magnification) *in situ* observation near a splat boundary will be required. Other considerations for material removal are the effects of projectile size, impact velocity, and substrate compliance. Based on the work by Dericioglu *et al*. [159], the combination of a large projectile, soft substrate, and intermediate impact velocity (100-200 m/s) favors extensive coating/substrate deformation instead of coating removal. However, as the sphere becomes smaller the localization of contact stress makes it behave as a sharp indenter [150,172]. In the current work, the latter behavior is observed during the initial stages of impact where the 1.5 mm sphere induces penetration and removal of the topcoat material. Additionally, more compliant substrates such as steel can absorb a significant amount of the impact energy via plastic deformation and this limits the extent of coating delamination. By contrast, the rigid SiC substrate used in the current work can typically displace only elastically during impact. This would then render more of the impact energy to be dissipated by the compliant coating (i.e. extensive damage is sustained by the coating material). In the case of impact induced delamination, the driving force would be the shear stress generated at interfaces during projectile penetration for both PSZ and Si_3N_4 projectiles. The latter has been identified in the FOD impact study by Faucett *et al*. [108] on thick APS yttria stabilized zirconia (YSZ) coatings where cracks propagating perpendicular (or lateral) to the impact direction were attributed to radial displacement of material by the partially penetrating sphere and the ensuing shear stress. This study also uncovers some unique damage mechanisms that arise in the underlying SiC substrate during impact. Similar to the analysis on the coating portion of the specimens, the follow-on sections render a fundamental understanding of the substrate response to FOD impact.

3.4.1 FOD impact response of the SiC substrate

The FOD impact behavior of uncoated SiC has been previously investigated in Chapter 2. Irrespective of the projectile material, a purely brittle elastic response was observed with primary Hertzian cone cracks. Figures 2.6a-c, in Chapter 2, show electron micrographs of recovered

fracture segments of samples impacted by PSZ and Si_3N_4 projectiles. For both impactor materials, advancing secondary (median and vertical) cracks are internally arrested and only the three-dimensional volumes are carved out by the primary cone cracks. By contrast, the current study on coated samples shows that the protective layer induces a moderate to significant change in the damage mechanisms of the underlying SiC substrate. The observed deviations are addressed next with aid from postmortem evaluations of fracture surface morphologies in recovered specimens.

For impact by a PSZ projectile, the underlying SiC substrate shows both conventional and unique fracture behaviors. The response of the coating and substrate were established in the *in situ* dynamic X-ray radiographs (see Figure 3.9). Fracture pieces for two of the four experiments were recovered and analyzed via SEM. Fracture surfaces for one of the two recovered samples which corresponds to the experiment in Figure 3.9 are shown here in Figures 3.11a and 3.11b. The fracture surfaces for the other sample which correspond to the experiment in Figure C.2 are also provided in Appendix C as Figures C.6a and C.6b for reference. In both cases, the fracture surfaces discern the demarcations of the Hertzian cone crack at the impact site. A half-apex cone crack angle of 49.0±3.4˚ was determined using the two recovered specimens. This angle is in close agreement with the value obtained from the *in situ* X-ray radiographs. Additionally, remnants of a secondary cone crack are found slightly above the primary cone crack in Figure 3.11b. The latter was not clearly observable in the X-ray radiographs due to overshadowing by the back-surface cracks. However, there have been previous accounts of secondary and even tertiary cone cracking [87,150]. The emergence of these cracks is attributed to continued loading of the surface by the deforming sphere and they appear for impact of uncoated specimens[160]. The investigation by Marimuthu *et al*. [148] also shows that the newly established stress field from the expanding sphere induces kinking (i.e. change in crack growth trajectory) of the primary cone crack and this is evidenced in the fracture surfaces. Localized investigations (magnified imaging) of the fracture surface also reveal primarily intragranular fracture near the point of impact, at the cone crack initiation points, as well as at the center and back of the sample. This is similar to the finding for uncoated specimens (see Chapter 2.3.4).

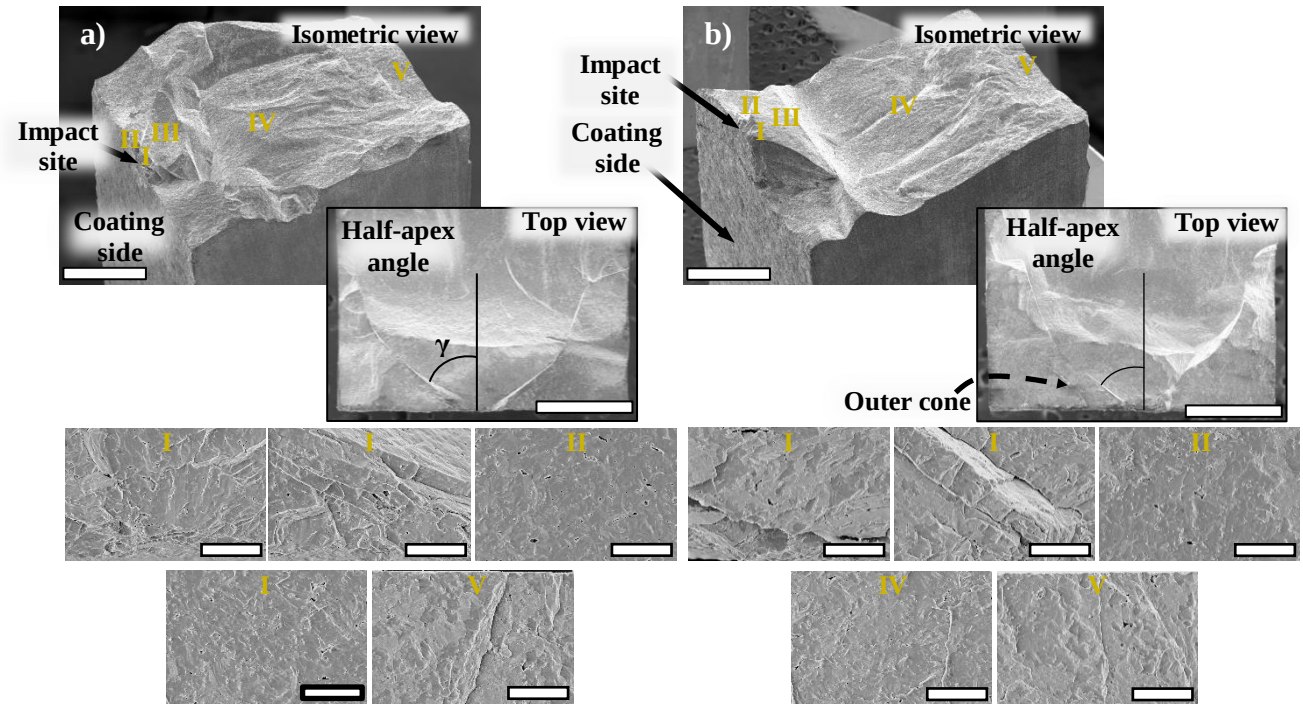

Figure 3.11. Postmortem fracture surfaces of the bottom (a) and top (b) portions of the sample impacted by a PSZ projectile in Figure 3.9. Scale bars for isometric and top surfaces – 1 mm. Scale bar for zoomed in surfaces – 50 µm.

In contrast, FOD impact of the coated SiC ceramic by Si_3N_4 projectiles is observed, in the X-ray radiographs, to only induce the propagation of cracks from the back-surface of the substrate after the sphere penetrates through to the bond coat. Both segments of the sample from the experiment in Figure C.4, Appendix C, were recovered and the resulting fracture surfaces are provided here in Figures 3.12a and 3.12b. The top half of the sample from the experiment in Figure 3.10 was also recovered and the resulting fracture surface is provided in Appendix C as Figure C.7 for reference. Clearly, there are no indications of cone crack formation. Similar to the observation for impact by PSZ projectile, a predominantly intragranular fracture pattern is observed in the localized fracture images. The latter is also similar to the observation for uncoated specimens in Chapter 2.3.4. This finding reveals that the presence of a protective coating layer alters the dominant crack type for failure without changing the inherent mode of fracture associated with SiC at both quasi-static and dynamic loading conditions.

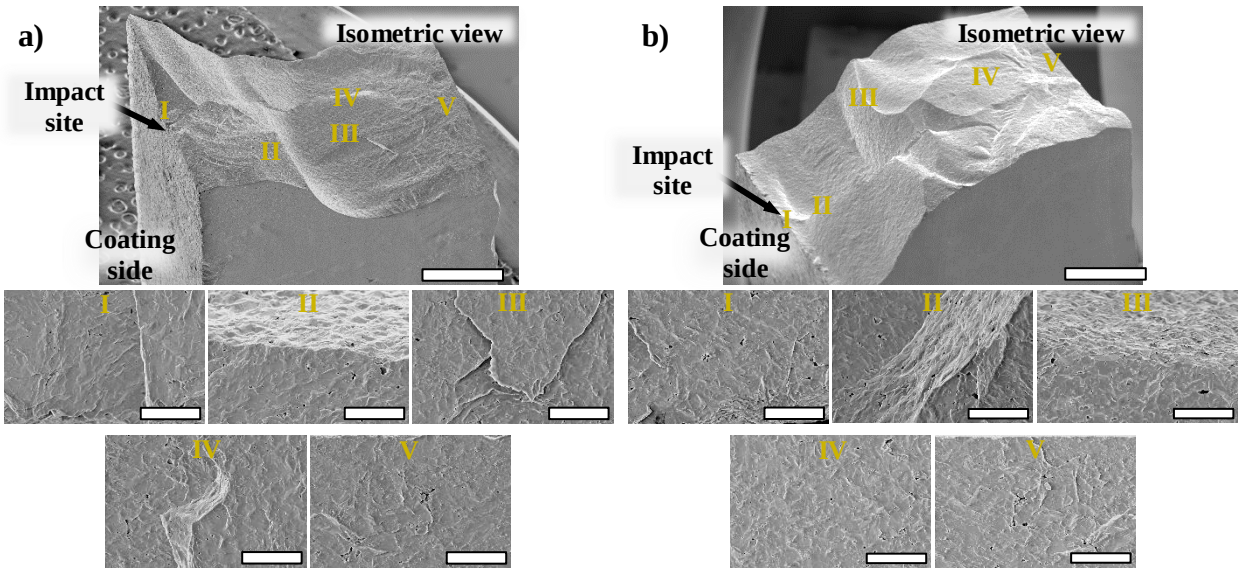

Figure 3.12. Postmortem fracture surfaces of the top (a) and bottom (b) portions of the sample impacted by a Si_3N_4 projectile in Appendix C, Figure C.4. Scale bar for isometric surfaces – 1 mm. Scale bar for zoomed in surfaces – 50 µm.

The *in situ* dynamic X-ray visualizations and postmortem fracture surface analysis presented above have enabled us to identify two distinct types of fracture processes that arise during impact of the coated SiC substrates. The first is *cone cracking*, which is only observed in samples impacted by PSZ projectiles. And the second is *back-surface cracking*, which is observed for impact with both PSZ and Si_3N_4 projectiles. Subsequently, each of these fracture types are addressed individually starting with cone crack formation.

3.4.1.1 Cone cracks from impact by PSZ projectiles

Under ideal conditions, the spherical impactor deforms elastically and forms a circular area of contact with the substrate. Near the perimeter of the circle of contact, a radial tensile stress, σ_r, acts to counter the confining compressive stresses by the elastic surrounds. This radial stress decays rapidly as the inverse square of the radial distance ($\sigma_r \propto r^{-2}$) along the surface. Ring cracks, which precede cone cracking, initiate on the surface of the substrate near the maximum of the surface radial stress. Downward extension of the ring cracks into fully developed cone cracks is subsequently driven by the component of the radial stress that is active in the region beneath the circle of contact. Based on the formulation by Johnson [153], the subsurface depth, z, of the active tensile stress field can be determined as a function of the measured contact radius, a, and has a

maximum value of ~ $1.42a$. Since the depth of coating penetration is limited to the topcoat–bond coat interface, for impact by PSZ projectiles, the extension of the stress from the bond coat to the SiC substrate needs to be considered. This is achieved during the quasi-plastic deformation of the PSZ projectile. The latter process yields an expanding circular area of contact through which the radial stress is established and propagated to the subsurface. Based on measurements of the fracture morphology (see Figures 3.11a and 3.11b), cone crack initiation in the SiC substrate occurs when the circle of contact with the bond coat attains a radius of 213.5±19.8 μm. Assuming ideal contact conditions, a maximum subsurface depth value of 303.2 μm is determined for the ensuing radial stress. In relation to the bond coat thickness (58.0 ± 2.3 μm), the radial stress persists to a depth that is at least five times greater. The PSZ projectiles would then have the capacity to induce the observed cone crack in the SiC substrate. By contrast, little to no deformation occurs for the brittle Si_3N_4 projectile after penetrating to the bond coat–substrate interface. Instead, the projectile fractures and any additional displacement (loading) result in the observed extension and bifurcation of the primary diametral cracks. The latter would effectively prevent the formation of a critical contact area with the SiC substrate and diminish the likelihood for the emergence of a radial stress (i.e. cone crack). The properties of the spherical projectiles are thus clearly significant for the observed fracture in the SiC substrate. This assessment suggests that unlike the brittle Si_3N_4 sphere, the tough PSZ sphere accommodates significant damage during impact, which leads to cone cracking in the underlying SiC substrate.

3.4.1.2 Back-surface cracks from impact by PSZ and Si_3N_4 projectiles

Based on the current evaluation of damage history in the *in situ* observations, two potential driving forces which would pose favorable conditions for the propagation of back-surface cracks in the SiC substrate during impact are identified. Specifically, the development of flexural loading in the substrate due to the initial interaction with compliant coating layer and the evolution of macroscopic bending from propagation of flexural stress waves are going to be qualitatively considered. These driving forces are advanced as complementary, and their aggregate effect is postulated to yield the observed back-surface cracks.

FOD impact induced deformation and penetration damage was observed in the coating layer before fracture occurring in the underlying substrate. The response of the ceramic coating is considered quasi-plastic and the resulting deformation is concentrated within the zone of high

compression and shear stress located below the contact interface with the impacting sphere [173,174]. It is very likely that the compliant coating layer will influence the stress developed in the substrate during impact. The exact nature of the response has yet to be elucidated for such transient loadings. There are, however, quasi-static indentation studies on similar coatings on metallic substrates which can be used to understand the high-rate observations in the current study. The first of these investigations was by Fisher-Cripps *et al.* [175] on the spherical indentation of APS alumina deposited onto a steel substrate. For the latter coating–substrate system, an empirically driven numerical analysis showed that in addition to the high shear within the coating, a zone of high compression and shear stress also develops inside the substrate. Further, these stress fields were projected to grow over time, provided the deformation in the substrate remained elastic and the coating continued to bear additional load. The latter prediction was experimentally and numerically verified in the study by Wuttiphan *et al*. [176] where a higher level of compression and shear stress was evolved for a (coated) high strength nickel superalloy substrate as compared to a (coated) compliant steel substrate. For the brittle elastic SiC substrate, used in the current work, the deformation of the coating layer is analogously expected to produce both compressive and shear stresses. The buildup in compression in the top layer of the substrate would induce a reactive tensile stress in the bottom layer and effectively promote a flexural loading condition. The overall state of flexure in the substrate would provide sufficient driving force for a critical flaw at the back-surface to initiate and unstably propagate to the bond coat interface. The latter phenomenon is observed irrespective of the spherical impactor material. However, a quasi-static displacement which requires an extended impact duration must be assumed [150,172]. The validity of such an assumption will be discussed next along with a justification for the impact induced shear stress by way of flexural wave propagation.

As noted, the observed back-surface cracking in the SiC substrate is distinctively similar to the response expected for a brittle material subject to a flexural loading condition. For the current FOD impact configuration, the spherical projectile would act as the central loading point. Although the specimen is supported on its back-surface, it is not constrained along its length or on the top surface and it has the freedom to extend laterally and bend outwards in response. Dynamically, this type of displacement would arise from propagation of flexural stress waves. Raman [177], Zener [178], and Koller and Kolsky [179] have previously addressed the latter concept in terms of the influence that the contact duration has on energy dissipation during impact. Specifically, an

inelastic impact condition prevails with longer contact times where a significant portion of the input kinetic energy is converted into energy for elastic wave propagation. The longer contact time also enables multiple reflections of both the primary waves (P-Waves) and the slower secondary waves (S-Waves) which are transverse (or flexural) in nature. The resulting particle motion can be treated as a displacement occurring by two rigid bodies under classical beam bending conditions. For the current study, the average contact times for impact by the PSZ and Si_3N_4 projectiles for these experiments were 4.0±0.4 μs and 0.9±0.2 μs respectively. The latter contact times were determined using the *in situ* dynamic X-ray radiographs with the contact time set to zero when the sphere touches the topcoat and at maximum when the fractured pieces rebound for Si_3N_4 sphere or completely fractures for PSZ sphere. The very long average contact time for impact by the PSZ spheres clearly permits the propagation of multiple P- and S-waves. It is thus very likely for flexural strains to develop and induce the observed back-surface cracking. On the contrary, only a single S-wave reflection is theoretically allowed for impact by the Si_3N_4 sphere[3]. The back-surface cracking must then develop from the action of a more complex dynamic process which has yet to be elucidated. Thus, additional numerical or analytical work will be required to model the driving forces already postulated for the observed damage mechanisms, as well as to comprehend the mechanisms which are not readily understood through qualitative analysis.

3.5 Summary and Implications

In this study, the viability of dynamic synchrotron X-rays for visualization of transient FOD impact phenomenon in coated silicon carbide specimens was investigated. The following summarizes key findings from the research effort:

1. Impact by partially stabilized zirconia (PSZ) projectiles results in penetration of the mullite topcoat. Upon reaching the silicon bond coat interface, the projectile starts to deform quasi-plastically in the radial direction and delaminates the topcoat. Cone and back-surface cracks are formed in the SiC substrate during subsequent loading. Complete coating removal occurs by ejection and erosion mechanisms.
2. In comparison, spherical projectiles made from brittle silicon nitride (Si_3N_4) are observed to penetrate both the topcoat and bond coat layers and sustain diametral fracture.

[3] Determined from the ratio of the substrate thickness to the shear wave velocity given in Table 3.2.

Delamination occurs at the bond coat–substrate interface. Only back-surface cracks emerge in the substrate with continued loading. Complete coating removal occurs via liftoff and fracture as the sphere fragments flay apart.

3. The initial deformation and penetration of the coating is ascribed to the inhomogeneous microstructure (i.e. porosities, microcracks, etc.) of coatings produced via air plasma spray (APS) process. These microstructural defects facilitate microfractures for erosion and ejection of the coating just below the penetrating projectile.
4. Delamination at the bond coat interface (impact by PSZ projectile) and the substrate interface (impact by Si_3N_4 projectile) occurs due to radial displacement of the coating material during penetration. The radial displacement of material induces a shear stress which overcomes the adhesion strength at the coating interface.
5. Evaluation of the fracture surfaces from recovered samples confirms the fracture patterns identified in the *in situ* observations. A predominantly intragranular fracture mode is also found to prevail for both coated and uncoated samples, as well as different projectile materials.
6. Hertzian cone cracks are only observed for impact by PSZ projectiles due to extended deformation of the projectile which enabled transmission of stress to the substrate.
7. Back-surface cracks which arise in the substrate for both types of impactors are postulated to result from flexural bending effects. The latter is qualitatively confirmed for impact by PSZ spheres, while an inconsistency was found for impact by Si_3N_4 spheres. A numerical approach is thus recommended as part of a future work to fully realize the validity of a flexure induced back-surface cracks.

This study showed that the dynamic X-ray visualization method can generate critical information on damage evolution of the coating and substrate during FOD impact. The limited work also illustrated that previous understandings of coating damage from *ex situ* inspections of impacted specimens fails to capture early stage failures via penetration. As observed, the latter is facilitated by the weak coating microstructure which undergoes erosive wear from impact loading by the hard projectiles. Past works often mistake this degradation as spallation failure. Furthermore, the role of projectile properties on the damage to a coated ceramic is ascertained for the first time. Increase in toughness and density of the projectile is found to enhance damage to the substrate

(cone and back-surface cracks for PSZ projectile vs back-surface crack for Si_3N_4 projectile). The latter is associated with increased deformation on the specimen and hence greater transfer of impact energy. Finally, the resistance to substrate fracture due to a coating layer is confirmed qualitatively. Lower level of cracking (especially cone cracks) is found in the coated samples relative to uncoated samples from a previous study (Chapter 2). This behavior is intuitively driven by dissipation of impact energy during penetration and delamination of the coating layer(s).

With this successful endeavor, follow-on research continues the investigation of FOD impact in the same coated silicon carbide ceramic with emphasis on the combined effects of specimen geometry and projectile material properties.

4. IMPACT DAMAGE OF NARROW SILICON CARBIDE (SIC) CERAMICS WITH AND WITHOUT COATINGS BY VARIOUS FOREIGN OBJECT DEBRIS (FOD) SIMULANTS

The following chapter contain content reproduced with permission from Kedir N, Garcia E, Kirk CD, Gao J, Guo Z, Zhai X, et al. Impact damage of narrow silicon carbide (SiC) ceramics with and without environmental barrier coatings (EBCs) by various foreign object debris (FOD) simulants. Surf Coat Technol. 2021;407:126779. DOI: 10.1016/j.surfcoat.2020.126779

4.1 Introduction

Investigation of FOD impact in environmental barrier coatings (EBCs) was first reported by Bhatt *et al*. [110] The latter study was conducted at ambient and elevated temperatures with impact velocities ranging between 100-375 m/s. Hardened steel spheres and woven silicon carbide (SiC_f/SiC) ceramic matrix composites (CMCs) with air plasma sprayed barium strontium aluminosilicate (BSAS) EBCs were respectively used as FOD simulants and targets. Irrespective of temperature, material removal (or cratering) via localized spallation was the primary damage attributed to the EBC. In terms of shielding, samples with thicker coatings were found to prevent perforation and significant loss in uniaxial strength. While the latter study provided crucial information on post-impact performance of the coated CMCs, very limited understanding was gained on the evolution of damage within the EBC layers during impact.

The work presented in Chapter 3 was the first effort which showed the capability of pulsed X-ray radiography to characterize, *in situ*, the underlying transient damage mechanisms during FOD impact of coated ceramic specimens composed of light elements (i.e. carbon, oxygen, silicon, and aluminum). Specifically, an air plasma sprayed EBC consisting of mullite topcoat and silicon bond coat layers was deposited on monolithic silicon carbide (SiC) substrates and the impact response was investigated using partially stabilized zirconia (PSZ) and silicon nitride (Si_3N_4) projectiles (FOD simulants) at velocities ranging between 300-350 m/s. The study showed that initial EBC removal occurs via localized microfracture and ejection (i.e. erosive wear) during penetration. Subsequent stages of coating and substrate damage were found to depend on the properties of the FOD simulant material. For the deformable PSZ, coating delamination was observed at the topcoat–bond coat interface, and cone cracking resulted in the SiC substrate. Conversely, the brittle Si_3N_4 which readily fractured was found to induce coating delamination at

the bond coat–substrate interface and flexural back-surface cracks in the SiC substrate. In both cases, the coated specimens showed lower level of cracking relative to the bare specimens.

Previous studies of FOD impact on EBCs [110,180], including the work in Chapter 3, are still limited in scope since they do not take into consideration the effects of specimen geometry. This concept is important to consider since critical hot-section components (e.g. inlet nozzles and turbine blades) contain round features with relatively low curvatures. Figure 4.1a depicts a simple three-dimensional model of a turbine blade with mock flow paths of combustion gas. Entrained FOD in this gas stream would directly encounter the narrow leading and trailing edges of the component (see Figure 4.1b). Head-on impact to these regions can yield drastic changes in damage modes due to lack of surrounding material (i.e. confinement). This boundary condition has been considered in a previous study by Presby *et al.* [101]. In the latter, FOD impact damage on uncoated SiC_f/SiC CMCs was found to be localized to the surface for curved specimens and distributed across the thickness (i.e. frontal and back-surface damage) for flat specimens. The corresponding material loss at sharp edges will inevitably yield stress concentration points for catastrophic and cascading failures of these brittle materials. It is, therefore, crucial to study and understand the effect of specimen geometry on FOD impact damage propagation in EBC coated ceramics and CMCs.

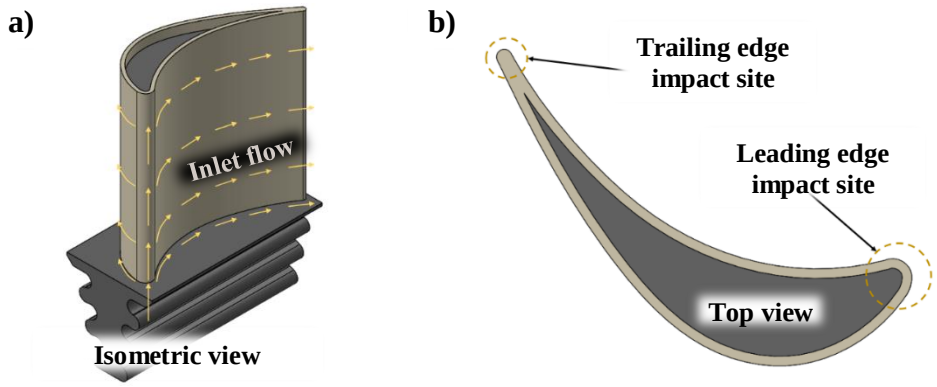

Figure 4.1. Turbine blade model (a) and blade cross-section (b) showing the leading and trailing edges.

The current study expands on previous works in Chapters 2 and 3 by considering the effect of specimen geometry on FOD impact response of uncoated and coated SiC ceramics. This is accomplished by the use of narrow specimens which simulate the low curvature features. These

samples are subject to impact by three types of FOD simulants and the propagation of damage is captured *in situ* using pulsed synchrotron X-ray radiography method. Detailed accounts of the damage histories, as well as elucidations of the underlying mechanisms, are extracted from the radiographic observations. Beyond this interpretation, the viability of the *in situ* characterization method is also evaluated for determining the level of protection (damage resistance) offered by the EBC to the narrow brittle substrate.

4.2 Experimental

4.2.1 Materials

The coated ceramic used for the narrow FOD impact experiments is the same as the one reported in Chapter 3.2.1. In brief, pressureless sintered alpha phase silicon carbide (SiC) (Hexoloy SA, Saint-Gobain Advanced Ceramics, Niagara, NY, USA) was used as the substrate. Before coating, the surface of the ceramic was grit blasted by #24 mesh SiC media to a roughness (Ra) of ~ 2.5±0.5 µm. Commercially available silicon powder (Metco 4810, Oerlikon Metco, Westbury, NY, USA) and mullite powder (#1020, Saint-Gobain Ceramic Materials, Latrobe, PA, USA) were used as feedstock materials for the bond coat and topcoat respectively. These powders were converted into coatings via air plasma spray (APS) process (see Table 3.1 in Chapter 3 for processing parameters). Optical measurements of the resulting EBC rendered a bond coat thickness of 58.2±2.3 µm and topcoat thickness of 165.8±2.2 µm. For the current process, a topcoat consisting of primary mullite phase and secondary alumina phase with a crystallinity of 68.28 % was determined via X-ray diffraction analysis (see Figure 3.6, Chapter 3).

Spheres of silicon nitride (Si_3N_4) (MSE Supplies, Tucson, AZ, USA), partially stabilized zirconia (PSZ) (5 wt% Y_2O_3-ZrO_2, Coors Tek, Golden, CO, USA), and chrome steel (52100, Fastenal, Winona, MN, USA) with nominal diameters of 1.5 mm were used as FOD simulants. Si_3N_4, PSZ, and steel materials were chosen to represent debris with brittle, quasi-plastic, and plastic deformation behaviors. These differences in deformation greatly influence the level of kinetic energy imparted to the target. The microstructure of these projectile materials also differs greatly as shown in Figure 2.1, Chapter 2. A selected set of mechanical and physical properties for both the spherical impactors and target are presented in Table 4.1 for reference. In this table, both nano and microhardness values are reported to illustrate the significant difference between the two.

This difference is associated with a larger probe area for microhardness measurements which captures the influence of microstructural defects such as pores and microcracks.

Table 4.1. Properties of the target and projectile materials at standard temperature and pressure.

Material		**Density, ρ (g/cm^3)**	**Elastic Modulus, E (GPa)**	**Poisson's ratio, ν**	**Hardness, H (GPa)**	**Fracture Toughness, K_{IC} (MPa$\sqrt{\text{m}}$)**	**Wave Speed, C_L (km/s)[4]**
Target	APS Mullite	3.00[1]	112.20± 8.40[2]	0.28[1]	8.80± 1.00[2] 5.42± 0.70[3]	-	6.10
	APS Silicon	2.20[1]	142.80± 7.60[2]	0.22[1]	10.80± 1.40[2] 5.97± 0.34[3]	-	8.10
	Hexoloy SiC	3.10[5]	407.60± 26.30[2]	0.14[5]	34.40± 3.70[2]	2.5± 0.10[6]	11.50
Projectiles	Si_3N_4[7]	3.20	320	0.26	15.50	6.00	10.00
	PSZ (5.2 wt % Y_2O_3)[8]	6.10	200	0.30	12.00	9.00	5.70
	Chrome Steel (AISI 52100)[9,10]	7.78	200	0.30	8.20	18.90	5.10

1. Based on reports by Richards *et al.* [71]
2. From nanoindentation experiments using a Berkovich diamond tip indenter at a maximum load of 250 mN. See Appendix B for information on experiment and data.
3. Obtained from Vickers hardness measurements using a load of 1.92 N and dwell of 15 s ($HV_{0.2}$). Experiments and data are provided in Appendix D.
4. Calculated directly assuming a 1-D (or longitudinal) wave and no lateral deformation, $C_L = \sqrt{E/\rho}$.
5. Density and Poisson's ratio – from Saint-Gobain Ceramics Hexoloy® SA technical datasheet.
6. Fracture Toughness – from Rahman *et al.* [136]
7. All properties obtained from supplier data sheet (Coors Tek, Inc).
8. All properties obtained from supplier data sheet (MSE Supplies LLC).
9. Density, Modulus, Poisson's ratio, and Vickers Hardness ($HV_{0.5}$) of 52100 Steel referenced from Choi [80].
10. Fracture toughness of 52100 Steel referenced from Nakazawa and Krauss [137].

Impact specimens from uncoated and coated substrates were extracted using a slow speed saw equipped with a diamond tipped wafering blade. It is important to note that the coated substrates were sectioned with the coating side facing the blade in order to place the surface under compression and minimize damage. As shown in the schematics of Figure 4.2, the coated and uncoated specimens retained as-processed thickness and similar dimensions in their width and length. The width of these specimens is equivalent (1:1) to the spherical projectile diameter and half in magnitude to specimens used in previous studies.

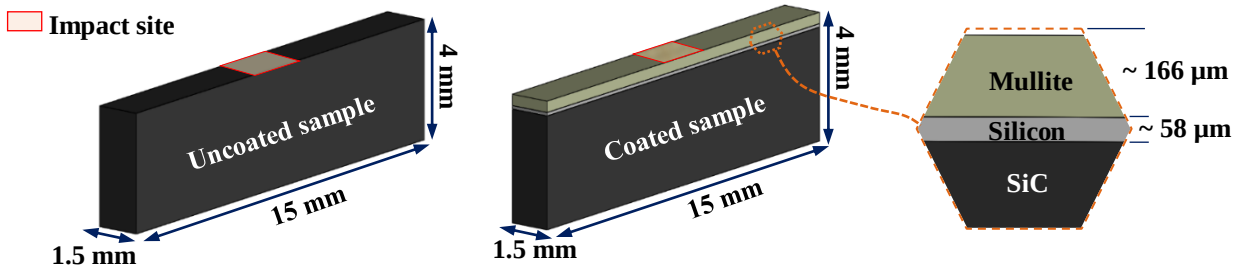

Figure 4.2. Three-dimensional schematics of the narrow uncoated (left) and coated (center) specimens with their respective dimensions.

One of the coated specimens was also mounted in epoxy with the long edge (cross-section) exposed and polished to a 0.25 µm finish for microstructural evaluation. The latter characterization was performed using a scanning electron microscope (SEM) (Quanta 650, FEI Technologies Inc., Hillsboro, OR, USA) in secondary electron (SE) and back-scattered electron (BSE) modes. A comprehensive evaluation of the microstructure and chemistry was provided in Chapter 3.3.1. Here, only a brief review is provided. Figures 4.3a and 4.3b depict typical SE and BSE micrographs for the coating cross-section. The SE and BSE micrographs highlight splat boundaries and porosities in the mullite topcoat. These same features for the silicon bond coat are more clearly observed in the BSE micrograph. Moreover, differences in chemistry between layers are highlighted in the BSE micrograph with the high atomic number silicon bond coat yielding greater intensity (brighter) region. The interface between the bond coat and substrate is found to retain multiple porous regions (Figure 4.3b). By comparison, a low level of porosity and uniform transition is associated with the topcoat–bond coat interface.

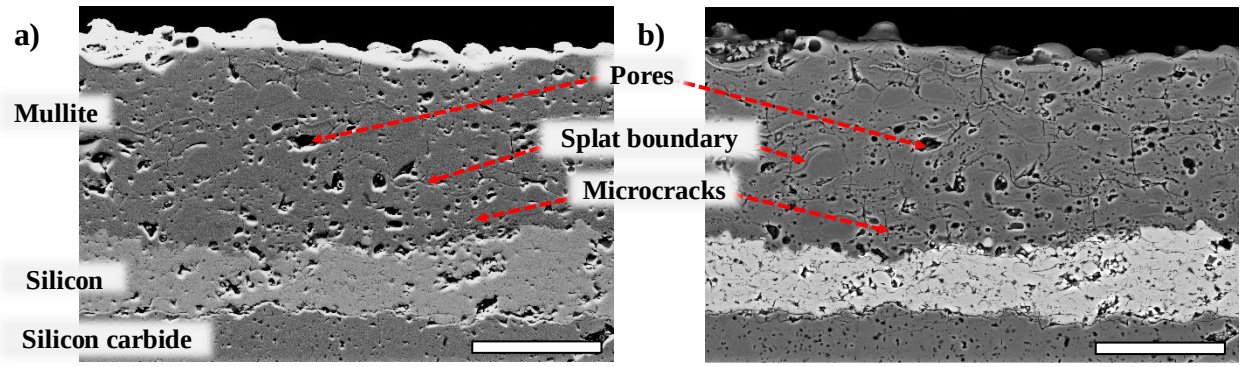

Figure 4.3. Scanning electron micrographs of the coated specimen cross-section showing the microstructure of the mullite topcoat and Si bond coat layers along with the SiC substrate. Secondary electron (SE) (a) and back-scattered electron (BSE) (b) modes are shown. Scale bars – 100 µm.

4.2.2 Real-time FOD impact characterization method

Detailed descriptions and schematics of the real-time FOD impact method are found in Chapters 2.2.2 and 3.2.3. Hence, only a succinct summary is provided here. The characterization method combines a light-gas gun with pulsed synchrotron X-ray radiography at the Advanced Photon Source (Argonne National Laboratory, 32-ID-B, Lemont, IL, USA) to yield two-dimensional renderings of the volumetric damage in opaque materials under dynamic loading conditions. In a typical experiment, helium gas is used to propel a spherical FOD impactor at normal incidence angle towards a specimen that is fully supported by a rigid steel fixture. Two lasers/detectors separated by ~ 11 mm and positioned 10 mm in front of the specimen sense the passage of the impactor and output trigger signals to delay generators (DGs). These DGs synchronize the emission of beamline X-rays and capture of high speed images during the FOD impact event. A single crystal $Lu_3Al_5O_{12}$:Ce scintillator (decay time: 70 ns, Crytur Ltd, Turnov, CZ) converts the X-rays that are transmitted through the specimen into visible light and an optics assembly consisting of a 45˚ mirror, 5x objective, and 1x tube lens projects this light into a high speed camera (Hyper Vision HPV-X2, Shimadzu Co., Kyoto, JP). In the current work, the X-ray source was operated in standard mode (24 equidistant singlets @ 6.5 MHz) with an undulator gap of 12 mm. The resulting polychromatic beam retained a fundamental harmonic energy of ~ 24 keV[1] and intensity of ~ $8x10^{13}$ Ph/(s·mm^2·0.1%BW). Propagation-based phase contrast imaging

[1] The X-ray beam energy is controlled by adjusting the gap of the X-ray collimating / insertion device or undulator magnet. In the current work an undulator gap of 12 mm was used and renders an energy of ~ 24 keV.

(PCI) configuration was used to capture internal damage features with a spatial resolution of ~ 6.4 μm/pixel (1.6 x 2.5 mm^2 image window). A camera frame rate of 2 MHz with 200 ns exposure and 256 total frames was used for most experiments. At least one experiment per category (coated-steel sphere, uncoated-PSZ sphere, etc.) was also imaged at a 5 MHz frame rate (110 ns exposure, 256 total frames) to obtain data at a higher temporal resolution.

4.3 Results

4.3.1 High speed X-ray radiographs

A total of twenty-one specimens, nine uncoated and twelve coated, were used for FOD impact experiments. These specimens were divided evenly among the three spherical impactors. The low specimen count for each impact condition was due to limitations in beamtime resources. Fiji (ImageJ), an open source image analysis software, was used to process the high speed X-ray radiographs. The observations are presented in three segments, each addressing the uncoated and coated targets for a given spherical impactor type (i.e. Si_3N_4, PSZ, steel). It is noted that all impact specimens fractured catastrophically at multiple locations and the fragments could not be retrieved for postmortem analysis.

4.3.1.1 FOD impact by Si_3N_4 projectile

A consistent damage evolution was observed for the three uncoated monolithic SiC specimens subject to FOD impact by Si_3N_4 sphere. Radiographs depicting the sequential damage in one of the specimens impacted at a velocity of 384.3 m/s are presented in Figure 4.4. Initially (before contact), both the sphere and substrate are elastically loaded[2] at the contact interface. Subsequent displacement beyond the elastic limit results in diametral cracks in the sphere, as well as Hertzian cone cracks, median cracks, and back-surface cracks in the substrate (Figure 4.4, t = 0.16 μs). Further displacement by the sphere results in opening of the diametral crack vents as well as initiation and growth of several vertical cracks (perpendicular to the impact direction) in the substrate (Figure 4.4, t = 1.16 μs). Opening of the diametral cracks leads to fragmentation and

[2] Figure E.2, Appendix E, provides radiographs obtained at 5MHz frame rate and at t = 0.25 μs the elastic deformation of the Si_3N_4 sphere is shown to occur prior to cracking.

radial flow of the sphere. The latter releases the compressive impact load on the substrate and causes additional vertical crack vents to grow and intersect the already formed cone and median cracks. (Figure 4.4, t = 2.16 μs). The sphere fragments are also observed to surpass the edge of the narrow specimen and continue to displace forward in the initial impact direction (Figure 4.4, t = 8.66 μs). Finally, the crack networks open and completely fracture the specimen. By comparison, the prior investigation (see Chapter 2.3.2) using specimens with wider (3 mm) geometries showed similar damage processes with limited levels of cone and vertical cracking. Notably, these wide specimens did not form back-surface cracks during impact unlike the narrow specimens used in this study.

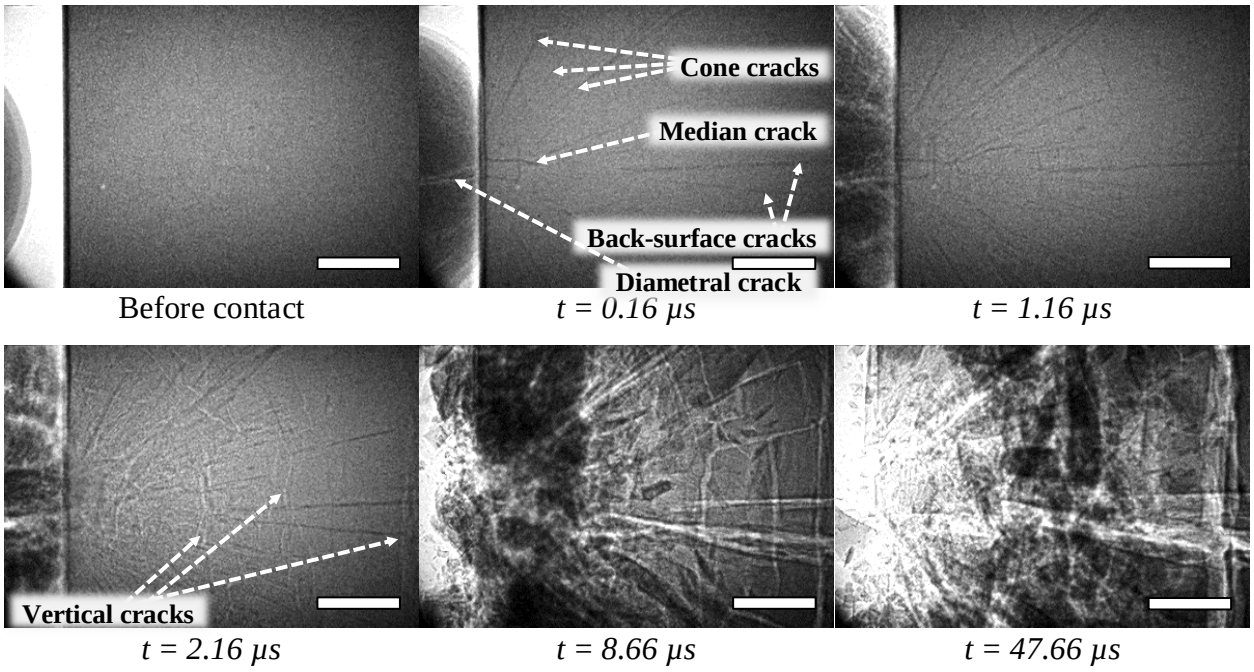

Figure 4.4. Pulsed X-ray radiographs of FOD impact in a narrow uncoated SiC substrate by a 1.5 mm diameter Si_3N_4 sphere at a velocity of 384.3 m/s. Images were recorded at 2M frames per second with an exposure time of 200 ns. Scale bars in each frame – 500 μm.

The observed damage processes within the coating and Si_3N_4 sphere are similar for all experiments. This was not the case for the underlying SiC substrate where slight deviations in the evolution of cracks persisted[3]. One of the coated specimens which was deemed to retain most of the prevalent damage features was thus selected to outline the general damage process. Figure 4.5 provides the corresponding radiographs obtained during impact at a velocity of 376.7 m/s. The first frame (before contact) shows an outline of the sphere and specimen prior to contact. In this frame, a clearly defined interface is observed between the EBC and SiC substrate. After contact, the initial deformation and then penetration of the topcoat by the intact sphere (Figure 4.5, t = 0.26 μs) is observed. Penetration is accommodated by pushout of the coating material around the sphere perimeter. Once the sphere reaches the bond coat–substrate interface, the displaced coating volume becomes too great to accommodate via radial pushout and material removal occurs via ejection (Figure 4.5, t = 0.76 μs). With continued displacement, the sphere deforms elastically and then develops diametral cracks upon reaching its elastic limit (Figure 4.5, t = 1.26 μs). Simultaneously, delamination of the coating and formation of cone, median, and back-surface cracks in the substrate are observed. Delamination at the bond coat–substrate interface is identified in the radiographs as an increase in the intensity of the transmitted X-ray beam (i.e. increased brightness). This delamination is associated with the weak interface (crack) at the bond coat–substrate interface (see Figure 4.3). Further deformation of the sphere is observed to result in opening of the diametral crack vents and the formation of fragments. The latter deformation also causes the cracks in the substrate to extend (Figure 4.5, t = 2.26 μs). As the sphere fragments flow radially, removal of remnant coating material occurs via erosion. Additionally, cracks in the substrate bifurcate and new vertical cracks emerge and intersect the prior cone and median cracks (Figure 4.3, t = 5.76 μs). In the final stages of failure, rebound of the sphere fragments occurs, while crack networks open and fracture the substrate into multiple segments and portions of the coating are lifted off.

[3] As shown in Figure E.3 (t = 1.13 μs) Appendix E, a vertical crack which precedes cone and median cracking emerges in one of the specimens. This is likely due to the initiation of a preexisting defect of critical size during elastic loading of the substrate by the sphere. Additionally, back-surface cracks are not observed in one of the four impact experiments (Figure and E.4).

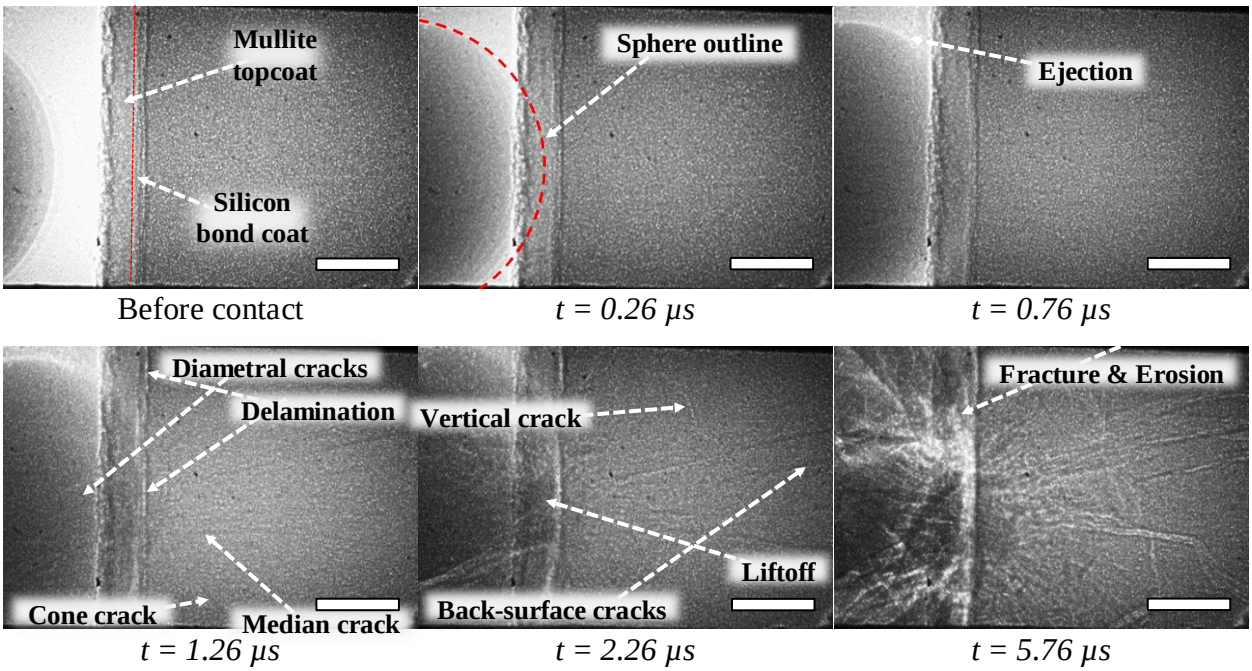

Figure 4.5. Pulsed X-ray radiographs of FOD impact in a narrow coated SiC substrate by a 1.5 mm diameter Si_3N_4 sphere at a velocity of 376.7 m/s. Images were recorded at 2M frames per second with an exposure time of 200 ns. Scale bars in each frame – 500 µm.

The narrow specimens exhibited similar FOD impact behavior with and without coatings. However, significant differences were observed when comparing narrow and wide coated specimens. For the narrow uncoated and coated specimens, primary cone and median cracks are initially formed in the SiC substrate followed by vertical cracks. Coalescence of these crack vents is also found to induce failure via complete fracture. The main differences between the coated and uncoated specimens are reduced level (number) of cracking in the coated specimen (i.e. lack of multiple cone cracks), as well as reduced fragmentation and subsequent rebound of the Si_3N_4 sphere impacting the coated specimen. In addition to higher intensity of cracking, the uncoated specimens also showed much rapid damage propagation. For the previously investigated wide (3 mm) coated specimens (see Chapter 3.3.3.2), penetration, ejection, and delamination of the coating were observed. The latter damage processes are identical to those observed in the current work for the narrow specimens. However, coating erosion was not observed for the wide specimens after delamination. The Si_3N_4 spheres also fragmented to the same degree, but the extent of fragment rebound and coating liftoff was greater for impact against the wide specimens. Lastly, the wide

coated specimens were observed to only form back-surface cracks with no indication of characteristic Hertzian cone and median cracks.

4.3.1.2 FOD impact by PSZ projectile

Similar to the FOD impact by Si_3N_4 spheres, impact by PSZ spheres was found to result in a consistent damage process across all uncoated SiC specimens. Consequently, radiographs for only one of the experiments conducted at an impact velocity of 336.4 m/s are presented in Figure 4.6 to describe the general evolution of damage. Initial damage, akin to observation for Si_3N_4 sphere, consists of elastic deformation of the PSZ sphere and SiC specimen after contact (Figure 4.6, t = 0.07 μs). Unlike the Si_3N_4 sphere, the tough PSZ sphere undergoes quasi-plastic deformation with subsequent displacements instead of brittle fracture. This deformation behavior is sustained via radial flow of material and it induces additional cone cracks and median cracks in the specimen (Figure 4.6, t = 0.57 μs). Continued deformation of the sphere leads to propagation of already formed cracks and formation of vertical cracks in the specimen (Figure 4.6, t = 1.07 μs). The latter is similar to the observations made during radial flow of the Si_3N_4 sphere fragments. After significant quasi-plastic deformation (Figure 4.6, 1.07 μs < t ≤ 0.16 μs), the sphere crumbles, and the resulting debris fly off to the edges of the specimen. Simultaneously, more vertical cracks and back-surface cracks emerge in the specimen, and the resulting crack networks open to induce complete fracture. By contrast, slightly different damage features and processes were observed in Chapter 2.3.1 for wide specimens (3 mm). Specifically, cone cracks were limited to two (instead of three) and median cracks were promoted during crushing of the PSZ sphere (instead of quasi-plastic loading). Moreover, quasi-plastic deformation of the sphere did not induce vertical cracks in the wide specimens and back-surface cracking was observed to occur in limited cases.

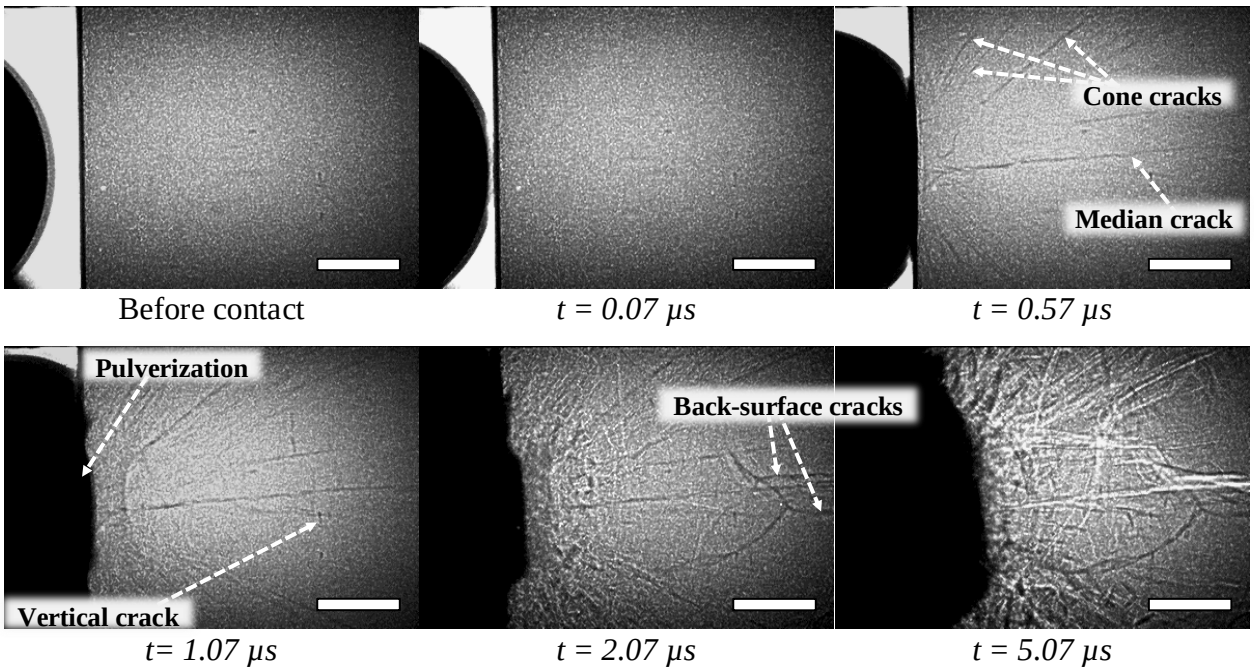

Figure 4.6. Pulsed X-ray radiographs of FOD impact in a narrow uncoated SiC substrate by a 1.5 mm diameter PSZ sphere at a velocity of 336.4 m/s. Images were recorded at 2M frames per second with an exposure time of 200 ns. Scale bars in each frame – 500 µm

The FOD impact experiments by PSZ spheres on coated specimens showed consistent damage processes. Figure 4.7 provides radiographs for one of these experiments in which the specimen was impacted at a velocity of 347.4 m/s. Initially, the PSZ sphere contacts and deforms the mullite topcoat (Figure 4.7, t = 0.5 µs). The latter is followed by continued displacement of the sphere which results in penetration of the topcoat and then the silicon bond coat (Figure 4.7, t = 1 µs). During penetration, the coating material is pushed radially and towards the surface where it accumulates around the perimeter of the sphere. Once the sphere comes into contact with the SiC substrate, the accumulated material is removed as crushed ejecta. Subsequent elastic loading of the substrate by the sphere primarily yields a single cone crack. The PSZ sphere displaces further via quasi-plastic deformation and produces more coating ejecta in addition to back-surface and vertical cracking in the substrate (Figure 4.7, t = 2.5 µs). In two of the four experiments[4], a median crack also formed during the latter process. Crack growth in the substrate and complete removal of the coating occurs, as the sphere deforms to its quasi-plastic limit and reaches the lateral edges of the specimen. Afterwards, the sphere crumbles, and the ensuing fragments flow forward to the sides

[4] Refer to Figure 4.7 provided here and Figure E.8 in Appendix E.

of the specimen. This translation of material unloads the compressive impact pressure on the specimen and opens up prior crack networks in the SiC substrate (Figure 4.7, t = 4.5 µs). Crack opening then induces complete fracture as a final stage of damage (Figure 4.7, t = 10.5 µs).

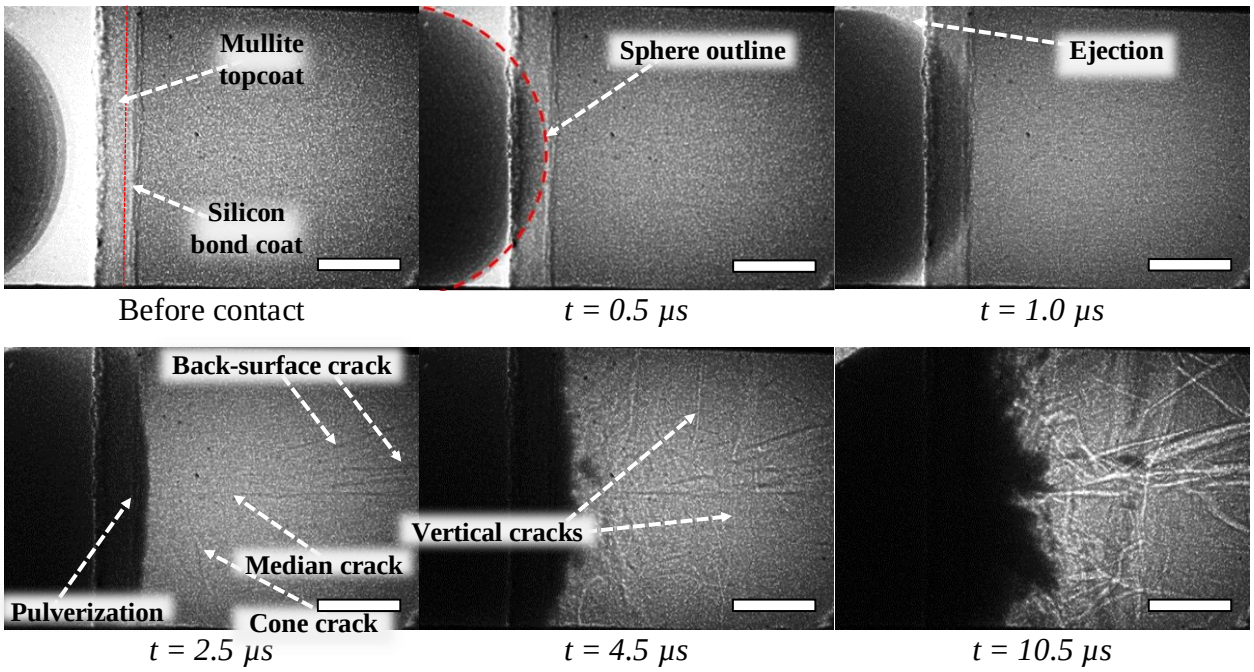

Figure 4.7. Pulsed X-ray radiographs of FOD impact in a narrow coated SiC substrate by a 1.5 mm diameter PSZ sphere at a velocity of 347.4 m/s. Images were recorded at 2M frames per second with an exposure time of 200 ns. Scale bars in each frame – 500 µm.

In comparison to the uncoated specimen (Figure 4.6), FOD impact by a PSZ sphere of the coated specimen yields similar damage processes in terms of crack evolution. The main difference between the two is the reduced level of cone and vertical cracking in the coated specimen. In addition to higher crack density, the propagation of damage was also higher for the uncoated specimen. Significant differences also emerge when comparing the FOD impact response of the coated specimen by impactor type (i.e. PSZ vs Si_3N_4). Starting with the coating, only delamination and coating liftoff are observed at the impact region for impact by Si_3N_4 projectile. This occurs despite the weak bond coat–substrate interface and it is due to elongated contact time for the PSZ sphere. Additionally, ejecta formation, which is the primary mode of coating material removal for impact by PSZ is limited for Si_3N_4 and erosion by radially flowing sphere fragments also occurs. For damage in the underlying SiC substrate, a median crack is found to accompany cone cracks in

the initial stages for impact by Si_3N_4, while it occurs in a few cases for the PSZ sphere. The level of cracking sustained in the coated SiC substrate for both impact conditions is significantly lower than the uncoated counterparts. Differences are also noted between the narrow coated specimens examined in this work and wide (3 mm) coated specimens investigated in Chapter 3.3.3.1 under similar conditions. During penetration by PSZ, the coating for the wide specimens was observed to expand outward (bulge) due to radial displacement and accumulation of material around the perimeter of the sphere. Despite radial displacement of the coating, significant accumulation around the impactor is not observed for the narrow specimens. Subsequent coating removal for the wide specimens also involved delamination at the topcoat–bond coat interface and erosion during rebound of the sphere fragments. Both of the latter damage modes are absent for the narrow coated specimens. Finally, the SiC substrate for the wide specimens was also shown to generally lack vertical and median cracks, and only produce back-surface cracks after cone crack formation.

4.3.1.3 FOD impact by steel projectile

All monolithic SiC samples showed consistent damage processes for impact by steel spheres. Radiographs for one of the samples impacted at a velocity of 315.5 m/s are presented in Figure 4.8. The damage evolution for impact by steel spheres is found to be nearly identical to that observed for PSZ spheres (see Figure 4.6). In the early stages of contact and deformation of the elastic–plastic sphere, cone and median cracks develop in the SiC specimen (Figure 4.8, t = 0.1 μs and t = 0.6 μs). The latter is followed by back-surface and vertical cracks with further deformation of the sphere (Figure 4.8, t = 1.6 μs). Finally, the crack networks open up and induce complete fracture as the sphere unloads from the contact surface (Figure 4.8, t = 2.6 μs and t = 7.1 μs). Some of the notable differences from impact by PSZ spheres are the initial lag in cracking with contact/elastic deformation of the steel sphere (Figure 4.8, t = 0.1 μs) and the rebound of an intact steel sphere instead of crumbling/fragmentation. Moreover, the rebounding spheres only retain 1.7±0.4 % of the input impact energy with the remainder being consumed through fracture of the specimen and deformation of the sphere. A previous study using wide (3 mm) specimens (see Chapter 2.3.3.) showed similar damage history and impact energy dissipation (2.3 %). The main difference was lack of vertical cracking in the wide specimen during deformation of the sphere on the contact surface.

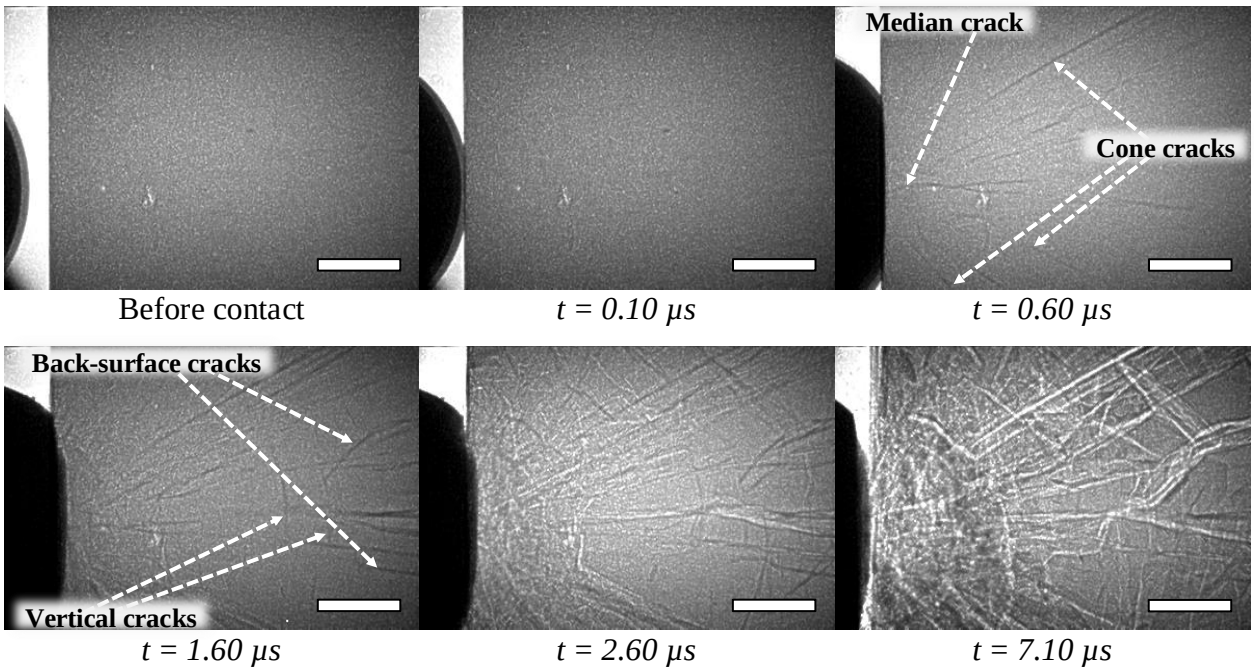

Figure 4.8. Pulsed X-ray radiographs of FOD impact in a narrow uncoated SiC substrate by a 1.5 mm diameter steel sphere at a velocity of 315.5 m/s. Images were recorded at 2M frames per second with an exposure time of 200 ns. Scale bars in each frame – 500 µm.

The four coated specimens subject to FOD impact by steel projectiles showed similar damage processes. Figure 4.9 provides representative radiographs for one of the specimens impacted at a velocity of 311.3 m/s. Coating deformation and then penetration occurs after contact (Figure 4.9, t = 0.46 µs). The latter is followed by coating ejection as the sphere reaches the substrate (Figure 4.9, t = 0.96 µs). Subsequent elastic deformation of the sphere does not induce damage to the substrate. However, follow-on plastic deformation is found to produce cone and back-surface cracks (in random order)[5] with continued ejection of coating material (Figure 4.9, t = 1.96 µs). Further deformation by the sphere leads to the formation of vertical cracks in the substrate and complete removal of the coating in the region of impact (Figure 4.9, t = 2.46 µs) via erosion. After extensive plastic deformation, the sphere begins to rebound from the surface and the crack network in the specimen opens up. The rebound energy ranges between 0.05-1.09 % of the impact energy. Complete fracture of the substrate occurs after crack opening, along with delamination (liftoff) of the coating away from the impact site (Figure 4.9, t = 8.96 µs).

[5] Cone and back-surface cracks occurred in random order for a given experiment.

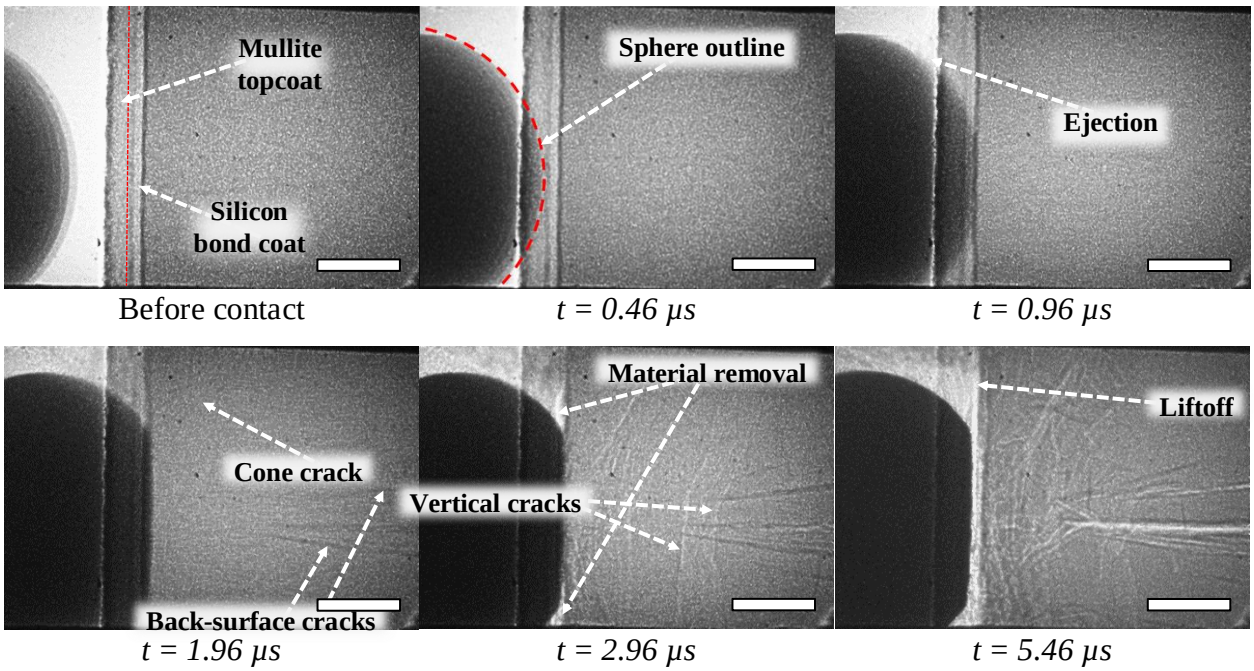

Figure 4.9. Pulsed X-ray radiographs of FOD impact in a narrow coated SiC substrate by a 1.5 mm diameter steel sphere at a velocity of 311.3 m/s. Images were recorded at 2M frames per second with an exposure time of 200 ns. Scale bars in each frame – 500 μm.

Initial coating damage for impact by steel projectiles is similar to that produced by Si_3N_4 and PSZ projectiles. All three cases show coating deformation, followed by penetration and then ejection. The next stage in coating damage is the same as that observed for impact by PSZ. Specifically, deformation of the projectile on the substrate leads to significant ejection of coating material in the impact region instead of delamination. Still, the intact steel sphere does not produce erosion to remove the remnant coating material, as in PSZ and Si_3N_4. Rather, the unimpacted coating is removed via liftoff during fracture of the substrate and rebound of the sphere. Again, the latter being facilitated by the weak bond coat–substrate interface. Within the substrate, the damage process is significantly different for impact by the three projectiles. For slight deformation of the steel projectile, back-surface cracks are formed in addition to cone cracks. This is not the case for PSZ projectile where significant amount of quasi-plastic deformation takes place before back-surface cracking in the substrate. For Si_3N_4 projectiles, a varied response by the substrate is observed where back-surface cracks, if formed, can emerge in either early or late stages of damage. Moreover, median cracks that tend to appear with cone cracks for Si_3N_4 and PSZ projectile impacts are generally not observed for steel projectiles. Relative to the coated specimens, the narrow

uncoated specimen (Figure 4.8) shows delayed back-surface cracks and early median cracks. Akin to observations for PSZ and Si_3N_4 projectile impacts, the level of cone and vertical cracking is also greater for the uncoated specimens. Besides a lower intensity of cracking, damage evolution in the coated specimen was also less rapid than the uncoated counterpart. Previous studies on wide (3 mm) coated specimens are not available, and the damage process cannot be readily compared.

4.3.2 Assessment of quantifiable damage features

As demonstrated in the above sections, the *in situ* experiments provide critical information on the evolution of FOD impact damage in both the uncoated and coated ceramic samples. In addition to this qualitative information, some quantitative data can also be extracted from direct measurements on the X-ray radiographs. In Chapters 2 and 3, only the elastic deformation of the sphere, cone crack half-apex angles, and contact times were explored. Here, the rate of coating penetration and cone crack half-apex angles are selectively considered for the narrow specimens.

4.3.2.1 Coating penetration

Progressive coating penetration depths were measured for all FOD impact experiments using series of X-ray radiographs. In most cases, the initial contact between the projectile and topcoat occurred between frames. Hence, the time of contact ($t = 0$ μs) was estimated by measuring the initial separation distance between the two bodies and then dividing by the measured impact velocity (V_{im}). The resulting plots of coating penetration depth, d_p, vs time, t, categorized by sphere type are provided in Figure 4.10a. A line of best fit constructed via simple linear regression analysis of the scatter data for each category is also provided with corresponding coefficients of determination (or R^2 values) and slopes (or m values). All three plots retain an $R^2 > 0.99$ indicating good fit of the linear regression to the data. The slopes, $m_{i\ (i = 1\text{-}3)}$, which indicate rate of penetration suggest that Si_3N_4 and PSZ projectiles penetrated the coating with less resistance than steel projectiles. This behavior may be associated with the high hardness of the two materials (see Table 4.1). A slightly greater penetration rate is found for Si_3N_4 projectiles relative to PSZ projectiles and this is possibly reflective of the slight difference in both hardness and impact velocity between the two. Given the variations in impact velocities for the three impactors, the relative coating

penetration depth (d_p/V_{im}) and the relative change in velocity ($\Delta V/V_{im} = |V(t_i) - V_{im}|/V_{im}$)[6] are also assessed as a function of time. Figure 4.10b shows that the relative penetration rate is highest for impact by PSZ sphere and lowest for impact by steel sphere. By contrast, Figure 4.10c shows an inverse response where the relative change in velocity is greatest for steel sphere impacts and lowest for PSZ sphere impacts. To understand this behavior, the impact energy must also be considered [in addition to hardness] to account for both mass and velocity of projectiles. The steel projectiles retain the highest impact energy (E_{im} = 0.67±0.04 J) and the lowest hardness (8.2 GPa), while the PSZ projectiles retain a slightly lower impact energy (E_{im} = 0.58±0.06 J) and high hardness (12 GPa). Thus, the PSZ projectiles are more effective in penetrating the coating (high d_p/V_{im}) with lower resistance (low $\Delta V/V_{im}$). The Si_3N_4 projectiles experience lower d_p/V_{im} and higher $\Delta V/V_{im}$, relative to PSZ projectiles, due to their lower impact energies (E_{im} = 0.4±0.01 J). This phenomenon is clearly shown in Figure 4.10d where the plateau (or maximum) values for $\Delta V/V_{im}$ and slopes of d_p/V_{im} curves are plotted against the combined hardness and impact energy of the projectiles ($H_p \cdot E_{im}$). The plot indicates that the relative rate of coating penetration increases with increasing $H_p \cdot E_{im}$, while the maximum relative change in velocity decreases. Furthermore, both $(\Delta V/V_{im})_{max}$ and $d/dt(d_p/V_{im})$ retain the following linear relationships,

$$\left(\frac{\Delta V}{V_{im}}\right)_{max} \approx \left(-H_p \cdot E_{im}\right) \tag{4.1}$$

$$\frac{d}{dt}\left(\frac{d_p}{V_{im}}\right) \approx \left(H_p \cdot E_{im}\right) \tag{4.2}$$

where H_p is the hardness of the projectile and the derivative is taken with respect to time.

Similar trends are found for the wide specimens (see Figure E.16, Appendix E), although a complete history of both the penetration depth and relative change in velocity could not be rendered due to lack of experiments at 5 MHz frame rates. These assessments are important in understanding the effectiveness of the coating in shielding the brittle substrate against FOD impact damage and the underlying data are only obtainable through *in situ* visualization approaches.

[6] $V(t_i)$ is the transient velocity determined for any specified time t_i after impact.

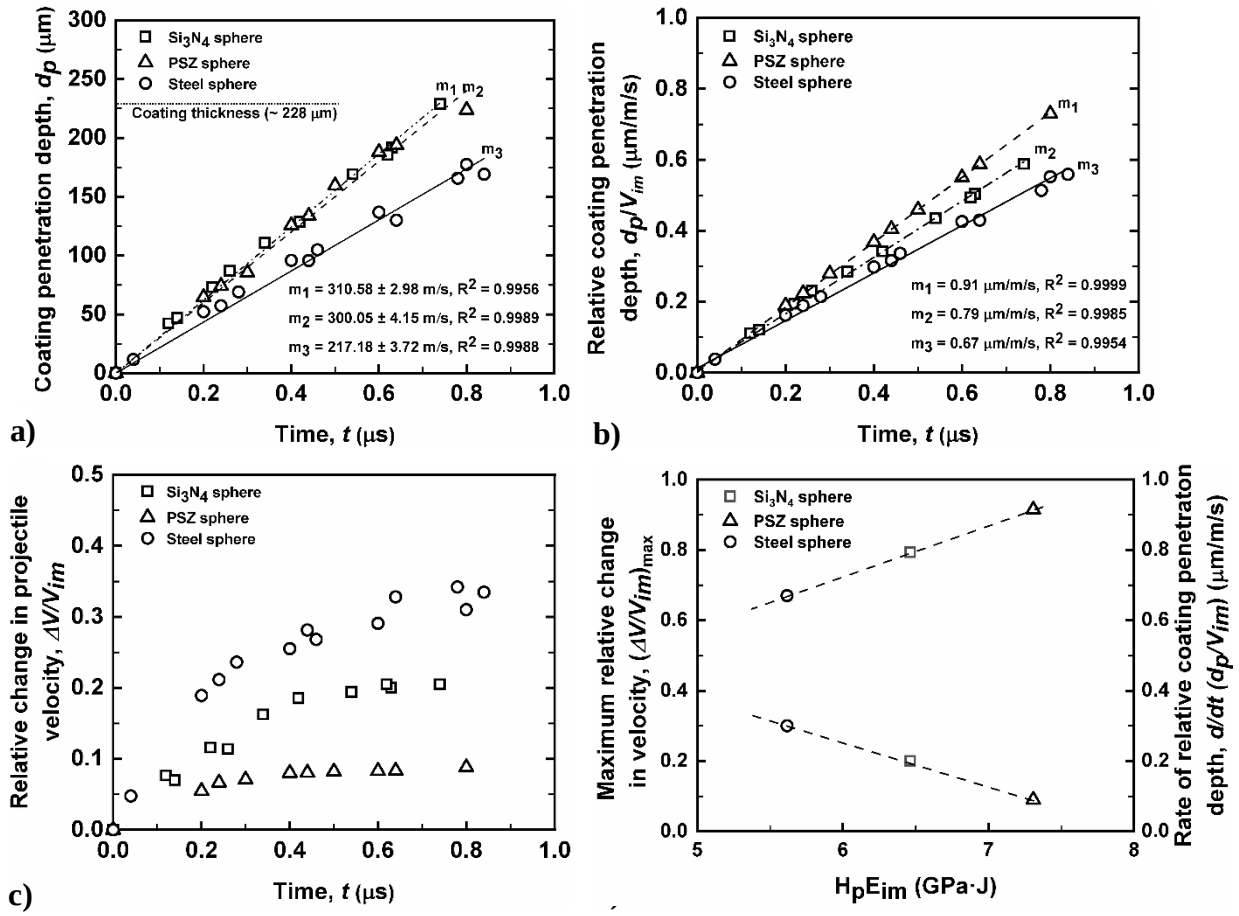

Figure 4.10. X-ray radiography based determinations of absolute coating penetration depth (a), relative coating penetration depth (by impact velocity) (b), and relative change in impactor velocity (c) as a function of time. The plot in (d) renders the maximum relative change in projectile velocity and rate of relative coating penetration depth as a function of combined projectile hardness and impact energy.

4.3.2.2 Hertzian cone cracks

Cone crack half-apex angles were also directly measured from the X-ray radiographs. Figure 4.11a provides a scatter plot of the measured cone crack half-apex angles as a function of impact velocity for both the coated and uncoated samples examined in this study. As noted above, impact of the uncoated samples typically results in three distinct cone cracks. For identification purposes, they are termed in Figure 4.11a as innermost ($\gamma \leq 40^{\circ}$), intermediate ($40^{\circ} < \gamma \leq 50^{\circ}$) and outermost ($\gamma > 50^{\circ}$) cone cracks. The resulting plot shows that the magnitude of the half-apex angles for the three crack types remains constant across different FOD simulant materials (i.e. Si_3N_4, PSZ, and steel projectiles) and impact velocities ranging between 300 to 400 m/s. By

comparison, only the intermediate cone crack emerges for impact of the coated samples under the same conditions. This behavior is likely due to shielding of the substrate by the coating and it will be explored further in the follow-on discussion section. Moreover, the magnitude of the half-apex intermediate cone crack angle between the coated and uncoated specimens are similar across the three impactors and examined impact velocity ranges.

The cone crack half-apex angles determined in this study were also compared with those reported previously for wide specimens as well as those established by other researchers. For clarity, the data is sorted by FOD impactor material type and identified by the ratio of sphere diameter (D_s) to specimen width (W for uncoated and W* for coated). Figure 4.11b shows the resulting plot for impact by Si_3N_4 projectiles. Here, cone cracks that developed in the wide specimens are found to correspond to the intermediate cone cracks in the narrow specimens. Additionally, the values of the intermediate cone crack half-apex angles remain very similar irrespective of changes in impact velocity or specimen width [91]. The half-apex angle data, for cone cracks evolved from FOD impact using PSZ projectiles, are plotted in Figure 4.11c. At least two cone cracks (intermediate and outermost for lower velocities, innermost and outermost for higher velocities) are formed in the wide specimens. The half-apex angles also tend to increase with decreasing velocity and this behavior is highlighted more clearly in the included data from Akimune *et al.* [92]. Further, the half-apex angles for the uncoated wide specimens are similar in magnitude to those for the uncoated narrow specimens. For the coated specimens, only intermediate cone cracks form irrespective of the specimen width and the half-apex angles are similar to the corresponding uncoated specimens. Lastly, the plots of half-apex angles for steel projectile impacts are provided in Figure 4.11d. Akin to the response for impact by PSZ projectiles, more than one cone crack forms in the wide specimens, and the resulting half-apex angles are observed to increase with decreasing impact velocity [92]. The outermost and innermost half-apex angles for the uncoated wide specimens also retain similar values to the narrow specimens. Comparison between coated specimens for steel sphere impacts, by specimen width, was not possible due to lack of experiments for the wide specimens. Overall, these plots show that wider specimens suppress the formation of multiple cone cracks and that this effect gets more pronounced with decreasing impact velocity where outermost cones become more favorable than innermost.

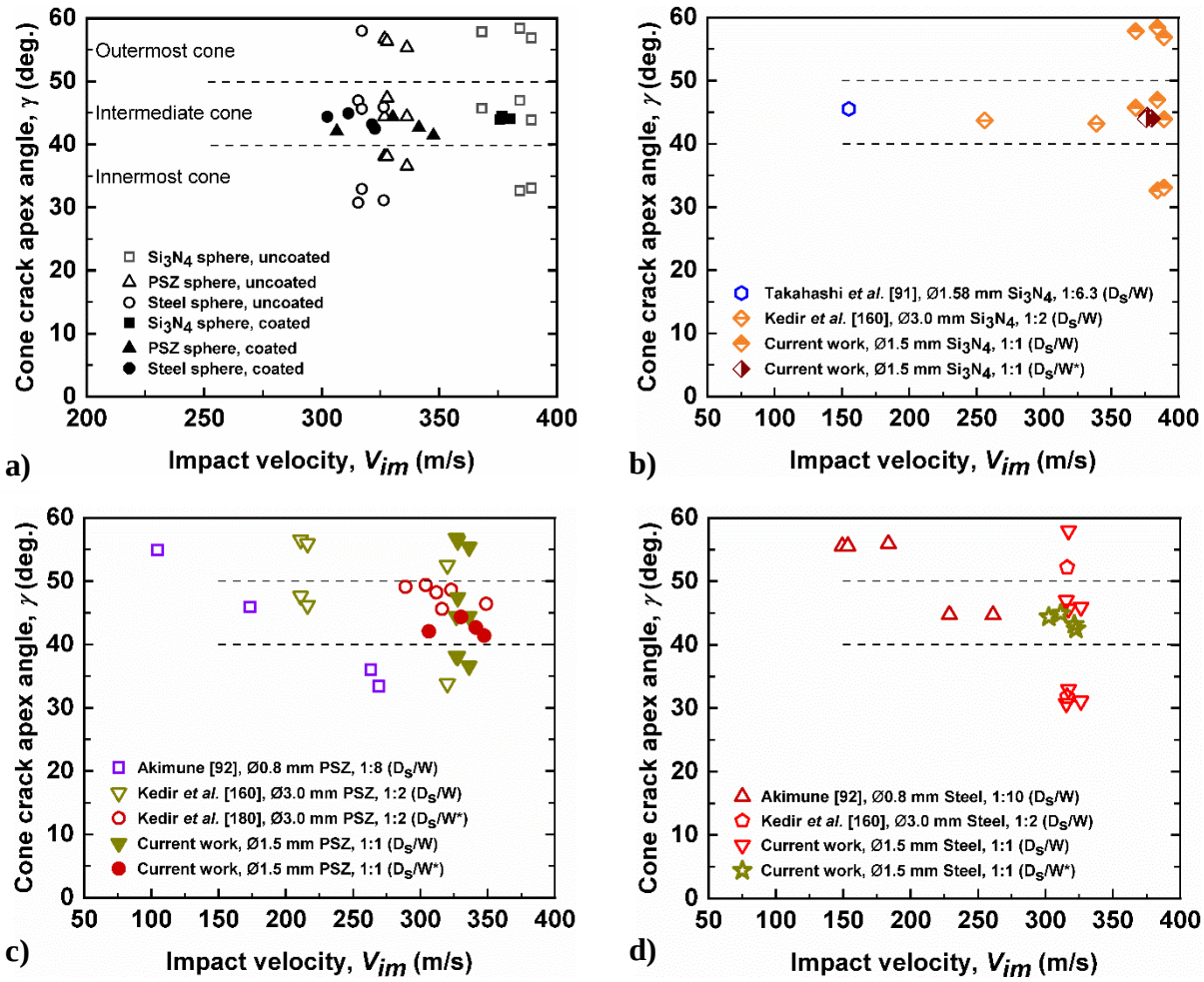

Figure 4.11. Half-apex cone crack angles for narrow coated and uncoated specimens (a). Comparisons of half-apex cone crack angles by impactor type (Si_3N_4 (b), PSZ (c), and steel (d)) for coated and uncoated specimens with varying widths. Ds – Impactor diameter, W and W* – Coated and uncoated specimen width respectively.

4.4 Discussion

4.4.1 Effects of debris simulant (projectile) material

Previous FOD impact studies on monolithic ceramics have shown that the properties of the impactor significantly influence the extent of damage. Specifically, increase in the hardness of the impactor was found to increase the type of cracks (i.e. cone, median, and radial) evolved during impact and decrease the post-impact residual strength of the ceramic [85,92,132,136]. In the

current study, the impactor initially comes into contact with a protective coating layer prior to reaching the ceramic. As reported above in Section 4.3.2.1, all impactors are observed to penetrate the coating and the rate of penetration is found to increase with an increase in hardness of the impactor (i.e. Si_3N_4 > PSZ > steel). The mode of penetration, as noted in a previous study for wide specimens (Chapter 3), is quasi-plastic deformation (or compaction) via pore closures and activation of microfractures at preexisting defect interfaces (microcracks and splat boundaries) for erosive wear. Subsequent elastic deformation of the impactors on the substrate leads to ejection of topcoat material due to erosion and limitation in radial displacement of the coating material. This form of compaction and material removal is similar to observations in monolithic ceramics under ballistic impact by long rod penetrators [181,182]. After reaching the elastic limit, delamination of the coating occurs for the brittle Si_3N_4 impactor due to limitation in continued deformation. By contrast, the tough PSZ and steel projectiles deform significantly, and the radial expansion of the coating material is accommodated through outward ejection of coating material. The steel impactor remains intact after reaching its plastic limit and rebounds, while the PSZ sphere crumbles. Hence, any remnant coating is lifted off the substrate along with the steel impactor. Rebound did not occur for Si_3N_4 and PSZ impactors. Instead, the Si_3N_4 fragments eroded the surrounding coating and the extended deformation of PSZ enhanced the formation of coating ejecta. Observation of penetration and ejecta formation in the coating prior to delamination/liftoff likely indicates a reduced level of influence by specimen edge effects on early stages of impact damage. This behavior is postulated to result from a loading rate effect where the damage front propagates slower than the high velocity impact process.

Relative to the response by the coating, the properties of the impactor do not appear to have a significant effect on the damage modes developed within the underlying narrow ceramic substrates. Both the narrow coated and uncoated specimens resulted in primary cone cracks which are induced by the maximum principal (radial) stress from Hertzian contact [85,91,132,160,180]. Additionally, all specimens showed secondary back-surface and vertical cracks. The back-surface cracks are formed due to compressive load at the impact surface which induces a tensile flexure stress on the back side of the narrow specimen [180,182,183]. On the other hand, the vertical cracks which occur at the center and near the back of the sample are likely the intersection of the cone cracks with the side walls of the narrow specimens. The reason that these cracks are not attributed as tensile vertical cracks is due to their formation prior to the initiation of the

unloading/release stress waves. Additionally, they retain a bowing geometry which contours around the cone cracks. The near surface vertical cracks do occur after unloading and they are likely induced by tensile stress generated from stress wave interactions. Median cracks also appear in the substrate for most cases except for FOD by steel impactors on coated specimens and this is likely associated with reduction in impact force (Figure 4.10c). Other damage features of interest are also linked to the load spreading effect of the coating layer which will be addressed in a later section.

An interesting aspect of the substrate damage that warrants consideration is the level of variation in cone crack angles with respect to impactor type and impact velocity for narrow and wide specimens. Akimune [92] suggests that the velocity dependence is associated with stress such that higher impact velocities induce greater levels of stress which results in narrower cone cracks. Additionally, the dependence on impactor type was assumed to result from differences in deformation behavior and its influence on the magnitude of contact area covered by the impactor for a given impact velocity. The work by Chaudhri [114] on impact of glass substrates by steel and glass spheres identifies similar behavior of the cone crack angle with respect to impact velocity. However, the ductile steel impactors were reported to yield narrower cone cracks for a given impact velocity than the glass impactors. Contrary to Akimune, Chaudhri attributed these findings to a combination of loading rate induced alteration of the principal stress trajectory in the specimen and higher loading rate imposed by the dense steel impactor. The current work shows that there is no noticeable dependence of the half-apex angle for narrow specimens with impactor type and possibly with impact velocity. However, for wide specimens, similar dependencies as in previous works by Akimune [92] and Takahashi *et al.* [91] are found. The explanation for impact velocity and impactor type dependence rendered here for the wide specimens is similar to that offered by Akimune, with the addition of rate dependent inertial effects. Following the reports by Dharan and Hauser [184] and later by Heard *et al.* [185], the acceleration in radial flow of the spherical impactors during impact (high-rate uniaxial loading) is limited/constrained due to lack of forces to instantaneously overcome the inertia. The corresponding reduction in contact area at higher loading rates (impact velocities) then leads to reduced cone angle for a given impactor type. Hence, the PSZ and steel spheres that deform markedly under quasi-static loading are constrained at higher loading rates due to the inertial effect. As noted by Akimune, the resulting change in contact area would directly affect the angle of the cone crack that is developed. Alternatively, the Si_3N_4

impactor which experiences very limited deformation at quasi-static rates of deformation is not likely to show drastic change at higher impact velocities. This insensitivity is thus translated to cone crack angles that are independent of impact velocity (Figure 4.11b). Chaudhris' assumption of stress trajectory alteration requires an associated change in Poisson's ratio of the substrate at high loading rates. To the author's best knowledge, significant evidence does not exist to endorse this rate dependence of Poisson's ratio for glass. Hence, the latter is not considered, at this moment, to play a role in determining the geometry of cone cracks. Finally, it is surmised that the inconsistency in reduction of cone crack angles between steel and PSZ impactors in the findings by Akimune and Chaudhri occurred due to changes in properties of the substrate material with the former using SiC (high hardness) and the latter glass (low hardness).

4.4.2 Effects of specimen size

A critical element of this study aimed to develop an understanding of the influence that specimen geometry has on FOD impact damage. As noted in the introduction, the emphasis on specimen size is associated with the design constraints presented by gas turbine blades (i.e. high curvature leading and trailing edges vs low curvature high- and low-pressure surfaces). If coating damage is considered independent of the substrate, very limited differences are found between the wide and narrow specimens. One of the differences that stands out is the lack of out of plane extrusion (bulging) of the topcoat about the PSZ impactor perimeter during the penetration process for narrow specimens. This behavior is likely associated with lower constraints in lateral displacement of narrow coating segments vs wide coating segments. Another difference is the lack of coating delamination for PSZ and steel impactors in narrow specimens. The latter and other differences in the late stages of coating failure are attributed to substrate size effects, as will be discussed next.

Starting with the uncoated specimens, multiple cone cracks, vertical cracks, and back-surface cracks are observed in the narrow specimens relative to the wide specimens irrespective of impactor type. The difference in cracking is postulated to result from difference in specimen width. Specifically, the confinement effect offered by surrounding material for the wide specimens is greater than that for the narrow specimens and this influences the level of cracking during FOD impact. The idea of confinement in impact of ceramics is not new, it was first reported by Hauver *et al.* [186] where different configurations of steel confinement on ceramic targets were used to

show the resistance to long rod penetration in favor of localized comminution below the impactor. More recently, the work by Pickering *et al*. [187] illustrated the lack of macrocracks (radial and cone) with increasing confinement of alumina targets by metal matrix composites (MMCs). In both cases (steel or MMC confinement), the material surrounding the ceramic applies a compressive stress which mimics a semi-infinite boundary for the impact surface and hence a large resisting force for radial displacement of the target material during impact. In the current work, there is no secondary material applying the confinement stress. However, there is a change in 'self-confinement' due to a 50 % reduction in volume between the narrow and wide specimens. The self-confinement effect was noted in the study by Holmquist *et al.* [188] and more thoroughly investigated by Carton and Roebroeks [189]. In the latter, an increase in projectile energy loss was reported to occur with increase in volume of alumina target, and this phenomenon was attributed to an increase in lateral self-confinement of fragments at the impact site. For the specific crack type, cone and back-surface cracking are identified as the two damage features that stand out when contrasting the FOD impact response of the narrow and wide uncoated specimens. Multiple cone cracks are almost always observed in the narrow specimens and this is again due to reduced confinement. In terms of the underlying source of multiple cone cracks, Iyer [190] notes that both interior and outer cone cracks emerge due to positive (tensile) principal Hertzian stresses at the perimeter of contact and subsurface of the specimen. The back-surface cracks are also signature features of narrow uncoated specimens and these occur due to associated increase in bending stress.

The narrow coated specimens are also observed to result in slightly different fracture behaviors during FOD impact relative to wide coated specimens. In the current case, impact of the narrow coated specimens by Si_3N_4 impactors leads to cone, median, back-surface, and vertical cracking. This is not the case for previous observations in wide coated specimens (Chapter 3.3.3.2) where predominant back-surface cracks are observed to be the source of fracture. This difference is again likely associated with change in lateral confinement such that cone and median cracking becomes favorable in narrow specimens. Additionally, it is noted that in Section 4.4.1 narrower specimens resulted in significant reduction of rebound for Si_3N_4 and PSZ impactors. The latter behavior is similarly associated with increased level of primary (cone and median) and secondary (vertical and back-surface) cracks. Subsequent degradation of the specimen via fragmentation and inward collapse then enables continued displacement of the impactor in the initial impact direction.

As previously noted, the reduced rebound also eliminates or minimizes coating delamination during impact despite the presence of a weak bond coat–substrate interface.

4.4.3 Effects of coating on FOD impact resistance

The *in situ* pulsed X-ray radiography approach used in the current study provides a clear determination of the damage propagation within the EBC and ceramic during simulated FOD impact experiments. A critical advantage rendered by this capability is that it offers a means to semi-quantitatively determine the level of protection afforded to the substrate by initial interaction of the impactor with the coating. The latter concept was introduced above (section 4.3.2.2) as relative change in impactor velocity during coating penetration. Here, another approach is introduced for evaluation of this shielding effect by considering the number of cracks that form within the SiC substrate in ≤ 0.6 μs of contact time. This time frame represents early stages of contact where primary and, to some extent, secondary cracks form and propagate in a stable condition. Results of the crack counts for the three impactor types are presented in Figure 4.12. These counts included cone, median, vertical and back-surface cracks as well as initial crack bifurcations. The plot clearly shows that the coated specimens develop fewer cracks (~ 42-58 % less) relative to uncoated specimens across all three impactors. This increase in resistance to FOD impact damage is associated primarily with reduction in cone cracking. Specifically, for each impactor type, the maximum cone crack was reduced by ~ 67 % in the coated specimens. Hence, it can be surmised that the EBC protects the brittle SiC substrate by absorbing the initial impact energy and reducing the contact force (i.e. yielding a lower principle Hertzian stress at the moment of contact). Further improvement in damage resistance is thus possible by effectively optimizing the coating thickness and increasing the coating toughness. Both of these approaches are expected to reduce the initial impact shock to the substrate [191,192] and dissipate much of the impactor kinetic energy.

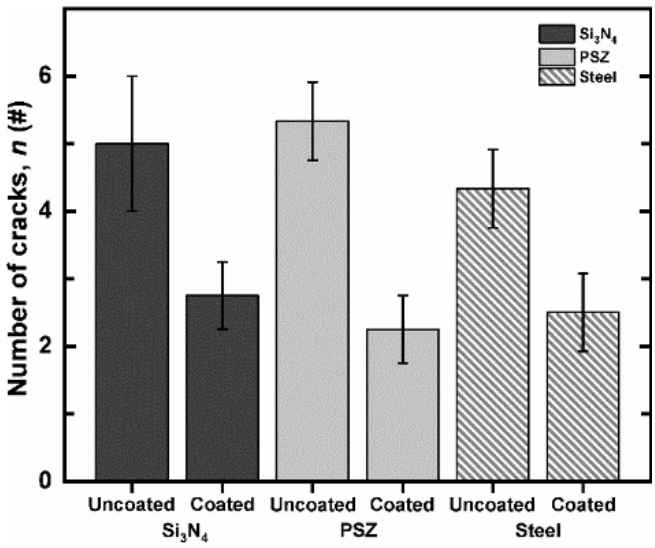

Figure 4.12. The number of cracks generated in the SiC substrate by Si_3N_4, PSZ, and steel impactors for both coated and uncoated specimens within 0.6 µs of contact time.

The current work was focused on mullite based EBCs and the findings must be applicable to more advanced EBC systems. One means by which this may be done is through a comparison of the coating properties. In the case of $Yb_2Si_2O_7$ and Yb_2SiO_5 APS coatings, the average Vickers hardness values are reported as 4.28 GPa [193] and 5.12 GPa [194] respectively. These hardness values are comparable to those for mullite (see Table 4.1). Additionally, the bulk form fracture toughness of the silicate coatings ranges between 2-2.8 $MPa \cdot m^{1/2}$ [195], while that for mullite ranges between 1.8-2.8 $MPa \cdot m^{1/2}$ [196]. Hence, a properties-based comparison leads us to postulate that the observed FOD impact response would remain similar if the more advanced coatings were examined under similar conditions.

The damage history of the coating, substrate, and impactor also provides critical information needed to construct an energy based analytical determination and/or numerical models of FOD impact. Previous studies which attempted to conduct analytical assessments of FOD impact were limited to incident and rebound kinetic energy measurements [132,136,197]. The current work would further enable determination of energy losses from several damage events including impactor deformation and fragmentation, coating ejection, and delamination, as well as substrate cracking and fracture. Due to the limited scope of this work, mor attention was given to understanding energy loss from coating penetration (see section 4.3.2.2). For numerical approaches, previous studies rely on postmortem morphology of the impact to assess the fidelity of simulations [133,198]. The latter approach requires assumptions on the transient damage mode

which may not necessarily be valid. Availability of high fidelity *in situ* data, such as that presented herein, would thus greatly reduce this uncertainty and serve as an excellent calibration tool. Such a combined approach would then ultimately provide a clearer understanding of FOD impact damage including the effects of coatings and part geometry. This knowledgebase ultimately enables the development of damage tolerant coatings required to transition advanced ceramics and CMCs from concept to components in next generation gas turbine engines.

4.5 Summary and Implications

The effect of specimen geometry on FOD impact damage behavior was investigated using pulsed X-ray radiography method. In previous studies (Chapters 2 and 3), the response of wide specimens was examined. Here, the response of narrow specimens was determined using spherical FOD simulants made from silicon nitride (Si_3N_4), partially stabilized zirconia (PSZ), and steel. The following renders a summary of the observations and understandings gained from this study:

(1) Irrespective of the FOD simulant material type, narrow uncoated specimens show cone, median, vertical, and back-surface cracks prior to complete fracture. Vertical cracks and increase in cone cracking are the major differences from impact of wide specimens.

(2) Coating penetration and ejecta formation are common damage modes observed for all narrow coated specimens. Coating delamination/liftoff occurs for impact by Si_3N_4 and steel spheres. The substrate forms identical crack types to the uncoated specimens. However, the level of cracking is significantly reduced. Under similar conditions, impact of wide coated specimens by Si_3N_4 and PSZ spheres shows more coating delamination and limited cracking of the SiC substrate.

(3) Innermost, intermediate, and outer cone cracks are formed for almost all of the uncoated specimens. The magnitude of half-apex angles for the three cone cracks are similar across all impactor types. Only intermediate cone cracks are formed in the coated specimens. A change in cone angle did not occur with slight variation in impact velocity, in contrast to wide specimens impacted by PSZ and steel spheres.

(4) The relative coating penetration depth, d_p/V_{im}, is lowest for steel projectile, intermediate for Si_3N_4 projectile, and highest for PSZ projectile. The relative change in impactor velocity during coating penetration, $\Delta V/V_{im}$, is lowest for PSZ sphere and highest for steel sphere. These behaviors are related to projectile properties: hardness and impact energy

($H_p \cdot E_{im}$). Higher $H_p \cdot E_{im}$ yields greater penetration for the impactor and lower resistance to penetration by the coating. A linear relationship is also established between $H_p \cdot E_{im}$ and the rate of relative coating penetration depth, $d/dt(d_p/V_{im})$, as well as the maximum relative change in projectile velocity $(\Delta V/V_{im})_{max}$.

(5) For all three impactors (irrespective of specimen geometry), the level of cracking in the substrate is significantly lower for the coated specimens. The energy absorbed during coating penetration appears to protect (or shield) the brittle substrate.

(6) Overall, the narrow specimens showed a greater tendency for cracking and fragmentation relative to wide specimens. It is surmised that a reduction in self-confinement occurs in the narrow specimens and this leads to increased lateral displacements (fracture).

(7) The *in situ* damage histories and critical findings on the effect of specimen geometry are critical for calibrating damage prediction models. Such an approach will lead to more reliable simulations of FOD impact in the future.

This study addressed a critical knowledge gap in current understanding of specimen geometry effects on damage evolution within the EBC and the underlying substrate during an FOD impact event. With the aid of *in situ* pulsed X-ray radiography, it was revealed that low curvature segments of a component sustain greater levels of damage (cracking) relative to flatter (wide) regions. The latter was also applicable irrespective of the presence or lack thereof of a coating layer or change in impactor material type. This increase in damage was attributed to reduction in lateral self-confinement which suppresses cracking during the impact event. Coating penetration was also identified to be dependent on projectile hardness and impact energy. A projectile with both high hardness and impact energy was found to be the most effective in penetrating through the coating layer. The projectile properties did not induce a significant change in damage mechanism within the coated substrate. The latter is again attributed to the reduced self-confinement. Most importantly, the coating was observed to provide some protection to the narrow substrate, as was the case for the wide substrate. Based on these observations, suppression of cone cracking was the most significant change with the coated samples, and this is postulated to arise from reduced impact load (i.e. dissipation of kinetic energy from coating penetration process). The latter indicates that an increase in coating thickness and toughness would further aid in dissipating the impact energy and thereby limit or eliminate the damage to the brittle substrate.

5. GLOBAL SUMMARY

This dissertation has examined the applicability of pulsed synchrotron X-ray radiography for *in situ* characterization of FOD impact damage in gas turbine grade ceramic monoliths with and without EBCs. In this effort, the facilities for the experimental evaluation were initially established and three studies were conducted: impact on bare ceramic, impact on coated ceramic, and impact on narrow uncoated and coated ceramic. The *in situ* characterization approach was found to effectively capture the damage history with high temporal and spatial resolutions in all three studies. For the first time, it was possible to track damage including deformation, material removal, crack initiation and propagation, as well as fragmentation accurately. Past efforts have relied solely on postmortem analysis and only obtained cumulative footprints of damage with no understanding of the damage kinetics. Such data is needed to establish fidelity in modeling efforts where transient damage propagation is critical. These high fidelity models can then be added to the overall life prediction for ceramic based gas turbine components where the effect of FOD impact is currently neglected or poorly captured.

Beyond confirming the efficacy of the *in situ* characterization method for FOD impact, the three studies have also yielded some critical information regarding the *effects of projectile properties*, the *role of an EBC in damage mitigation*, as well as the *significance of change in specimen geometry*. Before summarizing the findings, it is imperative to reiterate that these studies were performed using model materials consisting of Hexoloy (α-)SiC ceramic, and an EBC composed of a mullite topcoat and a silicon bond coat. While the SiC ceramic served as a substitute for advanced SiC_f/SiC CMCs, the EBC was chosen due to its low atomic mass for reduced attenuation of X-rays (i.e. greater level of through transmission). The critical properties of the EBC (toughness and hardness) were however similar to those for advanced ytterbium silicate and disilicate compositions. Hence, the findings from these studies remain valuable in understanding the FOD impact response for more technologically pertinent materials.

The *effect of projectile properties* (density, hardness, and toughness) on FOD impact response was examined in all three studies (Chapters 2 through 4). For the uncoated specimens, all projectiles (Si_3N_4, PSZ, and steel) induced cone cracks as primary damage after contact, followed by secondary cracks (i.e. back-surface, vertical, and/or median cracks). Projectiles with high toughness (PSZ and steel) were found to result in cone crack half-apex angles that increase

with decreasing impact velocity due to greater effect of inertial confinement (i.e. reduced deformation at higher strain rates). For the coated specimens (Chapters 3 and 4), all projectiles were found to initially deform and penetrate the EBC. The relative rate of coating penetration (how fast the projectile displaced within the EBC) and the relative change in velocity (how well the EBC decelerated the projectile from its initial impact velocity) were found to depend on both the hardness and impact energy of the projectile. Higher hardness and impact energy are associated with higher rate of penetration and hence a reduced level of resistance by the EBC. This response revealed for the first time that debris with maximum values in both hardness and impact energy are more effective in damaging EBCs. Coating delamination was found to be mostly insensitive to projectile properties. However, subsequent coating liftoff did depend on the deformation behavior of projectiles. For brittle elastic Si_3N_4 and plastic steel projectiles, liftoff was more likely due to rebound. By contrast, quasi-plastic PSZ projectiles were found to deform and crumble on the surface of the specimen. For substrate damage, Projectile properties were found to be more critical for the wide specimens (Chapter 3.3.3). Specifically, deformation of tough PSZ projectiles was found to enable transfer of Hertzian stress to the substrate through the coating and induce cone cracks. By contrast, the brittle Si_3N_4 projectile fractured immediately after penetrating the coating and only induced back-surface cracks. This response has revealed the importance of projectile toughness in determining the type of damage induced within substrates for wide coated specimens.

The *role of an EBC in damage mitigation* during FOD impact was studied in Chapters 3 and 4. As noted above, the initial coating damage consisted of penetration and ejecta formation. This was typically followed by delamination and then coating liftoff for rebounding projectiles. The penetration process has been postulated to result from an erosion like process facilitated by the weak microstructure of the EBC (i.e. pores, microcracks, and lamellar boundaries). This is the first account of such behavior for FOD impact in EBCs. The EBC was also found to significantly influence the damage induced within the brittle substrate during FOD impact. Specifically, a lower crack density was observed in specimens with coatings irrespective of projectile type or specimen geometry. This was attributed to the shielding effect where substantial amount of impact energy is dissipated during the coating penetration process. In addition, the lower crack density was primarily associated with reduction in the number of cone cracks (Figure 4.12 in Chapter 4.4.3). Since the cone crack is associated with magnitude of impact load, this finding showed that the EBC reduces the Hertzian stress on the brittle substrate. Another interesting finding was the

predominance of back-surface cracks for wide coated specimens (Chapter 3.3.3). This was attributed to an increase in flexural stress due to the compliant layer on the brittle substrate. In terms of enabling better damage mitigation, these studies have shown that thicker coatings would logically increase energy dissipation and hence reduce the damage to the substrate. Increasing the deformability of the EBC (i.e. toughness) would also enhance energy dissipation during impact as well as prevent significant coating removal.

The *significance of change in specimen geometry* in altering the FOD impact response was evaluated in Chapter 4. This study accounts for the three-dimensional aerodynamic design of nozzles and turbine blades which retain wide and narrow (low curvature) regions. Starting with the uncoated ceramic specimen, narrow specimens were found to sustain greater levels of cracking and bifurcation relative to wider specimens. The primary cracks were multiple cone cracks, and the secondary cracks often included vertical and back-surface cracks. In the latter, back-surface cracks were more predominant in all narrow specimens relative to wide specimens. The increase in crack density and enhanced fracture was attributed to a decrease in self-confinement for narrow specimens. Loss of material, or self-confinement, reduces the constraint on the local damage and allows for ease of propagation. Furthermore, bending is much more pronounced in narrow specimens and this was attributed to the increase in flexural back-surface cracking. For coated specimens, the initial penetration and ejecta formation damage was found to remain the same for both wide and narrow geometries. However, coating delamination was suppressed in narrow specimens for impact by PSZ and steel projectiles. This behavior was attributed to both increased fragmentation of narrow specimens and deformation behavior of the two projectile types. Similarly, these same factors also reduce liftoff of the coating (i.e. rebound of projectile). Unlike the wide coated specimens, cone cracks were formed for all projectile types in narrow coated specimens. The resulting cone crack half-apex angles were however not affected by the change in specimen geometry.

Table 5.1 renders a summary of the three impact parameters discussed above and their influence on specific damage features that evolved during an FOD impact event. It shows that *projectile properties* play a significant role in EBC damage. In addition, the *EBC layer and specimen geometry* are shown to be more critical for damage in the brittle substrate.

Table 5.1. Summary of influence by three FOD impact parameters on coating and substrate damage.

	EBC damage			**Substrate damage[a]**			
FOD impact parameters	Penetration / Ejection	Delamination	Liftoff	Cone crack formation	Cone crack half-apex angle	Back-surface crack formation	Fragmentation
Projectile properties							
EBC layer[b]							
Specimen geometry							

Red – indicates a direct effect by the FOD impact parameter on the specific damage.
Yellow – indicates a moderate to minor effect by the FOD impact parameter on the specific damage. Often involves/requires another FOD impact parameter (e,g. projectile properties are more influential in wide specimen geometries for determining cone crack formation).
Green – indicates little to no effect by the FOD impact parameter on the specific damage.
Grey – indicates no relationship between the FOD impact parameter and the specific damage.
Example – Projectile properties directly influence penetration and ejection of the EBC where projectiles with high hardness and density (for a given impact velocity) induce a greater rate of penetration (i.e. more effective damage).

a. This applies to both coated and uncoated substrates.
b. The effect of alteration in thickness or property of the coating was not studied in this dissertation. Therefore, the effect of a standard EBC layer on damage to the coating itself is null.

6. FUTURE WORK

The *effect of strain rate and impact angle* are two avenues of research that can be performed in the near future with little alteration to the materials and experimental setup used in this dissertation.

The SiC substrate is known to be strain rate sensitive (see Chapter 2.3.4). However, there is no account of the rate sensitivity for the EBC. Therefore, pulsed synchrotron X-ray radiography experiments at varying impact velocities are needed. Using trial samples (silicon/mullite EBC on Si_3N_4 substrate), one experiment at ~ 6 m/s was performed to assess if such a study was necessary. As shown in Figure 6.1, EBC penetration is significantly reduced for loading at 6 m/s. The EBC appears to experience a slight deformation followed by a flexural crack that runs from the bond coat–substrate interface to the loading point. Each segment of the cracked EBC is then removed via delamination at the bond coat–substrate interface. This observation clearly shows that a transition in damage from deformation and flexural fracture at low rate impact to deformation and penetration at high rate impact occurs. Additional studies in the future could provide information on the 'damage transition velocity'.

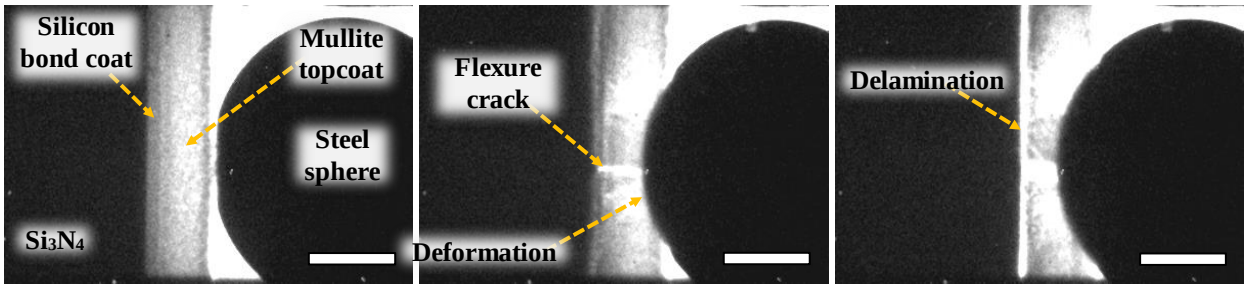

Figure 6.1. Impact of a stationary Si3N4 specimen (3 x 3 x 4 mm3) by a 1.5 mm diameter steel sphere at a velocity of ~ 6 m/s. The experiment was conducted using a modified Kolsky pressure bar (see Ref [139] for details on experimental setup). Scale bars – 500 µm.

Similar to the strain rate effect, impact angle is also known to influence FOD impact damage in SiC (see Chapter 1.4). There is however no study which has assessed the effect of damage in EBCs. There was no remaining material or beamtime resource to perform this type of experiment using pulsed synchrotron X-ray radiography in this dissertation. It is possible to

postulate that damage in the EBC increases with decreasing impact angle compared to the response by the SiC substrate. This is based on the understanding that ductile (or quasi-ductile in the case of EBCs) materials experience a greater level of erosion at acute angles of impact where shear induced deformation is more prominent. Still, empirical studies with varying impact angles are needed, in the future, to accurately understand the variation in the evolution of damage.

Besides the two studies mentioned above, other (more complex) potential research directions include *alteration of the coating material*, *consideration of CMC substrates*, *assessment of temperature effects*, *evaluation of irregular projectile geometries*, and *numerical model development*.

In this dissertation, a single coating thickness and microstructure was evaluated. The investigation by Bhatt *et al.* [110] has shown that thicker EBCs reduce FOD impact damage in the substrate. However, there was no indication of the mechanism by which this shielding takes effect. Based on the findings in Chapter 4.3.2.1, it is surmised that the thicker coating would present a greater travel distance during projectile penetration and hence enhance impact energy absorption. Additional work using the pulsed X-ray radiography approach is needed to confirm this hypothesis. Furthermore, the APS coating produces a relatively continuous microstructure with dispersed porosities and microcracks. This microstructure is desirable for EBCs since it is more effective in preventing detrimental oxygen and water vapor ingress at high temperatures. However, the columnar microstructure obtained via EB-PVD has been shown to be more effective in absorbing a greater level of strain during impact via column buckling, shearing, and compaction [106,107]. Hence, EB-PVD or other more complex plasma spray process (i.e. plasma spray physical vapor deposition (PSPVD), suspension plasma spray (SPS), and solution precursor plasma spray (SPPS)) may be used to deposit a sacrificial column layer on top of the traditional APS layer. A study of FOD impact damage for this tri-layer coating concept (e.g. APS silicon/APS mullite/SPS mullite) could then be performed with pulsed synchrotron X-ray radiography method. Besides this specific example, other approaches can also be considered including multilayer EBCs with a potential for crack deflection between layers during impact. For such a coating system, impact energy dissipation would result primarily from strain energy released during interfacial crack formation and propagation.

The current study considered a model monolithic SiC substrate instead of more technologically relevant SiC_f/SiC CMCs. As expected, a highly elastic-brittle response with

catastrophic fracture was observed, for SiC, in the pulsed synchrotron X-ray radiographs during FOD impact. However, CMCs are more damage resistant and capable of sustaining impact damage without complete loss of load bearing capacity. This has the potential to also influence the damage in the EBC layer, since impact energy can be dissipated through enhanced substrate damage. Future *in situ* studies may thus consider application of EBC coated CMCs with various architectures (unidirectional, woven, two- and three-dimensional, etc.) to understand how changes in substrate material properties influences the response to FOD impact.

All experiments conducted in this dissertation were performed at room temperature due to the complexity in integrating the X-ray/impact rig with a closed form heating apparatus (i.e. furnace). In the future, this limitation must be overcome, and *in situ* FOD impact studies must be conducted at high temperatures. This is important since gas turbine operation requires high temperature exposure. An *ex situ* study has already shown that impact at high temperatures results in lower levels of EBC and substrate damage [110]. This was attributed to the slight increase in compliance of the ceramic coating and substrate with an increase in temperature. In addition to temperature, future *in situ* studies may also incorporate other aspects of the engine environment (e.g. steam cycling and CMAS corrosion) with FOD impact.

In Chapter 1.4.1, the effect of projectile geometry on FOD impact was explored by referring to the limited studies that are currently available. The limitation in studying this phenomenon was identified to be the difficulty in performing impact with irregular projectiles. Additionally, it was made clear that impact by sharp particles induces greater levels of damage due to the formation of radial-median crack vents. Research efforts to develop experimental techniques for irregular particle impact studies are clearly needed. In the case of multi edge particles (e.g. approaching a dodecahedron), it may be possible to use a sabot method to carry the projectile and strip the carrier at the barrel exit using a stopper block. Alternatively, the particle may be driven by a high energy pulsed laser which rapidly ablates a polymer or metal surface to create momentum via vapor/plasma expansion. If a triangular particle is desired, it will be difficult to maintain the trajectory without spin. This may be overcome by performing reverse ballistic type experiments where the specimen is projected onto a fixed particle with the sharp edge facing the barrel exit. Still, the latter approach does have a downside when it comes to specimen recovery. These suggested approaches draw on existing techniques and more advanced techniques may be developed over time. Regardless of the technique chosen, it is recommended to incorporate the

pulsed synchrotron X-ray characterization established in this dissertation to obtain more meaningful results.

Finally, future studies should also include numerical modeling/simulation of FOD impact. Empirical studies are valuable in attaining a fundamental understanding of the damage process. However, a physics based quantitative understanding of the damage is also imperative. Simple analytical representations of the impact process are highly limited due to the transient nature of the process especially when deformation and fracture are involved (see Chapter 2.4.2). Numerical simulations backed by reliable empirical data and appropriate damage models are therefore more likely to yield better results. It is suggested that future studies employ the data generated in this dissertation (or similar sources) as a starting point for calibrating the damage models (e.g. Johnson-Holmquist (JH-2) or Drucker-Prager). Once an accurate model is identified, it will be possible to include it in the overall degradation/life span of ceramic based gas turbine components.

APPENDIX A: ADDITIONAL X-RAY RADIOGRAPHS FOR IMPACT OF BARE CERAMIC SAMPLES (CHAPTER 2)

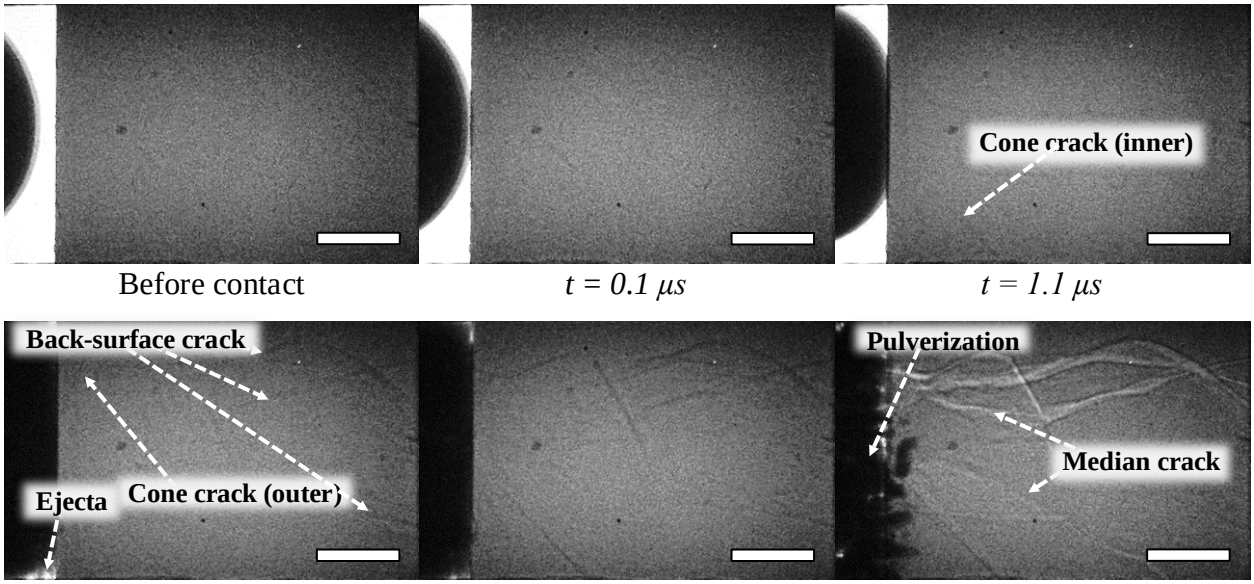

Figure A.1. X-ray radiographs depicting impact of 1.5 mm PSZ sphere on a Hexoloy SiC ceramic. Impact velocity of 216 m/s and high speed imagining at 2MHz. Scale bars in each frame – 500 μm.

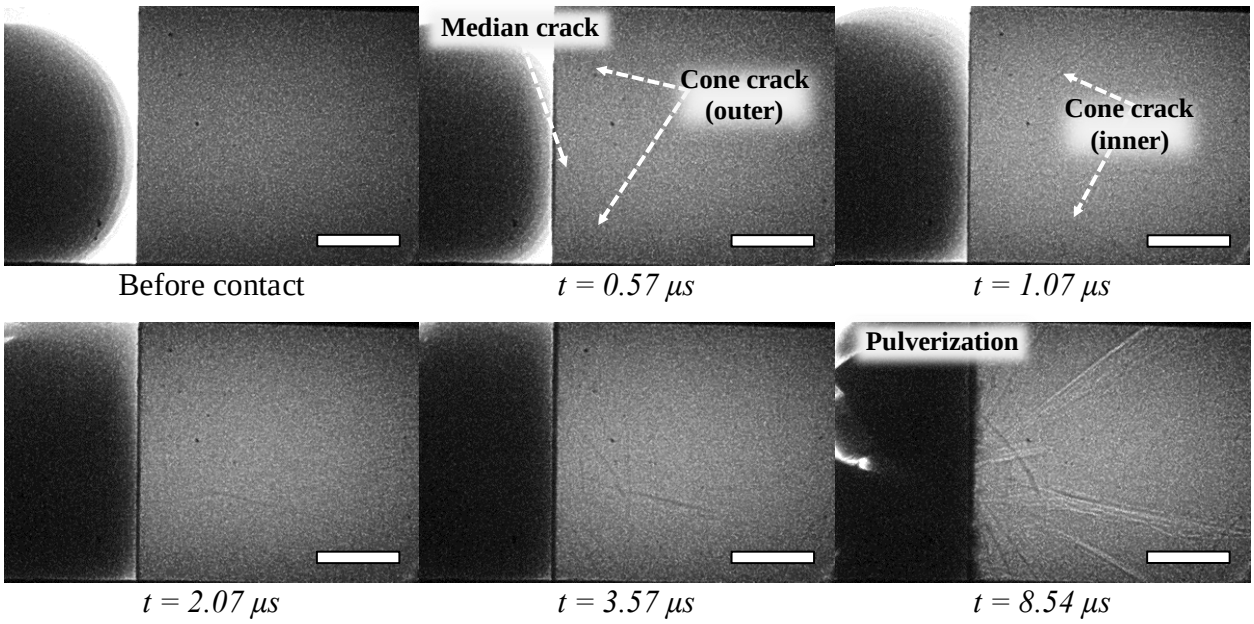

Figure A.2. X-ray radiographs depicting impact of 1.5 mm PSZ sphere on a Hexoloy SiC ceramic. Impact velocity of 320 m/s and high speed imagining at 2MHz. Scale bars in each frame – 500 μm

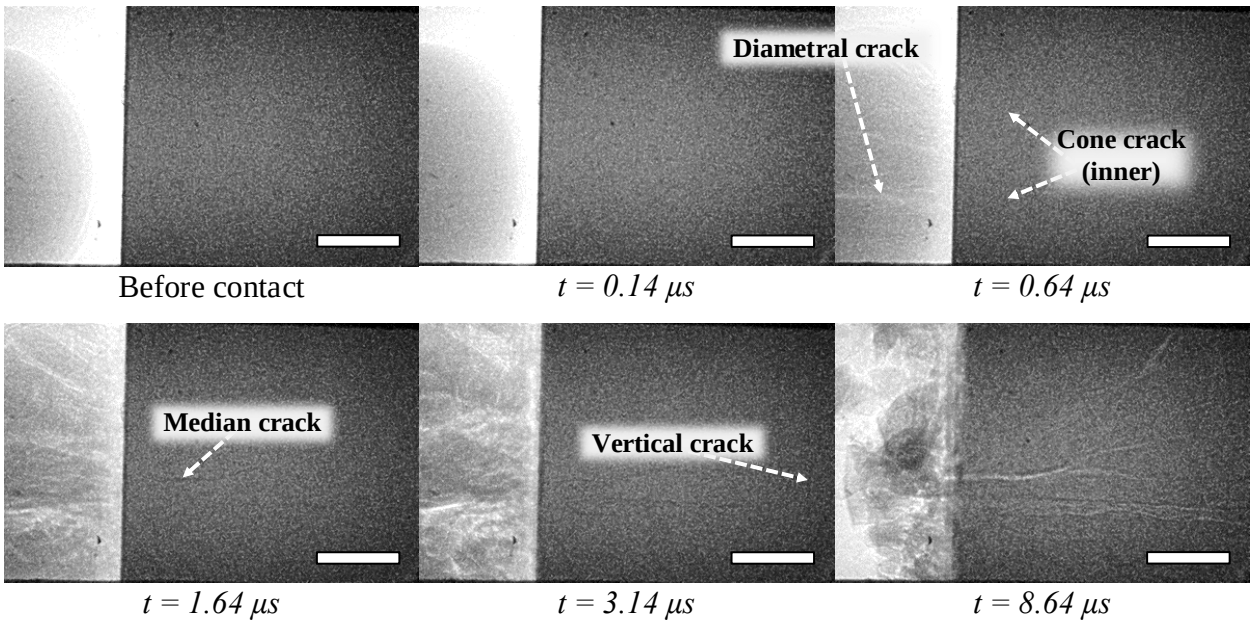

Figure A.3. X-ray radiographs depicting impact of 1.5 mm Si_3N_4 sphere on a Hexoloy SiC ceramic. Impact velocity of 339 m/s and high speed imagining at 2MHz. Scale bars in each frame – 500 μm.

APPENDIX B: NANOINDENTATION EXPERIMENTS

The polished cross-section of the coated sample presented in Figure 3.4 (Chapter 3) was used to conduct nanoindentation experiments. A Hysitron TI-950 TriboIndenter unit (Minneapolis, MN, USA) was used in forced-controlled progressive multi-cycle mode. For each indentation, the indentation force was increased gradually to the maximum value of 250 mN in five increments/cycles (50 mN, 86 mN, 130 mN, 186 mN, and 250 mN). In the first four cycles, a 50 % unloading was performed before reloading to the next load value (e.g. load to 50 mN and unload to 25 mN, then reload up to 86 mN). Each loading cycle was 15 s long, subdivided into three five second portions for the loading, hold, and unloading steps. Five indentations, each with five load-unload cycles, were performed for the SiC substrate, silicon bond coat, and mullite topcoat.

An automated calculation of the elastic properties and hardness was performed by implementing the built-in Oliver and Pharr method for curve fitting [199]. Initially, the slope for the unloading portion of the load (P) vs depth (h) curve was determined to obtain the unloading stiffness (S) value per Equation B.1,

$$S = \left.\frac{dP}{dh}\right|_{P=P_{max}} \tag{B.1}$$

where P_{max} is the maximum indentation load for the given cycle. This stiffness value was then used to determine the corrected contact depth (h_c) and the projected area of contact (A_p) according to Equations B.2 and B.3:

$$h_c = h_{max} - \varepsilon\frac{P_{max}}{S} \tag{B.2}$$

$$A_p = 24.5h_c^2 + \sum_{i=1}^{8} C_i h_c^{1/2^{i-1}} \tag{B.3}$$

where h_{max} is the depth at maximum load, ε is a geometric constant which depends on the type of indenter (0.75 for the Berkovich indenter used here [199]), and C_i are the constants which describe the deviation due to the indenter tip radius. The reduced modulus (E_r) and the hardness (H) can then be obtained using the following relations,

$$E_r = \frac{\sqrt{\pi}}{2}\frac{S}{\sqrt{A_p}} \tag{B.4}$$

$$H = \frac{P_{max}}{A_p}\cdot \tag{B.5}$$

Only three of the five experiments were found to be valid for the EBC layers while four out of five experiments were valid for the SiC substrate. Figure B.1 provides representative load–depth curves for the three materials. Visual evaluation of the indentation was also performed via SEM. The resulting micrographs are presented in Figure B.2 for reference. The micrographs show little to no pile-up at the edge of indentations for all three materials. Furthermore, the higher number of invalid experiments for the EBC was found to result from the sink-in effect (i.e. fracture via nearby and/or subsurface porosities).

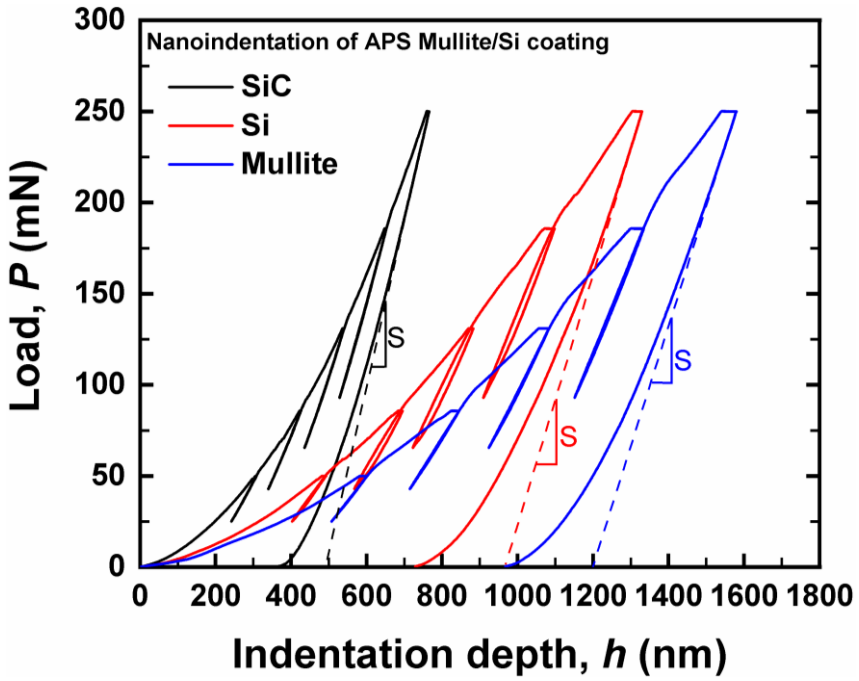

Figure B.1. Representative nanoindentation load-depth curves for the EBC layer (mullite topcoat and silicon bond coat) and SiC substrate. A force-controlled progressive multicycle mode was used with five load-unload cycles for each indentation.

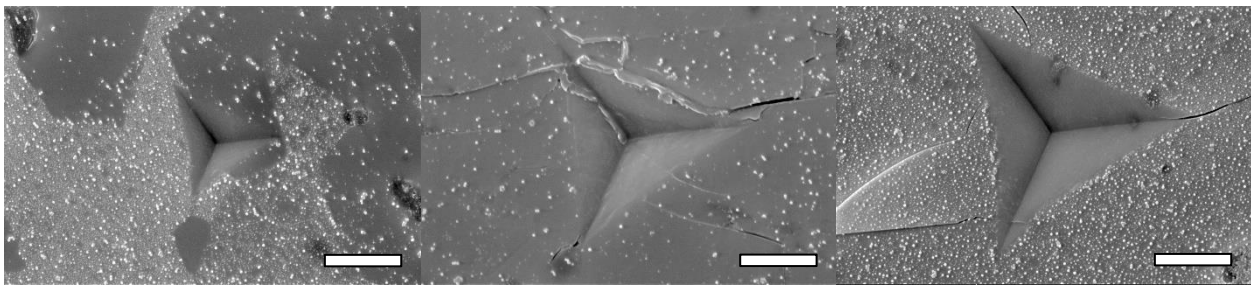

SiC substrate Silicon bond coat Mullite topcoat

Figure B.2. Representative nanoindentation micrographs for the SiC substrate, silicon bond coat, and mullite topcoat. All micrographs are for test # 4 in Table B.1 below. Scale bars in each – 3 μm.

Table B.1 provides all data for the reduced modulus and hardness. The specimen elastic modulus (E_s) was also determined using the following Hertzian contact relation,

$$\frac{1}{E_r} = \frac{(1-\nu_i^2)}{E_i} - \frac{(1-\nu_s^2)}{E_s} \tag{B.6}$$

Where E_i = 1141 GPa and ν_i = 0.07 are respectively the elastic modulus and poisons ratio for the diamond indenter [199], and ν_s is the poisons ratio for the specimen (see Table 4.1, Chapter 4). The elastic modulus and hardness for SiC was found to be 407.5±26.3 GPa and 34.4±3.7 GPa respectively. These values are similar to those provided by the supplier (see Table 2.1, Chapter 2). The APS silicon bond coat was found to retain an elastic modulus and hardness of 142.8±7.6 GPa and 10.8±1.5 GPa respectively. To the author's best knowledge there are no literature accounts of empirical nanoindentation results for APS silicon. However, average elastic modulus and hardness values of 169.5±1.2 GPa and 12.7±0.1 GPa were determined via nanoindentation by Jung *et al.* [200] for crystalline silicon with a (100) surface. The reduced values for the current work are likely due to imperfection in the APS silicon microstructure relative to the crystalline silicon. Finally, average elastic modulus and hardness values of 112.2±8.4 GPa and 8.8±1.0 GPa were determined for the APS mullite topcoat. These values are very similar to nanoindentation results reported by Cojocarus *et al.* [164] for similar APS mullite coatings (E_s = 126.6±16 GPa and H = 7.8±1.7 GPa).

Table B.1. Summary of nanoindentation experiment results for the SiC substrate, silicon bond coat, and mullite topcoat.

	Silicon Carbide											
	test #2			Test #3			Test #4			Test #5		
	Er (GPa)	H (GPa)	E_s (GPa)	Er (GPa)	H (GPa)	E_s (GPa)	Er (GPa)	H (GPa)	E_s (GPa)	Er (GPa)	H (GPa)	E_s (GPa)
cycle 1	290.203	31.349	380.926	330.835	37.986739	455.889	272.279	29.3641	350.071	315.331	37.493	426.421
cycle 2	279.959	30.848	363.135	320.842	37.927852	436.769	285.261	28.8511	372.29	314.367	36.8258	424.623
cycle 3	297.518	30.211	393.892	322.981	37.145458	440.823	305.851	29.8253	408.937	316.365	36.589	428.351
cycle 4	301.183	31.516	400.472	307.371	39.446067	411.713	300.045	32.0367	398.422	310.086	37.4879	416.697
cycle 5	303.299	32.748	404.298	309.681	39.311706	415.953	305.47	33.6811	408.243	308.375	37.5734	413.552
Avg.	294.433	31.334	388.545	318.342	38.363564	432.229	293.781	30.7517	387.593	312.905	37.1938	421.929
Stdev.	9.50118	0.9396	16.7538	9.73688	0.985699	18.3034	14.6329	2.03888	25.697	3.48091	0.45313	6.44616
	Silicon											
	test #2			Test #4			Test #5			**Average and standard deviation from all values**		
	Er (GPa)	H (GPa)	E_s (GPa)	Er (GPa)	H (GPa)	E_s (GPa)	Er (GPa)	H (GPa)	E_s (GPa)			
cycle 1	129.943	11.436	136.644	135.51	11.032644	143.283	147.375	12.649	157.679			
cycle 2	131.43	10.934	138.41	134.143	10.897355	141.647	142.301	11.892	151.481	**SiC**		
cycle 3	131.448	10.813	138.432	129.746	8.264284	136.411	145.906	12.13	155.878	Er (GPa)	H (GPa)	Es (GPa)
cycle 4	131.762	11.067	138.805	128.389	7.889759	134.804	140.342	11.8677	149.105	304.865	34.4108	407.574
cycle 5	137.175	11.152	145.282	132.962	8.370852	140.235	127.136	11.6433	133.325	14.5729	3.67053	26.3048
Avg.	132.351	11.08	139.515	132.15	9.2909788	139.276	140.612	12.0364	149.493			
Stdev.	2.78735	0.2368	3.33167	2.99371	1.5393176	3.56394	8.0356	0.38334	9.66034	**Silicon**		
	Mullite									Er (GPa)	H (GPa)	Es (GPa)
	test #2			test #4			test #5			135.038	10.8025	142.761
	Er (GPa)	H (GPa)	Es (GPa)	Er (GPa)	H (GPa)	E_s (GPa)	Er (GPa)	H (GPa)	E_s (GPa)	6.31521	1.4568	7.59952
cycle 1	120.1	10.465	127.658	101.094	8.475882	105.503	106.494	8.86672	111.715			
cycle 2	115.263	10.566	121.942	95.5621	7.881875	99.2049	100.857	8.61745	105.232	**Mullite**		
cycle 3	110.167	10.088	115.979	109.075	7.439069	114.708	104.995	8.38075	109.984	Er (GPa)	H (GPa)	Es (GPa)
cycle 4	103.09	9.8687	107.792	110.881	7.834397	116.811	102.979	8.18604	107.664	106.842	8.80016	112.172
cycle 5	98.5665	9.2434	102.617	119.191	8.063619	126.58	104.311	8.02517	109.196	7.24592	1.01262	8.41232
Avg.	109.437	10.046	115.198	107.161	7.9389684	112.561	103.927	8.41522	108.758			
Stdev.	8.75524	0.53	10.1793	9.13176	0.3767984	10.5758	2.13312	0.33564	2.45321			

APPENDIX C: ADDITIONAL X-RAY RADIOGRAPHS FOR IMPACT OF COATED CERAMICS SAMPLES (CHAPTER 3)

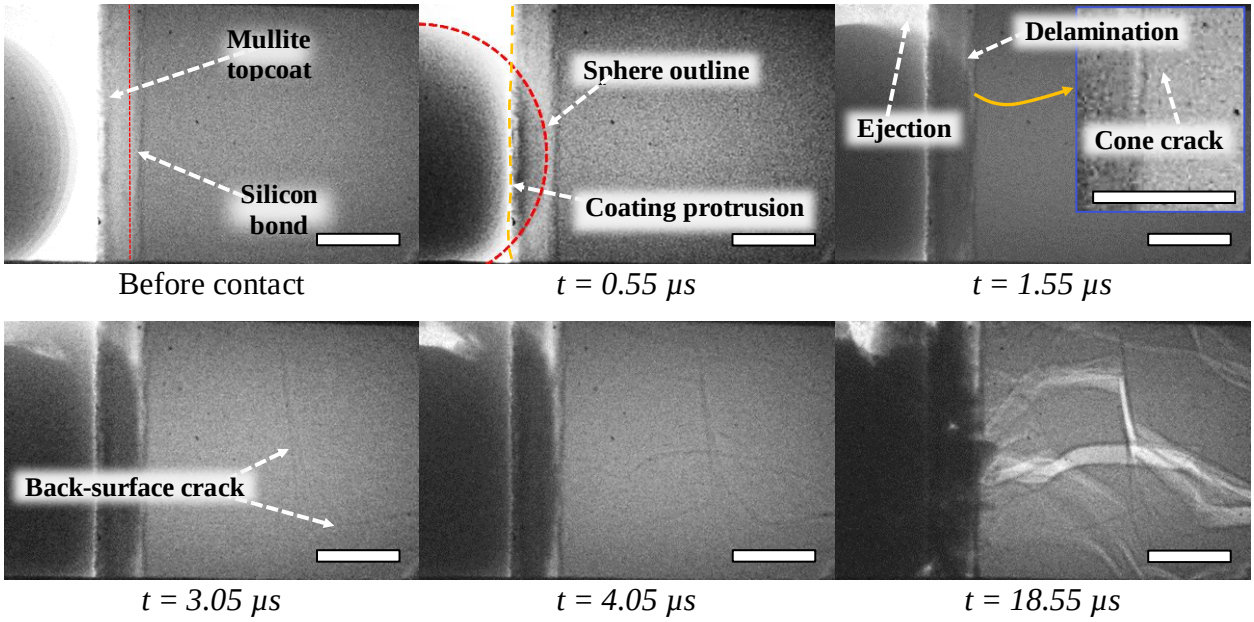

Before contact | *t = 0.55 µs* | *t = 1.55 µs*

t = 3.05 µs | *t = 4.05 µs* | *t = 18.55 µs*

Figure C.1. X-ray radiographs depicting impact of a coated SiC substrate by a spherical (1.5 mm diameter) PSZ projectile at a velocity of 300 m/s. Images were recorded at 2M frames per second with an exposure time of 200 ns. Scale bars in each frame – 500 µm.

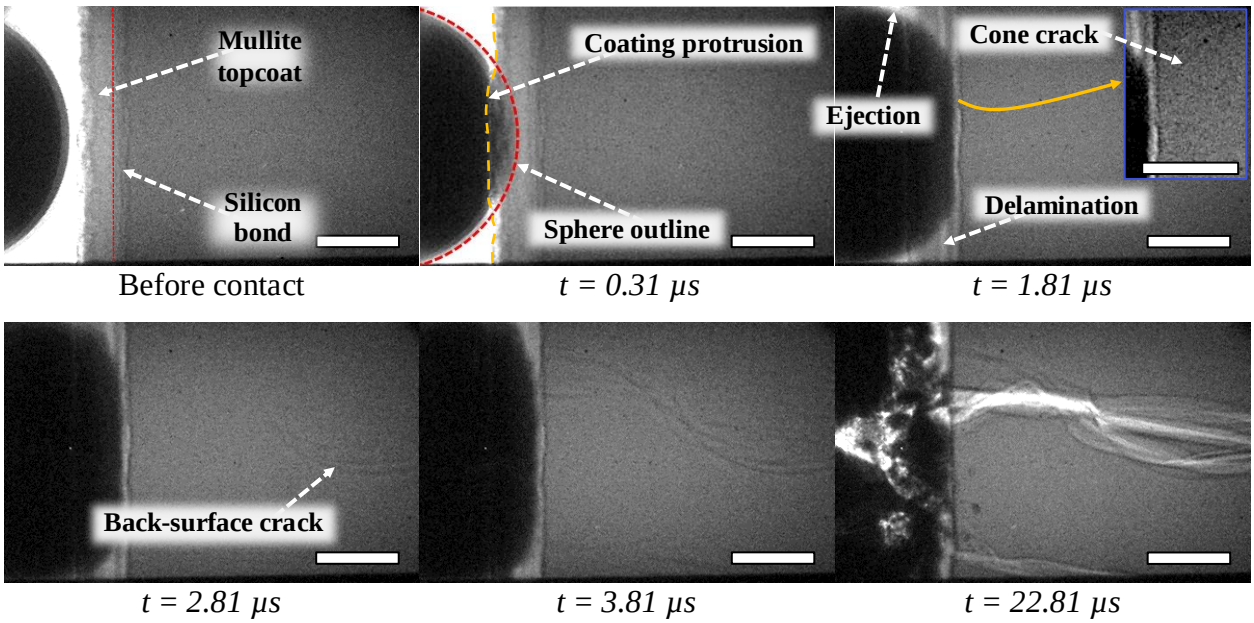

Figure C.2. X-ray radiographs depicting impact of a coated SiC substrate by a spherical (1.5 mm diameter) PSZ projectile at a velocity of 304 m/s. Images were recorded at 2M frames per second with an exposure time of 200 ns. Scale bars in each frame – 500 µm.

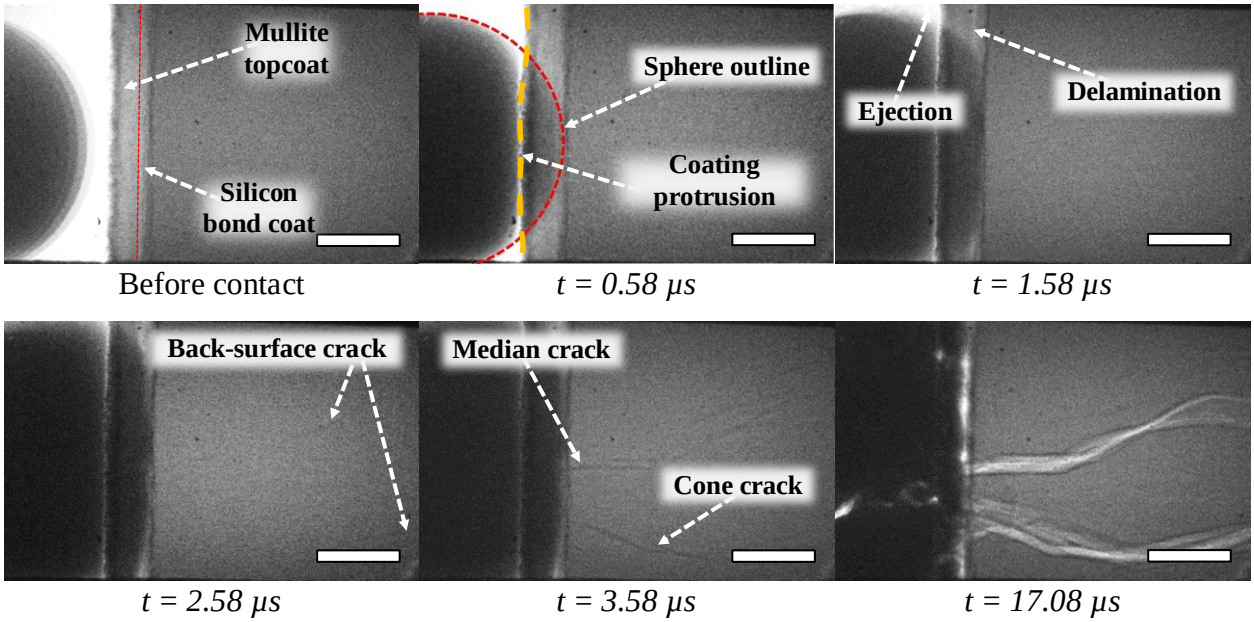

Figure C.3. X-ray radiographs depicting impact of a coated SiC substrate by a spherical (1.5 mm diameter) PSZ projectile at a velocity of 312 m/s. Images were recorded at 2M frames per second with an exposure time of 200 ns. Scale bars in each frame – 500 µm.

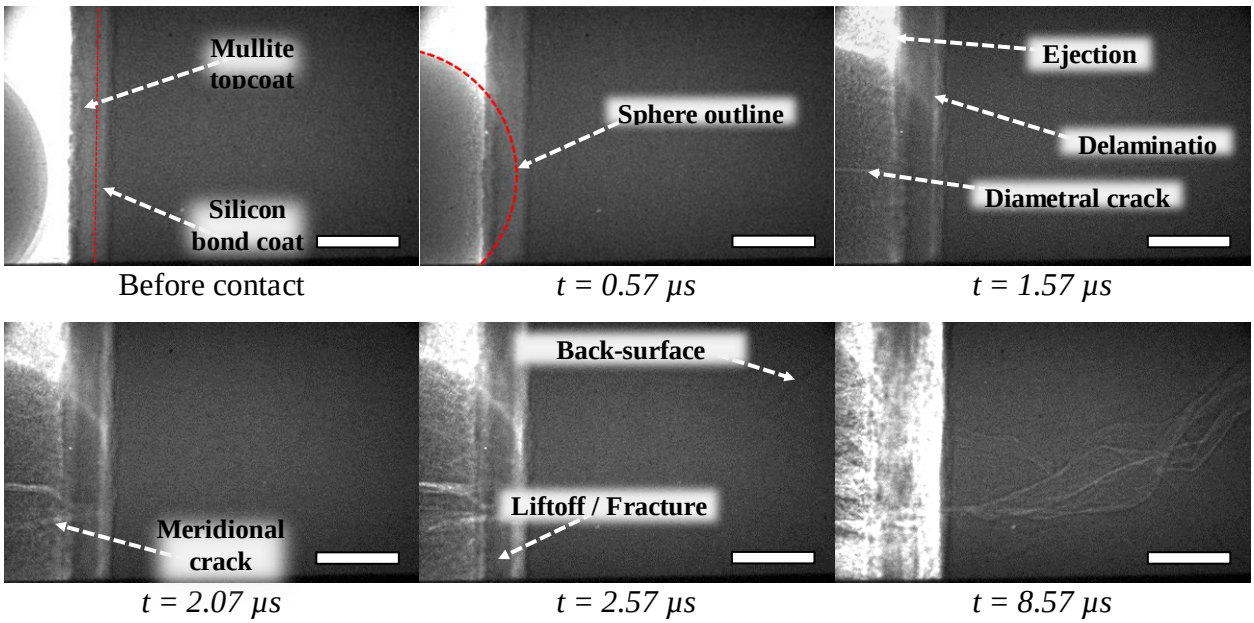

Before contact | *t = 0.57 µs* | *t = 1.57 µs*

t = 2.07 µs | *t = 2.57 µs* | *t = 8.57 µs*

Figure C.4. X-ray radiographs depicting impact of a coated SiC substrate by a spherical (1.5 mm diameter) Si_3N_4 projectile at a velocity of 322 m/s. Images were recorded at 2M frames per second with an exposure time of 200 ns. Scale bars in each frame – 500 µm.

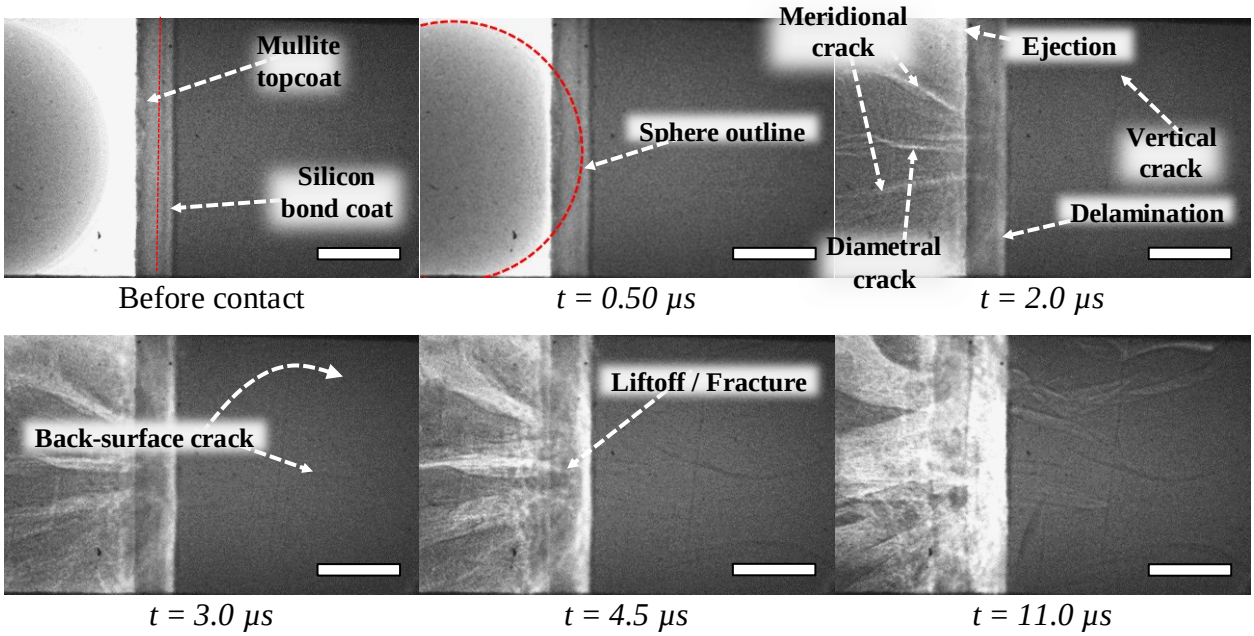

Before contact | *t = 0.50 µs* | *t = 2.0 µs*

t = 3.0 µs | *t = 4.5 µs* | *t = 11.0 µs*

Figure C.5. X-ray radiographs depicting impact of a coated SiC substrate by a spherical (1.5 mm diameter) Si_3N_4 projectile at a velocity of 355 m/s. Images were recorded at 2M frames per second with an exposure time of 200 ns. Scale bars in each frame – 500 µm.

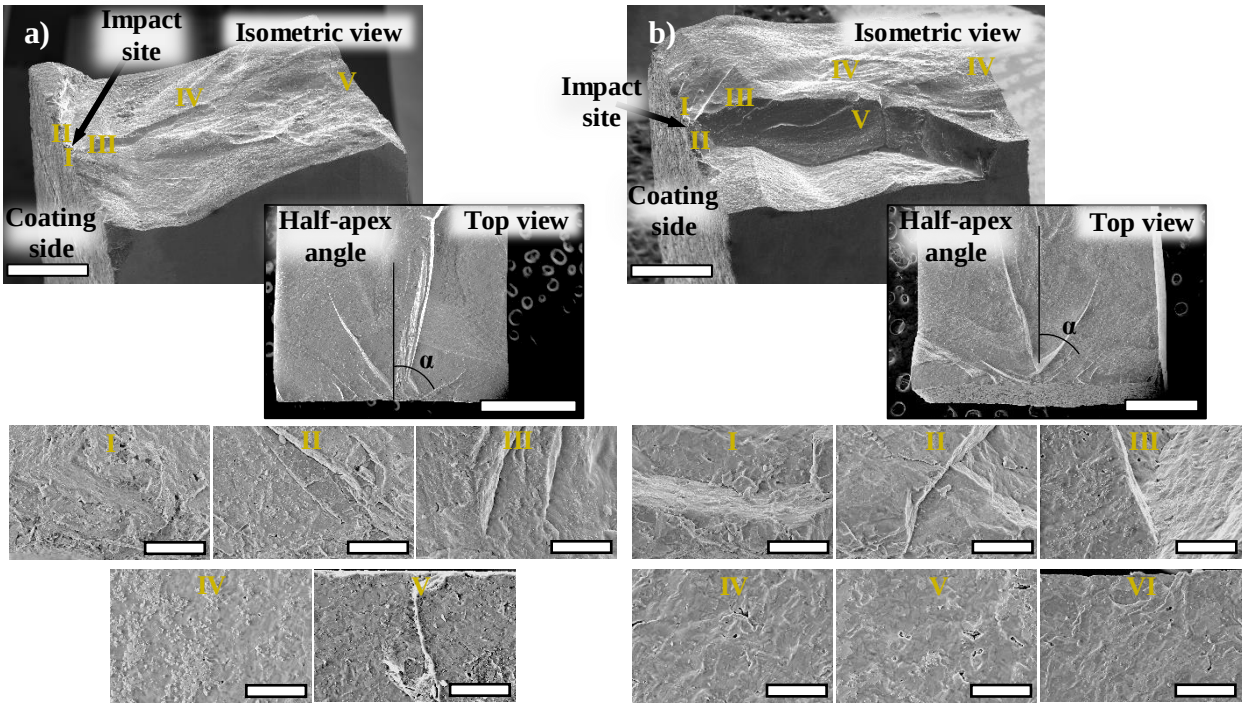

Figure C.6. Postmortem fracture surfaces of the top (a) and bottom (b) portions of the sample impacted by a PSZ projectile in Figure C.2. Scale bars for isometric and top surfaces – 1 mm. Scale bar for zoomed in surfaces – 50 μm.

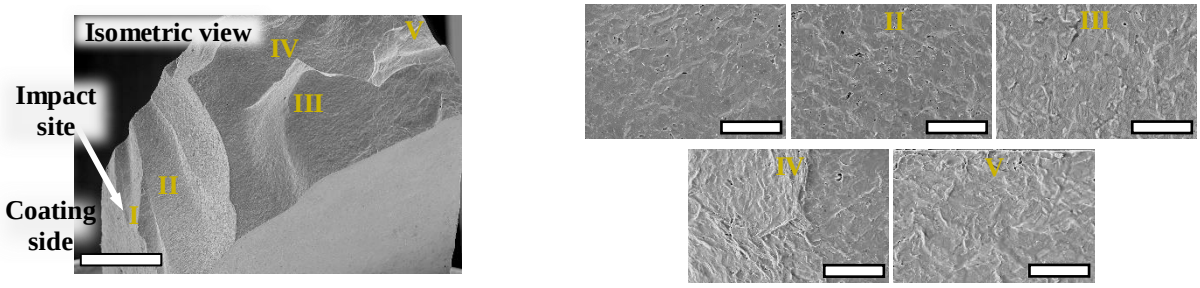

Figure C.7. Postmortem fracture surfaces of the top portion of the sample impacted by a Si_3N_4 projectile in Figure 3.10. Scale bars for isometric and top surfaces – 1 mm. Scale bar for zoomed in surfaces – 50 μm.

APPENDIX D: VICKERS INDENTATION EXPERIMENTS

The polished cross-section of the coated sample presented in Figure 4.3 (Chapter 4) was used to conduct Vickers indentation experiments. A Tukon 1202 unit (Buehler Co., Lake Bluff, IL, USA) was used to apply the indentations on the sample per the recommended procedures in ASTM C1327. Since the Vickers hardness for the SiC substrate has been reported elsewhere [136], only the mullite topcoat and silicon bond coat were examined here. ASTM C1327 recommends the use of a 1 kg load and this was attempted. However, significant crushing and fracture was observed due to the porous nature of the APS coating layers. A load of 0.2 kg was found to be the highest load which yields valid (i.e. measurable) indentations. The ramp rate to the maximum load was automatically controlled by the equipment and the time of load application (hold) before unloading was specified to be 15 s. After each indentation, a 50x filar micrometer eyepiece was available to measure the diagonals of the pyramidal imprint on the specimen. The hardness ($HV_{0.2}$) was determined using the following relation,

$$HV_{0.2} = 1.8544(P/d^2) \tag{D.1}$$

where P is the indentation load in kilograms force and d is the average of the two diagonals of indentation in millimeters. Note that the subscript in $HV_{0.2}$ corresponds to indentation load.

A total of 10 valid indentations were obtained for each of the EBC layers (silicon bond coat and mullite topcoat). The number of valid experiments was set to 10 due to the large density of porosities in the EBC which made it particularly difficult to avoid sink-in failures. Instead of the filar micrometer eyepiece, the diagonals of the indentations were also measured using SEM. This approach allowed observation of well-defined indentation edges (i.e. contrast) and thereby enabled more accurate measurements.

Figure D.1 provides representative micrographs of the indentations for the silicon bond coat and mullite topcoat. Relative to the nanoindentation evaluations (see Figure B.1, Appendix B), the larger Vickers indentations incorporate several features of the heterogeneous APS coating microstructure (i.e. porosities, microcracks, and spalt boundaries). This yields a more accurate description of the bulk material response in terms of hardness. Table D.1 provides a summary of the hardness data for each valid indentation experiment. The average hardness values for the silicon bond coat and mullite topcoat were respectively found to be 5.969±0.344 GPa and

5.418±0.696 GPa. These values are ~ 40 % lower than those reported for nanoindentation experiments (see Table B.1, Appendix B). This is due to the large sample area and hence the higher number of defects for the micro Vickers indentations.

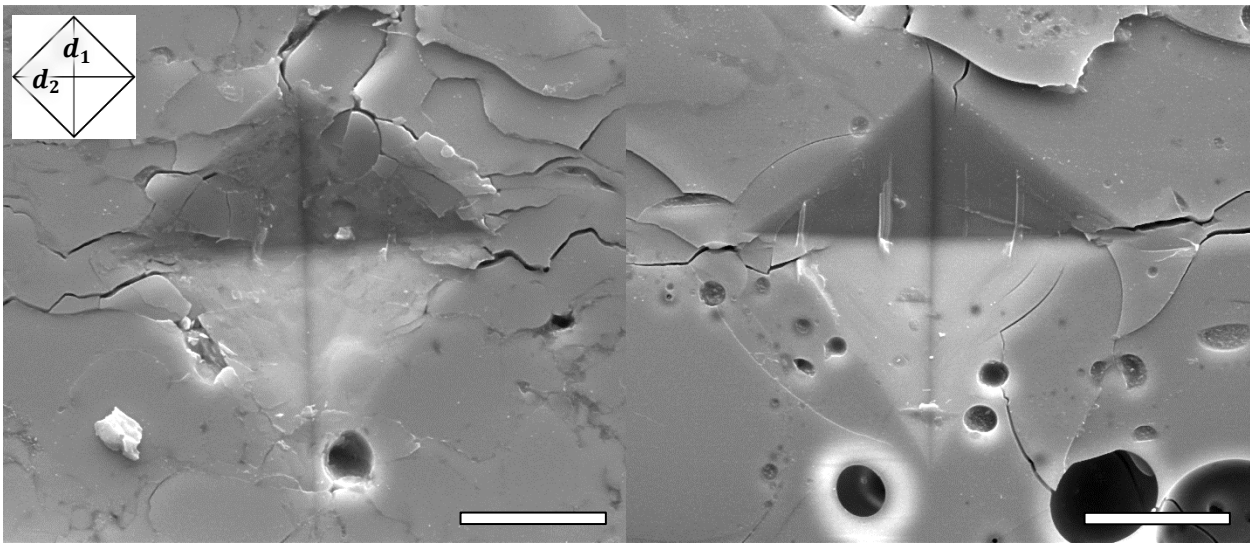

Silicon bond coat Mullite topcoat

Figure D.1. Representative micrographs of Vickers indentations for the silicon bond coat (test#4, Table D.1) and mullite topcoat (test#12, Table D.1). Scale bars in each – 10 µm.

Table D.1. Summary of Vickers indentation experiment results for the silicon bond coat and mullite topcoat.

Silicon				
test #	d1 (µm)	d2 (µm)	d_avg. (mm)	HV0.2 (GPa)
2	23.42	26.16	0.025	5.920
4	24.67	24.8	0.025	5.947
13	23.54	24.61	0.024	6.277
17	25.49	24.92	0.025	5.727
18	25.69	26.33	0.026	5.378
19	24.53	25.17	0.025	5.892
21	24.93	23.18	0.024	6.288
22	22.4	24.87	0.024	6.513
24	22.98	25.72	0.024	6.136
27	25.78	25.16	0.025	5.608
29	26.82	24.78	0.026	5.466
HV0.2_avg. (GPa)				5.969
Stdev. (GPa)				0.344

Mullite				
test #	d1 (µm)	d2 (µm)	d_avg. (mm)	HV0.2 (GPa)
10	26.12	26.68	0.026	5.220
12	26.91	26.91	0.027	5.024
14	23.24	24.53	0.024	6.378
15	27.04	26.37	0.027	5.102
19	28.17	23.9	0.026	5.368
22	25.63	25.76	0.026	5.511
27	28.52	29.43	0.029	4.334
28	22.06	24.39	0.023	6.745
29	25.16	26.21	0.026	5.515
32	26.25	27.78	0.027	4.985
HV0.2_avg. (GPa)				5.418
Stdev. (GPa)				0.696

APPENDIX E: ADDITIONAL X-RAY RADIOGRAPHS FOR IMPACT OF NARROW COATED CERAMIC SPECIMENS (CHAPTER 4)

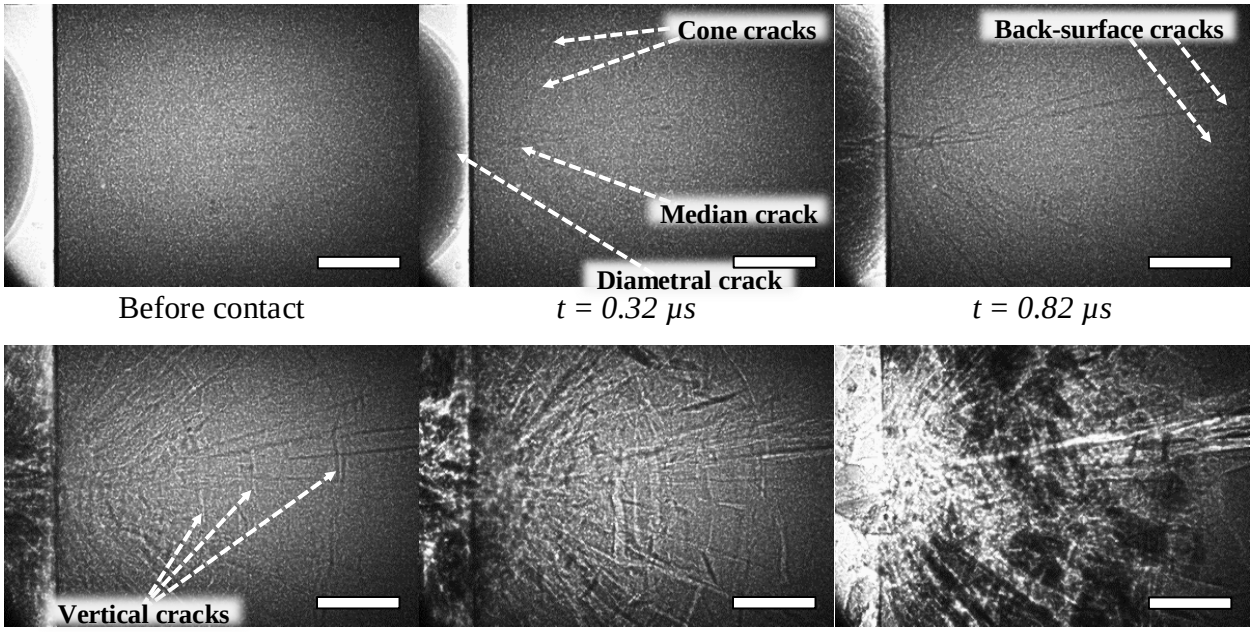

Before contact | *t = 0.32 µs* | *t = 0.82 µs*

t = 1.82 µs | *t = 5.82 µs* | *t = 34.82 µs*

Figure E.1. Pulsed X-ray radiographs of FOD impact in a narrow uncoated SiC substrate by a 1.5 mm diameter Si_3N_4 sphere at a velocity of 368.2 m/s. Images were recorded at 2M frames per second with an exposure time of 200 ns. Scale bars in each frame – 500 µm.

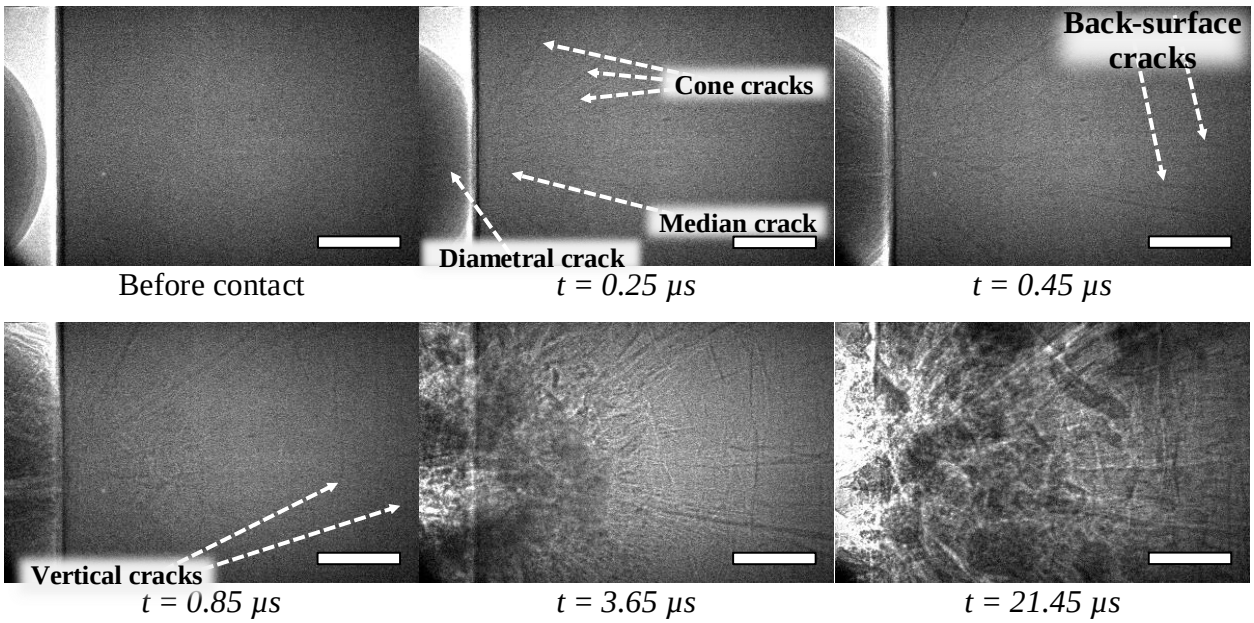

Figure E.2. Pulsed X-ray radiographs of FOD impact in a narrow uncoated SiC substrate by a 1.5 mm diameter Si_3N_4 sphere at a velocity of 389.2 m/s. Images were recorded at 5M frames per second with an exposure time of 110 ns. Scale bars in each frame – 500 µm.

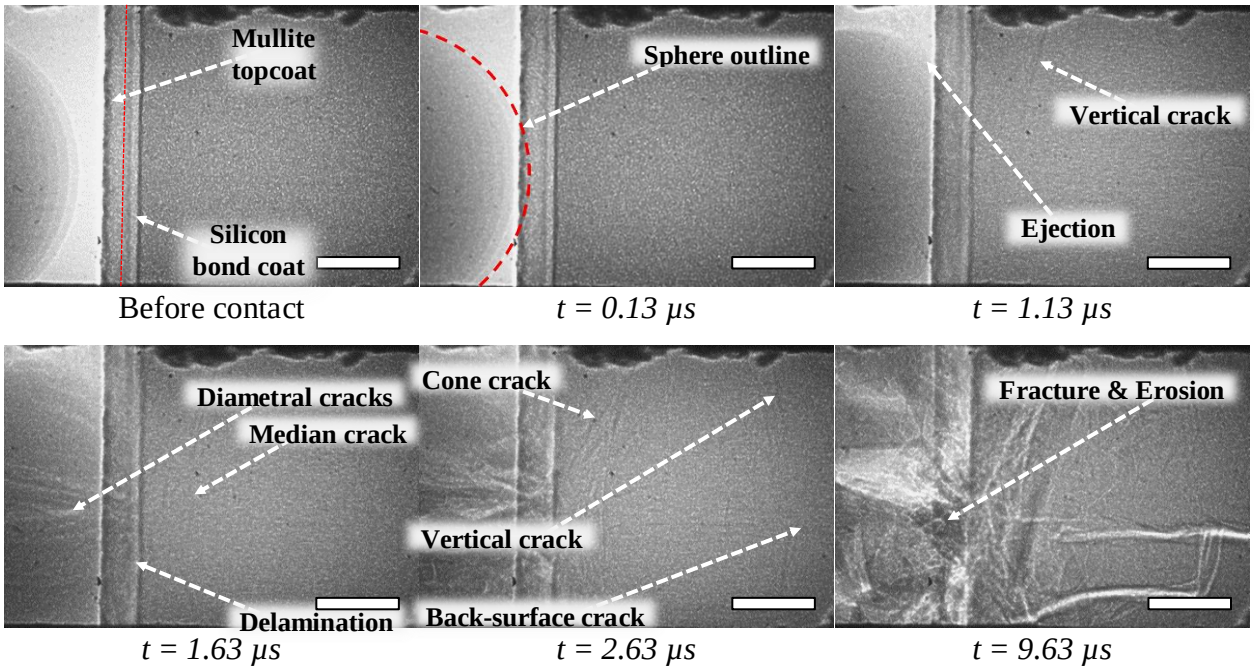

Figure E.3. Pulsed X-ray radiographs of FOD impact in a narrow coated SiC substrate by a 1.5 mm diameter Si_3N_4 sphere at a velocity of 380.1 m/s. Images were recorded at 2M frames per second with an exposure time of 200 ns. Scale bars in each frame – 500 µm.

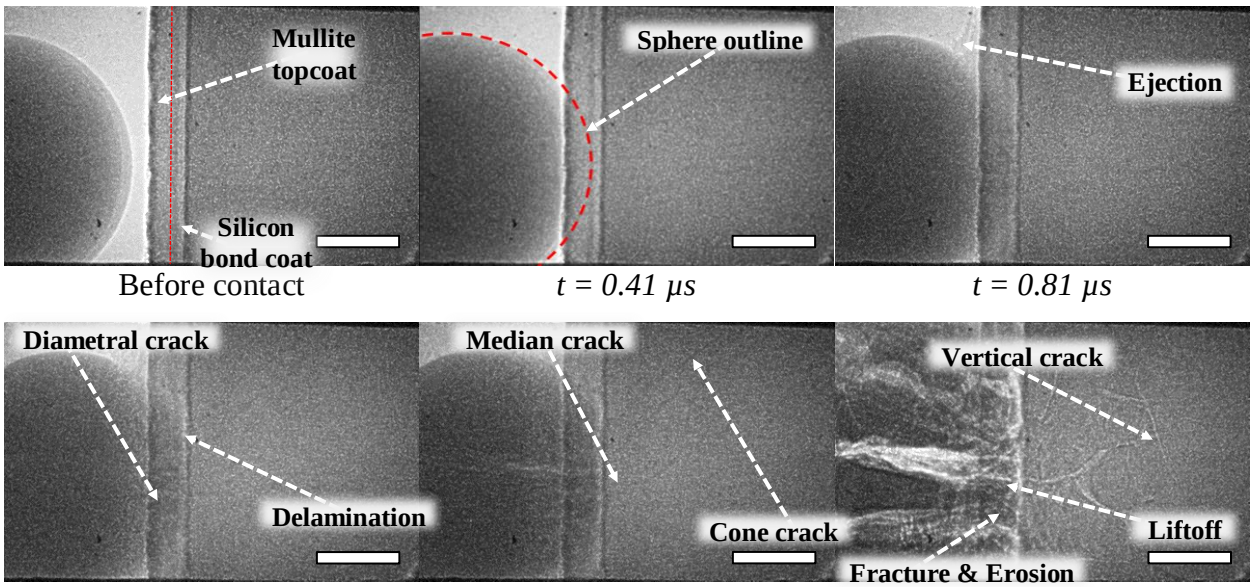

Before contact | *t = 0.41 µs* | *t = 0.81 µs*

t = 1.01 µs | *t = 1.41 µs* | *t = 4.21 µs*

Figure E.4. Pulsed X-ray radiographs of FOD impact in a narrow coated SiC substrate by a 1.5 mm diameter Si_3N_4 sphere at a velocity of 375.8 m/s. Images were recorded at 5M frames per second with an exposure time of 110 ns. Scale bars in each frame – 500 µm.

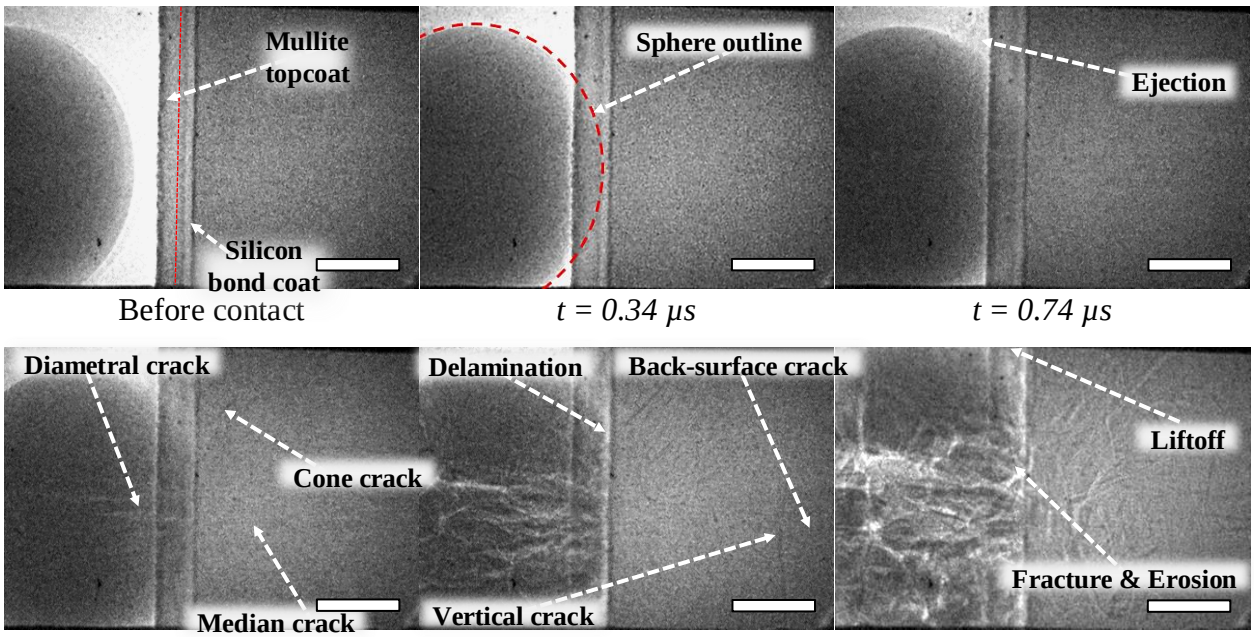

Before contact | *t = 0.34 µs* | *t = 0.74 µs*

t = 0.94 µs | *t = 1.34 µs* | *t = 3.74 µs*

Figure E.5. Pulsed X-ray radiographs of FOD impact in a narrow coated SiC substrate by a 1.5 mm diameter Si_3N_4 sphere at a velocity of 388.4 m/s. Images were recorded at 5M frames per second with an exposure time of 110 ns. Scale bars in each frame – 500 µm.

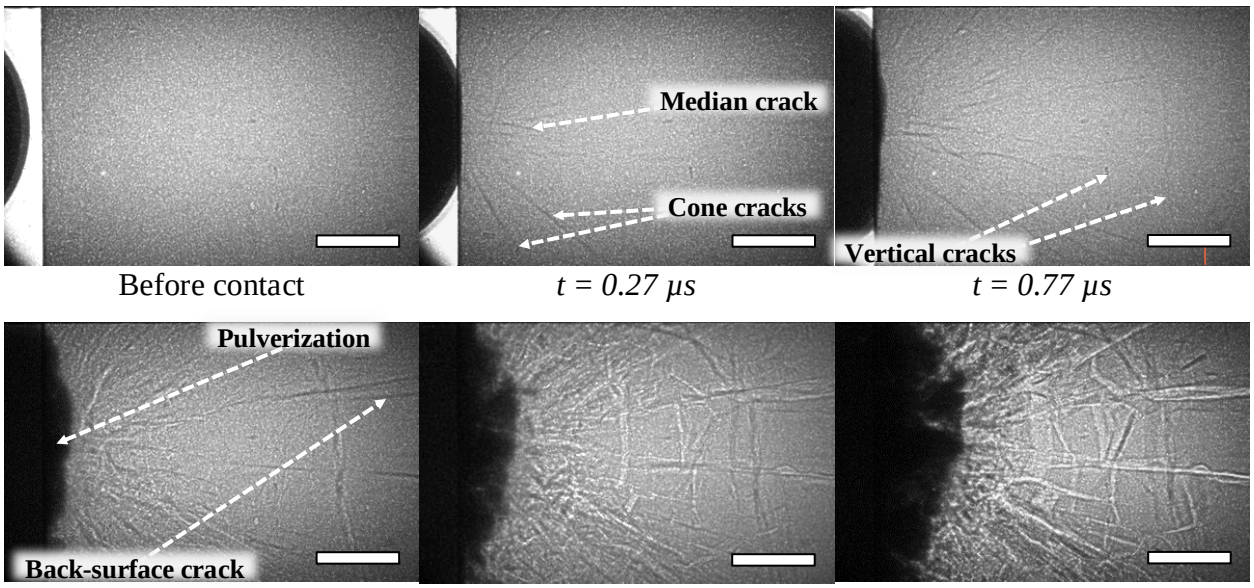

Before contact | *t = 0.27 µs* | *t = 0.77 µs*

t = 1.77 µs | *t = 3.77 µs* | *t = 5.77 µs*

Figure E.6. Pulsed X-ray radiographs of FOD impact in a narrow uncoated SiC substrate by a 1.5 mm diameter PSZ sphere at a velocity of 326.7 m/s. Images were recorded at 2M frames per second with an exposure time of 200 ns. Scale bars in each frame – 500 µm.

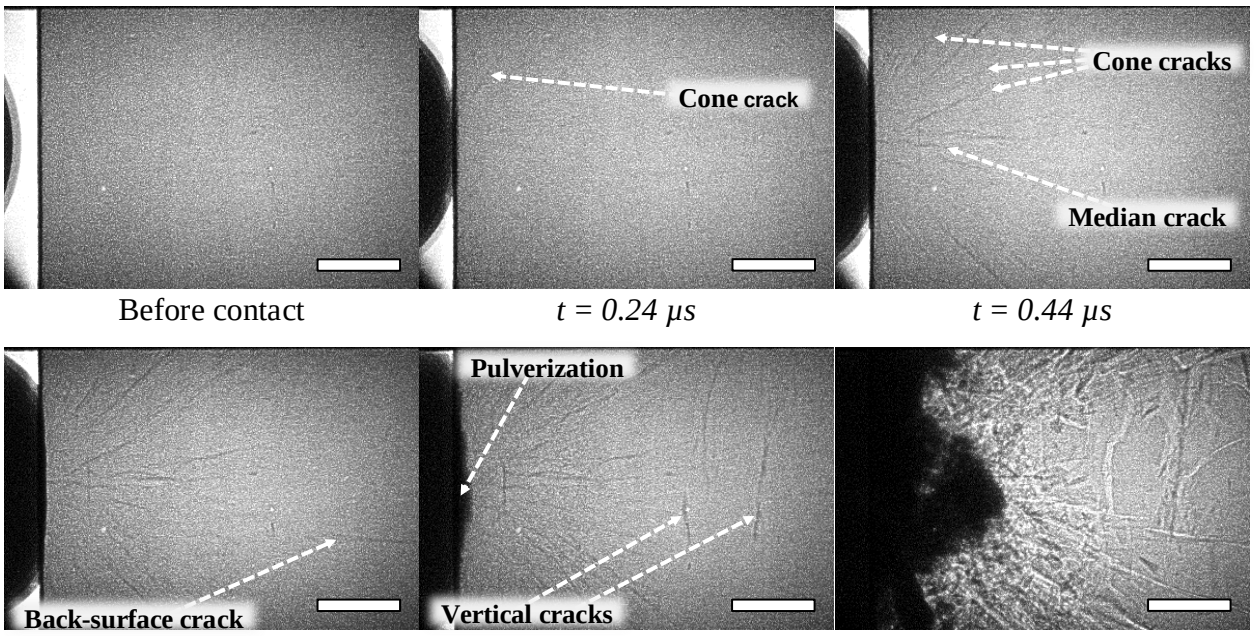

Before contact | *t = 0.24 µs* | *t = 0.44 µs*

t = 0.64 µs | *t = 1.04 µs* | *t = 7.84 µs*

Figure E.7. Pulsed X-ray radiographs of FOD impact in a narrow uncoated SiC substrate by a 1.5 mm diameter PSZ sphere at a velocity of 327.8 m/s. Images were recorded at 5M frames per second with an exposure time of 110 ns. Scale bars in each frame – 500 µm.

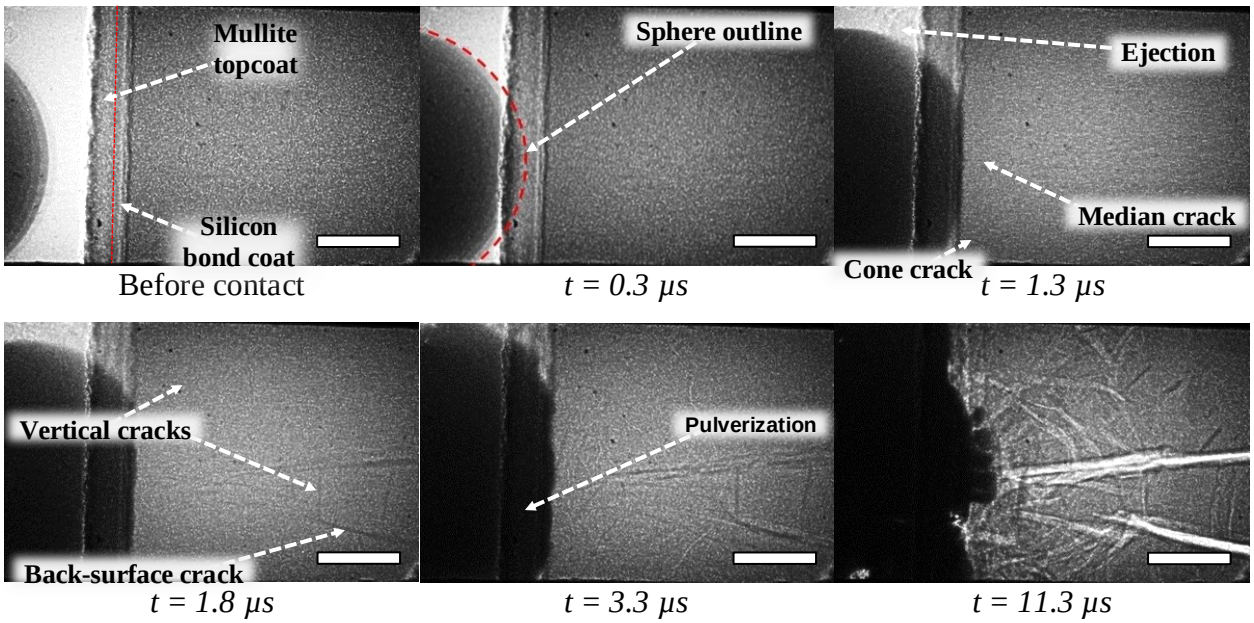

Figure E.8. Pulsed X-ray radiographs of FOD impact in a narrow coated SiC substrate by a 1.5 mm diameter PSZ sphere at a velocity of 306.4 m/s. Images were recorded at 2M frames per second with an exposure time of 200 ns. Scale bars in each frame – 500 µm.

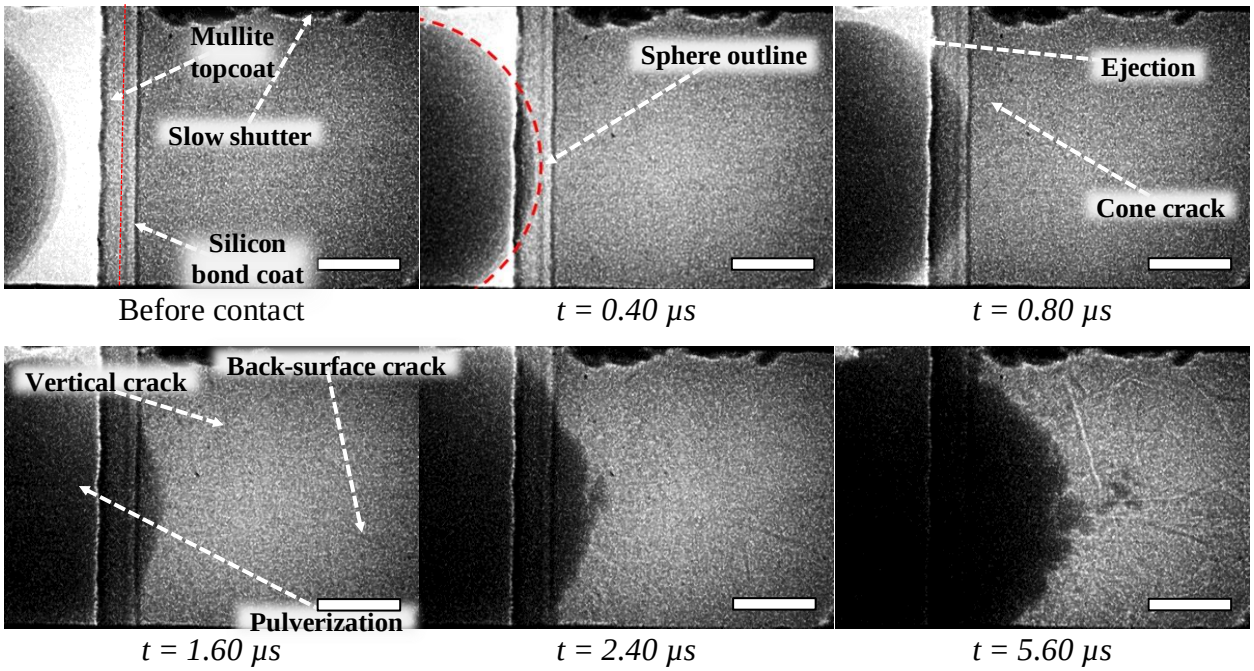

Figure E.9. Pulsed X-ray radiographs of FOD impact in a narrow coated SiC substrate by a 1.5 mm diameter PSZ sphere at a velocity of 341.3 m/s. Images were recorded at 5M frames per second with an exposure time of 110 ns. Scale bars in each frame – 500 µm.

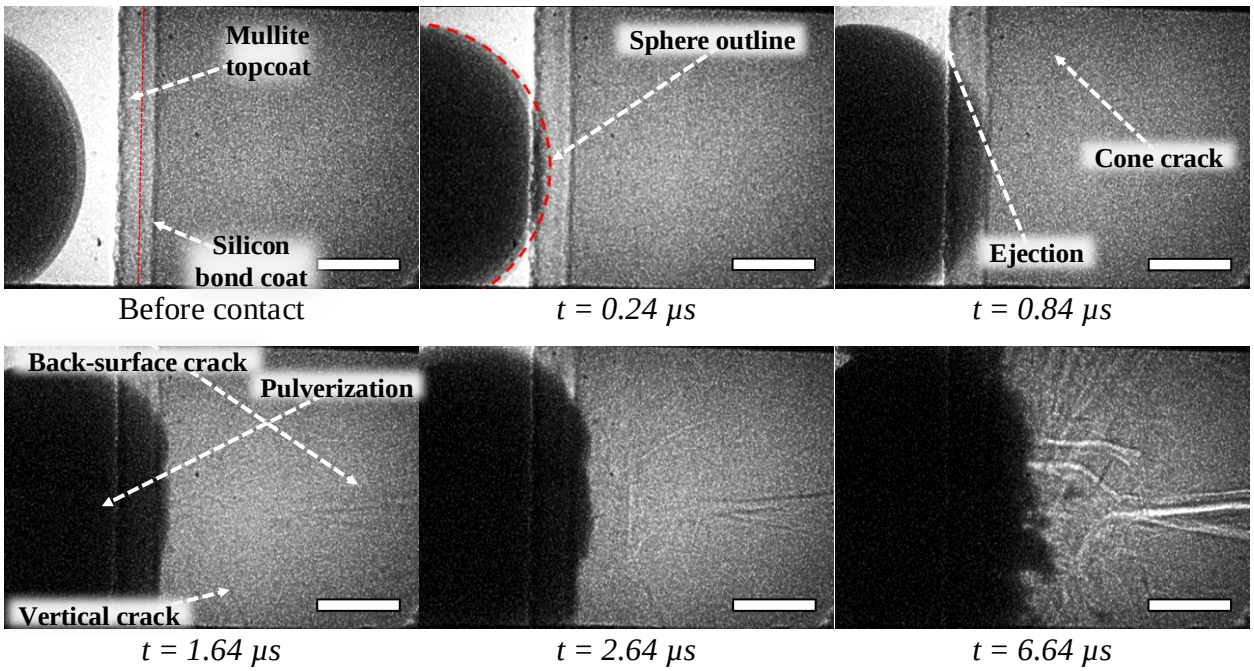

Before contact | *t = 0.24 μs* | *t = 0.84 μs*

t = 1.64 μs | *t = 2.64 μs* | *t = 6.64 μs*

Figure E.10. Pulsed X-ray radiographs of FOD impact in a narrow coated SiC substrate by a 1.5 mm diameter PSZ sphere at a velocity of 330.2 m/s. Images were recorded at 5M frames per second with an exposure time of 110 ns. Scale bars in each frame – 500 μm.

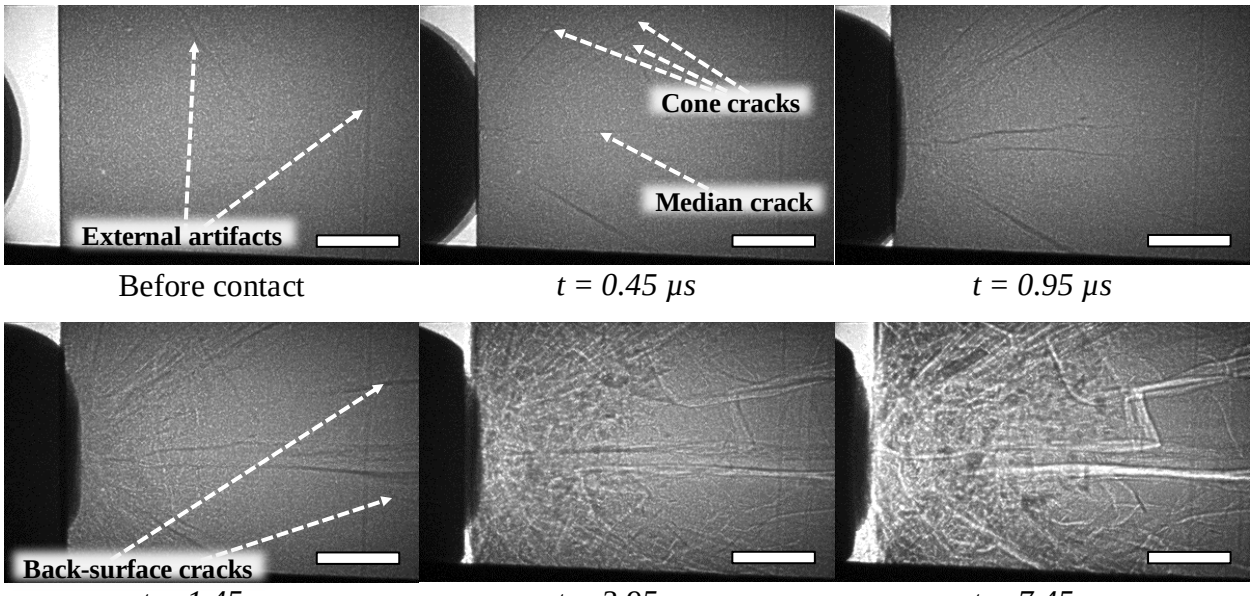

Before contact | *t = 0.45 μs* | *t = 0.95 μs*

t = 1.45 μs | *t = 3.95 μs* | *t = 7.45 μs*

Figure E.11. Pulsed X-ray radiographs of FOD impact in a narrow uncoated SiC substrate by a 1.5 mm diameter Steel sphere at a velocity of 326.3 m/s. Images were recorded at 2M frames per second with an exposure time of 200 ns. Scale bars in each frame – 500 μm.

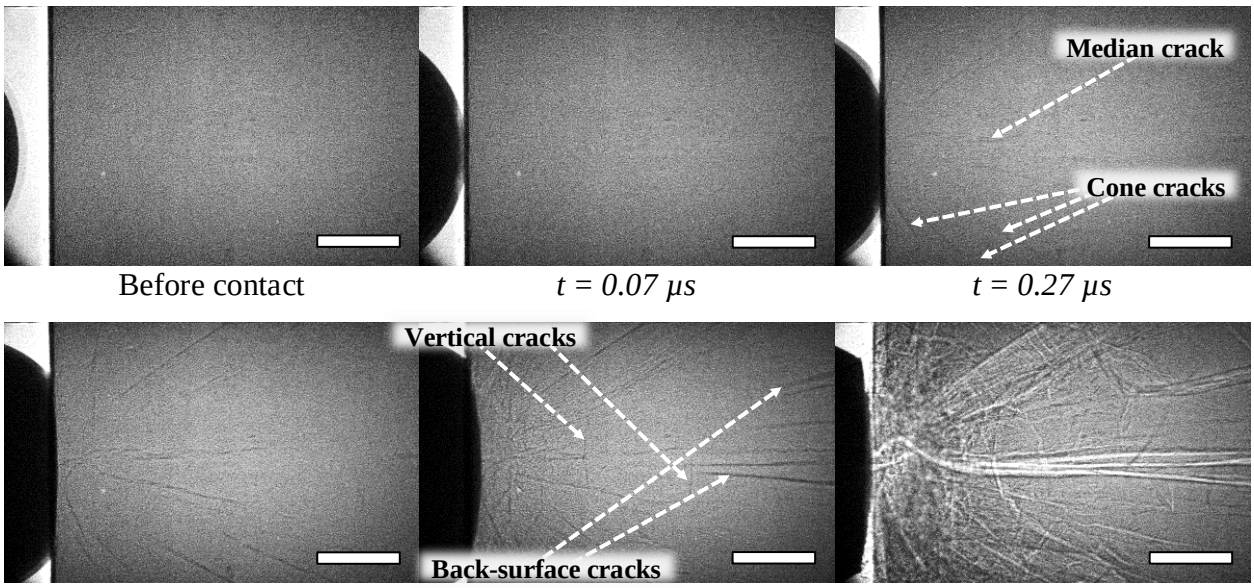

Figure E.12. Pulsed X-ray radiographs of FOD impact in a narrow uncoated SiC substrate by a 1.5 mm diameter Steel sphere at a velocity of 317.1 m/s. Images were recorded at 5M frames per second with an exposure time of 110 ns. Scale bars in each frame – 500 µm.

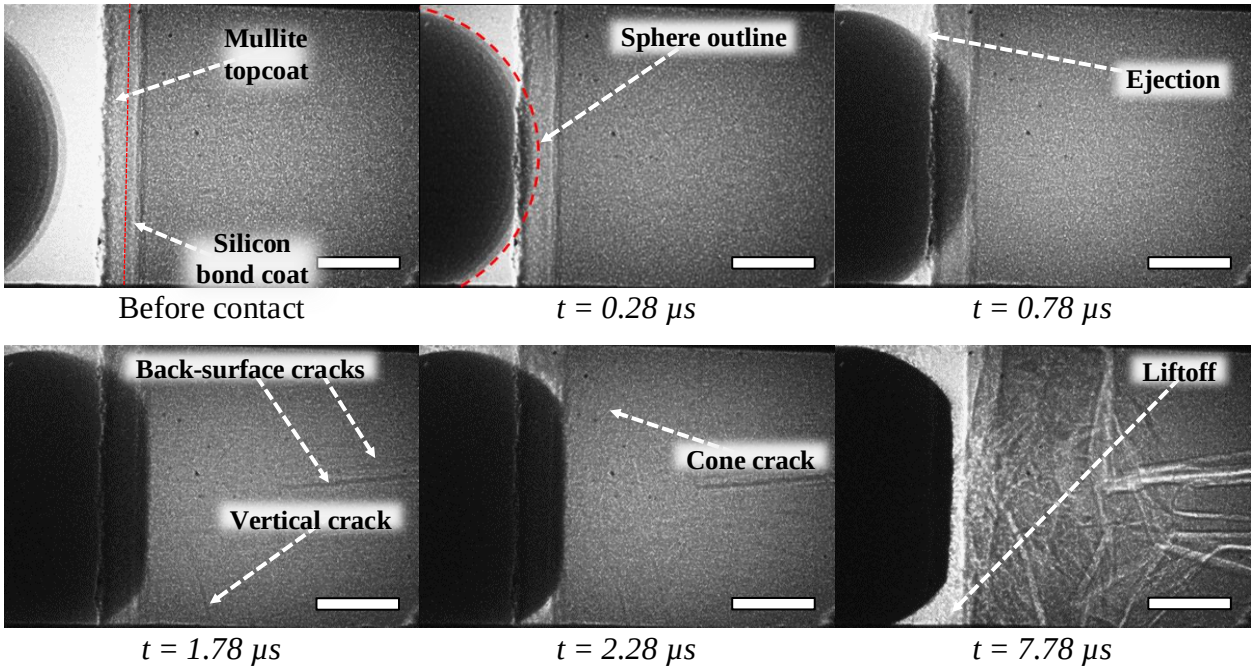

Figure C.13. Pulsed X-ray radiographs of FOD impact in a narrow coated SiC substrate by a 1.5 mm diameter Steel sphere at a velocity of 322.6 m/s. Images were recorded at 2M frames per second with an exposure time of 200 ns. Scale bars in each frame – 500 µm.

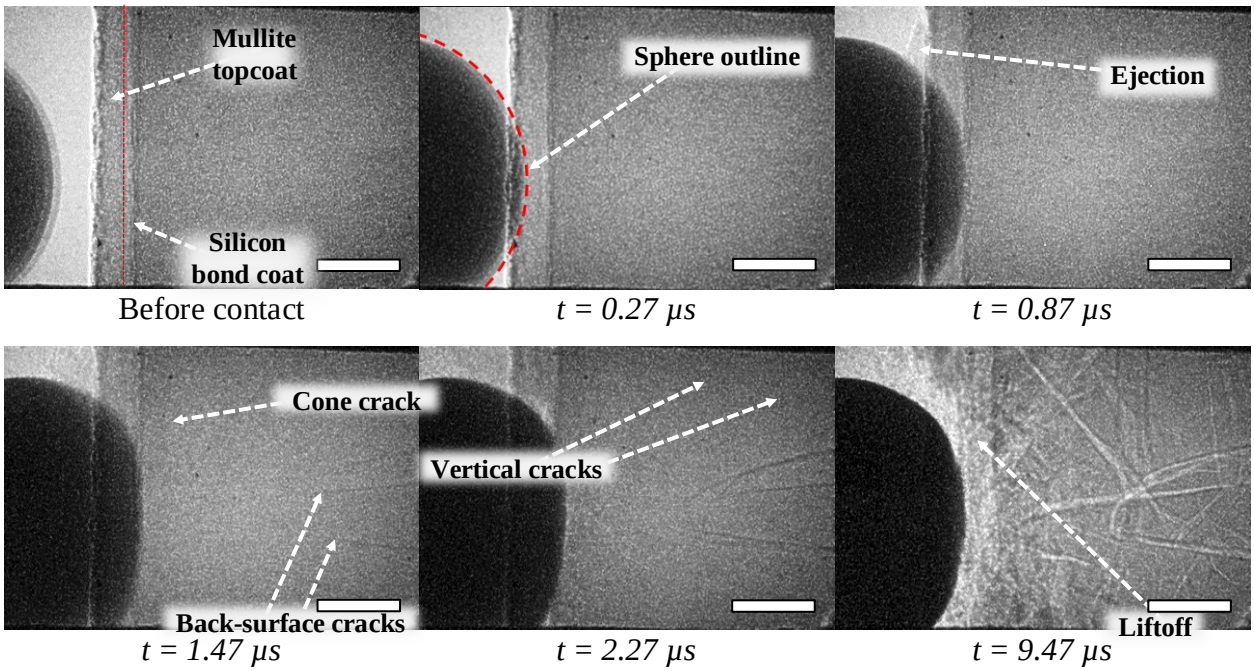

Figure E.14. Pulsed X-ray radiographs of FOD impact in a narrow coated SiC substrate by a 1.5 mm diameter Steel sphere at a velocity of 302.4 m/s. Images were recorded at 5M frames per second with an exposure time of 110 ns. Scale bars in each frame – 500 µm.

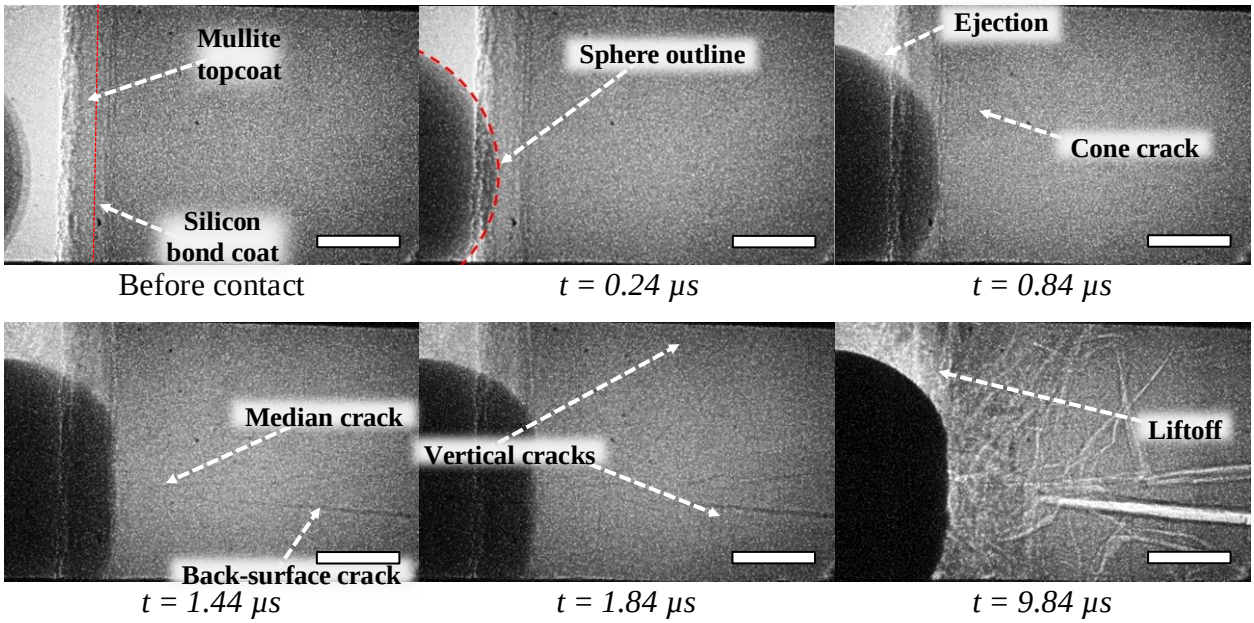

Figure E.15. Pulsed X-ray radiographs of FOD impact in a narrow coated SiC substrate by a 1.5 mm diameter Steel sphere at a velocity of 321.4 m/s. Images were recorded at 5M frames per second with an exposure time of 110 ns. Scale bars in each frame – 500 µm.

a)

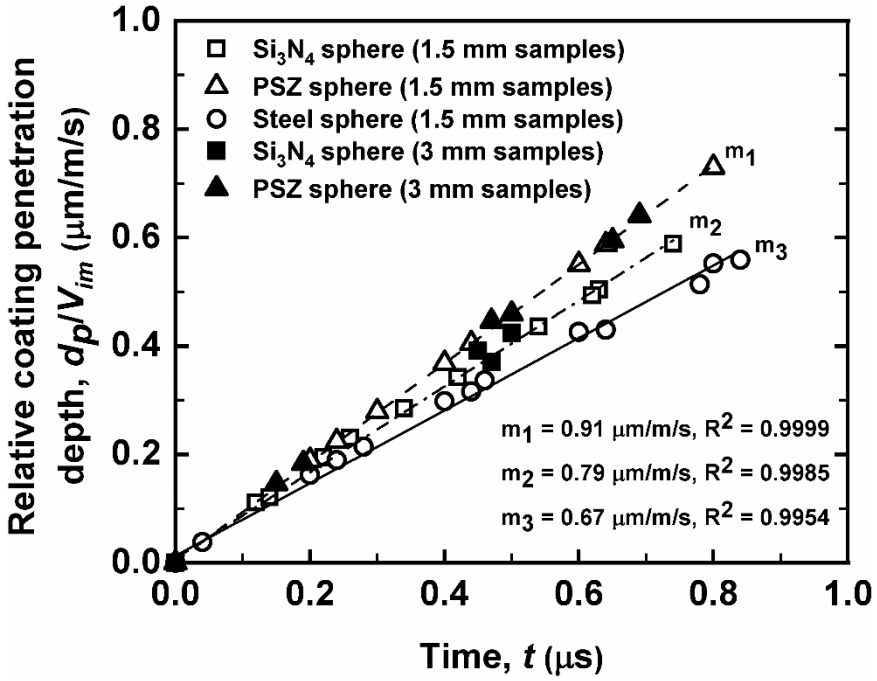

b)

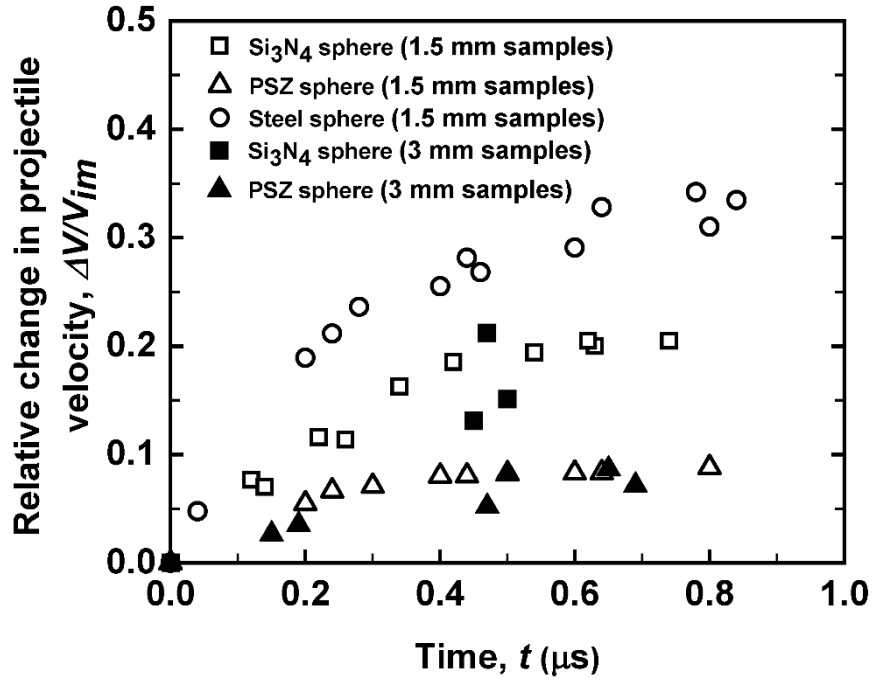

Figure E.16. X-ray radiography based determinations of relative coating penetration depth (a) and relative change in impactor velocity (b) as a function of time for both narrow (1.5 mm) and wide (3 mm) specimens.

REFERENCES

1. McCollum D, Gould G, Green D. Greenhouse gas emissions from aviation and marine transportation: mitigation potential and policies. 2009. Pew Center on Global Climate change. Solutions white paper series. https://escholarship.org/uc/item/5nz642qb.

2. Electricity – World Energy Outlook 2019 – Analysis [Internet]. IEA. 2019 [cited 2020Dec28]. Available from: https://www.iea.org/reports/world-energy-outlook-2019/electricity

3. Langston LS. Aspects of gas turbine thermal efficiency. Mech Eng. 2020;142(9):54-55.

4. Kotowicz J, Brzeczek M, Job M. The thermodynamic and economic characteristics of the modern combined cycle power plant with gas turbine steam cooling. Energy. 2018;164:359-376.

5. Epstein AH, O'Flarity SM. Considerations for reducing aviation CO_2 with aircraft electric propulsion. J Propuls Power. 2019;35(3):572-582.

6. Commercial aircraft propulsion and energy systems research: reducing global carbon emissions. Washington, DC: National Academies of Sciences, Engineering, and Medicine; 2016. The National Academies Press. doi:10.17226/23490

7. Zhu D, Harder B, Fox DS. Advanced processing and environmental barrier coating system development for SiC/SiC ceramic matrix composites. Symposium session presented at: Coatings to protect materials from extreme environments, Materials Science and Technology Conference and Exhibition; 2011 Oct 16-20; Columbus, OH.

8. Ohnabe H, Masaki S, Onozuka M, Miyahara K, Sasa T. Potential application of ceramic matrix composites to aero-engine components. Comp A. 1999;30(4):489-496.

9. Conway HM. The possible use of ceramic materials in aircraft propulsion systems. Langley Field: National Advisory Committee for Aeronautics; 1944. Langley Memorial Aeronautical Laboratory. Wartime Report. NACA-CB No.4D10.

10. Gangler JJ. Some physical properties of eight refractory oxides and carbides. J Am Ceram Soc. 1950;33(12):367-374.

11. Majumdar BL. Ceramic materials in high temperature hear engines: a review. Trans Indian Cram Soc. 1953;12(2):1-26.

12. Pechman A, Ceramics for high-temperature applications: a survey of materials used as coatings for, or in combustion with, metals. Aircr Eng Aerosp Tec. 1954;26(5):157-160.

13. Jacobson NS, Fox DS, Smialek JL, Opila E, Tortorelli PF, More KL, Nickel KG, Hirata T, Yoshida M, Yuri I. Corrosion issues for ceramics in gas turbines. Cleveland: NASA Glen Research Center; 2000. Technical Report / Preprint. No. 2001006139.

14. Richardson DW. Ceramic components in gas turbine engines: why has it taken so long?. Ceram Eng Sci Proc. 2004; 25(3):3-32.

15. Larson DC. Property screening and evaluation of ceramic turbine engine materials. Dayton: Airforce Materials Laboratory; 1984. Wright-Paterson Air Force Base, Air Force Systems Command. Final Technical Report. AFML-TR-83-4141.

16. Lindley MW, Godfrey DJ. Silicon nitride ceramic composites with high toughness. Nature. 1971;229:192-193.

17. Hoffmann MJ, Petzow G. ailored microstructure of silicon nitride ceramics. Pure & Appl Chem. 1994;66(9):1807-1814.

18. Cao JJ, MoberlyChan WJ, De Jonghe LC, Gilbert CJ, Ritchie RO. In situ toughened silicon carbide with Al-B-C additions. J Am Ceram Soc. 1996;79(2):461-469.

19. Corman GS, Luthra KL. Silicon melt infiltrated ceramic composites (HiPerComp^{TM}). In: Bansal NP, ed. Handbook of ceramic composites. Boston: Kluwer Academic Publishers, 2005; p. 99-115.

20. Kopeliovich D. Advances in the manufacturing of ceramic matrix composites using infiltration techniques. In: Low IM, ed. Advances in ceramic matrix composites. Philadelphia: Woodhead Publishing Ltd, 2014; p.79-108.

21. Lamon J. Chemical vapor infiltrated SiC/SiC composites (CVI SiC/SiC). In: Bansal NP, ed. Handbook of ceramic composites. Boston: Kluwer Academic Publishers, 2005; p.149-171.

22. Luo Z, Zhou X, Yu J. Sun K, Wang F. Mechanical properties of SiC/SiC composites fabricated by PIP process with a new precursor polymer. Ceram Int. 2014;40(1):1939-1944.

23. Hanjo K, Hashimoto R, Ogiyama H. Current status if 300 kW industrial ceramic gas turbine R&D in japan. J Eng Gas Turbines Power. 1993;115(1):51-57.

24. Shimada K, Ushijima H, Yabe A, Ogiyama H, Tsutsui Y. Advanced ceramic technology development for industrial 300 kW CGT (ceramic gas turbine) research and development project in japan. Proceedings of the ASME 1993 International Gas Turbine and Aeroengine Congress and Exhibition. New York, NY: American Society of Mechanical Engineers; 1993: p.1-6 (V03AT15A039).

25. Sakakida M, Sasa T, Akiyama K, Tanaka S. 300 kW class ceramic gas turbine development (CGT 301). Proceedings of the ASME 1994 International Gas Turbine and Aeroengine Congress and Exhibition. New York, NY: American Society of Mechanical Engineers; 1994: p.1-7 (V001T04A002).

26. Takehara I, Inobe I, Tatsumi T, Ichikawa Y, Kobayashi H. Research and development of ceramic gas turbine (CGT302). J Eng Gas Turbines Power. 1998;120(1):186-190.

27. Van Roode M, Brentnall WD, Norton PF, Boyd GL. Ceramic stationary gas turbine development program–first annual summary. Proceedings of the ASME 1994 International Gas Turbine and Aeroengine Congress and Exhibition. New York, NY: American Society of Mechanical Engineers; 1994: p.1-13 (V005T13A003).

28. Van Roode M, Brentnall WD, Smith KO, Edwards BD, Faulder LJ, Norton PF. Ceramic stationary gas turbine development program–third annual summary. Proceedings of the ASME 1996 International Gas Turbine and Aeroengine Congress and Exhibition. New York, NY: American Society of Mechanical Engineers; 1996: p.1-14 (V005T13A027).

29. Price J, Jimenez O, Miriyala N, Kimmel JB, Leroux D, Fahme T. Ceramic stationary gas turbine development program–eighth annual summary. Proceedings of the ASME Turbo Expo 2001: Power for Land, Sea, and Air. New York, NY: American Society of Mechanical Engineers; 2001: p. 1-11 (V004T02A014).

30. Nagata H, Karasawa W, Ichikawa Y, Tsuruzono S, Fukudome T. Development of the 8000 kW class hybrid gas turbine. Proceedings of the ASME Turbo Expo 2003: Power for Land, Sea, and Air. New York, NY: American Society of Mechanical Engineers; 2003: p. 613-619 (GT2003-38703).

31. Price JR. Advanced materials for mercury 50 gas turbine combustion system. San Diego: Solar Turbines Inc; 2008. U.S. Department of Energy. Final Report. No. SR01-R-6187-25.

32. Van Roode M. Ceramic gas turbine development: need for a 10 year plan. J Eng Gas Turbines Power. 2010;132(1):011301(1-8).

33. Fellet M, Rossner W. Ceramic-matrix composites take the heat. MRS Bull. 2015;40(11):916-918.

34. Glenny E, Taylor TA. Mechanical strength and thermal fatigue characteristics of silicon nitride. Powder Metall. 1961;4(8):164-195.

35. Marshal P, Jones RB. Creep of silicon carbide. Powder Metall. 1969;12(23):193-208.

36. Lane JE, Carter CH, Davis RF. Kinetics and mechanisms of high temperature creep in silicon carbide: III sintered α-silicon carbide. J Am Ceram Soc. 1988;71(4):281-295.

37. Godfrey DJ, Parr NL. A consideration of the possible use of refractory ceramic materials for advanced combustion chamber design. In: Smith IE, ed. Combustion in Advanced Gas Turbine Systems. Oxford: Pergamon Press Ltd, 1968; p.379-395.

38. Brooks A, Bellin AI. Benefits of ceramics to gas turbines. Proceedings of the 49th Meeting of the AGARD Structures and Materials Panel. London, UK: Technical Editing and Reproduction Ltd; 1980: p.27-51.

39. Marshal DB, Cox BN. Integral textile ceramic structures. Annu Rev Mater Res. 2008;38:425-443.

40. Dever JA, Nathal MV, DiCarlo JA. Research on high-temperature aerospace materials at NASA Glen Research Center. J Aero Eng. 2013;26(2):500-514.

41. Almansour AS, Morscher GN. Tensile creep behavior of SiC_f/SiC ceramic matrix minicomposites. J Euro Ceram Soc. 2020;40(15):5132-5146.

42. Ladeveze P, Genet M. A new approach to the subcritical cracking of ceramic fibers. Comp Sci Technol. 2010;70(11):1575-1583.

43. Jacobson NS. Corrosion of silicon-based ceramics in combustion environments. J Am Ceram Soc. 1993;76(1):3-28.

44. Tressler RE, Meiser MD, Yonushonis T. Molten salt corrosion of SiC and Si_3N_4 ceramics. J Am Ceram Soc. 1976;59(5-6):278-279.

45. Jacobson NS, Smialek JL. Corrosion pitting of SiC by molten salts. J Electrochem Soc. 1986;133:2615-2621.

46. Jacobson NS, Stearns CA, Smialek JL. Burner rig corrosion of SiC at 1000 °C. Adv Ceram Mat. 1988;1:154-161.

47. Jacobson NS. Sodium sulfate: deposition and dissolution of silica. Oxid Met. 1989;31:91-103.

48. Jacobson NS, Smialek JL, Fox DS. Molten salt corrosion of SiC and Si_3N_4. In: Cheremisinoff NP, ed. Handbook of ceramics and composites volume I. synthesis and properties. New York: Marcel Dekker, 1990; p.99-137.

49. Deal BE, Grove AS. General relationship for the thermal oxidation of silicon. J Appl Phys. 1965;36:3770-3778.

50. Opila EJ. Variation of the oxidation rate of silicon carbide with water-vapor pressure. J Am Ceram Soc. 1999;82(3):625-636.

51. Opila EJ, Fox DS, Jacobson NS. Mass spectrometric identification of Si-O-H(g) species from the reaction of silica with water vapor at atmospheric pressure. J Am Ceram Soc. 1997;80(4):1009-1012.

52. Opila EJ, Smialek JL, Robinson RC, Fox DS, Jacobson NS. SiC recession caused by SiO_2 scale volatility under combustion conditions: II, thermodynamics and gaseous diffusion model. J Am Ceram Soc. 1999;82(7):1826-1834.

53. Morscher GN. Stress environmental effects on fiber reinforced SiC based composites. In: Bansal NP, Lamon J, eds. Ceramic matrix composites: materials, modeling and technology. New Jersey: John Wiley & Sons Inc., 2015; p.334-352.

54. Herweyer LA, Opila EJ. Na_2SO_4 deposit-induced hot corrosion of BN-coated α-SiC. J Am Ceram Soc, 2020;104(3):1539-1553.

55. Bhatt RT, Choi SR, Cosgriff LM, Fox DS, Lee KN. Impact resistance of uncoated SiC/SiC composites. Mater Sci Eng A. 2008:476(1-2):20-28.

56. Nicholls JR, Jaslier Y, Rickerby DS. Erosion and foreign object damage of thermal barrier coatings. Mater Sci Forum. 1997;251-254:935-948.

57. Takehara I, Tatsumi T, Ichikawa Y. Summary of CGT302 ceramic gas turbine reaserch and development program. J Eng Gas Turbines Power. 2002;124(3):627-635.

58. Van Roode M, Price J, Kimmel J, Miriyala N, Leroux D, Fahme A, et al. Ceramic matrix combustor liners: a summary of field evaluations. J Eng Gas Turbines Power. 2005;129(1):21-30.

59. Federer JI. Alumina base coatings for protection of SiC ceramics. J Mater Eng. 1990;12:141-149.

60. Price JR, Van Roode M, Stala C. Ceramic oxide coated silicon carbide for high temperature corrosive environments. Key Eng Mater. 1992;72-74:71-84.

61. Lee KN, Fox DS, Bansal NP. Rare earth silicate environmental barrier coatings for SiC/SiC composites and Si_3N_4 ceramics. J Euro Ceram SoC. 2005;25(10):1705-1715.

62. Lee KN, Miller RA, Jacobson NS. New generation of plasma-sprayed mullite coatings on silicon carbide. J Am Ceram Soc. 1995;78(3):705-710.

63. Jacobson NS, Lee KN, Yoshio T. Corrosion of mullite by molten salts. J Am Ceram Soc. 1996;79(8):2161-2167.

64. Lee KN. Key durability issues with mullite-based environmental barrier coatings for Si-based ceramics. J Eng Gas Turbines Power. 2000;122(4):632-636.

65. Lee KN, Miller RA. Development and environmental barrier durability of mullite and mullite/YSZ dual layer coatings for SiC and Si_3N_4 ceramics. Surf Coat Technol. 1996;86-87:142-148.

66. Lee KN, Miller RA. Durability of mullite/YSZ-coated SiC in 90% H2O/O2. In: Singh JP, Bansal NP, eds. Advances in Ceramic Matrix Composites IV: Ceramic Transactions. Westerville: The American Ceramic Society,1999; p.17-25.

67. Lee KN. Degradation of environmental barrier coatings (EBCs) due to chemical and thermal expansion incompatibility. In: McNallan M, Opila E, eds. High temperature corrosion and materials chemistry III. Pennington: The Electrochemical Society, Inc. 2001; p.124-135.

68. Lee KN. Current Status of environmental barrier coatings for Si-based ceramics. Surf Coat Technol. 2000;133-134:1-7.

69. Lee KN, Fox DS, Eldridge JI, Zhu D, Robinson RC, Bansal NP, Miller RA. Upper temperature limit of environmental barrier coatings based on mullite and BSAS. J Am Ceram Soc. 2003;86(8):1299-1306.

70. Lee KN, Eldridge JI, Robinson RC. Residual stress and their effects on the durability of environmental barrier coatings for SiC ceramics. J Am Ceram Soc. 2005;88(12):3483-3488.

71. Richards BT, Wadley HNG. Plasma spray deposition of tri-layer environmental barrier coatings. J Euro Ceram Soc. 2014;34(12):3069-3083.

72. Richards BT, Begley MR, Wadley HNG. Mechanisms of ytterbium monosilicate/mullite/silicon coating failure during thermal cycling. J Am Ceram Soc. 2015;98(12):4066-4075.

73. Richards BT, Young KA, Francqueville F de, Sehr S, Begley MR, Wadley HNG. Response of ytterbium disilicate-silicon environmental barrier coatings to thermal cycling in water vapor. Acta Mater. 2016;106:1-14.

74. Richards BT, Zhu D, Ghosn LJ, Wadley HNG. Mechanical properties of air plasma sprayed environmental barrier coating (EBC) systems: preliminary assessment. In: Kriven WM, Wang J, Zhu D, Fischer T, eds. Developments in Strategic Ceramic Materials. Hoboken: John Wiley and Sons, Inc., 2016; p.219-238.

75. Zhu D, Harder B, Hurst JB, Good B, Costa G. Development of advanced environmental barrier coatings for SiC/SiC ceramic matrix composites: path toward 2700 °F temperature capability and beyond. Presented at: 41st Annual Conference on Composites, Materials, and Structures; 2017 Jan 23-27; Cocoa Beach, FL.

76. Wiesner V, Stokes J, Bansal N, Costa G, Kowalski B, Presby M, Bodenschatz C, Good B, Kulis M, Harder B. Advanced development of environmental barrier coatings resistant to attack by molten calcium-magnesium-aluminosilicate (CMAS). Presented at: 44th International Conference and Expo on Advanced Ceramics and Composites; 2020 Jan 26-31; Daytona Beach, FL.

77. Dao KC, Shockey DA, Seaman L, Curran DR, Rowcliffe DJ. Particle impact damage in silicon nitride. Menlo Park: SRI International; 1979. Office of Naval Research. Annual report. AD-A0773 570.

78. Akimune Y, Akiba T, Ogasawara T. Damage behavior of silicon nitride for automotive gas turbine use when impacted by several types of spherical particles. J Mater Sci. 1995;30:1000-1004.

79. Shin HS, Maekawa I. Characterization of particle impact damage and residual strength degradation behaviors in structural ceramics. JSME Int J Ser A Mech Matter Eng. 1998;38(1):116-122.

80. Choi SR. Foreign object damage behavior in a silicon nitride ceramic by spherical projectiles of steels and bras. Mater Sci Eng A. 2008;497(1-2):160-167.

81. Hara Y, Matsubara K, Mizuno K, Shimamori T, Yoshida H. Development and evaluation of silicon nitride components for ceramic gas turbine. Proceedings of the ASME 1998 International Gas Turbine and Aeroengine Congress and Exhibition. New York, NY: American Society of Mechanical Engineers; 1998: p.1-6 (V002T04A011).

82. Choi SR, Pereira JM, Janosik LA, Bhatt RT. Foreign object damage of two gas-turbine grade silicon nitrides in a thin disk configuration. Proceedings of the ASME Turbo Expo 2003: Power for Land, Sea, and Air. New York, NY: American Society of Mechanical Engineers; 2003: p. 1-11 (GT2003-38544).

83. Akimune Y, Akiba T, Hirosaki N, Ogasawara T. Thickness dependence of impact damage behavior in silicon nitride ceramic. J Euro Ceram Soc. 1993;11(5):425-429.

84. Akimune Y. Oblique impact of spherical particles onto silicon nitride. J Am Ceram Soc. 1990;73(12):3607-3610.

85. Shockey DA, Erlich DC, Dao KC. Particle impact damage in silicon nitride at 1400 °C. J Mater Sci. 1981;16:477-482.

86. Akimune Y, Katano Y, Matoba K. Spherical-impact damage and strength degradation in silicon nitrides for automotive turbocharger rotors. J Am Ceram Soc. 1989;72(8):1422-1428.

87. Akimune Y, Katano Y, Matoba K. Spherical-impact damage and strength degradation in silicon carbide whisker/silicon nitride composites. J Am Ceram Soc. 1989;72(5):791-798.

88. Akimune Y. Spherical-impact damage and strength degradation in Si_3N_4-SiC composites. J Mater Sci. 1990;25:3439-3448.

89. Choi SR, Pereira JM, Janosik LA, Bhatt RT. Foreign object damage in flexure bars of two gas-turbine grade silicon nitrides. Mater Sci Eng A. 2004;379(1-2):411-419.

90. Maekawa I, Shin HS, Miyata H. Particle impact damage on ceramics. Key Eng Mater. 1991;51-52:173-178.

91. Takahashi M, Yashiro S, Ogi K, Okabe N. Estimation of foreign-object damage to silicon carbide plates by silicon nitride spherical projectiles. Procedia Mater Sci. 2014;3:83-89.

92. Akimune Y. Hertzian cone crack in SiC caused by spherical particle impact. J Mater Sci. 1990;9:659-662.

93. Maekawa I, Shin HS. Damage induced in SiC by a particle impact. Eng Fract Mech. 1991;40(4-5):879-886.

94. Choi SR. Foreign object damage phenomenon by steel ball projectiles in a SiC/SiC ceramic matrix composite at ambient and elevated temperatures. J Am Ceram Soc. 2008;91(9):2963-2968.

95. Choi SR, Alexander DJ, Kowalik RW. Foreign object damage in an oxide/oxide composite at ambient temperature. J Eng Gas Turbines Power. 2009;131(2):021301(1-6).

96. Choi SR, Faucett DC, Alexander DJ. Foreign object damage by spherical steel projectiles in an N720/Alumina oxide/oxide ceramic matrix composites. J Am Ceram Soc. 2014;97(12):3926-3934.

97. Akimune Y, Ogasawara T, Akiba T, Hirosaki N. Spherical particle impact damage behavior of a SiC fiber-reinforced chemical vapor infiltrated SiC composite. J Mater Sci Let. 1991;10:689-692.

98. Faucett DC, Wright J, Ayer M, Choi SR. Effects of the mode of target supports on foreign object damage in an MI SiC/SiC ceramic matrix composite. In: Singh JP, Bansal NP, Goto T, Lamon J, Choi SR, Mahmoud MM, Link G, eds. Mechanical Properties and Performance of Engineering Ceramics and Composites VII. Hoboken: John Wiley and Sons, Inc., 2012; p.299-313.

99. Ogi K, Okabe T, Takahashi M, Yashiro S, Yoshimura A, Ogasawara T. Experimental characterization of high-speed impact damage behavior in a three-dimensionally woven SiC/SiC composite. Comp A. 2010;41(4):489-498.

100. Presby MJ, Morscher GN, Iwano C, Sullivan B. Foreign object damage in 3-D woven SiC/SiC ceramic matrix composites of varying architectures at ambient and high temperatures. Proceedings of the ASME Turbo Expo 2017: Power for Land, Sea, and Air. New York, NY: American Society of Mechanical Engineers; 2017: p. 1-9 (GT2017-63475).

101. Presby MJ, Mansour R, Manigandan K, Morscher GN, Abdi F, Godines C, et al. Characterization and simulation of foreign object damage in curved and flat SiC/SiC ceramic matrix composites. Ceram Int. 2019;45(2A):2635-2643.

102. Yashiro S, Ogi K, Oshita M. High-velocity impact damage behavior of plain-woven SiC/SiC composites after thermal loading. Comp B. 2012;43(3):1353-1362.

103. Choi SR, Faucett DC. Combined effects of CMAS and FOD in ceramic matrix composites. Proceedings of the ASME Turbo Expo 2012: Power for Land, Sea, and Air. New York, NY: American Society of Mechanical Engineers; 2012: p. 1-8 (GT2012-70049).

104. Kedir N, Faucett DC, Sanchez L, Choi SR. Foreign object damage in an oxide/oxide ceramic matrix composite under prescribed tensile loading. J Eng Turbines Power. 2017;139(2):021301(1-8).

105. Nicholls JR, Jaslier Y, Rickerby DS. Erosion and foreign object damage of thermal barrier coatings. Mater Sci Forum. 1997;2551-254:935-948.

106. Chen X, Wang R, Yao N, Evans AG, Hutchinson JW, Bruce RW. Foreign object damage in a thermal barrier system: mechanisms and simulations. Mater Sci Eng A. 2003;352(1-2):221-231.

107. Choi SR, Wright JM, Faucett DC, Ayer M. Phenomena of foreign object damage by spherical projectiles in EB-PVD thermal barrier coatings of turbine airfoils. J Eng Gas Turbines Power. 2014;136:102603(1-9).

108. Faucett DC, Wright J, Ayer M, Choi SR. Foreign object damage (FOD) in thermal barrier coatings. In: Singh JP, Bansal NP, Goto T, Lamon J, Choi SR, Mahmoud M, Link G, eds. Mechanical Processing and Properties of Advanced Ceramics and Composites IV. Hoboken: John Wiley and Sons, Inc., 2012; p.245-255.

109. Akimune Y, Akiba T, Hirosaki N, Izumi T. Impact damage behavior of CVD-coated silicon nitride for gas turbines. J Mater Sci. 1994;29:3243-3247.

110. Bhatt RT, Choi SR, Cosgriff LM, Fox DS. Lee KN. Impact resistance of environmental barrier coated SiC/SiC composites. Mater Sci Eng A. 2008;476(1-2):8-19.

111. Woodward RL, Baxter BJ. Ballistic evaluation of ceramics: Influence of test conditions. Int J Impact Eng. 1994;5(2):119-124.

112. Chaudhri MM, Brophy PA. Single particle impact damage of fused silica. J Mater Sci. 1980;15:345-352.

113. Chaudhri MM, Knight CG, Swain M. Impact of microparticles on brittle solids. Proceedings of SPIE 0097: 12th International Congress on High Speed Photography. Toronto CA: Society of Photographic Instrumentation Engineers; 1977: p.371-376.

114. Chaudhri MM. Dynamic fracture of inorganic glasses by hard spherical and conical projectiles. Phil Trans R Soc A. 2014;373:20140135(1-26).

115. Riou P, Denoual C, Cottenot CE. Visualization of the damage evolution in impacted silicon carbide ceramics. Int J Imp Eng. 1998;21(4):225-235.

116. Strassburger E. Visualization of impact damage in ceramics using edge-on impact technique. Int J Appl Ceram Technol. 2004;1(3):235-242.

117. Mattsson A. New developments in flash radiography. Proceedings of SPIE 0097: 27th International Congress on High Speed Photography and Photonics. Xi'an CN: Society of Photographic Instrumentation Engineers; 2006: p.1-11(62790Z).

118. Germer R. X-ray flash techniques. J Phys E Sci Instrum. 1979;12(5):336-350.

119. Zellner MB, Love MS, Chapley K. Development of ARL's multi-energy flash computed tomography diagnostic: capability to track mass-flux through a reconstruction volume. Proceedings of the 2019 Hyper Velocity Impact Symposium. New York, NY: American Society of Mechanical Engineers; 2020: p. 1-7(V001T08A001).

120. Luo SN, Jensen BJ, Hooks DE, Fezzaa K, Ramos KJ, Yeager JD, et al. Gas gun shock experiments with single pulse X-ray phase contrast imaging and diffraction at the advanced photon source. Rev Sci Instrum. 2012;83:073903(1-11).

121. Fenner RB. Introduction to the advanced photon source. Guide presented at; 2005; Argonne National Laboratory.

122. Nash B. Physics of the electron beam source: beam size, shape and lifetime and the relationship to the X-ray radiation properties. Lecture presented at; 2011; European Synchrotron Radiation Facility.

123. Lewis RA. Medical phase contrast X-ray imaging: current status and future prospects. Phys Med Biol. 2004;49:3573-3583.

124. Jensen BJ, Montgomery DS, Iverson AJ, Carlson CA, Clements B, Short M, et al. X-ray phase contrast imaging of granular systems. In: Vogler TJ, Fredenburg DA, eds. Shock phenomenon in granular and porous materials. Switzerland: Springer Nature Switzerland AG, 2019; p. 195-230.

125. Parab ND, Guo Z, Hudspeth MC, Claus BJ, Fezzaa K, Sun T, et al. Fracture mechanics of glass particles under dynamic compression. Int J Imp Eng. 2017;106:146-154.

126. Van Roode M, Price JR, Jimenez O, Miriyala N, Gates Jr S. Design and testing of ceramic components for industrial gas turbines. In: Heinrich JG, Aldinger F, eds. Chapter 3 in Ceramic Materials and Components for Engines. Weinheim, DE: WILEY-VCH Verlag GmbH; 2007:261-266.

127. Wiederhorn SM, Ferber MK. Silicon nitride for gas turbines. Curr Opin Solid State Mater Sci. 2001;5(4):311-316.

128. Zok F. Ceramic-matrix composites enable revolutionary gains in turbine engine efficiency. Am Ceram Soc Bull. 2016;95(5):22-28.

129. Lin HT, Ferber MK. Mechanical reliability evaluation of silicon nitride ceramic components after exposure in industrial gas turbines. J Eur Ceram Soc. 2002;22(14-15):2789-2797.

130. Evans AG. Strength degradation by projectile impacts. J Am Ceram Soc. 1973;56(8):405-409.

131. Wiederhorn SM, Lawn BR. Strength degradation of glass resulting from impact with spheres. J Am Ceram Soc. 1977;60(9):451-458.

132. Tsuruta H, Masuda M, Soma T, Matsui M. Foreign object damage resistance of silicon nitride and silicon carbide. J Am Ceram Soc. 1990;73(6):1714-1718.

133. Compton BG, Gamble EA, Deshpande VS, Zock FW. Damage development in an armor alumina impacted with ductile metal spheres. J Mech Mater Struct. 2012;7(6):575-590.

134. Kim DK, Lee CS, Kim YG, Kim CW, Chang SN. Dynamic indentation of ceramics. In: McCauley JW, Crowson A, Gooch Jr WA, Rajendran AM, Bless SJ, Logan K, Normandia M, Wax S, eds. Ceramic Transactions. Westerville, Ohio: The American Ceramic Society; 2002:261-268.

135. Chaudhri MM, Walley SM. Damage to glass surfaces by the impact of small glass and steel spheres. Philos Mag A. 1978;37(2):153-165.

136. Rahman A, Singh A, Harimkar SP, Singh RP. Mechanical characterization of fine grained silicon carbide consolidated using polymer pyrolysis and spark plasma sintering. Ceram Int. 2014;40(8):12081-12091.

137. Nakazawa K, Krauss G. Microstructure and fracture of 52100 steel. Metall Trans A. 1978;9:681-689.

138. Hudspeth MC, Claus B, Dubelman S, Black JT, Mondal A, Parab ND, et al. High speed synchrotron X-ray phase contrast imaging of dynamic material response to split hopkinson bar loading. Rev Sci Instrum. 2013;84(2):025102.

139. Chen WW, Hudspeth MC, Claus B, Parab ND, Black JT, Fezzaa K, et al. In situ damage assessment using synchrotron X-ray in materials loaded by a hopkinson bar. Philos Trans R Soc A. 2014;372(2015):20130191.

140. Rajendran AM, Bless SJ. High strain rate material behavior. Dayton: Materials Laboratory (AFWAL/ML); 1985. Air Force Wright Aeronautical Laboratories. Technical Report. AFWAL-TR-85-4009.

141. Chen WW, Song B. Split hopkinson (Kolsky) bar: design, testing and applications. 1st. New York, NY: Springer; 2011.

142. Wang Z, Li P, Song W. Inelastic deformation micromechanism and modified fragmentation model for silicon carbide under dynamic compression. Mater Des. 2018;157:244-250.

143. Zhang D, Zhao LG, Roy A. Mechanical behavior of silicon carbide under static and dynamic compression. J Eng Mater Technol. 2018;141(1):011007(1-10).

144. Lankford J. Mechanisms responsible for strain-rate-dependent compressive strength in ceramic materials. Comm Am Ceram Soc. 1981;64(2):c33-c34.

145. Healey A, Cotton J, Maclachlan S, Smith P, Yeomans J. Understanding the ballistic event: methodology and initial observations. J Mater Sci. 2017;52:3074-3085.

146. Shih CJ, Nesterenko VF, Meyers MA. High-strain-rate deformation and comminution of silicon carbide. J Appl Phys. 1998;83(9):4660-4671.

147. Lawn BR. Indentation of ceramics with spheres: a century after hertz. J Am Ceram Soc. 2005;81(8):1977-1994.

148. Marimuthu KP, Rickhey F, Lee JH, Lee H. Spherical indentation for brittle fracture toughness evaluation by considering kinked-cone-crack. J Eur Ceram Soc. 2017;37(1):381-391.

149. Akimune Y. Impact damage and strength degradation in a silicon carbide reinforced silicon nitride composite. J Am Ceram Soc. 1990;73(10):3019-3025.

150. Knight CG, Swain MV, Chaudhri MM. Impact of small steel spheres on glass surfaces. J Mater Sci. 1977;12:1573-1586.

151. Timoshenko SP, Goodier JN. Axially symmetrical stress distribution in a solid of revolution. Chapter 13 in Theory of Elasticity. New York, NY: McGraw-Hill; 1951,383-384.

152. Fisher-Cripps AC. Elastic contact. In: Ling FF, editor. Chapter 6 in Introduction to Contact Mechanics. New York, NY: Springer; 2007:101-114.

153. Johnson KL. Point loading of an elastic half-space. Chapter 3 in Contact Mechanics. New York, NY: Cambridge University Press; 1996:45-83.

154. Karanjgaokar N. Evaluation of energy contributions using inter-particle forces in granular materials under impact loading. Granul Matter. 2017;19:36(1-20).

155. Smialek JL, Jacobson NS. Mechanism of strength degradation for hot corrosion of α-SiC. J Am Ceram Soc. 1986;69(10):741-752.

156. Federer JI, Van Roode M, Price JR. Evaluation of ceramic coatings on silicon carbide. Surf Coat Technol. 1989;39/40(1):71-78.

157. Lee KN, Van Roode M. Environmental barrier coatings enhance performance of SiC/SiC ceramic matrix composites. Am Ceram Soc Bull. 2019;98(3):46-53.

158. Turcer LR. Padture NP. Towards multifunctional thermal environmental barrier coatings (TEBCs) based on rare-earth pyrosilicate solid-solution ceramics. Scr Mater. 2018;154:111-117.

159. Dericioglu AF, Zhu S, Kagawa Y, Kasano H. Damage behavior of air-plasma sprayed thermal barrier coatings under foreign object impact. Adv Eng Mater. 2003;5(10):735-737.

160. Kedir N, Kirk CD, Zherui G, Kreschen NE, Tao S, Fezza K, et al. Real-time visualization of impact damage in monolithic silicon carbide and fibrous silicon carbide ceramic composite. Int J Impact Eng. 2019;129:168-179.

161. Kerschen NE, Sorensen CJ, Guo Z, Mares JO, Fezzaa K, Sun T, et al. X-Ray phase contrast imaging of the impact of a single HMX particle in a polymeric matrix. Propellants, Explos, Pyrotech. 2019;44(4):447-454.

162. Herman H. Plasma-sprayed coatings. Sci Am. 1988;259(3):112-117.

163. Girolamo GD, Blasi C, Pilloni L, Schioppa M. Microstructural and thermal properties of plasma sprayed mullite coatings. Ceram Int. 2010;36(4):1389-1395.

164. Cojocaru CV, Wang Y, Moreau C, Lima RS, Mesquita-Guimaraes J, Garcia E, et al. Mechanical behavior of air plasma-sprayed YSZ functionally graded mullite coatings investigated via instrumented indentation. J Therm Spray Technol. 2011;20(1/2):100-107.

165. Yoo WS, Kim JH, Han SM. Multiwavelength Raman characterization of silicon stress near through-silicon vias and its inline monitoring applications. J Micro/Nanolith. 2014;13(1):011205(1-9).

166. Kalita P. High pressure behavior of mullite-type oxides: phase transitions, amorphization, negative linear compressibility and microstructural implications. Las Vegas, NV: Doctoral dissertation; University of Nevada, Las Vegas; 2015.

167. Matejicek J, Sampath S. In situ measurement of residual stresses and elastic moduli in thermal sprayed coatings Part 1: apparatus and analysis. Acta Mater. 2003;51(3):863-872.

168. Qian G, Nakamura T, Berndt CC. Effects of thermal gradient and residual stresses on thermal barrier coating fracture. Mech Mater. 1998;27(2):91-110.

169. Pajares A, Wei L, Lawn BR, Berndt CC. Contact damage in plasma-sprayed alumina based coatings. J Am Ceram Soc. 1996;79(7):1907-1914.

170. Pajares A, Wei L, Lawn BR, Padture N, Berndt CC. Mechanical characterization of plasma sprayed ceramic coatings on metal substrates by contact testing. Mater Sci Eng, A. 1996;208(2):158-165.

171. Tomasz S, Przemyslaw G. Numerical and experimental analysis of foreign object impact into the surface with TBC coating. Solid State Phenom. 2016;254;224-230.

172. Wiederhorn SM, Lawn BR. Strength degradation of glass impacted with sharp particles: I, Annealed surfaces. J Am Ceram Soc. 1979;62(1/2):66-70.

173. Lawn BR, Padture NP, Cai H, Guiberteau F. Making ceramics “Ductile”. Science. 1994;263(5150):1114-1116.

174. Lawn BR, Padture NP, Guiberteau F, Cai H. A model for microcrack initiation and propagation beneath hertzian contacts in polycrystalline ceramics. Acta Metall Mater. 1994;42(5):1683-1693.

175. Fischer-Cripps A, Lawn BR, Pajares A, Wei L. Stress analysis of elastic-plastic contact damage in ceramic coatings on metal substrates. J Am Ceram Soc. 1996;79(10):2619-2625.

176. Wuttiphan S, Pajares A, Lawn BR, Brendt CC. Effects of substrate and bond coat on contact damage in zirconia-based plasma-sprayed coatings. Thin Solid Films. 1997;293(1/2):251-260.

177. Raman CV. On some applications of hertz's theory of impact. Phys Rev. 1920;15(4):277-284.

178. Zener C. The intrinsic inelasticity of large plates. Phys Rev. 1941;59(8):669-673.

179. Koller MG, Kolsky H. Waves produced by the elastic impact of spheres on thick plates. Int J Solids Struct. 1987;23(10):1387-1400.

180. Kedir N, Garcia E, Kirk CD, Zherui G, Gao J, Zhai X, et al. In situ characterization of foreign object damage (FOD) in environmental-barrier-coated silicon carbide (SiC) ceramic. J Am Ceram Soc. 2020:103(8):4586-4601.

181. Klopp RW, Shockey DA. Tests for determining failure criteria of ceramics under ballistics impact. Menlo Park: SRI International; 1992. U.S. Army Research Office. Technical report. ARO26173.4-MS-A.

182. Chen WW, Rajendran AM, Song B, Nie X. Dynamic fracture of ceramics in armor applications. J Am Ceram Soc. 2007;90(4):1005-1018.

183. Wilkins ML. Mechanics of penetration and perforation. Int J Eng Sci. 1978;16(11):793-807.

184. Dharan CKH, Hauser FE. Determination of stress-strain characteristics at very high strain rates. Exp Mech. 1970;10:370-376.

185. Heard WF, Martin BE, Nie X, Slawson T, Basu PK. Annular pulse shaping technique for large-diameter kolsky bar experiments on concrete. Exp Mech. 2014;54:1343-1354.

186. Hauver GE, Netherwood PH, Benck RF, Gooch WA, Perciballi WJ, Burkins MS. Variation of target resistance during long rod penetration into ceramics. Proceedings of the 13th International Ballistic Symposium. Stockholm, Sweden; 1992: p. 257-264.

187. Pickering EG, O'Masta MR, Wadley HNG., Deshpande VS. Effect of confinement on the static and dynamic indentation response of model ceramic and cermet materials. Int J Imp Eng. 2016;110:123-137.

188. Holmquist TJ, Anderson Jr CE, Behner T, Orphal DL. Mechanics of dwell and post-dwell penetration. Adv App Ceram. 2010:109(8):467-479.

189. Carton E, Roebroeks G. Testing method for ceramic armor and bare ceramic tiles. In: LaSalvia JC, Gyekenyesi A, Halbig M, eds. In Advances in Ceramic Armor. Westerville, Ohio: The American Ceramic Society; 2015:1-12.

190. Iyer KA. Relationships between multiaxial stress states and internal fracture patterns in sphere-impacted silicon carbide. Int J Fract. 2007;146:1-18.

191. Holmquist TJ, Anderson Jr CE, Behner T. Design, analysis and testing of an unconfined ceramic target to induce dwell. Proceedings of the 22nd International Symposium on Ballistics. Lancaster, PA: DEStech Publications, Inc.; 2005: p. 860-868.

192. Behner T, Heine A, Wickert M. Dwell and penetration of tungsten heavy alloy long-rod penetrators impacting unconfined finite-thickness silicon carbide ceramic targets. Int J Imp Eng. 2016;95:54-60.

193. Zhong X, Niu Y, Huang L, Li H, Zheng X, Ding C, et al. Microstructure and thermal properties of atmospheric plasma-sprayed $Yb_2Si_2O_7$ coating. J Therm Spray Tech. 2017;26:203-210.

194. Zhong X, Niu Y, Huang L, Zeng Y, Zheng X, Ding C, et al. Microstructure evolution and thermomechanical properties of plasma-sprayed Yb_2SiO_5 coating during thermal aging. J Am Ceram Soc. 2017;100(5):1896-1906.

195. Han J, Wang Y, Liu R, Cao Y. Thermal shock behavior of mixed ytterbium disilicate and ytterbium monociliate composite environmental barrier coatings. Surf Coat Technol. 2018;352:348-353.

196. Glymond D, Vick MJ, Giuliani F, Vanderperre LJ. High-temperature fracture toughness of mullite with monoclinic zirconia. J Am Ceram Soc. 2017;100(4):1570-1577.

197. Ritter JE. Spherical particle impact damage. Key Eng Mater. 1992;71:107-120.

198. Grujicic M, Snipes J, Yavari R, Ramaswami S, Galgalikar R. Computational investigation of foreign object damage sustained by environmental barrier coatings (EBCs) and SiC/SiC ceramic-matrix composites (CMCs). Multidiscip Model Mater Struct. 2015;11(2):238-272.

199. Oliver WC, Pharr GM. Improved technique for determining hardness and elastic modulus using load and displacement sensing indentation experiments. J Mater Res. 1992;7(6):1564-1583.

200. Jung YG, Lawn BR, Martyniuk M, Huang H, Hu XZ. Evaluation of elastic modulus and hardness of thin filmsby nanoindentation. J Mater Res. 2004;19(10):3076-3080.

VITA

Nesredin F. Kedir

Education

- Ph.D., Materials Engineering, Purdue University, May 2021.
  "*In situ* Characterization of Damage Kinetics During Foreign Object Debris (FOD) Impact of Silicon Carbide"
- B.Sc., Materials Science and Engineering, University of Maryland, Dec 2013.

Academic Experience

- Graduate Research Assistant, School of Materials Engineering, Purdue University, Aug 2016 – May 2021. Research activities include: development of impact and laser irradiation facilities, application of pulsed synchrotron X-ray radiography techniques for *in situ* damage monitoring, processing and characterization of gas turbine EBCs and ceramics, evaluation of directed energy damage on polymer matrix composite structures.
- Graduate Teaching Assistant, School of Materials Engineering, Purdue University, Jan 2019 – May 2019. Responsibilities include: delivering pre-lab instruction to undergraduate students on safe and accurate implementation of X-ray diffraction technique/ instrumentation for determining phase and chemistry of unknown materials.
- Teaching Assistant, Department of Materials Science and Engineering, University of Maryland, Aug 2013 – Dec 2013. Responsibilities include: delivering pre-lab instructions to undergraduate students on safe operation of various mechanical test equipment's, advising on laboratory report writeups.

Industry Experience

- Materials Engineer, Metals and Ceramics Branch, Naval Air Warfare Center (NAVAIR), Feb 2014 – Jun 2016. Responsibilities included: developing subject matter expertise on metallic materials for fixed wing platforms, characterization of gas turbine grade ceramic matrix composites (CMCs), and nondestructive evaluation of aircraft components.

Lead Author Publications

- **N. Kedir**, J. Hernandez, B. Lim, J. Gao, X. Zhai, Y. Nie, C. Kirk, T. Tallman, W. Chen, "Time dependent response of carbon fiber reinforced plastic (CFRP) to irradiation by a short pulse near-infrared (NIR) laser", 2021, under review in *J Laser Appl*.

- **N. Kedir**, E. Garcia, C. Kirk, J. Gao, Z. Guo, X. Zhai, T. Sun, K.l Fezzaa, S. Sampath, W. Chen, "Impact damage of narrow silicon carbide (SiC) ceramics with and without environmental barrier coatings (EBCs) by various foreign object debris (FOD) simulants", 2020, accepted in *Surface and Coatings Technology*. https://doi.org/10.1016/j.surfcoat.2020.126779

- **N. Kedir**, E. Garcia, C. Kirk, Z. Guo, J. Gao, X. Zhai, T. Sun, K.l Fezzaa, S. Sampath, W. Chen, "In situ characterization of foreign object damage (FOD) in environmental-barrier-coated silicon carbide (SiC) ceramic", 2020, accepted in *Journal of American Ceramic Society*. https://doi.org/10.1111/jace.17165

- **N. Kedir**, C. Kirk, Z. Guo, N. Kerschen, T. Sun, K. Fezzaa, W. Chen, "Real-time visualization of impact damage in monolithic silicon carbide and fibrous silicon carbide ceramic composite", 2019, accepted in *International Journal of Impact Engineering*. https://doi.org/10.1016/j.ijimpeng.2019.01.012

- **N. Kedir**, D. Faucett, L. Sanchez, S. Choi, "Foreign object damage behavior of a silicon carbide fibrous ceramic composite", 2019, accepted in *Journal of Engineering for Gas Turbines and Power*. https://doi.org/10.1115/1.4041657

- **N. Kedir**, C. Gong, L. Sanchez, M. Presby, S. Kane, D. Faucett, S. Choi, "Erosion in gas-turbine grade ceramic matrix composites", 2019, accepted in *Journal of Engineering for Gas Turbines and Power*. https://doi.org/10.1115/1.4040848

- **N. Kedir**, D. Faucett, S. Choi, N. Bansal, "Slow-crack-growth and indentation damage in calcium magnesium aluminosilicate (CMAS) glass from desert sand", 2018, accepted in *Ceramics International*. https://doi.org/10.1016/j.ceramint.2017.10.194

- **N. Kedir**, D. Faucett, L. Sanchez, S. Choi, "Foreign object damage in an oxide/oxide ceramic matrix composite under prescribed tensile loading", 2017, accepted in *Journal of Engineering for Gas Turbines and Power*. https://doi.org/10.1115/1.4034360

Co-author Publications

- J. Copley, F. Coury, B. Ellyson, J. Klemm-Toole, **N. Kedir**, C. Kirk, W. Chen, N. Parab, T. Sun, K. Fezzaa, K. Clarke, A. Clarke, “In-situ observation of FCC to HCP transformation-induced plasticity behavior during dynamic deformation of CoCrNi multi-principle element alloys” 2021, under review in *Met Mater Trans A*.

- J. Copley, B. Ellyson, J. Klemm-Toole, J. Gao, **N. Kedir**, C. Kirk, W. Chen, N. Parab, T. Sun, K. Fezzaa, K. Clarke, A. Clarke, "HiSPoD as a preparatory tool for improving design of high-rate synchrotron diffraction experiments", 2021, under review in *J Synch Rad*.

- J. Gao, **N. Kedir**, C. Kirk, J. Hernandez, J. Wang, S. Paulson, X. Zhai, T. Horn, G. Kim, K. Fezzaa, F. De Carlo, P. Shevchenko, T. Tallman, R. Sterkenburg, W. Chen, "High-speed synchrotron X-ray phase contrast imaging for evaluation of microscale damage mechanisms and fracture toughness of cross-ply GFRCs", 2021, under review in *Comp Sci Technol.*

- J. Gao, **N. Kedir**, W. Chen, "Characterization of failure of single carbon nanotube fibers under extreme transverse loading" 2021, under review in *Carbon*.

- J. Gao, Z. Guo, J. Hernandez, F. Zhou, Y. Nie, J. Gao, B. Lim, **N. Kedir**, X. Zhai, J. Wang, J. Tsai, F. De Carlo, P. Shevchenko, T. Tallman, M. Jun, G. Palmese, W. Chen, "Transverse impact by RCCs on S-glass and Kevlar FRC strips", 2021, under review in *Comp Pt A*.

- J. Gao, **N. Kedir**, C. Kirk, J. Hernandez, J. Wang, S. Paulson, X. Zhai, T. Horn, G. Kim, J. Gao, K. Fezzaa, F. De Carlo, P. Shevchenko, T. Tallman, R. Sterkenburg, G. Palmese, W. Chen, "Real-time damage characterization for GFRCs using high-speed synchrotron X-ray phase contrast imaging", 2020, accepted in *Comp Part B: Eng*. https://doi.org/10.1016/j.compositesb.2020.108565

- J. Gao, B. Lim, X. Zhai, Y. Nie, **N. Kedir**, W. Chen, "Failure behaviors of single high-performance fibers under transverse dynamic cut", 2020, accepted in *International Journal of Impact Engineering*. https://doi.org/10.1016/j.ijimpeng.2020.103660

- J. Hernandez, **N. Kedir**, B. Lim, W. Chen, T. Tallman, "An experimental study on the piezoresistive and mechanical behavior of carbon nanocomposites subject to high-rate elastic loading", 2020, accepted in *Composites Science and Technology*. https://doi.org/10.1016/j.compscitech.2020.108285

- X. Zhai, Y. Nie, J. Gao, **N. Kedir**, B. Claus, T. Sun, K. Fezzaa, W. Chen, "The effect of loading direction on the fracture behaviors of cortical bone at a dynamic loading rate", 2020, accepted in *Journal of the Mechanics and Physics of Solids*. https://doi.org/10.1016/j.jmps.2020.104015

- J. Gao, Y. Nie, B. Lim, X. Zhai, **N. Kedir**, W. Chen, "In-situ observation of cutting-induced failure processes of single high-performance fibers inside a SEM", 2020, accepted in *Composites Part A*. https://doi.org/10.1016/j.compositesa.2020.105767

- M. Presby, C. Gong, S. Kane, **N. Kedir**, A. Stanley, D. Faucett, S. Choi, "Erosion in a Melt-Infiltrated SiC/SiC Ceramic Matrix Composite", 2020, accepted in *Journal of Engineering for Gas Turbines and Power*. https://doi.org/10.1115/1.4044900

- Y. Nie, B. Claus, J. Gao, X. Zhai, **N. Kedir**, J. Chu, T. Sun, K. Fezzaa, W. Chen, "In Situ Observation of Adiabatic Shear Band Formation in Aluminum Alloys", 2020, accepted in *Experimental Mechanics*. https://doi.org/10.1007/s11340-019-00544-w

- X. Zhai, J. Gao, Y. Nie, Z. Guo, **N. Kedir**, B. Claus, T. Sun, K. Fezzaa, X. Xiao, W. Chen, "Real-time visualization of dynamic fractures in porcine bones and the loading-rate effect on their fracture toughness", 2019, accepted in *Journal of the Mechanics and Physics of Solids*. https://doi.org/10.1016/j.jmps.2019.07.010

- C. Kirk, N. Parab, **N. Kedir**, Z. Guo, Y. Nie, S. Paulson, J. Thomas, K. Fezzaa, T. Sun, W. Chen, "In-Situ Visualization of Tensile Failure in Additively Manufactured 316 L Stainless Steel", 2019, accepted in *Experimental Mechanics*. https://doi.org/10.1007/s11340-019-00524-0

- J. Gao, Y. Nie, B. Lim, **N. Kedir**, W. Chen, "A Microscopic Experimental Method Transversely Loading on Single High-Performance Fibers", 2019, accepted in *Experimental Mechanics*. https://doi.org/10.1007/s11340-019-00518-y

- X. Zhai, Z. Guo, J. Gao, **N. Kedir**, Y. Nie, B. Claus, T. Sun, K. Fezzaa, X. Xiao, W. Chen, "High-speed X-ray visualization of dynamic crack initiation and propagation in bone", 2019, accepted in *Acta biomaterialia*. https://doi.org/10.1016/j.actbio.2019.03.045

- M. Presby, **N. Kedir**, L. Sanchez, D. Faucett, S. Choi, G. Morscher, "Life-limiting behavior of an oxide/oxide ceramic matrix composite at elevated temperature subject to foreign object damage", 2019, accepted in *Journal of Engineering for Gas Turbines and Power*. https://doi.org/10.1115/1.4041145

Conference Proceedings

- J. Gao, **N. Kedir**, C. Kirk, J. Hernandez, J. Wang, X. Zhai, T. Horn, G. Kim, K. Fezzaa, F. DeCarlo, P. Shevchenko, T. Tallman, R. Sterkenburger, W. Chen, "In-situ observation of dynamic damage evolution inside GFRCs through high-speed X-ray PCI", 2020, accepted in p*roceedings of the American Society for Composites—Thirty-fifth Technical Conference*. DOI 10.12783/asc35/34893

- J. Gao, Z. Guo, Y. Nie, J. Hernandez, B. Lim, **N. Kedir**, T. Tallman, W. Chen, "Transverse impact on a single layer S-Glass/SC15 Epoxy composite strip", 2019, accepted in *Proceedings of the American Society for Composites—Thirty-fourth Technical Conference*. DOI 10.12783/asc34/31271

- D. Shifler, L. Sanchez, **N. Kedir**, D. Faucett, R. Mahapatra, S. Choi, "Thermal stability of nickel-base alloys", 2016, accepted in *ASME Turbo Expo 2016: Turbomachinery Technical Conference and Exposition*. https://doi.org/10.1115/GT2016-57991

Book Chapters

- S. Paulson, **N. Kedir**, T. Sun, K. Fezzaa, Wa. Chen, "Observation of Dynamic Adhesive Behavior Using High-Speed Phase Contrast Imaging", 2020, accepted in *Dynamic Behavior of Materials*. https://doi.org/10.1007/978-3-030-30021-0_34

- **N. Kedir**, S. Paulson, C. Kirk, T. Sun, K. Fezzaa, W. Chen, "Observation of Dynamic Adhesive Behavior Using High-Speed Phase Contrast Imaging", 2020, accepted in *Dynamic Behavior of Materials*. https://doi.org/10.1007/978-3-030-30021-0_31

- M. Presby, **N. Kedir**, L. Sanchez, C. Gong, D. Faucett, S. Choi, G. Morscher, "Erosion behavior in a gas turbine grade Oxide/Oxide ceramic matrix composite", 2018, accepted in *Proceedings of the 42nd International Conference on Advanced Ceramics and Composites, Ceramic Engineering and Science Proceedings*. https://doi.org/10.1002/9781119543343.ch2

- **N. Kedir**, D. Faucett, L. Sanchez, S. Choi, "Foreign object damage in a SiC fibrous composite", 2018, accepted in *Ceramic Transactions*, https://doi.org/10.1002/9781119423829.ch4

- **N. Kedir**, G. Gilde, K. Cho, "Consolidation of aluminum magnesium boride ($AlMgB_{14}$) by pulsed electric current sintering (PECS) technique", 2013, accepted in *Advances in Ceramic Armor IX*, https://doi.org/10.1002/9781118807576.ch13

Conference Presentations

- **Speaker**, Materials Science and Technology, 2020.
- **Speaker**, Society of Experimental Mechanics Annual Conference, 2019.
- **Poster**, Mach Conference, 2019.
- **Speaker**, 42nd International Conference and Expo on Advanced Ceramics and Composites, 2018.
- **Speaker**, Turbo Machinery Technical Conference and Exposition, 2017.
- **Speaker**, Materials Science and Technology, 2016.

Awards

- **Outstanding Project Award for Basic and Applied Research** (2017): awarded by the Chief Technology Officer of the Naval Air Warfare Center Aircraft Division to sixteen projects out of three hundred and ninety-two submittals

- **Purdue Doctoral Fellowship** (2016): highly competitive award provided by the Graduate School to one incoming graduate student within each engineering department